Improvements in production and storage of HP-^{129}Xe

Dissertation

zur Erlangung des Grades
"Doktor der Naturwissenschaften"

am Fachbereich Physik, Mathematik und Informatik
der Johannes Gutenberg Universität
in Mainz

vorgelegt von

Maricel Teresa Repetto

geboren in Buenos Aires/Argentinien

Mainz, October 2015

D77

Termin der mündliche Prüfung: 13.11.2015

"Und das heisse mir aller Dinge unbefleckte
Erkenntniss, dass ich von den Dingen Nichts
will: ausser dass ich vor ihnen da liegen darf
wie ein Spiegel mit hundert Augen."

Friedrich Nietzsche, Also sprach Zarathustra

Abstract

Since its discovery in 1978, hyperpolarized (HP) ^{129}Xe has found numerous applications. Due to its high enhancement of NMR-signals it is typically used for tracer and surface studies; so as a clinical contrast agent in the gas phase for dynamic lung MRI or dissolved in blood or lipophilic liquids. In fundamental physics, HP-Xe is used in He-Xe co-magnetometers for measuring the electric dipole moment of Xe and testing Lorentz invariances. All these applications profit from a high polarization (P_{Xe}) in order to achieve extensively high signals and long storage times for preserving it. In this work, two mobile Xe-polarizers were constructed: one for fundamental physics experiments with a production rate of 400 mbar·l/h with $P_{Xe} \approx 5$ %. Another Xe-polarizer for medical applications, so far not tested, was designed to produce 1 bar·l/h with $P_{Xe} > 20$ %.

The working conditions of the Xe-polarizer for fundamental physics (gas mixture flow, temperature, pressure and amount of Xe) were varied in order to find the values which lead to the highest polarization possible with this setup. The maximum polarization achieved was 5.6 % using a gas mixture with 1% of Xe, 200 ml/min flow, 150°C and a total gas mixture pressure of 4 bar.

HP-Xe must be efficiently stored in order to minimize polarization losses for those applications where the HP-Xe must be transported to another facility and/or long spin coherence times are required e.g. He-Xe co-magnetometers. The greatest difficulty so far was to ensure the reproducibility of the measured storage times. In this work, the spin-lattice relaxation time (T_1) of hyperpolarized HP-^{129}Xe was significantly improved using uncoated, Rb-free, spherical cells made from aluminosilicate glass (GE-180). The T_1 was determined in a self-made low field NMR system (2 mT) for both: pure HP-Xe and HP-Xe in mixtures with N_2, SF_6 and CO_2. From these experiments, the limiting relaxation time for pure Xe (with 85% ^{129}Xe) was found to be (4.6 ± 0.1) h and typical wall relaxation times of about 18 h could be achieved for glass cells of 10 cm in diameter. Furthermore, it was found that especially CO_2 exhibited an unexpected high efficiency in shortening the lifetime of the Xe-Xe dimers and hence prolonging the total T_1. In the course of many experiments, an “aging” process of the wall relaxation was identified and studied by repeating measurements on the same cell. This effect could be easily undone by performing the initial cleaning procedure. In this way, a constant wall relaxation was ensured allowing very reproducible T_1-measurements. In addition, the limiting relaxation time for HP-Xe in natural abundance was determined in mixtures with SF_6. Surprisingly, this value turned out to be about 75% shorter when compared to that found for Xe with 85% isotopic enrichment. This effect was confirmed by three independent experiments since it is not deducible from the existing theory of Xe relaxation.

Finally, P_{Xe} is usually determined by comparing the NMR signals of HP-Xe with a

thermally polarized sample (typically $^{1}H_2O$ or Xe). The difference in comparing two different samples (different pressure, signal intensity and measurement procedure) could lead to many experimental uncertainties, which are not easy to estimate. Developing a simple, accurate and inexpensive method to determine P_{Xe} was developed by the direct measurement of its macroscopic magnetization in a static magnetic field avoids all these uncertainties. This method can determine polarizations ≥ 2 % with a sensitivity better than 10% with nearly no polarization losses. In addition, this method can be used without further modifications for all HP gases.

Zusammenfassung

Seit seiner Entdeckung im Jahre 1978 wurden für hyperpolarisiertes (HP) ^{129}Xe zahlreiche Anwendungen gefunden. Aufgrund seiner hohen Verstärkung von NMR-Signalen wird es dabei typischerweise für *Tracer*- und Oberflächenstudien verwendet. Im gasförmigen Zustand ist es ein interessantes, klinisches Kontrastmittel, welches für dynamische Lungen MRT genutzt oder auch in Blut oder lipophilen Flüssigkeiten gelöst werden kann. Weiterhin findet HP-Xe auch in der Grundlagenphysik in He-Xe Co-Magnetometern Verwendung, mit welchen z. B. das elektrische Dipolmoment von Xe bestimmt werden soll, oder es dient zur Überprüfung auf Lorentz-Invarianzen. Alle diese Anwendungen profitieren von einem hohen Polarisationsgrad (P_{Xe}), um hohe Signalstärken und lange Lagerzeiten zu erreichen.

In dieser Arbeit wurden zwei mobile Xe-Polarisatoren konstruiert: einer für Experimente in der Grundlagenphysik mit einer Produktionsrate von 400 mbar·l/h mit P_{Xe} ≈ 5%. Der zweite Xe-Polarisator wurde für medizinische Anwendungen entwickelt und soll 1 bar l/h mit P_{Xe} > 20% erzeugen. Der letztere wurde noch nicht getestet. Die Arbeitsbedingungen des Xe-Polarisators für Grundlagenphysik (Strömung des Gasgemischs, Temperatur, Druck und Konzentration von Xe) wurden variiert, um einen höchstmöglichen Polarisationsgrad zu erzielen. Die maximale Polarisation von 5,6 % wurde bei Verwendung eine Gasmischung von 1% Xe bei einem Durchfluss von 200 ml/min, einer Temperatur von 150°C und einem Gesamtdruck von 4 bar erreicht.

Weiterhin muss HP-Xe auch effizient gelagert werden, um Polarisationsverluste zu minimieren. Das ist besonders für solche Anwendungen notwendig, welche an einem entfernten Standort durchgeführt werden sollen oder auch wenn lange Spinkohärenzeiten gefordert sind, z.B. bei He-Xe Co-Magnetometern.

Hierbei bestand bisher die größte Schwierigkeit darin, die Reproduzierbarkeit der gemessenen Lagerzeiten sicherzustellen. In dieser Arbeit konnte die Spin-Gitter-Relaxationszeit (T_1) von HP-^{129}Xe in unbeschichteten, Rb-freien, sphärischen Zellen aus Aluminiumsilikatglas (GE-180) signifikant verbessert werden. Die T_1–Zeit wurde in einem selbstgebauten Niederfeld-NMR-System (2 mT) sowohl für reines HP-Xe als auch für HP-Xe in Mischungen mit N_2, SF_6 und CO_2 bestimmt. Bei diesen Experimenten wurde die maximale Relaxationszeit für reines Xe (85% ^{129} Xe) bei (4,6 ± 0,1) h festgestellt. Dabei lagen die typischen Wand-Relaxationszeiten bei ca. 18 h für Glaszellen mit einem Durchmesser von 10 cm. Des Weiteren wurde herausgefunden, dass CO_2 eine unerwartet hohe Effizienz bei der Verkürzung der Lebensdauer der Xe-Xe Moleküle zeigte und somit zu einer deutlichen Verlängerung der gesamten T_1-Zeit genutzt werden kann.

Im Verlauf vieler Experimente wurde durch wiederholte Messungen mit der gleichen Zelle, ein "Alterungsprozess“ bei der Wandrelaxation identifiziert und untersucht. Dieser

Effekt könnte leicht rückgängig gemacht werden, indem die anfängliche Reinigungsprozedur wiederholt wurde. Auf diese Weise kann eine konstante Wandrelaxation sichergestellt werden, durch die sehr reproduzierbare T_1-Messungen möglich werden.

Schließlich wurde die maximale Relaxationszeit für HP-Xe mit natürlicher Häufigkeit in Mischungen mit SF_6 bestimmt. Überraschenderweise war dieser Wert um ca. 75% niedriger als der Wert für Xenon, das zu 85% mit ^{129}Xe angereichert war. Dieser Effekt wurde durch drei unabhängige Experimente bestätigt, da er nicht von der bestehenden Theorie der Xe-Relaxation ableitbar ist.

Die Polarisation von HP-Xe, P_{Xe}, wird normalerweise durch den Vergleich der NMR-Signale des HP-Xe mit einer thermischen polarisierten Probe (z. B. ^1H_2O oder Xe) bestimmt. Dabei beinhaltet der Vergleich unterschiedlicher Messungen an verschiedenen Proben (unterschiedlicher Druck, Signalintensität und Messverfahren) viele experimentelle Unsicherheiten, welche sich oft nicht leicht bestimmen lassen. Eine einfache, genaue und kostengünstige Methode zur Bestimmung von P_{Xe} durch eine direkte Messung der makroskopischen Magnetisierung in einem statischen Magnetfeld vermeidet alle diese Unsicherheiten. Dieses Verfahren kann Polarisationen von > 2 % mit einer Genauigkeit von maximal 10% fast ohne Polarisationsverlust bestimmen. Zusätzlich kann diese Methode ohne weitere Änderungen auch für Bestimmungen des Polarisationsgrades anderer HP-Gase verwendet werden.

Contents

Abbreviations

HP	hyperpolarized
^{129}Xe	isotope of Xe with mass number 129
EDM	electric dipole moment
NMR	nuclear magnetic resonance
MRI	magnetic resonance imaging
GE-180	borosilicate glass produced by General Electric
SEOP	spin exchange optical pumping
MEOP	metastable optical pumping
MPIP	Max Planck Institute for Polymer Research
SQUID	superconducting quantum interference device
FWMH	full width at half maximum
OP	optical pumping
OP-cell	optical pumping cell
vdW	van der Waals
SD	spin-destruction
SE	spin-exchange
rms	root mean square
FID	free induction decay
RF	radio frequency
FVU	freeze/volatilization unit
FVS	freeze/volatilization structure
AC	accumulation cell
LN_2	liquid nitrogen
GMS	gas mixing system
DC	direct current

List of figures

List of Tables

Chapter 1: Introduction

The technique of nuclear magnetic resonance (NMR) is a versatile tool for modern science because it allows the non-invasive study of the structure and interactions of molecules which contain nuclei with non-zero spin. It has applications in physics, chemistry, biology and medicine [Lev08]. Some of the most important applications are the analysis of molecular structure in chemistry and biochemistry and, of course, imaging of the human body [Eli03].

The NMR method is based on measuring the interaction of the nuclear magnetization of a sample with an external magnetic field [Lev08]. This magnetization is proportional to the nuclear polarization which, in case of a system with nuclear spin 1/2, is given by the difference of population of the atomic levels for up and down spins.

The Boltzmann (or thermal) polarization P_B can be calculated for a nucleus with a gyromagnetic ratio γ placed in a magnetic field $\vec{B}_0$ at a temperature T. For high temperatures (e.g. room temperature) the energy of nuclear magnetization, $\gamma\hbar B_0$, is much smaller than the thermal energy, $k_B T$; P_B can be expressed as

$$P_B = \frac{N_+ - N_-}{N_+ + N_-} \approx \frac{\gamma\hbar B_0}{2k_B T} \ , \qquad [1.1]$$

where $N_\pm$ are the populations of the levels up and down respectively, and k_B is the Boltzmann constant. The values of P_B for ^{129}Xe at room temperature and $|B_0| \approx 1$ T are in the order of 10^{-5}. This small population difference is the limiting factor for the sensitivity of NMR.

However, the polarization can be boosted far beyond P_B reaching values close to unity. This polarization enhancement is colloquially termed "hyperpolarization" due to the almost six orders of magnitude increase. The most used method for achieving the hyperpolarized (HP) state are: parahydrogen induced polarization (PHIP) [Bow87] [Fra13], dynamic nuclear polarization (DNP) [Com10], brute force polarization [Fro98] [One08] and spin exchange optical pumping (SEOP) [Hap72] among others.

These techniques for enhancing the polarization can be applied to liquids, solids or gases. However, if the NMR-experiment must last several hours, i.e. have long longitudinal relaxation times (T_1), the most suitable samples are HP-^{3}He or HP-^{129}Xe because their T_1 could reach several hours under certain experimental conditions [Tul13] [Rep15]. The most popular method for producing hyperpolarized ^{3}He[1] and Xe is spin exchange optical pumping (SEOP) [God02] [Dri95]. SEOP is based on the transfer of angular momentum from circularly polarized laser light to the nuclear spin of a noble gas

[1] HP-^{3}He can be produced also by metastable spin exchange optical pumping (MEOP) [Bee03].

resulting in polarizations close to unity.

The production of HP-^{129}Xe (and ^{3}He as well) by SEOP was first reported by Grover *et al* in 1977 [Gro77]. Nowadays, SEOP can be performed not only with ^{129}Xe and ^{3}He [Bar98] but also with other noble gases such as ^{21}Ne [Gho09] and ^{83}Kr [Stu06] as well. From all these noble gases, the hyperpolarized gases with the broader application potential are ^{3}He and ^{129}Xe. In case of ^{3}He, nuclear spin polarizations close to unity can be reached with spin relaxation times longer than 100 h [Sur97] [Sch06] [Hie10] [Gen05].

SEOP achieves production rates of 0.5 bar liter per hour with P_{Xe} = 20% [God02] and P_{He}= 50 % using an economic experimental setup [Wal97].

HP-^{3}He is used mostly in fundamental physics for neutron spin filters [Kri11] or in precision magnetic field measurements (magnetometry) [Nik14] among other applications [Kar13]. In addition, it can be used as a contrast agent for magnetic resonance imaging (MRI) providing a revolutionary diagnostic method for lung diseases, since it can deliver static and dynamic high resolution images of the lung [Alb94] [Mei10] [Gül11] [Cha14]. The only drawback of ^{3}He is its very limited availability because its proportion in natural helium is only 1.38 ppm [Lae03].

HP-^{129}Xe has usually much lower polarization than ^{3}He and its spin relaxation time (pure) is also much shorter than for HP-He. This value is limited to 4.5 h when stored in magnetic fields below 0.1 T at room temperature [Cha02] [Ang08] [Rep15]. Nevertheless, ^{129}Xe has other properties related with its highly polarizable electron cloud resulting in a very large chemical shift range [Tor63]. Therefore, ^{129}Xe is very sensitive to its physico-chemical environment. In addition, Xe is also strongly lipophilic [Cle79] and it can be dissolved in non-polar solvents, fat, oil and blood [Ren89] [Bow99] [Che02] [Bai12]. This property enables a broad spectrum of experiments in spectroscopy as, for example, surface studies via NMR [Kna06] [Jän98] [Jän03]. HP-Xe is also used for human lung imaging, where its solubility in blood and chemical shift is often an advantage over ^{3}He. So, it is possible to detect HP-Xe in the blood vessels surrounding the lungs or dissolving it directly HP-Xe into blood [Wol99] [Amo09] [Nor15] for performing angiography[2] [Möl99]. Recent studies even allowed the detection of inhaled Xe in the human brain [Rao14].

Consequently, many applications of HP-Xe in chemistry and biology were published over the lasts years. For an overview, the reader is referred to [Che02], [Mee15] and [God02].

HP-^{129}Xe together with HP-^{3}He play an important role also in basic physics for the study of fundamental symmetries in nature and quantum spin systems due to their long spin coherence times. These experiments are performed with co-located HP He-Xe samples (co-magnetometer) which measure the free precession of the two co-located

[2] Technique used to visualize the inside of blood vessels and organs of the body.

hyperpolarized gases in a holding magnetic field using SQUIDs[3] as sensitive detectors [Hei13]. From the weighted frequency difference of He and Xe, valuable information about non-magnetic spin couplings can be extracted. This information can be used, e.g. for the search of a Lorentz violating sidereal modulation of the Larmor frequency [Gem10] [Bur11], the investigation of spin-dependent short-range interactions [Tul13] and the search for a finite permanent electric dipole moment (EDM) of ^{129}Xe [Hei13]. All these experiments require a frequency resolution in the order of pHz. This frequency resolution depends strongly on the spin coherence time and, therefore, the T_1 relaxation time of the spin species, in particular that of ^{129}Xe.

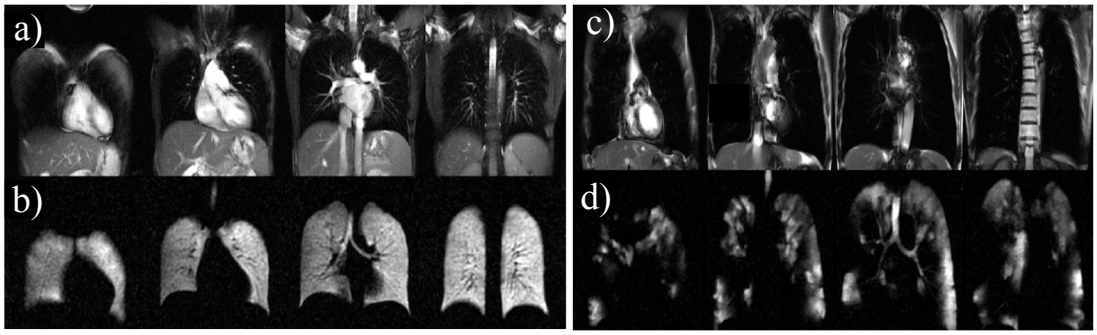

Fig 1.1: HP-Xe MRI of lungs. a) Proton-MRI of a healthy volunteer where the lung gives no NMR signal (dark area). b) Lung imaging of a healthy patients using HP-Xe. c) Proton-MRI of a patient with COPD (chronic obstructive lung desease). d) Lung imaging of a COPD patients using HP-Xe [Dri12]. The differences between b) and d) are evident. The areas of the lung affected by the disease can be determined precisely.

HP-^{3}He can be produced in Physics Institute of the Johannes Gutenberg University in Mainz at a stationary polarizer, filled into transport cells and then transported in magnetic boxes to the experimental site [Hie10] or, alternatively, the HP gas is produced in a somewhat smaller but mobile He-polarizer which can be installed on site [Mro11]. In this context, the motivation of this work was to apply the vast knowledge of the group in HP-^{3}He to HP-^{129}Xe with the aim to construct a facility able to produce it, store it and characterize it efficiently.

At the beginning of my work (May 2010), the Institute of Physics in Mainz had no Xe-polarizer. The only source of HP-Xe available was installed at the Max Planck Institute for Polymer Research (MPIP) (see Appendix 5) [App04]. This Xe-polarizer was built following the standard design given by [Dri95] and it could provide sufficient HP-Xe for the experiments performed at that time [Amo09]. However, some modifications to the original design had to be made in order to increase the polarization level, turn it into a mobile facility and to provide a proper way to store or mix HP-Xe with other gases. These modifications were done during my PhD obtaining a mobile Xe-polarizer essentially for

[3] Superconducting quantum interference device, i.e. high precision magnetometer.

fundamental physics applications with HP-Xe production rates of about 500 mbar·l/h.

The improvements identified during the upgrade of the former MPIP-polarizer were directly incorporated into the construction of another Xe-polarizer, which was assembled almost in parallel to the construction of the polarizer for fundamental physics. This machine was planned for medical applications, therefore it has a much higher throughput (about 2 bar·l/h) following the design presented in [Rus06]. At the end of this work (June 2015), the assembly of the Xe-polarizer for medical applications was essentially ready for operation; it only had to be filled with Rb. The commissioning of this polarizer and the subsequent testing phase, however, could not be carried out during this work due to time constraints.

In addition, the production of HP-Xe requires also diagnostic tools in the intermediate and final stages of the process in order to determine its polarization. Therefore, I constructed a low field NMR-system for determining the (relative) nuclear polarization. This device is also useful to measure the conditions for obtaining long longitudinal relaxation times which minimize polarization losses due to storage and transport. Finally, the NMR method was only able to measure relative polarization values, thus I developed a precise method to determine the absolute polarization of HP-Xe.

1.1 Summary of this work

The construction of both Xe-polarizers, the optimization of the spin relaxation times of HP-Xe and the measurement of its absolute spin polarization will be described in the following chapters:

Chapter 2: Theoretical aspects for the production of HP-^{129}Xe: spin exchange optical pumping, cryogenic separation and storage. This chapter describes the theoretical background required for the production of HP-Xe samples. This production process is divided in three parts: 1) Production of HP-Xe via SEOP which explains how the Xe is brought to HP state.

2) Cryogenic separation where the HP-Xe is separated from the buffer gases required for an efficient SEOP.

3) Storage of the HP-Xe sample.

Each stage will be described emphasizing technical aspects which are crucial for the reduction of the polarization losses in order to achieve the highest polarization.

Chapter 3: Detection of HP-Xe via NMR and measurement of its storage times. The technique used in this work to determine the polarization and the storage times of HP-Xe was NMR. For this purpose, a low field NMR system was built and characterized. In this chapter, the theory required for its construction and the interpretation of the NMR

signal is explained. The NMR technique allowed for relative measurements of the sample polarization (magnetization) which is also necessary to investigate the longitudinal spin relaxation time (T_1) of HP-^{129}Xe .

Chapter 4: Construction and characterization of a Xe-polarizer. In this chapter, the construction and optimization of the Xe-polarizer for fundamental physics experiments is discussed in detail.

Chapter 5: Systematic improvement of the storage times of HP-Xe. Here the focus lies on extend the T_1-relaxation time of HP-Xe. The longitudinal relaxation of HP-Xe was measured by NMR under different conditions: i) mixtures with buffer gases, ii) use of special, low-relaxation spherical glass vessels of different sizes. Most of the content of this chapter is published in Journal of Magnetic Resonance [Rep15]. This publication can be found in Appendix 6 of this work.

Chapter 6: Absolute measurement of the polarization of HP-Xe. A new technique for the measurement of the Xe polarization was developed which relies on the measurement of the static magnetic field produced by HP-Xe stored in a spherical glass cell. This method is able to measure a polarization of 2%·with an uncertainty of 10% in a spherical cell of 6 cm filled with about 600 mbar of HP-Xe (85% ^{129}Xe) with minimal polarization losses. In addition, this method can be used for measuring the polarization of other HP gases without further improvements. The content of this chapter is submitted to Journal of Applied Physics.

Chapter 7: Conclusions and outlook

Chapter 2: Theoretical aspects of the production of HP-^{129}Xe: spin exchange optical pumping, cryogenic separation and storage

HP-Xe is produced via spin exchange optical pumping (SEOP) in a Xe-polarizer. In this machine, small amounts of Xe (< 50 mbar) are mixed with He and N_2 reaching total pressures between 0.7 to 10 bars [Dri96] [Rus05]. This gas mixture is heated with a drop of Rb reaching Rb vapor pressures up to 0.1 mbar [Dit41]. The gas mixture and the Rb vapor flow into the optical pumping (OP) cell, which is basically a cylindrical glass container placed in a homogeneous static magnetic field. The OP-cell has a gas inlet and outlet so that the gas mixture can flow through it.

The OP-cell filled with He, Xe, N_2 and Rb vapor is illuminated with circularly polarized monochromatic light. The frequency of the light is chosen to be the resonant D1 line of the Rb valence electron. The polarized photons are absorbed by the valence electrons transferring their angular momentum. This process is called “optical pumping”.

The polarization of the Rb valence electron is transferred to the ^{129}Xe nucleus through the Fermi contact interaction resulting in polarized ^{129}Xe (HP-Xe). Finally, the gas mixture containing HP-^{129}Xe gas leaves the OP-cell while the rubidium vapor condenses in the region at the outlet of the cell where the temperature is below 39°C. The produced HP-Xe can be used directly after this procedure, i.e. in the mixture with the buffer gases, or it can be separated cryogenically from the gas mixture, concentrated and stored.

The cryogenic separation of HP-Xe is based on the difference between the melting points of the gases in the gas mixture. Xenon has a melting point of 161.2 K while nitrogen and helium have 63.15 K and 1.1 K, respectively. This gas mixture flows through a trap at liquid N_2 temperature (77 K) where the HP-Xe freezes out while the buffer gases remain in the gas phase and flow through the trap. In this way, the amount of HP-Xe required for an experiment can be accumulated as frozen HP-Xe in the accumulation cell.

Once enough HP-Xe is accumulated in solid state, the rest of the buffer gases are evacuated and the HP-Xe ice is heated up until it volatilizes or boils. Finally, the HP-Xe in gas phase is stored in a glass vessel placed in a holding magnetic field for further experiments.

The procedure for the production of HP-Xe described above is illustrated in Fig. 2.1. According to this description, the production of a sample of HP-Xe gas can be divided in three stages: spin exchange optical pumping, cryogenic separation and storage. These processes occur in well-differentiated parts of the Xe-polarizer which are also marked in Fig. 2.1.

The description of each stage in the production of a HP-Xe sample was already

performed in detail by [Rus05]. In this work, Ruset summarized carefully many years of research on spin exchange optical pumping. To avoid an unnecessary repetition of his work, this chapter will review only the necessary theoretical aspects for the construction of a Xe-polarizer emphasizing the practical aspects. In the following, it will be shown that once the operation conditions of the polarizing apparatus are set, the main optimization strategy is focused on minimizing losses of the Xe polarization via relaxation mechanisms.

Each stage of the production process of HP-Xe will be described identifying the mechanisms which may contribute to polarization losses. Consequently, those mechanisms can be minimized leading to the production of HP-Xe with high polarization.

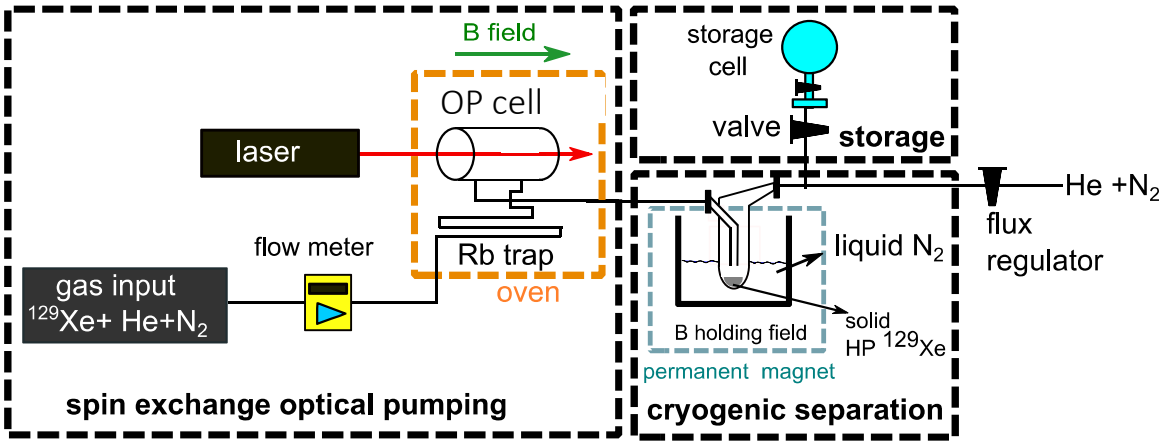

Fig 2.1: The production of HP-Xe is divided in three main parts: 1) "spin exchange optical pumping" stage, 2) "cryogenic separation" stage and 3) the "storage" stage in a glass vessel. On the first stage, a gas mixture composed by He, N_2 and Xe flows through a Rb saturator at 100 – 200 °C into the OP-cell. Here, the Xe is hyperpolarized via SEOP. The HP-Xe mixed with the buffer gases flows into the accumulation cell and is frozen out at liquid nitrogen temperatures while He and N_2 flow through the cell (second stage). Once enough HP-Xe has been accumulated in solid phase, the rest of the buffer gases are evacuated and the solid HP-Xe is volatilized and stored in a glass cell.

2.1 Processes inside the OP-cell: Spin Exchange Optical Pumping (SEOP)

As mentioned before, SEOP is the mechanism used to enhance the nuclear polarization of the ^{129}Xe nuclei. This mechanism of polarization enhancement is basically a two-step process which is schematized in Fig. 2.2. First, optical pumping where the spin polarization of the valence electron of an alkali metal atom (in this case Rb) is enhanced due to the interaction with resonant circularly polarized light. Second, the subsequent transfer of its polarization to the ^{129}Xe –nucleus through spin-exchange via Fermi contact interaction.

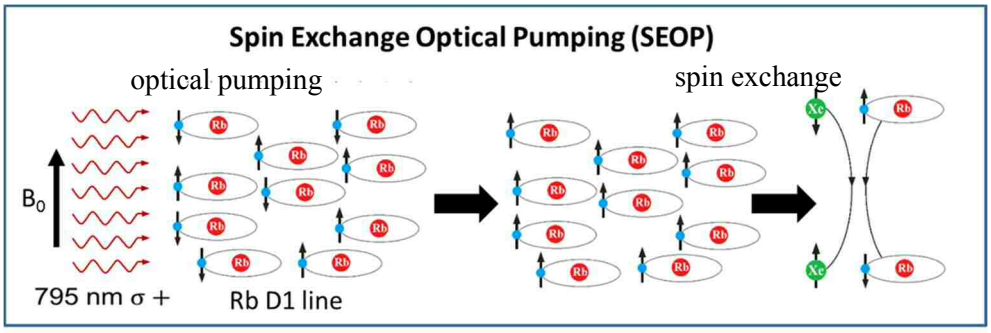

Fig. 2.2: Sketch of the SEOP method. Polarized laser light polarizes the valence electrons of Rb (optical pumping). This polarization is transferred to the nucleus of ^{129}Xe via Fermi contact interaction (spin exchange).

2.1.1 Rubidium in an external magnetic field

In principle, any of the alkali metals are suitable for SEOP. However, rubidium presents several advantages such as a high spin-exchange cross-section with ^{129}Xe and the big spectral gap between the D1 and the D2 line permits a selective excitation with economic tunable lasers [Whi11]. Finally, its high vapor pressure allows working temperatures between 100 - 200°C without significant chemical damage of the container [BabD05].

Rubidium is the alkali metal atom with atomic number 37 and has a single valence electron in the 5 $S_{1/2}$ state with an ionization potential of 4.13 eV. It is found in nature in two stable isotopes: 72.2 % ^{85}Rb with nuclear spin I = 5/2 and ^{87}Rb (27.8 %) with I = 3/2. The melting point of Rb is 39°C and its number density in thermal equilibrium is related to the absolute temperature T by [Kil27]

$$[\mathrm{Rb}] = \frac{10^{10.55-\frac{4132}{T[\mathrm{K}]}}}{1.38\times10^{-16}\,T[\mathrm{K}]}[\mathrm{cm}^{-3}]\,. \qquad [2.1]$$

Eq. [2.1] is plotted in Fig. 2.3 where the red stripe indicates the working temperature range of SEOP (100 to 200°C). For these values, the Rb number density is between $5\cdot10^{13}$ and $1\cdot10^{15}$ cm^{-3}. For an OP-cell with a volume of 100 ml, this density corresponds to approximately 20 µg or 0.2 nmol.

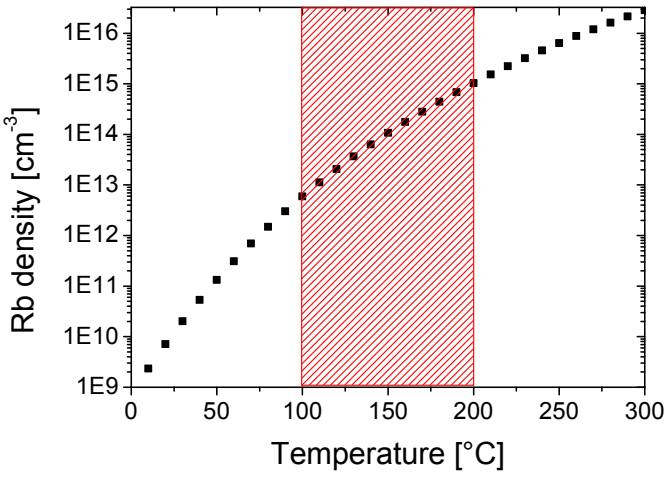

Fig. 2.3: Rubidium number density in cm^{-3} vs. temperature. The working temperature range of SEOP is between 100 and 200 °C. This area is marked in the graphic by a red striped area.

For optical pumping, the Rb vapor (inside the OP-cell) is placed inside a holding magnetic field $\overrightarrow{B_0} = B_0 \hat{z}$. Hence, the Hamiltonian for each alkali atom (α) is given by

$$H_a = H_0 + A_a \vec{I}_a \cdot \vec{S} + g_s \mu_B S_z B_0 - \frac{\mu_a}{I_a} I_{az} B_0. \qquad [2.2]$$

The first term, H_0, describes the spin-independent Hamiltonian (mostly Coulomb-potential). The second term represents the hyperfine interaction between the electron and the nucleus. $\vec{I}_a$ is the nuclear spin; $\vec{S}$ is the electron spin and A_α the hyperfine coupling constant. This interaction is dominant for magnetic fields below 0.1 T which is the range of interest in this work. In that regime of magnetic field strength, the eigenstates of H_α are also eigenstates of $\vec{F} = \vec{S} + \vec{I}_a$ and its projection F_z along the external field [Wal97]. The case $|B_0| > 0.3$ T is described in [Ric02].

The third and fourth term represent the Zeeman interaction, i.e. the coupling of the electron and the nuclear magnetic moment to the external magnetic field $\vec{B}_0$. g_s is the g factor of the electron spin and μ_B is the Bohr magneton. These terms are dominant for magnetic fields > 0.3 T following the Breit-Rabi-formula [Coh93]. A detailed calculation of the energy levels obtained from Eq. [2.2] can be found in [Ben65].

The energy levels resulting from the Hamiltonian for ^{87}Rb are shown in Fig. 2.4. This graph is not to scale. The diagram for the ^{85}Rb isotope is analogous to ^{87}Rb, but the total angular momentum values are F = 2, 3 for the ground state 5 S and the first excited state 5 P.

The valence electron of Rb can absorb resonant light, being excited to higher energetic levels. The first excited states are: 5 $^2P_{1/2}$ with the corresponding D1 line at

λ_1=794.7 nm and 5 $^2P_{3/2}$ with the corresponding D2 line at λ_2=780.0 nm.

The transition between the ground and the first excited state is the key for enhancing the polarization of the valence electron in optical pumping of Rb.

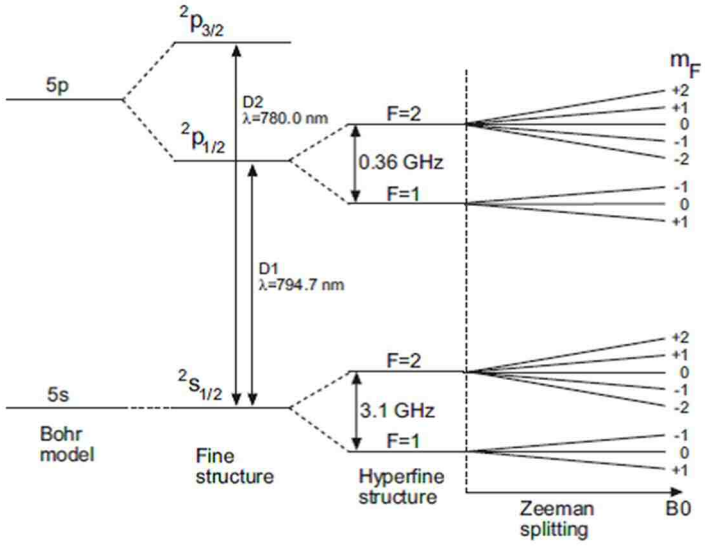

Fig. 2.4: Schematic diagram of the ^{87}Rb energy levels. The separation between the energy levels in the diagram are not to scale. The Bohr energy levels are separated by energies in the order of 1 eV, the fine structure substates, such as 5 $^2P_{3/2}$ and 5 $^2P_{1/2}$, are separated by energies in the order of 10^{-3} eV, and the hyperfine states are separated by energies in the order of 10^{-6} eV. The Zeeman levels (only the linear Zeeman splitting of the hyperfine levels for $B_0 << 0.3$ T are shown) are separated by energies in the radio frequency (RF) range and are proportional with the applied field. The separation between two consecutive Zeeman levels is in the order of 0.5 MHz/G. This figure was extracted from [Rus05].

2.1.2 Optical pumping of Rb

Optical pumping is a method to enhance the polarization of the valence electrons of an ensemble of Rb atoms [Hap84]. This method is based on the interaction of circularly polarized photons ($\sigma^{\pm}$) and the Rb valence electron as shown in Fig. 2.5. This process takes place inside the optical pumping cell.

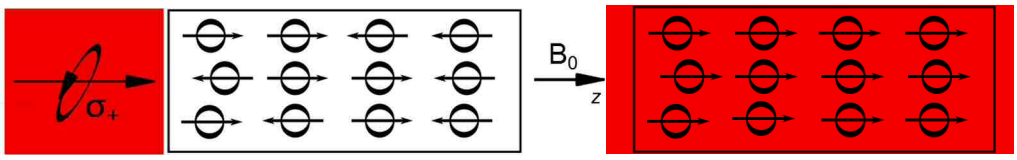

Fig. 2.5: Rb atoms are immersed in a magnetic field $\overrightarrow{B_0} = B_0\hat{z}$. A beam of circular polarized light of helicity σ^+ illuminates the cell polarizing the valence electron of Rb.

The temperature of the cell is between 100 - 200°C obtaining a Rb density of about 10^{12} -10^{15} cm^{-3} (see Fig 2.3 vapor pressure curve). The cell is placed in an external

magnetic field $\overrightarrow{B_0} = B_0 \hat{z}$, which defines the spin quantization axis.

Typically, the magnetic fields used for optical pumping are in the order of 1 to 3mT. At these fields, the ground state 5 $^2S_{1/2}$ with (m_s = 1/2) and 5 $^2S_{-1/2}$ with (m_s = -1/2) are nearly equally populated. Therefore, the thermal polarization of the Rb-valence electrons in that regime of operation is practically zero (see Eq. [1.1]).

The Rb electrons are excited into the 5 $^2P_{1/2}$ state when the Rb ground state atoms are irradiated with resonant laser light at λ=794.7 nm (D1-line). This resonant light is circularly polarized consequently it carries angular momentum. This angular momentum together with the energy is conserved for the interaction between the polarized photon and the Rb electron. For incident circularly polarized light with helicity σ^+, the variation of the projection of the spin quantum number m_s is $\Delta m_s = +1$ according to the selection rules of an electric dipole transition. So, only the transition 5 $^2S_{-1/2}$ to 5 $^2P_{1/2}$ is possible as shown in Fig. 2.6a. The lifetime of the excited 5 $^2P_{1/2}$ state is 27.75(8) ns and decays into the atomic ground state by re-emitting a photon. The probability to repopulate the 5 $^2S_{-1/2}$ state is 2/3 whereas the probability of populating 5 $^2S_{1/2}$ is 1/3. Repeating this absorption and reemission process, the gain in polarization after n cycles is

$$P_{\mathrm{Rb}} = \frac{N(m_s = +1/2) - N(m_s = -1/2)}{N(m_s = +1/2) + N(m_s = -1/2)} = 1 - \left(\frac{2}{3}\right)^n . \qquad [2.3a]$$

From Eq. [2.3] it can be deduced that the Rb-valence electrons are fully polarized after an average of $n > 4$ cycles per atom. The average number of photons required to polarize the atom gives a clear idea of the ideal efficiency of the optical pumping i.e. without considering relaxation mechanisms.

The amount of cycles n in Eq. [2.3] decreases if buffer gases are added. These gases scramble the excited state population since collisional mixing leads to equal population among the m_s magnetic sublevels of the 5 $^2P_{1/2}$ state during its lifetime. In addition, buffer gases randomize the transition probabilities. Therefore, the relative probabilities of emission from the excited state are 1/2 for the 5 $^2S_{1/2}$ state and 1/2 for the 5 $^2S_{-1/2}$. Then, the Rb polarization is given by

$$P_{\mathrm{Rb}} = 1 - \left(\frac{1}{2}\right)^n \qquad [2.3b]$$

and the average number of photons required to polarize the atom in the presence of buffer gas within this model is $n > 1$ (see Fig. 2.6b).

The spin of the Rb nucleus has been neglected in this description of the optical pumping process. This approximation is valid in such environments where the time-scale of the Rb interactions is much longer than the pump-up time (10 - 20 ms). If this condition is not fulfilled and the nuclear spin of Rb has to be considered, the final polarization is the same than the value predicted by Eq. [2.7], but with a larger time constant [Rus05]

[Wal02] [Wag94].

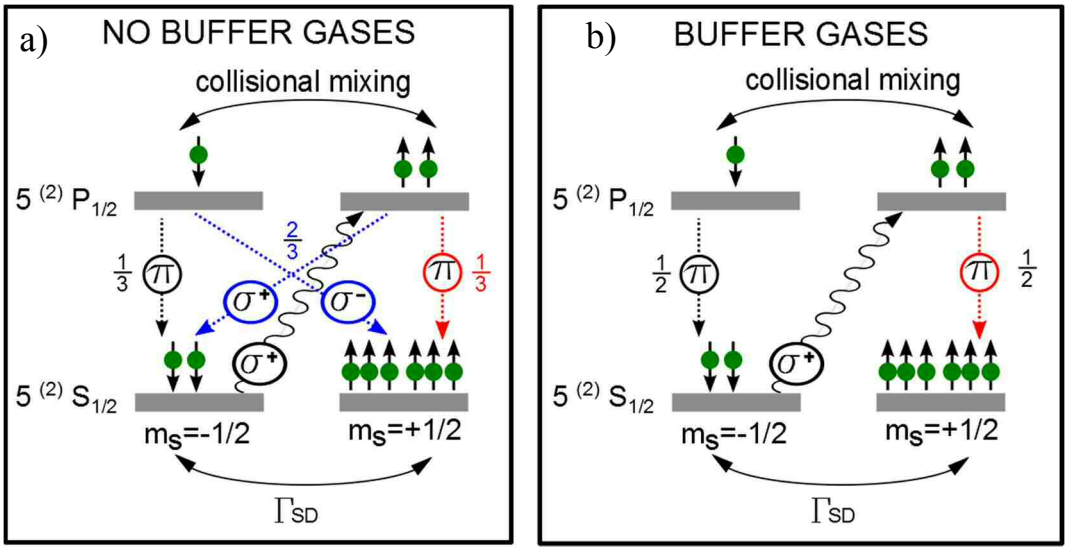

Fig. 2.6: Optical pumping of the valence electron of Rb due to the interaction with circularly polarized light. The valence electron of Rb atoms on the state 5 $^2S_{-1/2}$ interact with resonant σ^+circular polarized photons. The Rb electrons are excited into the 5 $^2P_{1/2}$ state. The populations on the level 5 $^2P_{1/2}$ are mixed through collisional mixing. The probabilities of decay of the population in the level 5 $^2P_{1/2}$ are related with presence of buffer gases: a) If no buffer gases are added, the population on the level 5 $^2P_{1/2}$ decays to 5 $^2S_{1/2}$ through emission of a π photon. The probability for this process is 1/3 while it is 2/3 for the decay from the level 5 $^2P_{1/2}$ to 5 $^2S_{-1/2}$ by emission of σ^+ photons. The population of the level 5 $^2P_{-1/2}$ behaves analogously decaying to 5 $^2S_{1/2}$ with a probability of 2/3 and 5 $^2S_{-1/2}$ with a probability of 1/3. b) In presence of buffer gases, the probability of decay from 5 $^2P_{1/2}$ to 5 $^2S_{1/2}$ is 1/2. The same value is valid for the transition from 5 $^2P_{-1/2}$ to 5 $^2S_{-1/2}$.

The Rb polarization P_{Rb} can be expressed in terms of the normalized population density ρ of each state as

$$P_{Rb} = \rho_{+1/2} - \rho_{-1/2}, \qquad [2.4]$$

where $\rho_{+1/2}$ is the population in the 5 $S_{+1/2}$ state and $\rho_{-1/2}$ is the corresponding population in the 5 $S_{-1/2}$ state. These populations are normalized as following

$$\rho_{+1/2} + \rho_{-1/2} = 1. \qquad [2.5]$$

The differential equation that describes the population of the ground state levels is given by

$$\frac{d\rho_{\pm 1/2}}{dt} = \pm(\gamma_{opt} + \frac{\Gamma_{SD}}{2}) \cdot \rho_{-1/2} \mp \frac{\Gamma_{SD}}{2} \cdot \rho_{+1/2}. \qquad [2.6]$$

Here γ_{opt} is the optical pumping efficiency and Γ_{SD} is the spin-destruction rate, which will be analyzed in Sec. 2.1.8. Considering Eq. [2.4], Eq. [2.6] can be expressed as

$$\frac{dP_{\mathrm{Rb}}}{dt} = \gamma_{opt}(1 - P_{\mathrm{Rb}}) - \Gamma_{SD} P_{\mathrm{Rb}}. \qquad [2.7]$$

If the initial condition P_{Rb} (t = 0) = 0, the solution of this differential equation is given by

$$P_{\mathrm{Rb}}(t) = \frac{\gamma_{opt}}{\gamma_{opt} + \Gamma_{SD}}[1 - e^{-(\gamma_{opt} + \Gamma_{SD})t}], \qquad [2.8]$$

with the stationary solution

$$P_{Rb} = \frac{\gamma_{opt}}{\gamma_{opt} + \Gamma_{SD}}. \qquad [2.9]$$

Therefore, the population differences that arise during optical pumping are simply determined by the balances of polarizing and depolarizing rates. In this way, circular polarized light brings the atomic system from a disordered state (equal populations in the degenerate state) into an ordered state.

From Eq. [2.9] it can be deduced that the influence of the relaxation mechanisms on the final polarization is minimal when $\gamma_{\mathrm{opt}} >> \Gamma_{\mathrm{SD}}$. For this reason, high values of P_{Rb} require high values of γ_{opt} and/or low values of Γ_{SD}. The contributions to Γ_{SD} of polarized Rb include:

- Interaction with photons of the wrong polarization (σ^-, π). These photons could be re-emitted photons from the optical pumping process. This source of relaxation can be significantly reduced by adding a buffer gas as shown in Fig. 2.6. This mechanism will be explained in the next section. Another source of photons with wrong polarization is reflections inside the OP-cell. Those reflections are in general not polarization conserving and generate a mixture of light polarization components given by the Fresnel formula [Fuc13]. This mechanism can be eliminated with a proper alignment of the optics assuring that the direction of propagation of light is parallel to the symmetry axis of the OP-cell. Such is the case of the polarizer for fundamental physics applications described in Chapter 4.

- Collisions with the wall: This mechanism is difficult to model mainly because of the limitation on the characterization of properties of the interior of the internal wall of the OP-cell. In addition, those properties are changing constantly over time due to condensation of Rb on the wall during the polarization procedure.

This relaxation mechanism is relevant for static production of HP-Xe by SEOP. In this case, the gas mixture (He, N_2 and Xe) is inside a sealed OP-cell which is illuminated with the laser beam until the highest polarization is reached. In this case, the residence time of the mixture inside the OP-cell is usually longer than 30 minutes. In continuous flow Xe-polarizers, the residence time of the gas mixture inside the OP-cell is usually much shorter (about 1 minute). So, the relaxation of Rb due to interaction with the wall should not be relevant. However, this has to be verified individually for each OP-cell in order to detect impurities on the glass which could increase dramatically the wall

relaxation [Sch06].

- Interaction with other atoms such as Rb or gases of the mixture: this mechanism is the most relevant in an optimized SEOP system and it will be described in Sec. 2.1.7.

2.1.3 Quenching

As it was described above, the addition of buffer gases improved the optical pumping process by reducing the radiative decay. According to Fig. 2.6, the radiative emission from the excited 5 $^2P_{1/2}$ levels leads to circularly polarized $\sigma^{\pm}$ photons with $\Delta m_s = \pm 1$ or linearly polarized π photons with $\Delta m_s = 0$. Since they can be resonantly absorbed again by the polarized Rb atoms, the reabsorption of the almost unpolarized fluorescence light will reduce the optical-pumping efficiency considerably resulting in a reduction of the Rb polarization. This problem can be solved by adding N_2 as a buffer gas for de-excitation of the excited states via non-radiative vibrational levels. This procedure reduces the lifetime of the excited Rb atoms from 28 ns to about 1 ns [Ros01].

The N_2 quenching cross-section for the excited 5 $P_{1/2}$ state was measured to be 58 Å^2 [Wag91]. This value was used by Wagshul and Chupp [Wag89] to calculate the probability (R_d) for radiative decay of the excited Rb atoms which is given by

$$R_d \approx \frac{3}{3 + 750 \dfrac{p_{N_2}}{\text{bar}}}. \qquad [2.10]$$

p_{N2} is the partial pressure of N_2 in units of bar. From this equation, the probability of decay is less than 5 % for p_{N2} of about 100 mbar. However, it was observed in this work that higher amounts of N_2 have a negative impact on the Xe polarization which can only be explained through a reduction of the Rb polarization (see Fig. 4.24b).

The optimum amount of N_2 required for an efficient quenching of Rb is related with the Rb relaxation rate and Rb number density as shown in Fig. 2.7 [Kad01]. This graphic relates the Rb densities with the relevant interactions, which contribute to the Rb relaxation. Those interactions are explained in detail in [Wal97] [Eri00] [Leo98] [Gup74] and [Kad01].

Since the working temperature of SEOP determines the Rb density, only the area between the two red lines will be relevant for the purpose of this work. In this area, the Rb density can be related to a determined minimum Rb relaxation rate via the amount of N_2 present in the gas mixture. For example, at 150°C the Rb density is about 10^{14} cm^{-3}. Using a partial pressure of N_2 of about 100 Torr (~130 mbar), the minimum relaxation rate is 30 s^{-1}. According to Eq. [2.10], the probability of radiative decay results in $R_d \approx 0.03$. This value is acceptable for the optical pumping process.

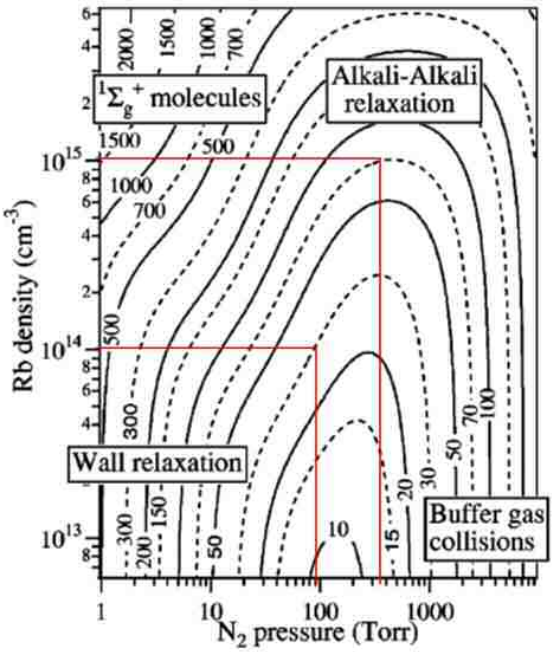

Fig. 2.7: Summary of the Rb relaxation rates for different Rb densities and partial pressures of N_2 for low magnetic fields [Kad01]. This graphic provides the amount of N_2 which leads to a smaller Rb relaxation rate. The relaxation rates are represented as contour lines in Hz. Text inserts name the interactions with Rb which represent the dominant relaxation mechanism in each Rb (N_2) density area. The Rb density in SEOP is on the range of 10^{14} - 10^{15} cm^{-3}, for this densities the N_2 pressure necessary to obtain the minimum Rb relaxation rate is between 90 to 300 mbar (red lines). Using Eq. [2.10], R_d is between 2.2 and 3 %.

2.1.4 Consequences of quenching: temperature of the OP-cell

The quenching of the excited states of Rb leads to vibrational excitation of N_2 molecules. This energy is dissipated through collisions with the gas atoms in the optical pumping cell. As a result, the temperature of the optical pumping system increases. The heat load is considerable especially for absorbed laser powers exceeding 20 W. In [Wal01], Walter measured the temperature of the gas mixture inside a cylindrical optical pumping cell via Raman scattering [Com94] and compared it with the temperature measured on its surface. These measurements were performed in a cell of 40 cm^3 with 2 atm of He and 0.33 atm of N_2 at 170°C. The result of this experiment is shown in Fig. 2.8. From these plots, it can be deduced that the measured temperature on the surface of the optical pumping cell is significantly lower than the temperature of the gas mixture inside the cell. Therefore, the temperature on the surface of the OP-cell cannot be interpreted as an absolute parameter but as an empirical reference for the reproducibility of the OP conditions of a Xe-polarizer.

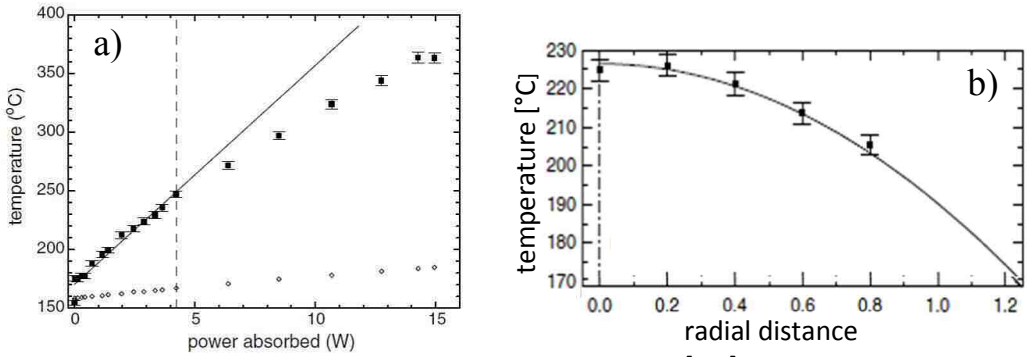

Fig. 2.8: Heating effects in the OP-cell due to quenching (extracted from [Wal00]). a) Temperature of the OP-cell vs. pumping laser power. The diamond points represent the temperature on the surface of the OP-cell while the black dots represent the temperature of the gas mixture measured by Raman scattering. b) Radial distribution of the temperature over a cylindrical OP-cell for a laser of 2.9 W measured with Raman scattering.

The consequence of the temperature distribution shown in Fig. 2.8b is an inhomogeneous Rb distribution inside the OP-cell due to evaporation of the Rb layer deposited on the walls. These high temperatures registered inside the OP-cell could generate clouds of high Rb density which can absorb locally most laser power. This "clouds" are commonly known as Rb runaways [Wit14].

Even if the distribution of the incident laser power is homogeneous, this high density Rb clouds inside of the OP-cell lead to a position dependent light absorption. Therefore, γ_{opt} decreases or even can be zero locally inside the cell which has a direct impact in the Rb polarization.

In addition, the incoming gas mixture has a much lower temperature than the gas mixture inside the OP-cell will contribute to the generation of turbulent flow. This process also leads to an inhomogeneous distribution of Rb in the OP-cell and, in consequence, a reduction of the polarization [Fin07].

2.1.5 Rb- light interaction

Nowadays, the light source for optical pumping of Rb is diode lasers. The number of photons per unit of area and time provided by this source is given by the photon flux Φ. This function describes the spatial and spectral distribution of the incoming laser beam. Φ can be expressed as the product of the spatial distribution $\chi(\vec{r})$ and the frequency spectrum ψ (ν) given by

$$\Phi(\vec{r},\nu) = \chi(\vec{r})\psi(\nu)\,. \qquad [2.11]$$

Usually, the diode lasers used for SEOP have a Gaussian spatial distribution and a Lorentzian frequency distribution.

The intensity I_L and the laser power P_L can be calculated using Φ as

$$I_L(\vec{r}) = \int_0^\infty \Phi(\vec{r},\nu)d\nu \qquad [2.12]$$

and

$$P_L = \int_S dS \int_0^\infty \Phi(\vec{r},\nu)d\nu\,, \qquad [2.13]$$

where dS represents the cross-section area of the beam. The optical pumping efficiency γ_{opt} is defined as the convolution of $\Phi(\vec{r},\nu)$ with the Rb absorption cross-section $\sigma(\nu)$ as

$$\gamma_{opt}(\vec{r}) = \int_0^\infty \Phi(\vec{r},\nu)\sigma(\nu)d\nu. \qquad [2.14]$$

The absorption cross-section of Rb $\sigma(\nu)$ is given by[4] [Lar91]

$$\sigma(\nu) = \sigma_0 \frac{\Gamma_{abs}^2}{4(\nu-\nu_0)^2 + \Gamma_{abs}^2} \qquad [2.15]$$

where Γ_{abs} represents the width of the Rb D1 absorption line. $\sigma_0 = 3.2\cdot10^{-13}\text{cm}^2$ was calculated by Wagshul and Chupp in [Wag94].

The parameter Γ_{abs} can be expressed as

$$\Gamma_{abs} = \Gamma_{abs}^{Doppler} + \Gamma_{abs}^{pres}\,, \qquad [2.15a]$$

where $\Gamma_{abs}^{Doppler}$ is the Doppler broadening and Γ_{abs}^{pres} is the pressure broadening.

The first term represents the broadening of the spectral line due to the distribution of velocities of the atoms. The line broadening due to this effect is described by

$$\Gamma_{abs}^{Doppler} = \frac{\nu_0}{c}\sqrt{\frac{8k_B T[\text{K}]\ln 2}{m}}\,, \qquad [2.16]$$

where ν_0 is the central frequency, c is the speed of light, k_B is the Boltzmann constant, T is the absolute temperature and m is the mass of the emitting/absorbing particle. For a range of 150 to 200°C, $\Gamma_{abs}^{Doppler}$ is approximately 0.5 to 1 GHz.

The second contribution to Γ_{abs} is the pressure (or collisional) broadening, which is caused by collisions of Rb with the buffer gases. This parameter depends on the total gas pressure and is approximately 18 GHz[5] per bar for the buffer gases used here. Comparing both values, the pressure broadening is the dominant mechanism and the Doppler broadening can be neglected under the conditions of the experimental setup used in this work.

The linewidth of the available diode lasers is usually between 0.1 and 3 nm. Therefore, Γ_{abs} can be adjusted to these bandwidths in order to use the available laser

[4] The term which parameterizes the asymmetry of the peak of the Lorentzian function was neglected.
[5] 0.04 nm/bar

power effectively (see Fig. 2.9a). This tuning is usually done by increasing the total pressure by adding ^{4}He as a buffer gas. Helium is preferred over other gases because it has a low spin-destruction rate for polarized Rb as it will be shown in Eq. [2.25]. Considering, in addition, the presence of N_2 needed for quenching the excited Rb states, Γ_{abs} is given by [Rom97]

$$\Gamma_{abs} = [(18.0 \pm 0.2) p_{He} + (17.8 \pm 0.3) p_{N_2} + (19.2 \pm 2) p_{Xe}] \frac{T_0}{T} [\text{GHz}] . \qquad [2.17]$$

The coefficients of Eq. [2.17] are in units of GHz/bar. p_i is the partial pressures of He, N_2 and Xe respectively in units of bar. T_0 is the normal temperature (273 K) and T is the temperature of the system. Moreover, the use of He and N_2 as buffer gases produces also a shift, ν_{shift}, of the central transition frequency (ν_0) given by

$$\nu_{shift} = [(4.3 \pm 0.01) p_{He} - (8.27 \pm 0.15) p_{N_2} - (6.95 \pm 0.70) p_{Xe}] \frac{T_0}{T} [\text{GHz}] . \qquad [2.18]$$

Typically, a Xe-polarizer operates in a pressure range between 1 and 7 bar, as is the case of the Xe-polarizer developed in this work. For this pressure range, the pressure broadening Γ_{abs} and the frequency shift ν_{shift} are plotted in Fig. 2.9.

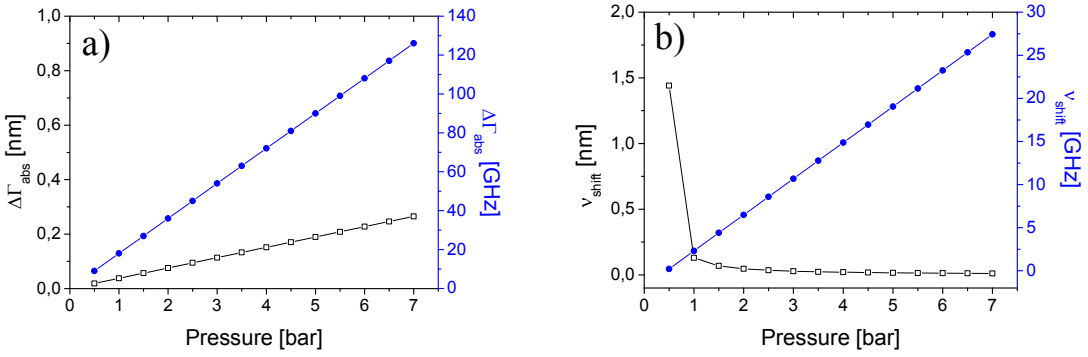

Fig. 2.9: Effects of the buffer gases on the absorption line of Rb calculated for a sample with 1 to 7 bar total gas mixture pressure, 1% of the gas mixture corresponds to Xe and 150 mbar of N_2. The black line and axis are expressed in nm while the blue line and axis are calculated in GHz. a) Pressure broadening expressed according to Eq. [2.15]. b) Line shift calculated according to Eq. [2.16].

Besides radiative quenching and matching of the absorption line, the use of buffer gases has other benefits such as:

-Reduction of Rb diffusion to the wall.

-Contribution to the formation of van der Waals molecules (Rb-Xe) which has an impact on the overall Rb-Xe spin-exchange process.

- Destruction of van der Waals Xe-Xe molecules which is a source of relaxation for HP-Xe. In consequence, the lifetime of nuclear spin polarized Xe in the OP-cell is extended.

2.1.6 Absorption of light inside the OP-cell

The absorption of the incident laser light due to interaction with the Rb electron can be easily understood by considering a cylindrical OP-cell filled which contains a homogeneous Rb density illuminated by a beam with Gaussian profile. For this explanation, the OP-cell is also divided in transverse slices as is shown in Fig. 2.10[6] where the laser light illuminates the OP-cell with certain initial power P_0.

The first "slice" of Rb interacts with the polarized photons as described in Fig. [2.6] and Eq. [2.14] absorbing certain amount of power given by the Lambert-Beer law (see Eq. [4.2]). In this slice, the Rb is optically polarized, i.e. its energetic state is 5 $S_{1/2}$. In this way, this slice of the cell cannot absorb more incoming polarized laser light and the rest of the available photons interact in the same way with the second slice and so forth until the last slice. This description was performed neglecting the relaxation mechanisms of Rb.

If the laser power would be infinite, the laser light would illuminate the entire OP-cell polarizing all the Rb atoms reaching the equilibrium described by Eq. [2.9]. However, the Gaussian beam profile of finite power leads to regions in the OP-cell illuminated with less laser power (or dark areas) and thus, reduced Rb polarization (specially towards the walls). This effect can be avoided by adjusting the width of the Gaussian profile in such a way that the laser power is sufficient to polarize the last slice of Rb atoms in the OP-cell. In consequence, the initial laser power is reduced due to the shaping of the beam but this should not be an inconvenient for high power light sources matched to the absorption spectral profile.

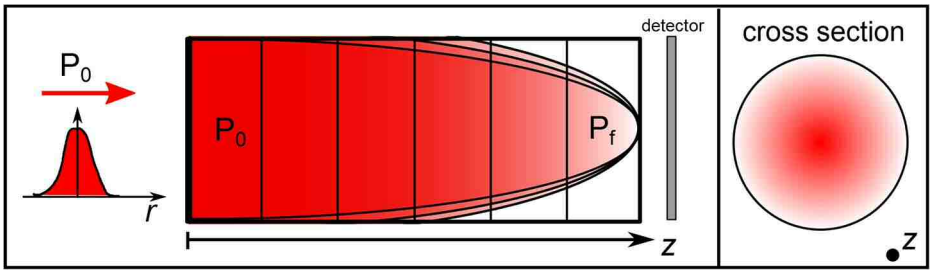

Fig. 2.10: Absorption of a laser beam with a Gaussian beam profile in the transverse plane of a cylindrical OP-cell filled with a homogeneous density of Rb. The different lines on the profile represent different widhts on the Gaussian profile. The incident power is P_0. The power at the end of the OP-cell is measured with a detector.

Another factor to consider on the description of the absorption is that differently absorbed power leads also to a different temperature of the cell due to quenching. In consequence, the Rb density exhibits a dependence in z.

This qualitative description for the propagation of light over the symmetry axis (z)

[6] The complexities of the illumination of the OP-cell with a dynamic gas mixture will be analyzed in Fig. 4.19.

of the OP-cell can be expressed mathematically as [Sch09]:

$$\frac{d\Phi(z,\nu)}{dz} = -\lambda^{-1}(z,\nu)\Phi(z,\nu)\,. \qquad [2.19]$$

In Eq. [2.19], $d\Phi/dz$ is the photon flux absorbed per unit of length and λ is the absorption length given by

$$\lambda^{-1}(z,\nu) = -\sigma(\nu)[\mathrm{Rb}(z)](1-P_{\mathrm{Rb}}(z))\,. \qquad [2.20]$$

λ depends both on z and ν. The dependence on z appears due to the possible differences on Rb density and Rb polarization over the axis of the OP-cell. Using Eq. [2.19] and Eq. [2.20], the photon flux absorption then is given by

$$\frac{d\Phi(z,\nu)}{dz} = -\sigma(\nu)[\mathrm{Rb}(z)](1-P_{\mathrm{Rb}}(z))\Phi(z,\nu)\,. \qquad [2.21]$$

From the equation above, it can be concluded that for $P_{\mathrm{Rb}} = 1$ no photon is absorbed so the laser light propagates unattenuated through the cell. If Eq. [2.9] is considered, this stage can be achieved only if $\gamma_{opt} >> \Gamma_{SD}$. This condition is then fulfilled only if the OP-cell is completely illuminated (no dark areas) with sufficient power to polarize all Rb atoms. For this, it is crucial that the laser frequency and bandwidth are optimally matched to the pressure broadened Rb absorption line.

On the other hand, the maximum photon flux absorption occurs if $P_{\mathrm{Rb}} = 0$. This condition arises if $\gamma_{opt} << \Gamma_{SD}$, especially if $\gamma_{opt} = 0$.

2.1.7 Interaction of Rb with atoms of the gas mixture

Once the valence electron of Rb is polarized, this atom can lose its polarization via interactions with other atoms of the gas mixture. This interactions occur by two main mechanisms: two body collisions and van der Waals (vdW) interactions.

Two body collisions or binary collisions are just the collision of Rb with another atom. The timescale of this interaction is about $\Delta s/v_{rel} \sim 1$ ps, where Δs is the atomic size (10^{-8} cm) and v_{rel} is the relative velocity of the colliding atoms ($v_{rel} \sim 100$ m/s at room temperature). Depending on the process of spin-transfer, this interaction leads either to spin-destruction or a polarization preserving spin-exchange. Spin-destruction occurs when the spin-polarization is lost in the collision process, e.g., by transfer to external translational angular momenta. On the other hand, spin-exchange occurs when the Rb spin polarization is transferred via Fermi contact interaction to the other atom. A simple expression of both processes as presented in [Rus05] is:

Spin-destruction: $\mathrm{Rb}(\uparrow) + \mathrm{X} \rightarrow \mathrm{Rb}(\downarrow) + \mathrm{X}$ [2.22a]

Spin-exchange: $$\mathrm{Rb}(\uparrow)+\mathrm{X}(\downarrow)\rightarrow\mathrm{Rb}(\downarrow)+\mathrm{X}(\uparrow) \quad [2.22b]$$

where X is the colliding atom. For the spin destruction, X can be any atom of the gas mixture while spin-exchange only occurs with Xe and Rb. A sketch of this interaction is shown in Fig. 2.11a.

The spin-destruction (SD) rate for a binary collision is given by

$$\Gamma_{SD}^{X}=[\mathrm{X}]\kappa_{\mathrm{Rb-X}}, \quad [2.23]$$

where [X] is the number density (in cm^{-3}) of the interacting gas. $\kappa_{Rb\text{-}X} = \langle\sigma_{Rb\text{-}X}\, v_{rel}\rangle$ is the spin-destruction coefficient given by the time averaged product of the elementary cross-section $\sigma_{Rb\text{-}X}$ and the relative velocity v_{rel} of the colliding atoms. This term is neither pressure nor field dependent. The temperature dependence enters via the relative velocity v_{rel} which is proportional to $T^{1/2}$.

The spin-destruction rate coefficients due to binary collisions with He and N_2 are given by [Wal02]:

$$\kappa_{Rb-N_2}=6.33\left(1+\frac{T[^{\circ}\mathrm{C}]-90^{\circ}\mathrm{C}}{194.3^{\circ}\mathrm{C}}\right)\times10^{-18}\,\mathrm{cm}^3/\mathrm{s} \quad [2.24]$$

and

$$\kappa_{Rb-He}=\left(T[\mathrm{K}]^{4.26}\times10^{-29}-6.7\times10^{-20}\right)\ \mathrm{cm}^3/\mathrm{s}\,. \quad [2.25]$$

Eq. [2.25] corresponds to ^{3}He as buffer gas and not ^{4}He, but this difference should not change κ substantially. For temperatures between 100 and 200 °C, $\kappa_{Rb\text{-}N2}$ is between $6.7\cdot10^{-18}$ and $9.1\cdot10^{-18}$ $cm^3\ s^{-1}$ while $\kappa_{Rb\text{-}He}$ is between $8.4\cdot10^{-19}$ and $2.4\cdot10^{-18}$ $cm^3\ s^{-1}$. With these values, 150 mbar of N_2 result in $\Gamma_{SD}^{N_2}\approx 19\ s^{-1}$ for 100°C and 23 s^{-1} for 200°C . For He pressures between 1 and 7 bar, Γ_{SD}^{He} is in the range of 14 to 110 s^{-1} for 100°C and 31 and 250 s^{-1} for 200°C.

The spin-destruction coefficient corresponding to the Rb-Rb interaction is given by

$$\kappa_{Rb-Rb}=(3.9\pm0.4)\times10^{-14}\,\mathrm{cm}^3/\mathrm{s}\,.$$

This value was extracted from [Bar98] and it was measured for ^{3}He using N_2 as buffer gas at 3 mT. For the Rb densities used in this work, Γ_{SD}^{Rb} is on the range of 2.4 to 420 s^{-1}. Finally, the spin-destruction coefficient of Rb due to the interaction with Xe is

$$\kappa_{Rb-Xe}=(0.91\pm0.06)\times10^{-14}\,\mathrm{cm}^3/\mathrm{s}\,.$$

The destruction rate for the binary collision interaction was determined for two different temperatures 80°C and 150°C by Nelson in [Nel02]. Only the one measured at approximately 150 °C is considered here since it is closest to the working temperatures used here. In this work, partial pressures of Xe between 20 and 70 mbar will be used (1 %

of a total pressure from 2 to 7 bar) resulting in Γ_{SD}^{Xe} between $1.3 \cdot 10^4$ and $9 \cdot 10^4$ s^{-1}.

So far, the spin-destruction rate of the Rb-Xe interaction dominates the Rb relaxation due to binary collisions. For this reason, low amounts of Xe are used in an efficient production of HP-Xe [Rus05] [Fin05] [Sch09] [Rut99].

The binary collisions also contribute to the spin-exchange rate of Rb and Xe as

$$\gamma_{SE}^{bin} = \kappa_{SE}^{Rb-Xe}[\mathrm{Rb}], \qquad [2.26]$$

where κ_{SE}^{Rb-Xe} is the spin-exchange coefficient rate given by [Jau03]

$$\kappa_{SE}^{Rb-Xe} = 2.17 \times 10^{-16}\,\mathrm{cm}^3/\mathrm{s}$$

and [Rb] is the Rb number density in cm^{-3}. For the conditions of this work, γ_{SE}^{bin} is about 0.0013 s^{-1}.

Three body collisions. Rubidium atoms can form van der Waals (vdW) molecules with all gases in the mixture with different lifetimes. The most relevant one, however, is the Rb-Xe molecule due to the polar nature of Xe. The formation of this molecule can be expressed as

$$\mathrm{Rb} + \mathrm{Xe} + \mathrm{Y}_i \leftrightarrow \mathrm{RbXe} + \mathrm{Y}_\mathrm{i}, \qquad [2.27]$$

where Y_i is the third body necessary for the formation which could be Xe or the buffer gases N_2 and He, or Rb itself. However, the formation of Rb-Rb Σ^+ [7] molecules is not relevant due to the low Rb densities and partial pressures of N_2 used on this work (see Fig. 2.7).

This interaction generates a stable molecule of Rb-Xe held together by vdW forces forming clusters which are usually called vdW molecules. A three body collision which conserves energy and momentum is required to obtain the binding energy of the Rb-Xe pair. This energy is about 20 meV and the lifetime of this molecule is between 10^{-7} - 10^{-11} s [Pas74] [Gol76]. It is commonly assumed that a single collision can destroy the Rb-Xe vdW molecule [Cha02] [Ang08]. Therefore, the molecular lifetime is expected to be inversely proportional to the total pressure [Cha02] [Bra11].

The three body interaction contributes to both spin-destruction of Rb and spin-exchange of Rb and Xe as shown in Fig. 2.11b. The contribution to the Rb relaxation due to van der Waals molecules is given by

$$\Gamma_{SD}^{vdW} = \frac{66183}{1 + 0.92\frac{[\mathrm{N_2}]}{[\mathrm{Xe}]} + 0.31\frac{[\mathrm{He}]}{[\mathrm{Xe}]}} \cdot \left(\frac{T[\mathrm{K}]}{423\mathrm{K}}\right)^{-2.5} \mathrm{s}^{-1}. \qquad [2.28]$$

[7] Symmetric diatomic molecule.

This expression was determined by Nelson [Nel02] using a gas composition of 1% Xe, 1% N_2 and 98% He. A similar gas composition is used in this work.

For a pressure range of 2 to 7 bar, Γ_{SD}^{vdW} is 2.2 to $2.7 \cdot 10^3$ s^{-1} at 100°C and $1.2 \cdot 10^3$ to $1.5 \cdot 10^3$ s^{-1} at 200°C. Finally, the spin-exchange of Rb-Xe is given by [Nel02] [Rus05]

$$\gamma_{SE}^{vdW} = \left(\frac{[\mathrm{Xe}]}{\gamma_{SE}^{Xe}} + \frac{[\mathrm{N_2}]}{\gamma_{SE}^{N_2}} + \frac{[\mathrm{He}]}{\gamma_{SE}^{He}} \right)^{-1} [\mathrm{Rb}]\ \mathrm{s}^{-1}, \qquad [2.29]$$

with γ_{Xe}= 5230 s^{-1}[Cat92], γ_{N2}= 5700 s^{-1} [Ric02] and γ_{He}= 17000 s^{-1} [Dri96]. For a pressure range of 2 to 7 bar, γ_{SE}^{vdW} is between 0.0038 to $7 \cdot 10^{-4}$ s^{-1} at 100°C and 0.84 to 0.15 s^{-1} at 200°C.

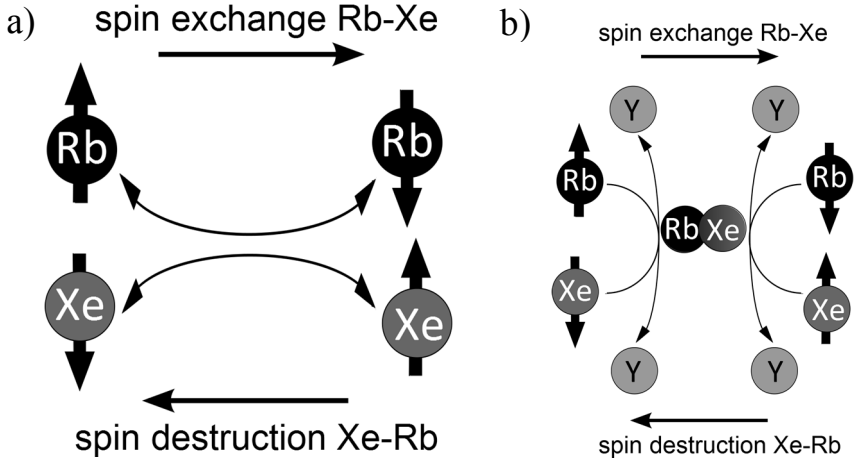

Fig. 2.11: Interaction of a Rb atom with a ^{129}Xe atom. From left to right corresponds to spin exhange while right to left corresponds to spin-destruction of Xe. a) Two body collision. b) Three body collision forming an intermediate van der Waals molecule. Y can be any atom of the gas mixture.

The contribution of the vdW molecules to the spin exchange is at least 3 times higher than the contribution of the binary collisions. These values are in agreement with the values calculated in [Rus05] and [Nor14].

2.1.8 Spin-destruction of Rb

Summarizing the results from above, the spin-destruction rate Γ_{SD} of the Rb electron in a gas mixture composed by Xe, N_2 and He at total pressure p_{tot} > 1 bar is given by

$$\Gamma_{SD} = [\mathrm{He}]\kappa_{Rb-He} + [\mathrm{N_2}]\kappa_{Rb-N_2} + [\mathrm{Rb}]\kappa_{Rb-Rb} + [\mathrm{Xe}]\kappa_{Rb-Xe} + \Gamma_{SD}^{vdW}. \qquad [2.30]$$

This equation includes the contributions of the spin-destruction rate for binary and

three-body collision. Considering the working regime of the Xe-polarizer in this work, the Rb relaxation rate of Eq. [2.30] is calculated and shown in Fig. 2.12.

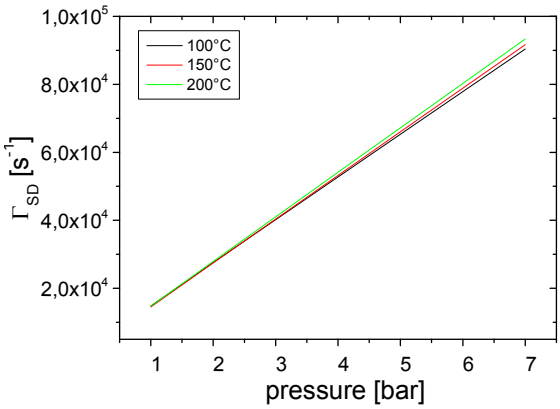

Fig. 2.12: Rb relaxation rate for three different temperatures (100, 150 and 200°C) for pressures between 1 to 7 bar. The gas mixture considered was 1% Xe (total pressure), 150 mbar of N_2 and the rest He.

The dominant contribution to the relaxation of Rb is the interaction with Xe given by the 4th and 5th term of Eq. [2.30]. As expected, the relaxation rate of Rb seen in Fig. 2.12 grows linear with the total pressure of the mixture. However, it showed nearly no temperature dependence especially for working pressures below 4 bar.

2.1.9 Spin-exchange Rb-Xe

The spin-exchange of Rb-Xe contains the contributions of the binary collisions γ_{SE}^{bin} and the van der Waals molecules γ_{SE}^{vdW} as $\gamma_{SE} = \gamma_{SE}^{bin} + \gamma_{SE}^{vdW}$ where γ_{SE} was calculated from Eq. [2.26] and Eq. [2.29] considering the working conditions already mentioned. The results are displayed in Fig. 2.13.

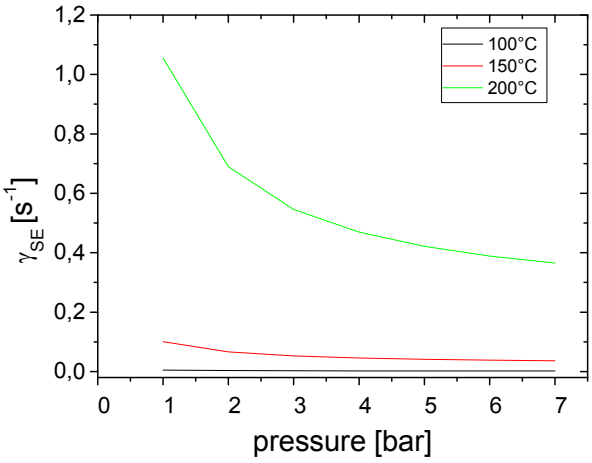

Fig. 2.13: Spin-exchange γ_{SE} due to binary and three body collisions at three different temperatures (100, 150 and 200°C) and total gas pressures between 1 and 7 bar. The gas mixture considered was 1% Xe (total pressure), 150 mbar of N_2 and the rest He.

The spin-exchange between Rb and Xe decreases as the total pressure of the gas mixture increases. This is an advantage for those Xe-polarizers which work at low pressures (high flow) such as [Rus05] and [Sch09]. In addition, the spin-exchange increases significantly for temperatures over 150°C. However, such high temperatures could lead to a non-homogeneous illumination of the OP-cell (see Fig. 4.21).

The values for the spin-exchange and spin-destruction coefficients calculated above are summarized in Table 2.1.

Table 2.1: Spin-destruction rate of Rb and spin-exchange rates Rb-Xe via binary collisions and vdW molecules for a gas mixture total pressure from 2 to 7 bar, with 1% of Xe, 150 mbar of N_2 and 150°C.

	spin-destruction rate of Rb			spin-exchange rate Rb-Xe		
X	κ_{Rb-X} [10^{-18} cm^3/s]	Γ_{SD} [s^{-1}]	Γ_{SD}^{vdW} [s^{-1}]	κ_{SE}^{bin} [10^{-18} cm^3/s]	γ_{SE}^{bin} [s^{-1}]	γ_{SE}^{vdW} [s^{-1}]
He	0.84 - 2.4	14 - 250	--	--	--	--
N_2	6.7 - 9.1	19 - 23	--	--	--	--
Rb	39000	2.4 - 420	--	217	0.0013	--
Xe	9100	1.3 - 9.4·10^4	--	--	--	--
total	--	1.3 - 9.5·10^4	2.2 - 2.7·10^3	--	0.0013	$7\cdot10^{-4}$- 0.84

Comparing the values of columns 2 (Γ_{SD}) and 6 (γ_{SE}^{vdW}), it can be concluded that the spin-destruction rate is, at least, 4 orders of magnitude higher than the spin-exchange rate.

2.1.10 Xe polarization

With the information of the polarization transfer from Rb to Xe, the polarization built up of Xe can be calculated as

$$\frac{\mathrm{d}P_{\mathrm{Xe}}(t)}{\mathrm{d}t} = \gamma_{SE}\left[P_{\mathrm{Rb}}(t) - P_{\mathrm{Xe}}(t)\right] - \Gamma P_{\mathrm{Xe}}(t)\,. \qquad [2.32]$$

In the equation above, Γ is the relaxation of HP-Xe in the gas phase which will be described in the next section. The solution of this differential equation is given by

$$P_{\mathrm{Xe}}(t) = \frac{\gamma_{SE}}{\gamma_{SE}+\Gamma} P_{\mathrm{Rb}}\left[1 - e^{-(\gamma_{SE}+\Gamma)\mathrm{t}}\right]. \qquad [2.33]$$

If $P_{\mathrm{Xe}}(t = 0) = 0$, the stationary solution of Eq. [2.33] is given by

$$P_{\mathrm{Xe}} = \frac{\gamma_{SE}}{\gamma_{SE}+\Gamma} P_{\mathrm{Rb}}. \qquad [2.34]$$

Since P_{Xe} is linear in P_{Rb}, an implicit dependence on the position z is present in

equations [2.32], [2.33] and [2.34] according to the description of Sec. 2.1.6. Consequently, the highest achievable polarization occurs if $P_{Rb} \approx 1$ and $\gamma_{SE} >> \Gamma$. Since γ_{opt} is fixed for the conditions of the experiment, the latter requirement can only be achieved by minimizing the Xe relaxation (Γ) in the OP-cell.

The relaxation rate of HP-Xe, Γ, has two contributions: an intrinsic relaxation Γ_{int} and an extrinsic relaxation Γ_{ext}.

The intrinsic relaxation mechanism describes the relaxation of HP-Xe due to the formation of transient and persistent dimers. This mechanism does not contribute significantly to the relaxation of HP-Xe in the OP-cell because the time scale of these interactions is in the order of hours. However, this mechanism is decisive for the storage stage of HP-Xe and it will be described in Sec. 2.3.

The extrinsic relaxation mechanism Γ_{ext} includes the relaxation of HP-Xe due to: collisions with the wall, interaction with paramagnetic gases (typically oxygen), diffusion through magnetic field gradients and, of course, unpolarized Rb. These factors are related to the experimental conditions which can be optimized in order to minimize Γ_{ext}. The working conditions of an optimized system include $p_{O2} < 10^{-3}$ mbar, magnetic field gradients below 10^{-2} cm^{-1} and wall relaxations times of about 1 h. These values lead to $\Gamma < 10^{-3}$ s^{-1} as it is going to be shown in Sec. 2.3.2. Under these conditions and considering that the residence time of HP-Xe in the OP-cell is about 1 minute, the most relevant relaxation mechanism inside the OP-cell is the interaction with unpolarized Rb. This contribution is more than five orders of magnitude higher than the other mechanisms. For this reason, it is crucial to minimize the contact of Rb vapor with HP-Xe in the areas of the OP-cell which are not illuminated by the laser. Therefore, Rb vapor must be trapped directly at the outlet of the OP-cell.

As a final remark, the models for the prediction of the final polarization of HP-Xe based on Eq. [2.33] require so far several empirical corrections. For example, in Schrank *et al* [Sch09], the results of the calculations of the final polarization are multiplied by 0.4 in order to match the simulations to the experimental results. Corrections of the same order had to be introduced in [Nor13]. The only work was this model seems to fit without further considerations is [Rus05]. In this work, a novel design of a Xe-polarizer is presented (see Appendix 2). The critical difference seems to be the pre-heating of the gas mixture before entering the OP- cell. The simulations in [Fin07] support this claim.

2.2 Cryogenic separation of HP-Xe

As it was shown in Sec. 2.1.8, a low partial pressure of Xe is required to obtain an efficient optical pumping process. Therefore, the HP-Xe must be separated from the gas mixture for those applications where high concentrations of this gas are needed. So far, the

most efficient way to separate HP-Xe from the buffer gases is cryogenically[8]. This method is based on freezing out the HP-Xe inside a cold accumulation trap while the buffer gases flow through it. In this way, the HP-Xe is accumulated in solid state inside this cold trap until the required amount is reached. Then, the buffer gases are evacuated while the HP-Xe is still frozen. Finally, the HP- Xe ice is turned into gas by immersing the cold trap in hot water.

According to the phase diagram of Xe shown Fig. 2.14, the transition of HP-Xe gas to solid occurs at liquid nitrogen temperatures for pressures below 818 mbar. For higher total pressures, the gas first liquefies and then solidifies or vice-versa for bringing HP-Xe ice into the gas phase. For the conditions of the Xe-polarizer described in this work, the solidification of HP-Xe passes through the liquid phase to the solid phase (blue line in Fig. 2.14). However, when the ice is later vaporized, the buffer gases are previously evacuated, resulting in a much lower pressure (a few mbars). This pressure is typically below the triple point of Xe (0.8177 bar and 161.4 K). In Fig. 2.14, the red line shows the process of volatilization when the Xe ice is heated at pressures below the triple point.

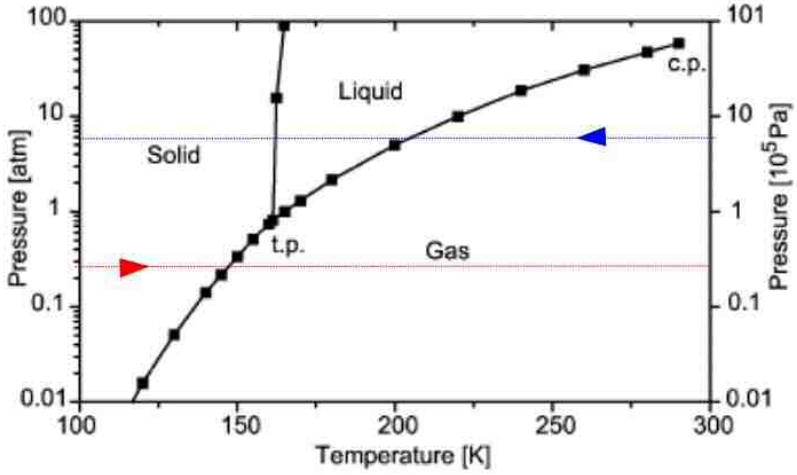

Fig. 2.14: Phase diagram of Xe. The triple point (t.p.) is 161.3 K and 818 mbar. The blue line shows the freezing procedure while the red line shows the volatilization process of HP-Xe in the cold trap. The critical point (c.p.) is 289.7 K and 58.8 bar. Graphic extracted from [Coo61].

The mechanisms of relaxation in the solid phase and in the liquid phase will be described in order to find those conditions, which minimize the polarization losses during the cryogenic separation.

[8] The group in Nottingham proposes expansion or combustion as alternative separation method [Ril13][Mee15].

2.2.1 Relaxation of HP-Xe in the liquid phase

The relaxation of HP-Xe in liquid phase was first studied by Carr and collaborators [Str61] [Bri62] [Hun63] obtaining relaxation times about 16 minutes at 14 kG and 200 K. Some years later, K. Sauer [Sau97] published extensive research on liquid HP-Xe obtaining relaxation times over 30 minutes at 180 K. Her work confirms the spin rotation interaction as the main relaxation mechanism of HP-Xe in the liquid phase due to its temperature dependence.

Spin rotation interaction is the main mechanism of relaxation also in the gas phase and it will be described in detail in Sec. 2.3.1. In addition, the relaxation of HP-Xe in liquid phase is extremely sensitive to oxygen contamination [Hun63].

The dependence of the relaxation rate of liquid HP-Xe on the holding magnetic field at different temperatures is shown in Fig. 2.15. On the ordinate, the total relaxation rate is given by the spin rotation interaction and the wall relaxation assuming the latter to be constant. According to Fig. 2.15, lower relaxation rates are found for fields over 80 G and low temperatures. Particularly, at liquid nitrogen temperatures (77 K) and fields over 120 G, the relaxation of Xe in the liquid phase is about 20 minutes. The polarization losses in the cold trap for pressures higher than the triple point can be minimized by shortening the freezing time by providing an accumulation cell with a high surface-to-volume ratio which can provide a good thermal contact with the walls cooled with liquid nitrogen bath. For example, in case of thawing, the time in the liquid phase can be shortened by thawing the HP-Xe quickly applying a large reservoir with high heat capacity i.e. boiling water.

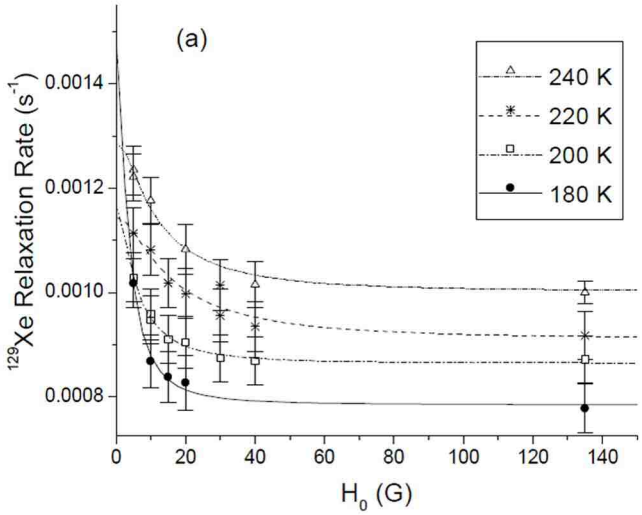

Fig. 2.15: Relaxation rate of HP-Xe in liquid phase vs. magnetic field at different temperatures [Sau97]. The relaxation rate on the ordinate corresponds to the spin rotation interaction and the wall relaxation.

2.2.2 Relaxation of HP-Xe in the solid phase

Depending on the temperature regime, there are different relaxation mechanisms for solid[9] Xe.

At temperatures below 50 K, the dominant mechanism responsible is the dipole-dipole interaction between ^{131}Xe and ^{129}Xe

$$V_{dd} = \frac{\mu_\alpha \mu_\beta}{I_\alpha I_\beta r_{\alpha\beta}^{\ 3}} \left[I_\alpha \cdot I_\beta - 3 \frac{(I_\alpha r_{\alpha\beta}) \cdot (r_{\alpha\beta} I_\beta)}{r_{\alpha\beta}^{\ 2}} \right], \qquad [2.35]$$

where μ_i is the magnetic moment of ^{129}Xe (α) and ^{131}Xe (β), I_i are their nuclear magnetic moments and $r_{\alpha\beta}$ is the distance between both atoms.

At temperatures in the range of 50 - 120 K, the dominant mechanism is the spin rotation interaction with the nearest-neighbor in the crystal lattice. In this case, it gives rise to Raman scattering of phonons [Adr64].

For temperatures above 120 K, the HP-^{129}Xe ice relaxation can be several orders of magnitude shorter than predicted by the phonon scattering mediated by the spin rotation interaction [Kuz02]. An additional mechanism acts there, which is the dipole-dipole interaction modulated by vacancy diffusion. This mechanism has strong dependence on the temperature because of the Arrhenius activation of the vacancy density and hopping rate. Furthermore, the relaxation rates of HP-^{129}Xe in solid phase depend strongly on the magnetic field (below 1 T) as a result of cross-relaxation to ^{131}Xe[10]. This isotope has a very short relaxation time, which shortens the relaxation time of ^{129}Xe through spin transfer mechanisms [Gat93].

The relaxation rate/time vs. temperature for HP-^{129}Xe in natural and enriched abundance is shown in Fig. 2.16a displaying how critical the relaxation depends on the temperature during the thawing/volatilization process of HP-Xe ice. In this graphic, the relaxation time of solid HP-Xe at liquid N_2 temperature and moderately high fields (0.1 T) is about 2.5 h. For temperatures close to the melting point (161 K), the relaxation times are about one minute or even less. This relaxation time increases for fields above 1 T to 15 - 20 minutes. For temperatures about 4.2 K, the relaxation time of solid HP-Xe can exceed 30 h [Lan02].

A simulation of the magnetization in the accumulation cell vs. accumulation time is shown and in Fig. 2.14b. The dotted line represents the limit of no polarization losses where the magnetization increases linearly with the accumulation time. For each magnetic field, the magnetization decreases because of the thermal gradients between the outer and the inner part of the reservoir of the cold accumulation trap. Those temperature gradients

[9] Solid Xe is here referred to ice/snow. The crystalline structure of solid Xe under the conditions of cryogenic separation cannot be easily defined because of annealing and temperature (pressure) gradients inside of the accumulation cell.

[10] However, calculations from Waller [Wal32] predicts that the relaxation through the phonon scattering due to dipole-dipole interaction should be negligible.

increase as long as the Xe-ice layer increases its thickness considering that the conductivity of Xe in solid state is about 4.5 to 2.9 mW/cm in the range from 80 to 160 K respectively [Kon01].

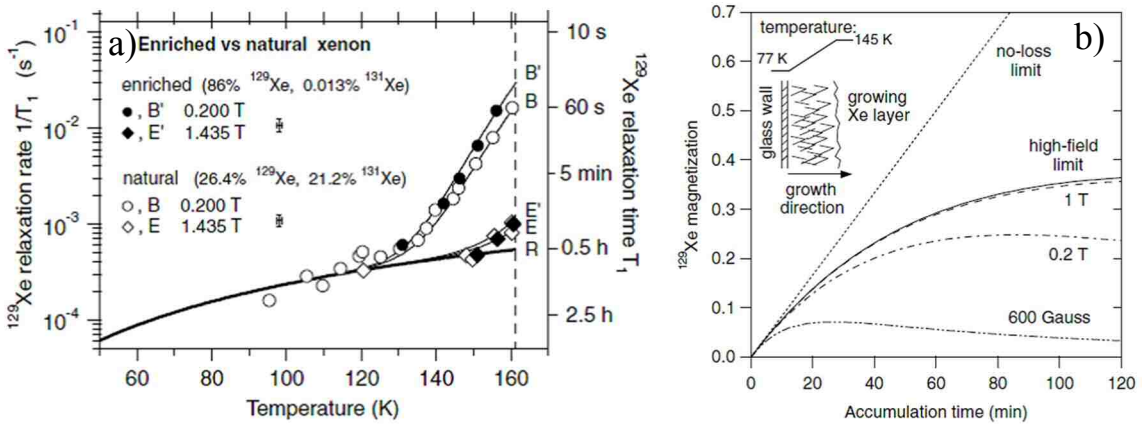

Fig. 2.16: a) Relaxation rate (time) of natural and enriched HP-^{129}Xe in solid state vs. temperature for several holding magnetic fields. b) Model of accumulation of HP-^{129}Xe ice in a cold trap: magnetization in arbitrary units vs. accumulation time. The magnetization should grow linearly assuming a constant flow of gas (dotted line) without polarization losses. As the ice layer thickens, the temperature gradient between outside of the cell (77 K) and inside the cell (dash- dotted lines and solid line) increases, reducing dramaticaly the relaxation times [Kuz02].

From Fig. 2.16, it is concluded that the accumulation of HP-Xe in solid phase must be performed at the highest magnetic field possible and the transition time of HP- Xe ice from the accumulation temperature (77 K) to room temperature must be a short as possible. These conditions are again fulfilled by an accumulation cell with a high surface-to-volume ratio.

In addition, the temperature gradients over the HP-Xe ice layer should be minimized during the separation of HP-Xe from the gas mixture. Especially because the warm gas mixture (T > 300 K) is constantly flowing warming up the surface of the HP-Xe ice. An efficient accumulation trap requires a large accumulation surface with a good thermal contact. This also minimizes the temperature gradients over the HP-Xe ice layer and minimizes the transition times between gas-solid and solid-gas. The relaxation of HP-Xe in solid phase is therefore a characteristic of the design of each system and it depends on the structure and history (annealing) of the HP Xe-ice.

2.3 Storage of HP-Xe in the gas phase

Once produced, the HP-Xe must be stored properly in order to preserve its polarization as long as possible. This requirement is valid for transport to the facility where

it will be used or for experiments which require long measurement times. However, an effective storage of HP-Xe is not only required to preserve the polarization during transport, some applications related to fundamental physics require long acquisition times. This precision of the measurement scales with $t^{-3/2}$ being t the measurement time [Gem10] [Tul13]. These long detection times can only be achieved via minimization of the spin-destruction rate of Eq. [2.36].

The transport and storage of HP-Xe can be performed is solid phase [Alb94] [Rus05]. The typical storage times of HP-Xe ice are about 2 h which is enough for transport over short distances. The advantage of this method is that high amounts of HP-Xe can be transported. This procedure depends critically on temperature and magnetic fields and it demands mobile strong magnets and containers at liquid N_2 temperatures. However, pure HP-Xe in gas phase can be stored longer than 3 h (see Chapter 5) allowing the long measurement times required for fundamental physics applications.

The storage conditions for HP-Xe gas in this work are simple, economic and reproducible:

1) Room temperature ($T \approx 293$ K).

2) Holding magnetic fields about 2 mT. This value is usually sufficient to define a magnetic field along one direction reducing the influence of the transverse components of the earth magnetic field on the relaxation times (see Eq. [2.43]). This range of magnetic fields can be easily produced by a system of air coils and a standard power supply or battery. Higher magnetic fields require higher input powers with thermal stabilization in order to compensate the heat dissipation. Such stabilized holding fields increase significantly the complexity and costs of the system. In addition, magnetic fields over 0.1 T could magnetize ferromagnetic impurities of the storage vessel [Sch06] sacrificing its quality and, in consequence, the storage time of Xe.

3) The range of storage pressures of pure Xe will be between 0.1 and 0.7 bar.

4) The storage vessels used in this work are spherical glass cells of 6 to 10 cm diameter. The used glass is a special aluminum-silicate glass with low iron content called GE-180. The storage vessels are free of Rb and no coatings are used. These vessels already shown an excellent performance for storage of ^{3}He [Gem10] [Tul13].

5) Due to extreme careful manipulation, the partial pressure of oxygen is kept below 10^{-4} mbar.

The spin-destruction rate Γ of Xe in gas phase in magnetic fields below 0.1 T[11], as it was mentioned before, is composed by several interaction which can be classified by intrinsic and extrinsic origins.

$$\Gamma = \underbrace{\Gamma^{\mathrm{dip}} + \Gamma^{\mathrm{vdW}}}_{\text{intrinsic}} + \underbrace{\Gamma^{\mathrm{O_2}} + \Gamma^{dB} + \Gamma^{wall}}_{\text{extrinsic}}. \qquad [2.36]$$

[11] For magnetic fields over 0.1 T see [Ang08]

The intrinsic relaxation mechanisms include: the relaxation rate due to the transient dimers Γ^{dip} and the relaxation rate due to the persistent dimers or van der Waals molecules given by Γ^{vdW}.

The extrinsic relaxation mechanisms include the polarization losses due to the interaction with oxygen Γ^{O2}, relaxation rate due to the diffusion of HP-Xe in magnetic field gradients Γ^{dB} and the relaxation rate due to the collision with the walls of the container Γ^{wall}.

The relaxation rates of Eq. [2.36] can be also expressed in terms of the longitudinal or spin-lattice relaxation time T_1 (see Sec. 3.1.4) as

$$\Gamma^i = \frac{1}{T_1^i}. \qquad [2.37]$$

T_1 is the characteristic time of the exponential decay of the polarization (or magnetization) over time. The details of the determination of T_1 will be discussed in the next chapter.

The different relaxation mechanisms of Eq. [2.36] will be described in detail below.

2.3.1 Relaxation rate due to intrinsic mechanisms

The ^{129}Xe spin relaxation due to intrinsic mechanisms is governed by the spin rotation interaction generated when a dimer ^{129}Xe-Xe is formed:

$$H_{sr} = c_k(R)\vec{K}\cdot\vec{N}, \qquad [2.38]$$

where c_k is a coupling constant which depends on the distance, R, between the interacting atoms. $\vec{K}$ is the spin of the nucleus (Xe) and $\vec{N}$ is the angular momentum of the molecule. This term is responsible for the spin relaxation either through binary collisions or van der Waals molecules. The binary collisions are considered to form transient dimers while the three body collisions form persistent dimers also called van der Waals molecules.

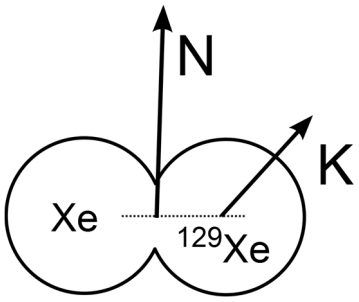

Fig. 2.17: Spin rotation interaction of a ^{129}Xe-Xe molecule. $\vec{N}$ is the angular momentum of the molecule and $\vec{K}$ is the nuclear spin of ^{129}Xe.

2.3.1.1 Relaxation rate due to binary collisions

Binary collisions generate transient dimers whose lifetimes are in the order of ps.

The relaxation rate Γ^{dip} due to this interaction is given by

$$\Gamma_t^{sr} = \sigma_{sr}(R,T) v_{rms}[Xe] = K(R,T)[\mathrm{Xe}]. \qquad [2.39]$$

$\sigma_{sr}(R,T)$ is the average spin relaxation cross-section which depends on the temperature T and R though c_k of spin-rotation interaction given in Eq. [2.38]. v_{rms} is the relative root-mean-square speed of the interacting Xe atoms. However, the experiment measures directly $K(R,T)$ which considers the contributions of $\sigma_{sr}(R,T)$ and v_{rms} together.

This process was investigated by the first time in 1963 by E. Hunt and H. Carr [Hun63] who studied the Xe relaxation at different pressures above 50 bar obtaining the graphic of Fig 2.18. This study was performed with holding fields of 5, 12.2 and 25 kG obtaining the same relaxation rates.

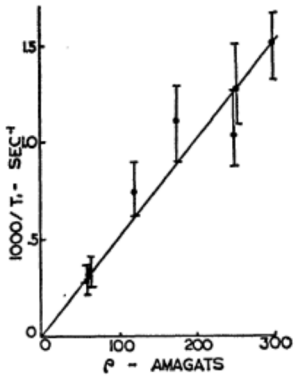

Fig. 2.18: Relaxation rate of ^{129}Xe for pressures over 50 bar [Hun63]. This behavior is independent of the holding magnetic field and it was confirmed by Moudrakovski [Mou01].The units of the abscissa are in amagats (1 amagat ≈ 1 bar for an ideal gas).

The linear dependence of the relaxation rate versus pressure is characteristic of the interactions due to binary collisions. In this way, the contribution to the relaxation by transient dimers was derived to be

$$\Gamma^{dip}\left[\mathrm{h}^{-1}\right] = \frac{p_{\mathrm{Xe}}[\mathrm{bar}]}{1\,\mathrm{bar}} \cdot \frac{1}{56\mathrm{h}} \cdot \frac{T[\mathrm{K}]}{273\mathrm{K}}, \qquad [2.40]$$

where p_{Xe} is the partial pressure of Xe in bar and T is the absolute temperature. These results were recently confirmed by Moudrakovski [Mou01] extending the study to high magnetic fields (4.7 and 9.4 T) and lower densities. In addition, a quadratic dependence of the relaxation rate on the magnetic field was found.

The contribution to the relaxation rate due to this mechanism is smaller than 0.012 h^{-1} since the maximum Xe partial pressure used in this work is about 0.7 bar (see Chapter 6). This relaxation rate leads to $T_1^{dip} \approx 82$ h. This relaxation mechanism can be neglected when compared with the contributions of the relaxation mechanisms which will be described in the following sections.

2.3.1.2 Relaxation rate due to persistent dimers: Xe-Xe van der Waals (*vdW*) molecules

As explained before, persistent dimers result from a three-body collision. The ^{129}Xe-Xe molecule was first observed by Bernardes and Primakoff [Ber59] who estimated a concentration of 0.5% Xe-Xe dimers in approximately 1 bar of Xe at room temperature. The lifetime of these Xe-Xe molecules is about 100 ps. For many years, the relaxation mechanism of ^{129}Xe due to the vdW molecules was not identified until 2002. In this year, the relaxation rate was described in [Cha02] as follows[12]

$$\Gamma^{\mathrm{vdW}} = \left[T_1^{\mathrm{Xe\text{-}Xe}} (1 + r\, p_{\mathrm{B}} / p_{\mathrm{Xe}}) \right]^{-1}. \qquad [2.41]$$

T_1^{XeXe} is the relaxation time of HP-^{129}Xe due to the formation of vdW molecules. This value is independent of the Xe pressure. p_{Xe} is the partial pressure of Xe and p_{B} is the partial pressure of a buffer gas. r is the destruction rate coefficient of the vdW molecule which depends on the characteristics of the buffer gas "B". Note that if $p_{\mathrm{B}} = 0$, the relaxation rate $\Gamma^{\mathrm{vdW}} = 1/T_1^{\mathrm{XeXe}} = \Gamma^{\mathrm{XeXe}}$.

Chann *et al* [Cha02] extracted the value of Γ^{XeXe} and r from measurements of Xe relaxation with He, N_2 and Ar as buffer gases at low fields and room temperature. The value obtained for Γ^{XeXe} was $(6.72 \pm 0.1) \cdot 10^{-5}$ s^{-1} which leads to a limiting relaxation time of only 4.1 h. The highest destruction rate was obtained for N_2 with $r = 1$. The group of Brian Saam has extracted Γ^{XeXe} and r from the relaxation rate of Xe at high fields obtaining $T_1^{\mathrm{XeXe}} = (4.59 \pm 0.4)$ h [Ang08] and $r = 0.5$ for N_2 (see Table 5.1).

This relaxation mechanism is the most important in this work and it will be studied in detail in Chapter 5.

2.3.2 Relaxation rate due to extrinsic mechanisms

2.3.2.1 Relaxation due to the interaction with paramagnetic gases

The interaction with paramagnetic gases, i.e. usually oxygen was determined by Jameson in [Jam88]. For a fixed temperature, the relaxation rate due to this interaction is proportional to the oxygen partial pressure as shown in Fig. 2.19. A fit to this graphic gives

$$\Gamma^{O_2}[\mathrm{s}^{-1}] = 0.388 \frac{p_{O_2}[\mathrm{bar}]}{1.013} \frac{273}{T[\mathrm{K}]} \mathrm{s}^{-1}, \qquad [2.42]$$

where p_{O2} is the partial pressure of oxygen.

For p_{O2} corresponding to atmospheric pressure, the relaxation time is about 13 s. However, the values of p_{O2} of this work are below 10^{-4} mbar. This value leads to $\Gamma^{O2} \approx 3.6\ 10^{-8}$ s^{-1} or $T_1^{O2} \approx 7780$ h. This relaxation time is much longer than the relaxation time due

[12] The detailed derivation of Eq. [2.41] can be found in [Cha03]

to formation of vdW molecules and therefore, it can be neglected.

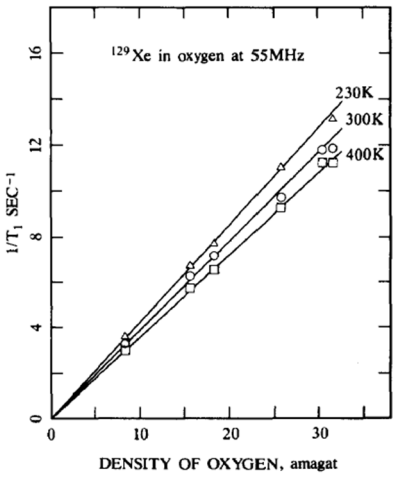

Fig. 2.19: Relaxation rate of HP-^{129}Xe due to the interaction with paramagnetic oxygen. The relation between the relaxation rate and the partial pressure of oxygen is linear at a given temperature. Figure extracted from [Jam88].

2.3.2.2 Relaxation due to diffusion in gradients of the holding magnetic field

The relaxation due diffusive motion of HP-Xe in magnetic field gradients in the high-pressure regime[13] is given by the product of the diffusion coefficient of Xe $D_{\mathrm{Xe}}^{\mathrm{GM}}$ and the absolute gradients as

$$\Gamma^{dB} = D_{\mathrm{Xe}}^{\mathrm{GM}} \frac{\left|\vec{\nabla}B_x\right|^2 + \left|\vec{\nabla}B_y\right|^2}{B_0{}^2}, \qquad [2.43]$$

where $\vec{B}_0$ is the magnetic field in the direction of interest and B_i is the magnetic field in the transverse direction with $i = x, y$ assuming that $|B_0| >> |B_i|$ [Cat88]. *T*he diffusion coefficient of Xe in a gas mixture given by

$$\frac{1}{D_{\mathrm{Xe}}^{\mathrm{GM}}} = \left(\frac{p_{\mathrm{Xe}}}{D_{\mathrm{Xe}}} + \frac{p_{\mathrm{He}}}{D_{\mathrm{He\text{-}Xe}}} + \frac{p_{\mathrm{N_2}}}{D_{\mathrm{N_2\text{-}Xe}}} \right) \frac{1}{p_0} \left(\frac{T_0}{T} \right)^{3/2}. \qquad [2.44]$$

In the equation above, p_i is the partial pressure of each gas; p_0 is the total pressure of the mixture. D_{Xe} is the self-diffusion coefficient of Xe and $D_{\mathrm{i\text{-}Xe}}$ is the diffusion coefficient of Xe in *i*= He, N_2. Those coefficients are summarized in Table 2.2.

[13] $R^2\omega_L >> D_{\mathrm{Xe}}$ with *R* the radius of the sphere and ω_L the Larmor frequency. For more details see [Cat88]

Table 2.2: Self-diffusion coefficient of pure Xe and Xe mixed with N_2 and He measured at 1 mbar [Aco06].

	Diffusion coefficient [cm²/s]	Temperature [K]
D_{Xe}	58	300
$D_{Xe\text{-}N2}$	210	353
$D_{Xe\text{-}He}$	790	300

For a magnetic field with cylindrical symmetry, the absolute gradients defined in Eq. [2.43] can be simplified [Hie06] as

$$\frac{\left|\nabla B_x\right|^2 + \left|\nabla B_y\right|^2}{{B_0}^2} \leq \frac{\left|\nabla B_z\right|^2}{{B_0}^2}.$$

In this way, the homogeneity H of the magnetic field is given by

$$H = \frac{\left|\nabla B_z\right|}{B_0}. \qquad [2.45]$$

Finally, the diffusion coefficients of the polarizing gas mixture with a total pressure of 2 and 7 bar are 1.14 cm²/s and 0.37 cm²/s respectively. The maximum D_{Xe} of this work is expected during the storage at 0.13 bar of Xe with 2 bar of N_2 resulting in D_{Xe} = 0.09 cm²/s. Considering a homogeneity $H < 10^{-3}$ cm^{-1}, the relaxation time due to diffusion in magnetic field gradients T_1^{dB} is longer than 240 h in the first case and longer than 3000 h in the second case. In consequence, this contribution to the HP-Xe relaxation can also be neglected.

2.3.2.3 Relaxation due to collisions with the container Γ^{wall}

Γ^{wall} describes the relaxation rate due to collisions with the inner walls of the container. This relaxation mechanism depends on the surface to volume ratio of the container vessel as

$$\Gamma^{wall} = \eta \frac{S}{V}. \qquad [2.46]$$

The relaxivity η, is assumed to be a constant for each vessel and related to the interaction between the HP gas with para- or ferromagnetic centers on top or close to the inner surface. More explicitly, $\eta = \alpha \bar{v}/4$, where α is the probability for a spin flip per wall encounter and $\bar{v}$ is the root mean square (rms) speed of the atoms colliding with the wall [Ric02]. This relaxation mechanism is pressure independent since the number of collisions of Xe with the internal walls of the vessel is proportional to the number of atoms.

The wall relaxation mechanism was studied for glass vessels with silohexane-based

coatings [Zen83] [Nic84] [Dri95] with Surfasil being the most popular [Bre00]. The original purpose of these coatings was to prevent the corrosion of the glass surface due to the contact with Rb and to reduce the dispersion of the T_1 values in cells of the same characteristics [Mee15]. In this work, no coatings were used at all.

So far, no reports were published analyzing in detail the interaction of Xe with bare glass walls. However, recent results at very high magnetic fields > 1 T [Ang08] suggest that a Fermi-contact interaction between the spin of the valence electrons (radicals) on the glass surface and the Xe nuclear spin is obviously responsible mechanism for the wall relaxation.

In case of ^{3}He, the wall relaxation mechanisms were studied by Schmiedeskamp *et al.* [Sch06]. Here it was demonstrated that relaxation via the Fermi-contact interaction is the dominant relaxation mode during wall collisions.

2.3.3 Summary of the relaxation times in storage conditions

From all relaxation mechanisms mentioned above, the dominating contributions to the relaxation of HP-Xe in gas phase (293 K and 2 mT) are given by

$$\frac{1}{T_1} = \frac{1}{T_1^{\text{wall}}} + \frac{1}{T_1^{\text{vdW}}} = \frac{1}{T_1^{\text{wall}}} + \frac{1}{T_1^{\text{Xe-Xe}}(1+r\,p_{\text{B}}/p_{\text{Xe}})}. \qquad [2.47]$$

The relaxation time due to interaction with the wall and the vdW relaxation cannot be inferred from this equation by performing a single measurement with pure HP-Xe. This distinction can be performed only if HP-Xe is mixed with different buffer gases. This topic will be exhaustively studied in Chapter 5.

Finally, the T_1 times must be measured at the same conditions as being the case for the storage. The construction, optimization and characterization of a low field NMR system for determining the storage times (T_1) of HP-^{129}Xe will be explained in the next chapter.

Chapter 3: NMR spectrometer for the determination of ^{129}Xe storage times

The previous chapter exposed the different relaxation mechanisms, which may occur during optical pumping of ^{129}Xe, the subsequent cryogenic separation process and finally during the storage of the HP-Xe gas. The polarization of the HP-Xe gas has to be measured at these intermediate steps in order to identify possible polarization losses. In this way, the single steps can be optimized in regards to a maximum achievable nuclear polarization. These measurements are performed in this work using the well-established technique of nuclear magnetic resonance (NMR) [Abr83]. This technique will be applied for relative measurements of the nuclear polarization in each step of the production of HP-^{129}Xe.

This chapter describes an NMR spectrometer, which was specially designed to detect weak NMR signals from spin samples of HP-^{129}Xe at relative low polarization (~ 1%) and holding magnetic fields of about 2.3 mT. At such fields, the absolute measurement of the nuclear polarization of a spin sample by NMR is possible, in principle, but it requires sophisticated calibration techniques as described for example in [Sha00] [Sch09]. For this reason, a more reliable and simple technique for the measurement of the absolute polarization was used instead. This technique uses highly sensitive fluxgates in order to detect the static magnetic field from a magnetized spin sample of spherical symmetry. The detailed discussion can be found in Chapter 6. This absolute polarization detection method was used as a final check after all optimization procedures of the Xe-polarizer were done, for which a relative monitoring of the polarization via NMR was sufficient. The NMR spectrometer had not only provided information on relative polarization losses, it also contributed to investigate and to improve the longitudinal relaxation time T_1 [Sli96] of the spin sample in different container vessels and using buffer gas mixtures. For these studies, the detection sensitivity of the NMR spectrometer is crucial. For example, HP-^{3}He can be used as a reference for existing NMR spectrometers working at magnetic fields of around 1 mT. The expected NMR signal from HP-^{129}Xe compared with the signal of HP-^{3}He is about a factor of 70 less. This simply follows from the fact that the signal amplitude S_n obtained is proportional to the polarization P_n as following [Abr83]

$$S_n \propto P_n \mu_n \beta_n [n] \qquad [3.1]$$

where μ_n is the magnetic moment, β_n is the isotopic abundance of the element n and [n] is its number density. When compared for the same number density, the signal of HP-^{3}He is, at least, 70 times higher than the signal coming from HP-^{129}Xe as:

$$\frac{S_{Xe}}{S_{He}} = \frac{P_{Xe}\ \beta_{129Xe}\ \mu_{Xe}}{P_{He}\ \mu_{He}} \approx \frac{0.05 \cdot 0.26}{0.5 \cdot 1.75} \approx \frac{1}{70}$$

with $\mu_{He}/\mu_{Xe} = 1.75$, considering natural Xe ($\beta_{129Xe} = 0.26$) and taking typical values of the polarization for ^{3}He and ^{129}Xe equal to 0.5 and 0.05 respectively.

An overview on the theoretical aspects of NMR necessary to describe the construction of the spectrometer and the NMR measurements is given on the first part of this chapter. It follows a detailed description of the low field NMR system together with the procedure to measure the NMR signal and to extract the characteristic T_1 relaxation times.

3.1 NMR principles

Nuclear magnetic resonance (NMR) is a physical phenomenon in which nuclei with spin $\vec{I} \neq 0$ placed in a magnetic field absorb and re-emit electromagnetic radiation. This energy corresponds to a specific resonance frequency which depends on the strength of the magnetic field and the magnetic properties of the NMR active nuclei such as ^{1}H and ^{13}C or, in this case, ^{129}Xe (nuclear spin $I = 1/2$). The resonance frequency [Lev07] is given by

$$\vec{\omega}_L = \gamma \vec{B}_0 . \qquad [3.2]$$

In Eq. [3.2], $\vec{\omega}_L$ is known as the Larmor frequency and γ is the gyromagnetic ratio. This value represents the intensity of the coupling between the nuclear spin and the magnetic field. Each nucleus with $\vec{I} \neq 0$ has a distinctive value of γ given by

$$\gamma = g\, \mu_n / \hbar , \qquad [3.3]$$

where g is the nuclear g-factor, $\hbar$ is the Planck constant divided by 2π, and μ_n is the nuclear magneton which is given by $\mu_n = e\hbar/2m_p$ where e is the electron charge and m_p the mass of the proton.

In this study, only HP-^{129}Xe will be investigated with $g_{129Xe} = -1.544978008 \cdot 10^7$ [Hus79] resulting in $\gamma_{Xe} = -1.17767397$ kHz/G , according to Eq. [3.3].

The nuclear spin $\vec{I}$ follows the rules of any quantum mechanical angular momentum [Coh92]. The absolute value is given by $\sqrt{I(I+1)}\ \hbar$ and its observable projections along the quantization axis (z-axis) are $m_I \cdot \hbar$ with $m_I = -I, -I+1, \ldots, I-1, I$.

If a nucleus with magnetic moment $\vec{\mu} \neq 0$ ($\vec{\mu} = \gamma \hbar \vec{I}$) is placed in a homogeneous magnetic field $\vec{B}_0 = B_0 \hat{z}$, it acquires a Zeeman energy given by $E = -\vec{\mu} \cdot \vec{B}_0$ [Zee82]. As a result, the two possible quantum mechanical projections (Zeeman-splitting) for the ^{129}Xe nuclear spin are revealed with $m_I = \pm 1/2$ as is shown in Fig. 3.1. In case of ^{129}Xe $\vec{\mu}_{Xe} < 0$, then the energy levels are given by $E_0 + |\vec{\mu}|\vec{B}_0$ for $m_I = -1/2$ and $E_0 - |\vec{\mu}|\vec{B}_0$ for $m_I = 1/2$.

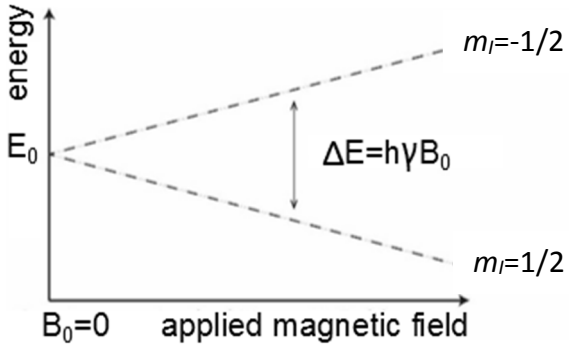

Fig. 3.1: The energy levels of an ensemble of atoms with $I = 1/2$ and $\vec{\mu} < 0$ split when immersed in a magnetic field $\vec{B}_0$. The separation is proportional to the strength of $\vec{B}_0$.

The magnetic moment and, with it, the spin of the nucleus can be tilted out of the quantization axis by applying a resonant radiofrequency (RF) pulse perpendicular to the magnetic field with frequency given by Eq. [3.2]. The magnetic moment will then precess around the quantization axis with Larmor frequency ω_L. The classical analogy of the classical precessional motion of a rotating or spinning body such as a toy top or gyroscope can serve as a basis for understanding the quantum model. The angular momentum vector of a spinning top sweeps out a cone in space as it precesses about the axis of rotation and the tip of the vector sweeps out a circle (see Fig. 3.2). The precession cone of a spinning top possesses an identical geometric form to the cone of potential orientations that are possible for the quantum spin vector.

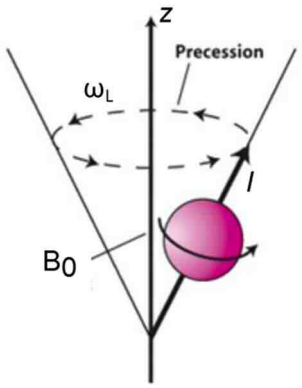

Fig 3.2: Nuclear spin $\vec{I}$ precessing in an external magnetic field $B_0\hat{z}$.

The macroscopic magnetization of a spin sample of volume V is defined as follows:

$$\vec{M} = \frac{1}{V}\sum\left\langle\vec{\mu}\right\rangle. \qquad [3.4]$$

The nuclear magnetization $\vec{M} = (M_x, M_y, M_z)$ as a function of time can be calculated by a set of macroscopic equations called Bloch equations. These equations were first introduced by Felix Bloch in 1946 [Blo46]. The equations of motion of nuclear magnetization are derived from the torque on the magnetic moment as

$$\frac{d\vec{M}}{dt} = \gamma \cdot \vec{M} \times \vec{B}_0. \qquad [3.5]$$

Eq. [3.5] represents the equations of motion for the magnetization $\vec{M}$ without dissipation. Bloch introduced phenomenologically two relaxation rates $1/T_1$ and $1/T_2$ where T_1 is the longitudinal relaxation time and T_2 is the transverse relaxation time. The introduction of these relaxation terms assures, that the magnetization $\vec{M}$ returns to the thermal equilibrium magnetization $\vec{M}_0$ in exponential decay.

$$\begin{aligned} \frac{dM_x}{dt} &= \gamma \cdot M_y \cdot B_0 - \frac{M_x}{T_2} \\ \frac{dM_y}{dt} &= -\gamma \cdot M_x \cdot B_0 - \frac{M_y}{T_2} \\ \frac{dM_z}{dt} &= \frac{M_0 - M_z}{T_1} \end{aligned} \qquad [3.6]$$

For many applications it is convenient to introduce the rotating frame of reference: x', y'and z' which rotates with an angular frequency $\vec{\omega}_R = -\omega\,\hat{z}'$ with $z = z$' axis. The equations of motion in this rotating reference frame lead to an effective magnetic field $\tilde{B}_0$ given by

$$\vec{\tilde{B}}_0 = \vec{B}_0 + \frac{\vec{\omega}}{\gamma}. \qquad [3.7]$$

If the angular frequency of the system is $\vec{\omega} = -\gamma \vec{B}_0$, the effective magnetic field $|\tilde{B}_0| = 0$. Thus, there is no effective magnetic field in the frame of reference. Consequently, the magnetization $\vec{M}$ in the rotating frame of reference is constant.

On the other hand, if an alternating magnetic field is applied following

$$\vec{B}_1(t) = B_1 \cdot \cos(\omega t) \cdot \hat{x} + B_1 \cdot \sin(\omega t) \cdot \hat{y}. \qquad [3.8]$$

This alternating magnetic field is stationary along the x' direction on the rotating frame of reference and the effective field in that case is given by

$$\vec{B}_{eff} = \left(B_1, 0, \tilde{B}_0\right). \qquad [3.9]$$

The resulting Bloch equations with an alternating magnetic field and relaxation are

$$\begin{aligned} \frac{dM_x'}{dt} &= \Delta\omega \cdot M_y' - \frac{M_x'}{T_2} \\ \frac{dM_y'}{dt} &= -\Delta\omega \cdot M_x' - \frac{M_y'}{T_2} - \omega_1 M_z' \\ \frac{dM_z'}{dt} &= \omega_1 M_y' - \frac{\left(M_z' - M_0\right)}{T_1} \end{aligned} \qquad [3.10]$$

Those equations describe a driven, damped oscillating system. The solutions for the

magnetization will show a resonance phenomenon. Finally, the Bloch equations are now expressed in a particular convenient form by defining the quantities ω_L (Larmor frequency), $\vec{\omega}_1 = \gamma \vec{B}_1$ (Rabi frequency) and $\Delta\vec{\omega} = \vec{\omega}_L - \vec{\omega}$ (difference between the Larmor frequency and the frequency of the reference system).

3.1.1 Free induction decay

Summing up the description of the last section: if a sample of HP-^{129}Xe is placed in a holding magnetic field $\vec{B}_0$, the spins will align in the direction of this magnetic field. The aligment of the spins generates a static macroscopic magnetization $\vec{M}$. In order to detect this magnetization, a resonant $\vec{B}_1$ field ($\omega_L = \omega$) as described above is applied during a certain time interval t_p. This perturbation tilts the magnetization by a certain flip angle α (see Fig. 3.3a) which depends on the duration t_p and the amplitude of the perturbation B_1 as[14]

$$\alpha = \gamma \frac{B_1}{2} t_p \,. \qquad [3.11]$$

This equation assumes that the frequency of the RF excitation pulse is equal to the Larmor frequency. In case this condition is not fulfilled, the flip angle is given by the Majorana equation [Maj32] as

$$\cos\alpha = \frac{\Delta\omega^2 + \omega_1^2 \cos\left(t_p \sqrt{\Delta\omega^2 + \omega_1^2}\right)}{\Delta\omega^2 + \omega_1^2} \,. \qquad [3.12]$$

After the excitation pulse, the M_x and M_y components of the magnetization precess with the Larmor frequency ω_L in the equatorial plane of the lab-system. In a semiclassical picture, the precessing components of the magnetization vector produces a changing magnetic flux within a circuit which could be a pick-up coil or closed loop wire. The change of magnetic flux produces an induced electromotive force, or voltage, within the circuit following the Faraday law. This induced current (or voltage) can be therefore detected, amplified and processed by a spectrometer. Finally, the signal picked up by the pick-up coil is given by

$$S(t) = S_0 \sin(\alpha) \exp(-t / T_2^*) \exp(-i\omega_L t + \varphi) \,, \qquad [3.13]$$

where $S_0 \sin(\alpha)$ is the amplitude of the signal which reaches its maximum for $\alpha = 90^0$. T_2^* represents the characteristic transverse coherence time and φ is the phase of the signal. This exponential signal decays in NMR is usually termed "free induction decay" or simply FID. Fig. 3.3b shows the precession of the magnetization projected in the *x*-*y* plane which

[14] Eq. [3.11] is obtained for a linear polarized $\vec{B}_1$ field. In case of a circular polarized oscillating field (see Eq. [3.8]), the factor 2 has to be replaced by 1.

induces a current in the pick-up coil generating a sinusoidal signal modulated by an exponential decay.

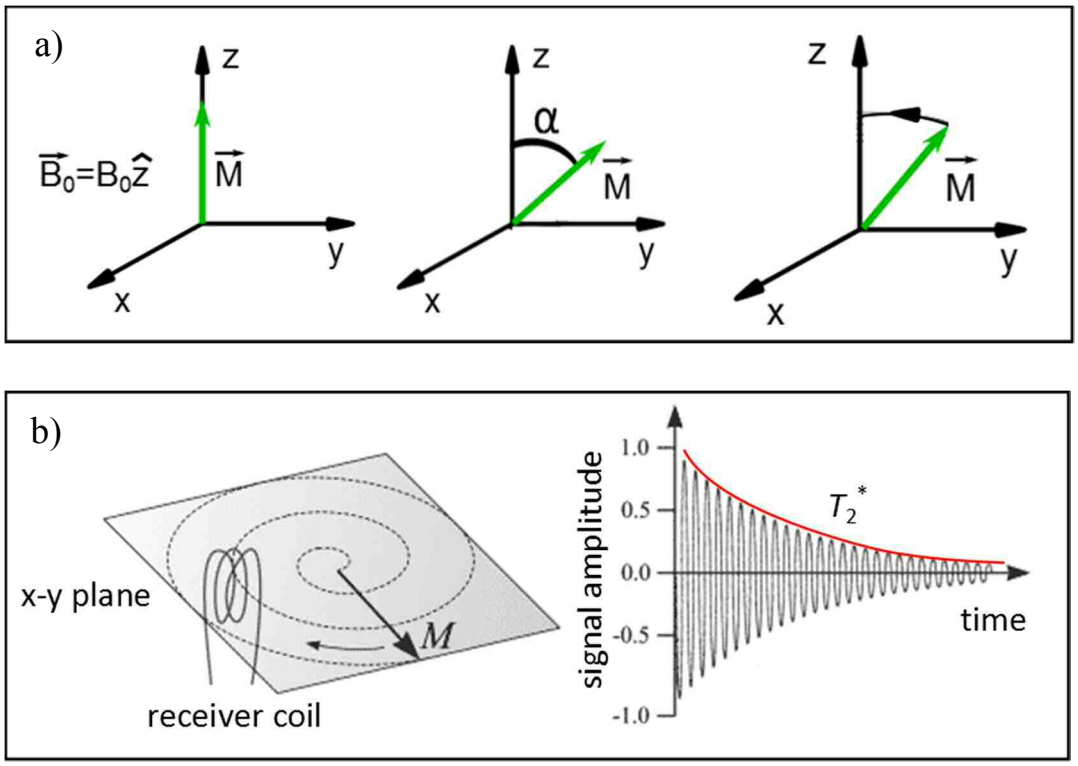

Fig 3.3: Procedure for obtaining an FID signal: a) initially the magnetization is aligned to the holding magnetic field. Then a resonant RF pulse (B_1) along the *x*-axis (not shown) tilts the magnetization of a certain angle α in the *y* -*z* plane of the rotating reference frame. The magnetization vector returns to thermal equilibrium characterized by the phenomenological relaxation times T_1 and T_2. b) FID signal collected by means of a pick-up or receiver coil tuned to the resonant frequency. The exponential signal decay is characterized by the time constant T_2* which will be discussed in more detail below.

In the following description, it was assumed that the resonant RF pulse lasts a time interval much shorter than the damping term of the recorded FID signal amplitude given by Eq. [3.13]. This equation can be directly derived from the last Bloch equation (Eq. [3.10]) setting $\omega_1 = \Delta\omega = 0$ and by back transformation of the motion of the magnetization vector into the lab-system.

3.1.2 Transverse spin relaxation T_2

The first two equations in Eq. [3.10] can be easily solved taking advantage of the cylindrical symmetry of the problem. These equations are coupled with a simple change of variables $M_{xy} = M_x + iM_y$. The resulting time evolution for the transverse magnetization vector $\vec{M}_\perp$ (in the lab system) is derived to be:

$$\vec{M}_\perp = M_\perp(0)\cdot\exp(-t/T_2)\cdot\cos\left(\omega_L\cdot t+\phi\right). \qquad [3.14]$$

T_2 is called transverse or spin-spin relaxation time. This relaxation mechanism is related to the energy exchange of the spin system with itself and it determines the coherence of the spin ensemble. Pure T_2 decay can only be observed with specially designed pulse sequences e.g. employing spin echos [Hah50]. If a faster decay than T_2 is observed, this difference is usually related, for example, to magnetic field inhomogeneities of the static $\vec{B}_0$ field. These inhomogeneities lead to a faster dephasing of the transverse component of the magnetization[15]. The effect is described by a time constant T_2', thus the sum of the rates of both dephasing processes is characterized by T_2^* [Sli90]:

$$\frac{1}{T_2^*} = \frac{1}{T_2'} + \frac{1}{T_1}. \qquad [3.15]$$

Under the conditions of this work, the dephasing due to the residual field gradients is dominant, therefore $T_2^* \cong T_2' \equiv T_{2,\mathrm{dB}}$ and T_1 is the longitudinal relaxation which will be explained on the next section. Here it was assumed $T_2 \approx T_2^*$ which is a good approximation for gases. The field gradient induced dephasing time $T_{2,\mathrm{dB}}$ can be estimated as follows: the pressure range of a ^{129}Xe spin sample of p_{Xe} is about 0.5 bar. Using Eq. [2.44], the self-diffusion coefficient of Xe is $D_{\mathrm{Xe}} \sim 0.12$ cm^2/s. Therefore, the self-diffusion time throughout a spherical cell of R= 6 cm is $\tau_D = R^2 / D \approx 200$ s. In consequence, the static picture can be used to estimate the expected T_2^* time which according to Slichter [Sli96] is given by

$$\frac{1}{T_2^*} \approx \gamma_{Xe} \cdot \Delta B. \qquad [3.16]$$

In addition, the duration of the RF pulse t_p must be smaller than the lifetime of the signal T_2^*. This value can be estimated by considering the field change across the sample cell given by $\Delta B \approx \left|\nabla B_z / B_0\right| B_0 (2R)$.

If the homogeneity is about 10^{-4} cm^{-1} and the sample is about 6 cm; $T_2^* \approx 10$ ms for an applied magnetic field of 10 G. The duration of the RF pulse used in this work will be t_p = 1 ms which satisfies the condition $t_p << T_2^*$.

3.1.3 Longitudinal relaxation (T_1) of HP-Xe

Under the same conditions mentioned above, the z-component of Eq. [3.10] can be deduced to be:

$$\frac{dM_z'}{dt} = -\frac{(M_z - M_0)}{T_1} \Rightarrow M_z'(t) = \left[M_z'(t) - M_0\right] \cdot \exp(-t/T_1) + M_0. \qquad [3.17]$$

where the thermal equilibrium magnetization $\vec{M}_0$ can be set to 0. T_1 represents the energy

[15] Decoherence because of magnetic field inhomogeneity is not a true "relaxation" process; it is not random, but dependent on the location of the molecule in the static magnetic field. For molecules that are not moving, the deviation from ideal relaxation is consistent over time, and the signal can be recovered by performing a spin echo experiment.

exchange of the spins with the environment and it is related to the spin populations (while T_2 is related to the coherence of the spin ensemble). Thus, it is called "spin-lattice" or "longitudinal" relaxation time.

For HP gases, T_1 is the characteristic time constant for the "lifetime" of the HP state. The spin-lattice relaxation will represent the storage time of a HP gas and more details on the different relaxation mechanisms contributing to T_1 were already discussed in Sec. 2.3.

The determination of T_1 in HP-Xe is based on the measurement of the magnetization losses over time. For this purpose, the HP-Xe sample is excited with an RF pulse with ω_L and a certain flip angle α given by Eq. [3.11]. The FID signal is collected after this RF excitation. This procedure is repeated on regular time intervals over a total duration of at least $3T_1$.

After each NMR excitation pulse (n), the remaining magnetization M_R^n is given by $M_R^n = \cos(\alpha) \cdot M_R^{n-1}$. For example, a first pulse with α = 90° (n = 1) results on the maximum obtainable FID signal according to Eq. [3.13]. On the other hand, this pulse will destroy the magnetization of the HP gas, namely $M_R^1 = 0$. Therefore, no remaining magnetization is available for a second scan. For this reason, the determination of T_1 requires small flip angles to allow several scans. In addition, the magnetization losses of the spin system due to the excitation pulses has to be considered in order to correct for this effect and to give the real decay (T_1).

The polarization losses due to small flip angles can be incorporated in the longitudinal relaxation by including $\cos(\alpha)^{n-1}$ to Eq. [3.17]. Considering n as the number of excitations (or pulses) and Δt as the time between measurements. In this way,

$$S(n) = S_0 \cos(\alpha)^{n-1} \exp\left[\frac{-(n-1)\Delta t}{T_1}\right]. \qquad [3.18]$$

This equation can be simplified to the form of Eq. [3.17] by taking the logarithm

$$\ln(S(n)) = \ln\left(S_0 \cos(\alpha)^{n-1} \exp\left[\frac{-(n-1)\Delta t}{T_1}\right]\right), \qquad [3.18a]$$

then

$$\ln(S(n)) = \ln S_0 + (n-1)\ln(\cos(\alpha)) + \frac{(n-1)(-\Delta t)}{T_1}. \qquad [3.18b]$$

If the correction time T_α and the effective relaxation time T_{eff} are defined as

$$\frac{1}{T_\alpha} = \frac{\ln(\cos(\alpha))}{(-\Delta t)} \quad [3.19] \quad \text{and} \quad \frac{1}{T_{eff}} = \frac{1}{T_\alpha} + \frac{1}{T_1} \quad [3.20].$$

Eq. [3.18b] can be rewritten as

$$\ln(S(n)) = \ln S_0 + (n-1)(-\Delta t)\frac{1}{T_{eff}}. \qquad [3.20a]$$

Applying the exponential function to recover the original expression, Eq. [3.18] results in

$$S(n) = S_0 \exp\left[\frac{-(n-1)\Delta t}{T_{eff}}\right]. \qquad [3.21]$$

Eq. [3.21] shows that the measurements can be performed following the same procedure than described before extracting T_{eff} from the fit of the exponential decay and calculating T_1 from Eq. [3.21].

An accurate determination of T_1 through the equations [3.19] and [3.20] requires a precise determination of the flip angle due to the significance of T_α in the error propagation of T_1. The measurement of the flip angle will be described in detail in Sec. 3.3.

3.2 Construction and characterization of a low field NMR system

A low field NMR system was constructed for the measurement of the magnetization of a spherical sample of HP-^{129}Xe. This system is able to measure the NMR signal (FID) and, therefore, the longitudinal relaxation time T_1 of HP-^{129}Xe under the conditions mentioned in Section 2.3. The applied magnetic field is about 23 G and the operational frequency is 27 kHz for ^{129}Xe. A detailed description of the construction and the characterization of the components will be presented.

3.2.1. Low-field NMR-System

The low field NMR system consists of a holding field, an aluminum shield, excitation B_1-coils, receiver (or pick up) coils and a spectrometer as shown in Fig. 3.4.

The excitation pulse and acquisition of the signal are controlled by a spectrometer connected to a PC. The spectrometer generates the RF pulse with the preset frequency, intensity and length. Then, this pulse is amplified and transmitted to the sample via the B_1-coils. The electromagnetic signal generated by the sample is collected by the pick-up coils, pre-amplified in the internal amplifier of the spectrometer and analyzed. The output of the measurement is shown on the PC through a graphical interface.

The holding field $\vec{B}_0$ is generated by five circular coils, each wound from 1 mm copper wire around aluminum wheel rims of 28", i.e., $r \approx 29$ cm. Each of the two outermost coils have 229 turns each, while each of the inner coils have 158 each. The distance between the inner coils is 16.3 cm whereas the distance between the inner and the outer coils is 13.0 cm.

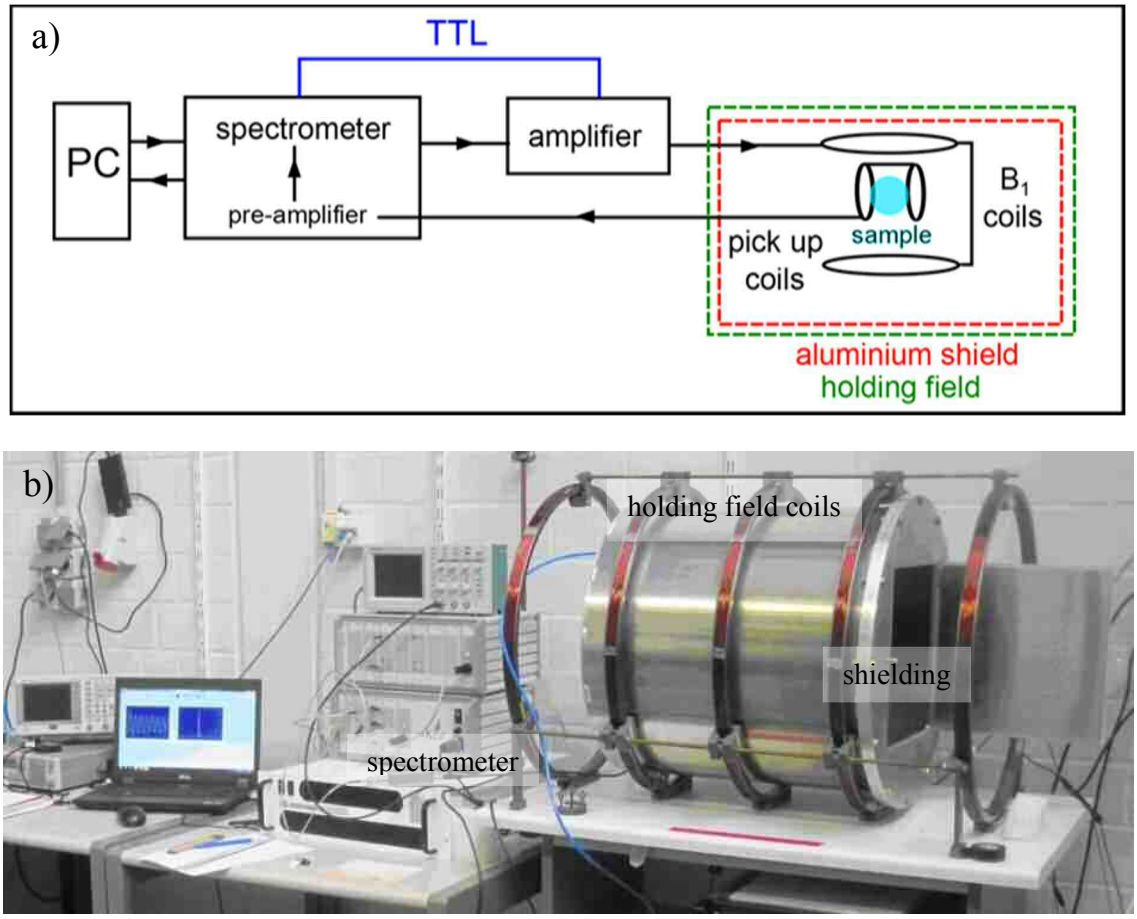

Fig. 3.4: a) Sketch of the low field NMR system. The characteristics of the NMR pulse are determined in the PC. The spectrometer produces the pulse and transmits it to the amplifier which is transmited to the sample through the B_1-coils. The signal generated by the sample is collected by the pick-up coils, pre-amplified, digitalized and analyzed in the spectrometer. The result is shown in a graphical interface of the PC. b) Picture of the low field NMR. The aluminum shield is placed inside the holding field coils. The spectrometer is connected to the B_1 and pick-up coils through BNC feedthroughs which are insulated from the aluminium shield.

The coil system is connected to a DC power supply (GPO250-3R, Takasago). The magnetic field was measured with two devices: a Hall probe with a resolution of 0.1 G (10 μT) (Lakeshore, USA) and a flux-gate (Bartington, UK) with a resolution of 10^{-3} G. The Hall probe was used to measure the value of the magnetic field at the working conditions, i.e. with the power supply set at $I = 3$A ($U = 70$V) resulting in a magnetic field of about 23 G in the central area of the NMR spectrometer. However, the resolution of the Hall probe is not sufficient for an accurate measurement of the homogeneity. For this reason, the measurements of the magnetic field for the calculation of the homogeneity were performed using the fluxgate which has a high resolution but its measurement range is limited to 10 G ($I = 1.4$ A). The magnetic field was then measured using steps of 1 cm along the symmetry axis as shown in Fig. 3.5a. The calculation of the homogeneity according to Eq. [2.45] can be performed with lower values of the magnetic field due to the linear dependence of the

magnetic field with the applied current in the Biot-Savart equation. The homogeneity of the holding magnetic field was determined using Eq. [2.45] with the measured values for the holding magnetic field of the Fig. 3.5a. The results of this calculation are shown in Fig. 3.5b and 3.5c. According to the latter, the homogeneity of the magnetic field over the size of a 10 cm spherical cell placed in the central measurement area (33 - 43 cm) is about ~10^{-4} cm^{-1}. According to Eq. [2.45], this relative field homogeneity results in a field gradient induced T_1 relaxation of T_1^{dB} >5000 h for a HP-Xe sample of p_{Xe} = 100 mbar.

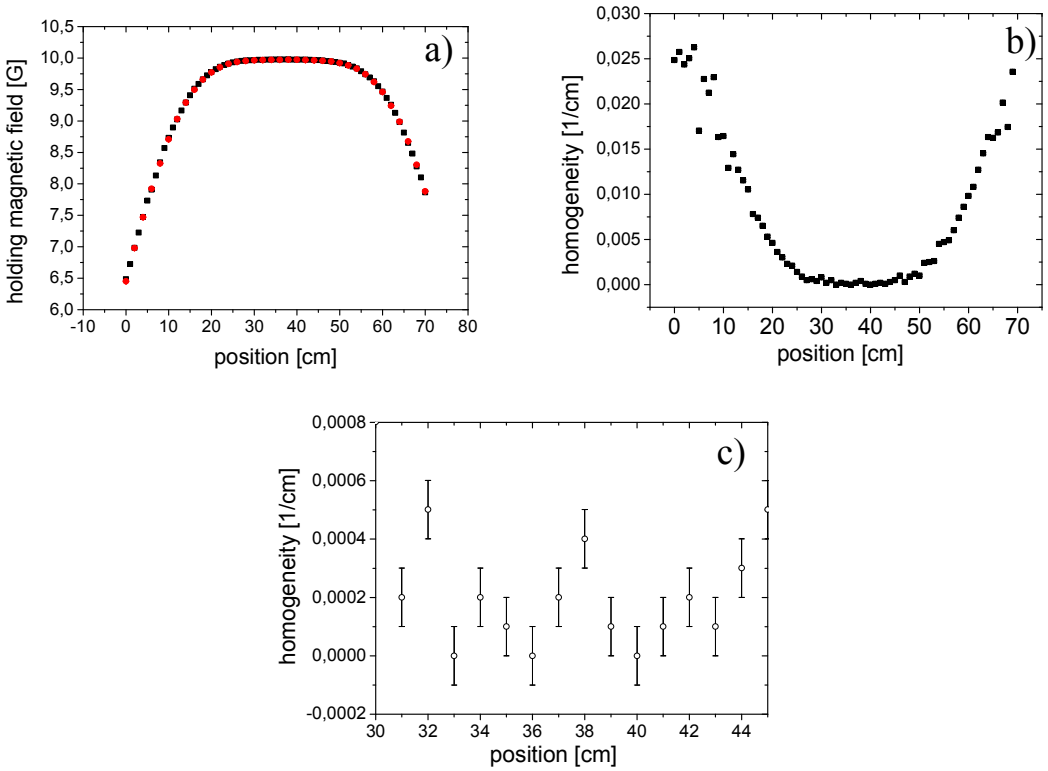

Fig. 3.5: Determination of the homogeneity of the holding field of the low field NMR system along the symmetry axis of the coil system. a) Measurement of the magnetic field at ≈ 10 G. The different colors (black, red) represent two consecutive measurements. b) Homogeneity on the full length of the coil system in units of 1/cm. c) Zoom of b) to the area where the sample is placed.

An aluminum shield is placed inside this system of coils for decreasing the electromagnetic noise. The size of this shield is 53 cm in length, 55 cm in diameter with 5 mm wall thickness. The thickness was selected due to the characteristic skin depth of 0.5 mm [Hue11] at the used frequency. According to this, 5 mm of aluminum would theoretically attenuate external electromagnetic fields on the frequency range of 20 - 30 kHz by a factor of 370. That condition was necessary to improve the signal-to-noise ratio of the FID signal. The quality of the electromagnetic shield strongly depends on the quality of the electric contacts between the different parts of the shield. Otherwise, insulated parts can act as antennas and even intensify the noise signal. The electric contact between the aluminum parts was significantly improved (see Fig. 3.6) by using screws with toothed

washers, a metallic mesh at the doorframe and BNC feedthroughs insulated from the shielding [Hue11].

All components used on the construction of the shield are non-magnetic to avoid perturbations on the magnetic field, which may affect the homogeneity over the sample.

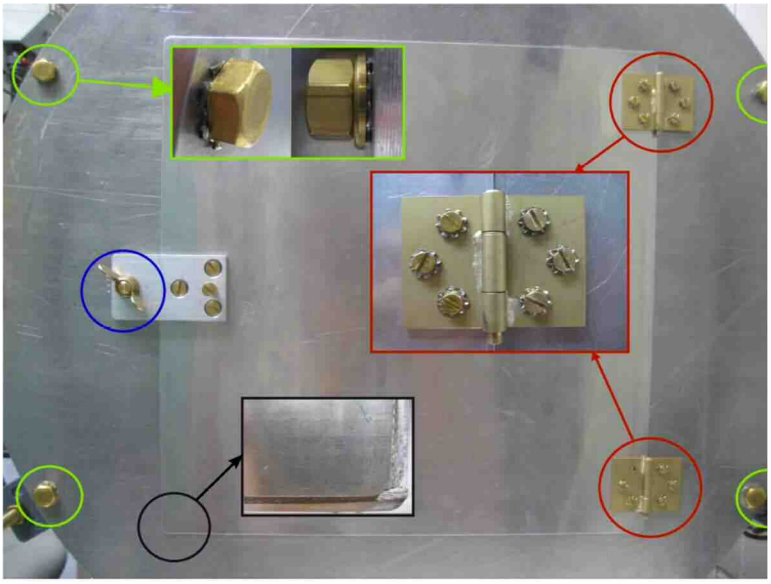

Fig. 3.6: The shield quality was significantly enhanced by improving the electric contact between different parts of the shield (screws with toothed washers at existing holes, metallic mesh at the inside door frame, etc).

The B_1-coils, pick-up coils and the sample are placed inside the aluminum shield as shown in Fig. 3.7.

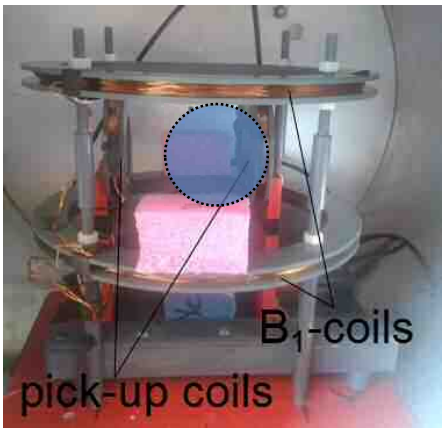

Fig. 3.7: Photograph of the excitation and receiver coils inside the aluminum shield. The sample cell (blue circle) is positioned at the center.

The B_1-coils consist in two plastic frames of 25 cm diameter and 1 cm thickness. Each frame holds 30 turns of electrically insulated copper wire of 1 mm diameter. Both frames are connected via plastic threads as distance holder which allows variation of the distance between them in a range from 10 to 15 cm. This distance was kept in Helmholtz

configuration, i.e. d = 12.5, cm over all experiments. The B_1-coils are connected via a 10 Ω resistance to ground potential. This configuration is called directional coupler and is shown in Fig. 3.8a. The voltage drop across the resistance can be used to monitor the RF excitation pulse as shown in Fig. 3.8b. The total serial resistance of the B_1-coil and directional coupler together is (11.4 ± 0.1) Ω and the inductance is (1.2 ± 0.1) mH.

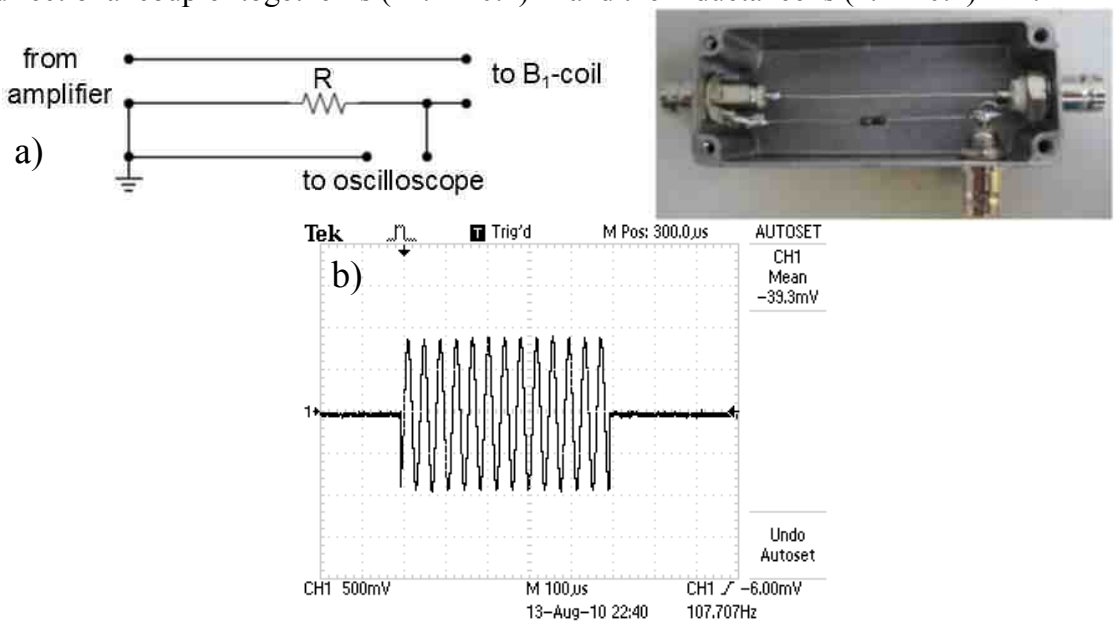

Fig 3.8: a) Directional coupler made by a resistor connected to the B_1-coils for monitoring of the excitation pulse (R = 10 Ω). b) Excitation pulse acquired with the oscilloscope. In this case, the pulse length is 0.5 ms and the amplitude is about 2 V.

The pick-up coils consist of two coils each 5.6 cm in diameter and 1 cm in width with 50 turns of litz-wire of 1 mm diameter in order to reduce the influence of the skin effect and the proximity effect. The signal obtained with the litz-wire was 15 % higher than using normal wire. The radius of the pick-up coils was optimized to have an optimum filling factor for spherical sample cells of sizes between 6 and 12 cm diameter. The coils are connected to an NMR resonant circuit, which include a capacitor and an external inductance (toroid ferrite). This circuit has to provide the proper inductance to match the Larmor frequency of ^{129}Xe at 23 G according to $\omega_L = (C \cdot L)^{-1/2} \approx 27$ kHz. This circuit is shown in Fig. 3.9a where the capacitance is C =16 nF and the inductance is L = (2.6 ± 0.1) mH while the inductance of the coils is L_{coil} = (0.9 ± 0.1) mH.

The resonance frequency of the pick-up coils was measured by applying a variable frequency using a constant amplitude of the input signal and varying the frequency. An antenna constructed from five loops of copper wire (1 cm in diameter) connected to an oscilloscope collected the signal generated by the pick-up coils. The resonance frequency of this antenna is about 1 GHz, so a constant detection range is ensured. The result of this measurement was a Lorentzian function of the form $y = y_0 + y_1 (\Delta f / (4(f - f_L)^2 + \Delta f^2))$ were f_L is the resonant frequency given by $f_L = 2\pi\omega_L$ and Δf is the full width at half maximum (FWHM). From these two values, the quality factor of the circuit can be calculated as Q =

$f/\Delta f$ (see Fig. 3.9b). The resonance frequency f_0 of these coils resulted in (26.98 ± 0.01) kHz and the width Δf = (0.82 ± 0.04) kHz. Finally, the quality factor of the NMR circuit results to be $Q \approx 37$ for 27 kHz.

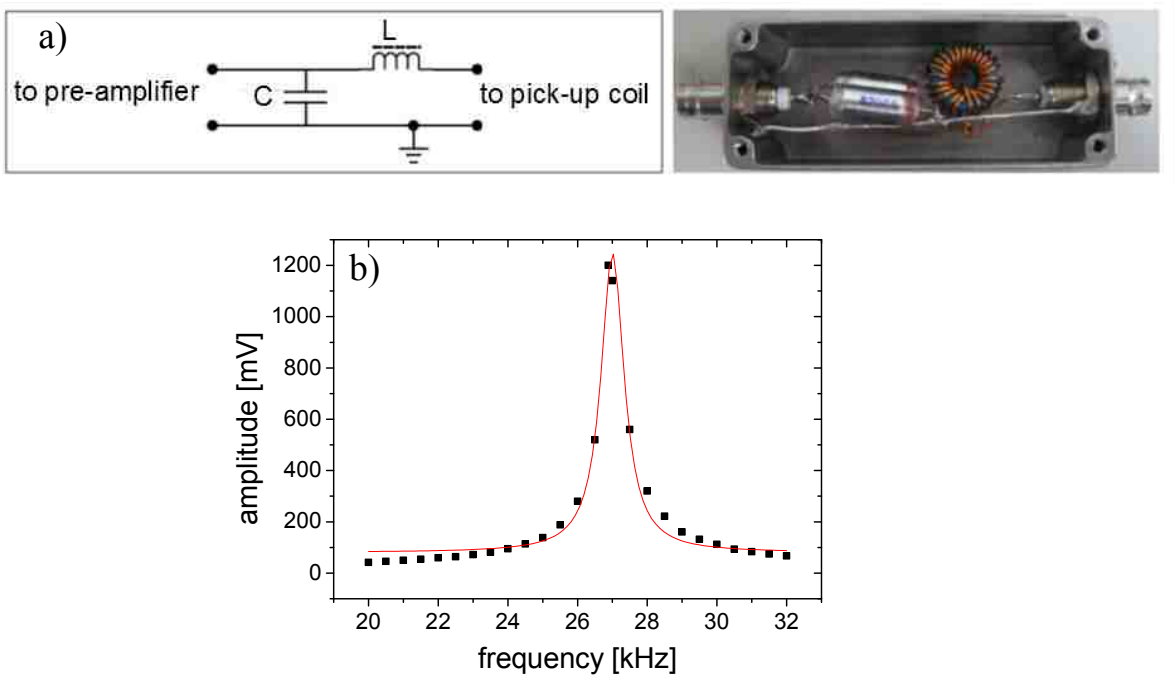

Fig. 3.9: a) Circuit connected to the pick-up coils to tune the resonance frequencyof the NMR circuit to the Larmor frequency for ^{129}Xe at B_0= 23 G. L=1.7 mH and C= 16 nF. b) Resonance curve of the pick-up coils. The curve is fitted with a lorentzian function. The result for the resonance frequency is 27.1 kHz and the Q value is about 37.

A commercial spectrometer (Kea, Magritek, Wellington, NZ) controls the RF excitation of the HP-Xe sample and the acquisition of the FID signal. This device produces the excitation pulse which is then amplified by an external amplifier (Tomco, NZ) and it is transferred to the sample via the B_1-coils. The signal generated by the nuclear spins of the sample is collected by the pick-up coils, transmitted to the spectrometer where it is pre-amplified, analyzed and displayed on the PC.

The characteristics of the excitation pulse and the acquisition parameters can be set in the graphical interface of the spectrometer called Prospa [Pro10]. This program is divided in four sections: pulse sequence, acquisition, filtering and data settings. The first two are shown in Fig. 3.10. The output of each scan is a matrix with three columns: time, as well as real and imaginary part of the signal.

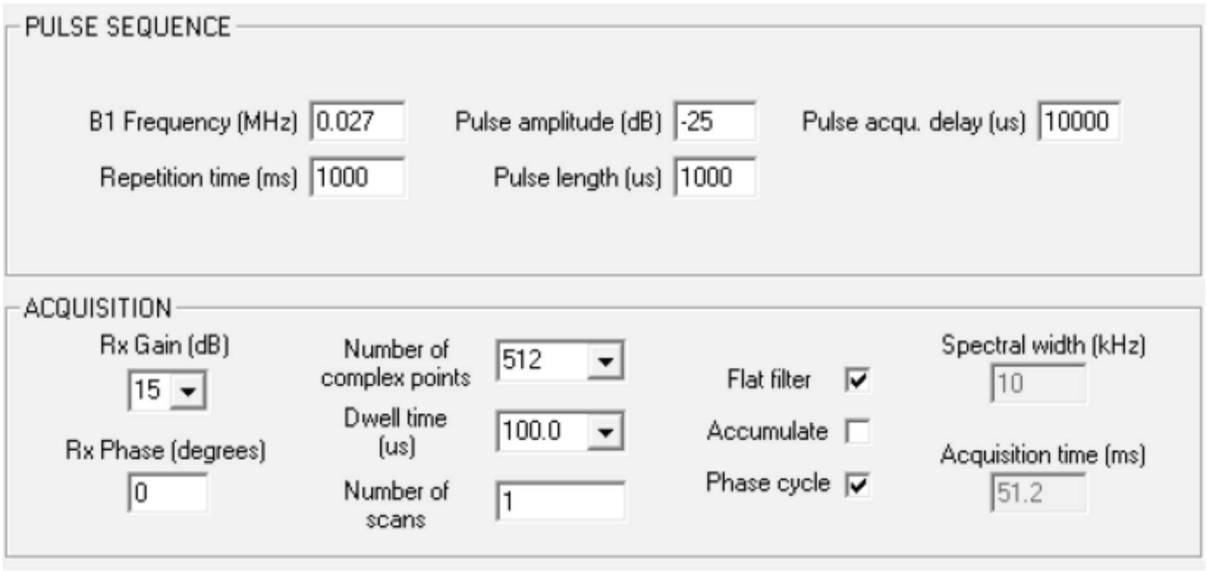

Fig 3.10: Graphical interface of Prospa: The parameters needed to generate the RF-pulse are set in "pulse sequence" and the parameters required for the acquisition of the FID signal are set in "acquisition".

The pulse sequence parameters used in this work are: B_1 reference frequency f_R= 27 kHz. This reference frequency determines the central frequency of the acquisition window. The pulse length was set to 1 ms, the acquisition delay to 10 ms and the pulse amplitude to -40 dB[16]. More details of the pulse sequence window and the determination of its parameters can be found on [Pro10].

The acquisition window contains the following parameters: *number of complex points* which is the number of points acquired in each FID and the *dwell time* which is the time between each measurement point. The product of these two parameters results in the acquisition time of the measurement. The inverse of the dwell time determines the bandwidth of the acquisition. In the experiments presented in this work, the dwell time is 200 µs, hence the bandwidth is 5 kHz and the number of complex points is 1024. The acquisition time window is then 102.4 ms which is sufficient to resolve a $T_2^* \approx 20$ - 50 ms.

3.2.2 Free induction decay of HP-Xe FID

The first step to obtain an FID signal from a sample of HP-^{129}Xe is the adjustment of the holding magnetic field to match the Larmor frequency of the sample with resonance frequency of the circuit. For this, the magnetic field of the coils is measured at the position of the cell with a Hall probe. Due to the geometrical differences between the sensor and the HP-Xe sample, the adjustment of the magnetic field requires a fine-tuning. This fine-tuning is performed varying the holding magnetic field and measuring the NMR signal until the Larmor frequency matches the frequency of the resonant circuit. Usually, the standard Hall probes are not sufficiently accurate to avoid this second step.

[16] These conditions were used for all measurements unless different conditions are explicitly indicated.

This procedure was performed in a sample of 200 mbar of HP-Xe filled in a 6 cm spherical glass cell. Successive FID signals of small amplitude were acquired while the magnetic field was varied until finding the value of the magnetic field that matches with the resonance frequency of the circuit. The Fourier transform of the FID signals (spectra) at different holding magnetic fields are shown in Fig. 3.11 where the blue curve corresponds to the tuned magnetic field.

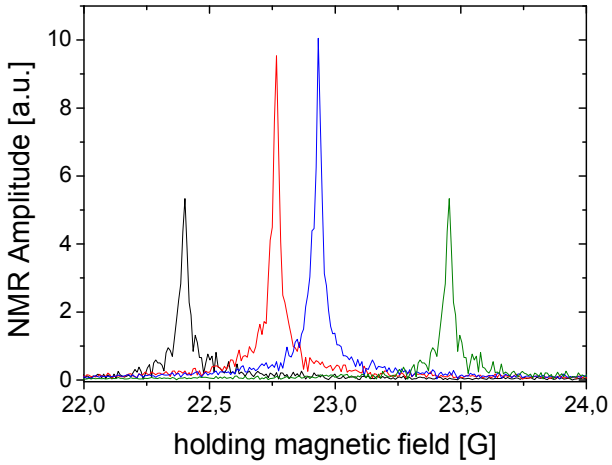

Fig. 3.11: The fine tuning of the magnetic field was performed by changing the external magnetic field and acquiring the NMR signal until the maximum amplitude was found (blue curve).

The FWHM of the blue spectrum in Fig. 3.11 is (0.054 ± 0.001) kHz. Using this value, an estimation of the homogeneity over the sample can be deduced using

$$H = \left| \frac{\nabla B_{0\perp}}{B_0} \right| \approx \frac{|\Delta B_0|}{|B_0| d} = \frac{|\Delta \omega|}{|B_0| \gamma d}.$$

According to the equation above, if the diameter of the cell d =6 cm and B_0 is 23 G, the homogeneity is about $1.4 \cdot 10^{-4}$ 1/cm, which is in excellent agreement with the measurements presented in Fig. 3.5c.

Finally, the NMR amplitude of the FID signal will be defined in this work as the maximum of the Fourier transform because this value is less sensitive to the noise level (see Appendix 1). This becomes necessary, especially for T_1 measurements where the FID signals are recorded from magnetizations, which already decreased by more than a factor of 10 due to the relaxation mechanisms.

A typical NMR measurement of a sample of HP-Xe on the graphical interface of the spectrometer is presented in Fig. 3.12. On the left hand side, the FID (real and imaginary part) is displayed where the abscissa is the acquisition time and the ordinate is the amplitude. The frequency of the oscillating signal is given by the difference of the reference signal of the spectrometer f_R with the signal of the sample f_L.

The right hand side shows the corresponding absolute value of the Fourier transform

of the FID. The frequency scale is centered at the reference frequency (27 kHz). The positive frequencies are below 27 kHz whole the negative values correspond to frequencies over 27 kHz with a spectrum bandwidth of 5 kHz.

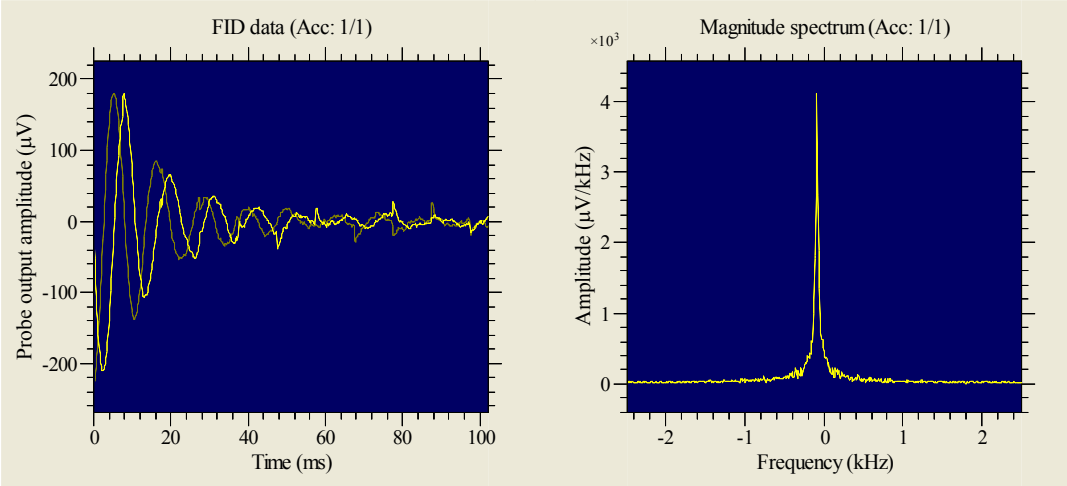

Fig 3.12: Output of a measurement displayed by the graphical interface of the spectrometer (Prospa). Left: FID signal. The two curves correspond to its real and imaginary part. The beat frequency is given by the difference of the Larmor frequency of the HP sample and the reference frequency. The acquisition time is 102.4 ms. Right: absolute value of the Fourier transform of the FID signal considering both, real and imaginary part.

3.2.3 Noise analysis

If an "FID signal" is acquired without a spin sample, the pick-up coil collects signal coming from the environment[17]. This signal is colloquially called "environmental noise" and it has to be reduced as much as possible for ensuring high quality of the measurements. The determination of the noise level is fundamental for defining the resolution of the NMR system because it will introduce an offset in the T_1 measurements (in Eq. [3.18] with $S(n\rightarrow\infty) \neq 0$).

The sources of noise are principally microphony and vibrations on the environment originated, for example, by pumps, PC and power supplies. At the frequency range of study, the contributions to the noise seem to have no main frequency and it can be treated as white noise.

The noise level was reduced by a factor of about 20 by placing the pick-up coils inside the aluminum shield and it could be further reduced by improving the electrical contacts of the shield (x10), so in total by a factor of 200. The details of the results of this test can be found in [Hue11]. To maintain good shielding performance, the shielding requires periodic maintenance e.g., by cleaning the contacts between the aluminum parts

[17] No load for the pick-up coils is required for measuring noise due to the small flip angles used in this work.

with sandpaper.

The noise level was determined by acquiring an "FID" either without a sample or without sending an excitation pulse (amplifier off) obtaining in both cases the same results. The noise collected by the pick-up coils is about 11 μV_{pp} as shown in Fig. 3.13a. The Fourier transform of the signal obtained by the pick-up coils is shown in Fig. 3.13b. The resonant structure of this noise is due to the acquisition circuit, which amplifies the signals corresponding to the frequencies that match to the Q of the pick-up coil. This fact was confirmed by fitting a Lorentzian function to the spectrum shown in Fig. 3.13b. The central frequency was f_0= 26.96 kHz and the width resulted to be Δf = 0.58 kHz leading to a $Q \approx 46$ which is in good agreement with the Q of the pick-up coils in Fig. 3.9b.

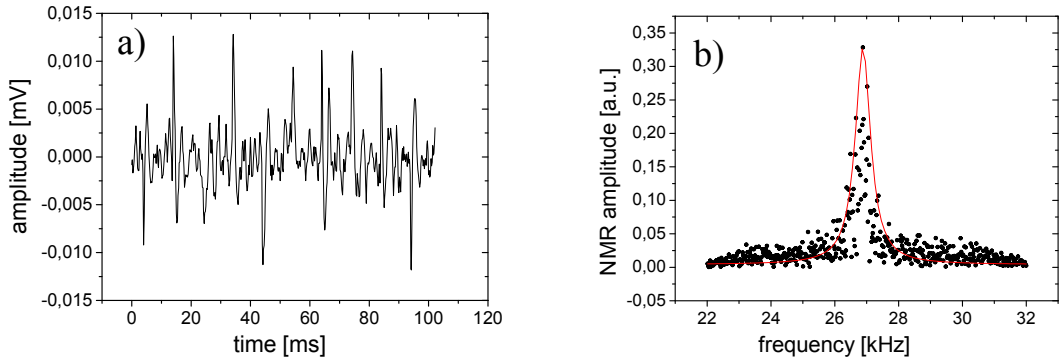

Fig 3.13: Noise level of the low field NMR system. a) Signal collected after a single FID with no sample inside. b) The black points are the Fourier transform of the signal shown. The red line is the fit of a Lorentzian function in order to extract the central frequency and the width. The Q obtained is about 46.

3.3 Flip angle calibration

The flip angle α is a crucial parameter in the determination of the spin lattice relaxation T_1 described in Eq. [3.21]. As mentioned above, a precise measurement of T_1 requires a precise measurement of α. In order to determine this parameter, first the complete range of flip angles was determined with the purpose to find approximately the pulse amplitude of the excitation pulse which leads to $\alpha = \pi/2$. With this value, it is possible to find an approximated pulse amplitude, which leads to $\alpha \approx 10°$. The flip angle α and its error will be precisely determined for this pulse amplitude.

The complete range of flip angles was studied placing a HP-Xe sample of 6 cm diameter in the low field NMR. This experiment was done by recording successive scans varying the pulse amplitude with a constant pulse length and normalizing by a reference amplitude in order to correct the losses due to the previous scans. Due to the high polarization losses on the 90° region, this experiment was performed using eight HP-Xe samples of similar characteristics.

The NMR amplitudes were obtained with RF pulses of 27 kHz and constant pulse

lengths (1 ms). The excitation pulse amplitude was measured using the circuit shown in Fig. 3.8. Finally, the signal of each scan vs. voltage on the B_1-coils was plotted and fitted using $S(v) = A\,|\sin(\pi\,(v)/v_{180})|$ where A is the amplitude and v_{180} is the voltage corresponding to a 180° flip of the magnetization. The parameters obtained were $A = (6.7 \pm 0.4)$ a.u. and $v_{180} = (16.78 \pm 0.42)$ V with a normalized $\chi^2 = 1.86$ (see Fig. 3.14a). Finally, the voltage v corresponding to $\alpha = 90°$ is about 8.4 V which corresponds to an amplitude of the excitation pulse of -11.6 dB in Fig. 3.10.

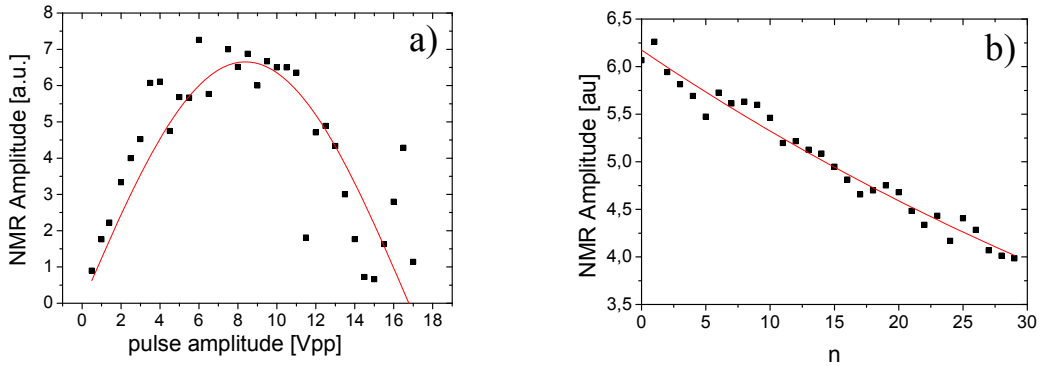

Fig 3.14: Calibration of the flip angle using a pulse length of 1 ms. a) Complete flip angle scan over 180° of HP-Xe. b) Precise determination of small flip angles: FID measurements ($n \sim 30$) with the same RF pulse amplitude and length with a repetition time Δt short enough to fulfill $\Delta t \cdot n << T_1$. The result was adjusted to $A_0\cos(\alpha)^{n-1}$ (see Eq. [3.18]) obtaining a flip angle of $\alpha = (9.84 \pm 0.16)°$.

Once the rough value of a small flip angle was identified, a precise determination was performed by recording a successive FID at a fixed amplitude and pulse length. The time between scans should be much shorter than T_1 so the exponential part of Eq. [3.18] can be approximated to a constant and therefore can be reduced to $A(t) \approx A_0\,\cos(\alpha)^{n-1}$. The result of this measurement is shown in Fig. 3.14b obtained with an amplitude of -40 db and a pulse length of 1 ms. The flip angle obtained from these results is $\alpha = (9.84 \pm 0.16)°$ with a normalized $\chi^2 = 0.013$.

3.4 Longitudinal relaxation (T_1) measurements

In this work, the measurements of the longitudinal relaxation, T_1, are performed using a routine, which repeatedly records an FID signal after a fixed time interval, usually about 20 minutes. The output of this routine is a matrix which has time in the first column, real and imaginary part of the FID in the second and third column, respectively. The next columns are filled with the respective data from the next scan until the measurement was stopped when reaching n scans.

The output matrix is processed to provide the maximum of the Fourier transform of each FID (NMR amplitude). Then, the NMR amplitude vs. time is plotted using Eq. [3.21] and adding a term for the background according to

$$A(\mathrm{t}) = A_0 \exp(-t/T_{eff}) + A_1 . \qquad [3.22]$$

A measurement of the relaxation time of a sample of 150 mbar of enriched Xe filled in a glass cell of 10 cm in diameter cell using a flip angle of $\alpha = (9.84 \pm 0.16)°$ is shown in Fig. 3.15. Through Eq. [3.19], this flip angle value leads to $T_\alpha = (1350 \pm 3)$ min. The time constant T_{eff} was extracted from the fit of Eq. [3.22] to Fig. 3.15 obtaining $T_{\mathrm{eff}} = (188 \pm 10)$ min and $A_1 = (0.48 \pm 0.07)$. Finally T_1 is calculated from this fit according to Eq. [3.21] obtaining $T_1 = (218 \pm 11)$ min.

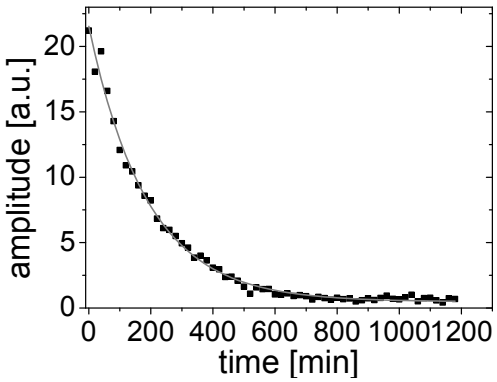

Fig. 3.15: NMR amplitude vs. time. The fit line corresponds to Eq. [3.22] resulting in $T_{\mathrm{eff}} = (188 \pm 10)$ min and $T_1 = (218 \pm 11)$ min.

The value of T_1 extracted from Fig. 3.15 (3.6 h) is close to the theoretical limit of 4.1 h established in [Cha02]. According to Eq. [2.47], the relaxation due to collisions with the wall is about 20 h. For this reason, this glass cell provides suitable conditions for studying the relaxation mechanisms of HP-Xe described in Sec. 2.3 and its reproducibility. These studies will be presented in Chapter 5.

Chapter 4: Construction and characterization of a mobile Xe-polarizer

In case of HP-^{3}He, the storage times can be longer than 100 h. This gas is then shipped around the world in boxes with an internal magnetic field with minimal polarization losses [Thi08]. Such long transport times are not possible with HP-Xe because T_1 is limited to less than 10 h as it will be shown in Chapter 5. The short storage times of HP-Xe often limit possible experiments if the gas must be transported over long distances. This is a problem specially for such experiments which require a high signal to noise ratio. One possible solution to this problem is developing mobile Xe-polarizers, which can be transported and used directly next to the facility where they are needed.

In this work, a mobile Xe-polarizer was built for applications, which require production rates of about 400 mbar·l/ h, for example, fundamental physics experiments such as the search for the electric dipole moment of ^{129}Xe.

The Xe-polarizer presented in this chapter was fabricated employing parts of a Xe-polarizer constructed by Appelt in [App04] which was used for small scale imaging and spectroscopy at the MPIP [Aco06][Amo09]. Originally, the MPIP Xe-polarizer was not suitable for transport and for producing variable mixtures of HP-Xe with other gases. This machine was upgraded to a compact and robust design suitable for transportation and with an integrated mixing gas station. These modifications allow production of HP-Xe, its separation form the buffer gases, filling it into storage cells and mixing it with different gases. These procedures are performed in the facility where it will be used and in a single production cycle. Therefore, HP-Xe samples can be produced continuously and in a reproducible way because the system does not need to be opened to air. This fact greatly simplifies the operation because it diminishes the evacuation times and, in consequence, polarization losses. Additionally, some modifications were added to achieve higher polarization levels, reproducible results and simplify the operating conditions.

In parallel to the upgrade of this Xe-polarizer, a Xe-polarizer for medical applications was constructed with a production rate over 1 bar·l/h. This high production rate is achieved using an OP-cell which has volume about 16 times bigger that the OP-cell of the polarizer for fundamental physics applications. The rest of the system, such as cryogenic separation and gas mixing, are similar to those, which will be described hereunder. Since the construction of the Xe-polarizer for medical applications resembles in many aspects the Xe-polarizer for fundamental physics applications, only the latter will be described on this chapter. The Xe-polarizer for medical applications was brought to a state where only Rb had to be filled to start with the production of HP-Xe and its description and characterization will be discussed in Appendix 2.

The Xe-polarizer for fundamental physics applications can be used to polarize ^{129}Xe

in continuous flow and batch mode[18]. The continuous flow operation is used for experiments where the HP-Xe has to continuously flow through a sample, e.g., to be dissolved on different liquids [Kha15][Möl99][Amo09] e.g. to study its solubility and T_1.

The batch mode is used for experiments where pure Xe is needed which could then later be mixed with other gases. The polarizer can operate in a pressure range of 1 to 7 bar, with a flow from 100 to 300 ml/min[19] and with a gas mixture from 0.5 to 7.5 % of Xe. At 1% of Xe, the production rate is 400 mbar·l/h and the mean polarization obtained is around 5% (see Chapter 6). These values are produced with a gas mixture of 1% Xe, 6% N_2 and 93% He flowing at 200 ml/min at a total pressure of 4 bar.

This Xe-polarizer is running since June 2013 and it is used almost daily at the physics institute in Mainz for T_1 measurements and NMR spectroscopy. All results presented in this work were produced with this polarizer. However, it is planned to transport it to the Jülich Research Center for the measurement of the electric dipole moment of ^{129}Xe [Hei13].

Due to its mobile condition, the Xe-polarizer fits through standard doors (2 m long and 1 m wide). Additionally, the room where it will be installed requires a line for compressed air and two standard sockets (250 V). The laser light is completely shielded inside an aluminum case and the area of the optical pumping cell is closed during operation with doors of anodized aluminum. Under these conditions, the class 4 laser (795 nm, 30 W) can be considered a class 1 laser. Therefore, the operation room does not require installation of interlocks or a safety light according to [GUV87].

As described in Chapter 2, the process for production of a sample of HP-Xe can be divided in three stages: spin-exchange optical pumping, cryogenic separation and storage, which of course, are all included in this mobile polarizer. The front part of the Xe-polarizer is shown on Figure 4.1 where the SEOP stage consists of a flow control unit, temperature controller, spectrometer, polarizer box, coils for the holding magnetic field, oven and optical pumping (OP) assembly. The cryogenic separation is performed by freeze/volatilization unit (FVU) composed by a Halbach magnet, an accumulation cell and a freeze/volatilization structure (FVS). The storage stage consists of the filling system and the storage cell. The holding field for storage is provided by the same coil system than for the OP-cell. For transport of the cell, a magnetic box [Hie10] or a solenoid (see Section 6.2) can be used.

The back part of the Xe-polarizer is shown in Fig. 4.2. This part is not manned during the production of HP-Xe and it contains the rest of components which are relevant to the SEOP process. These components are: gas bottles, power supplies for coils and laser, pump system, pressure sensor and readout of the pressure sensor. The covered part is

[18] Preparation of a batch of HP-Xe via cryogenic separation.
[19] ml/min is determined at normal conditions (273 K, 1.013 bar). These conditions are established by the manufacturer.

the shield for the laser light.

This chapter is giving a detailed description and characterization of the mentioned parts of this Xe-polarizer. The description is divided in three sections SEOP stage, cryogenic separation stage and storage stage. The polarization losses will be analyzed and the optimal operation conditions will be found for each stage.

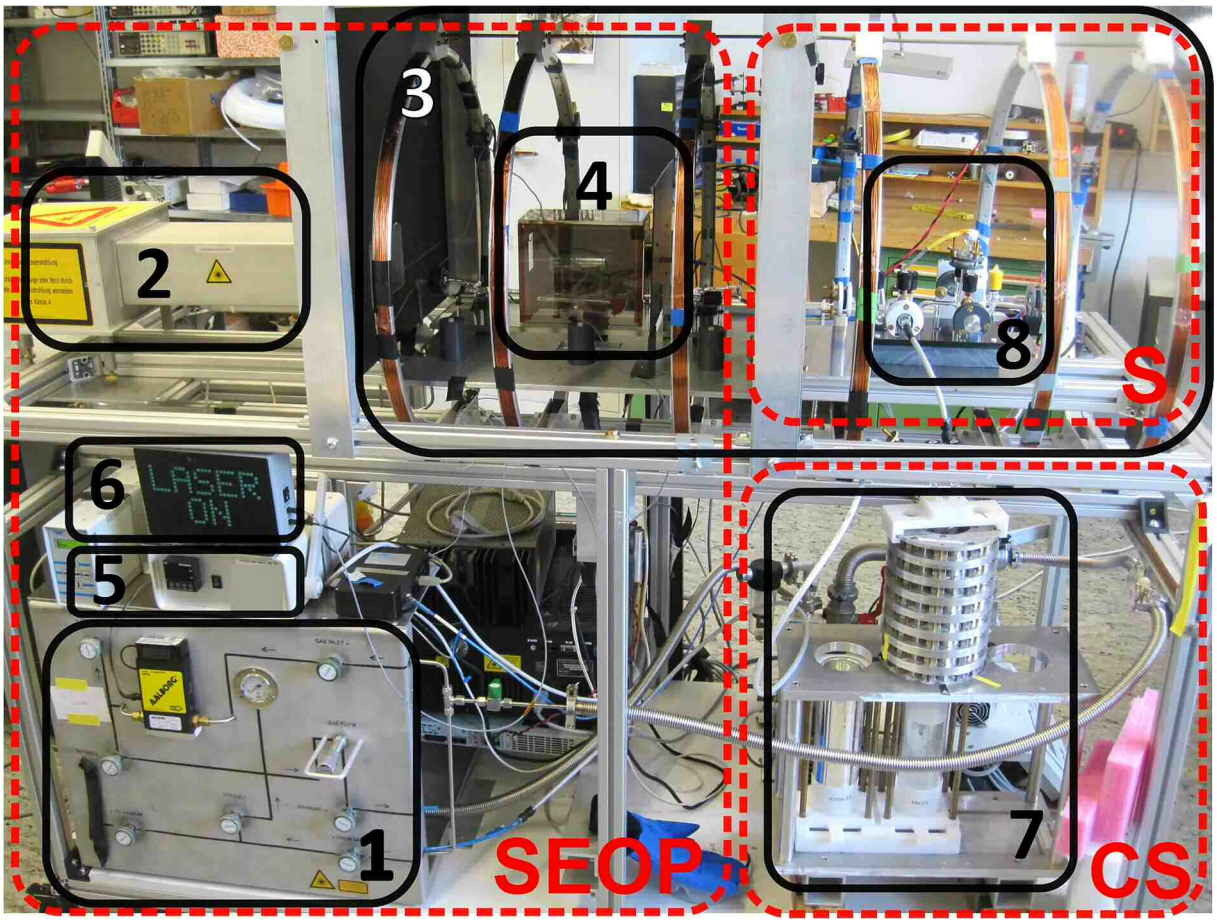

Fig 4.1: Front part of the Xe-polarizer for fundamental physics applications. The areas of the polarizer where the three stages of production of HP-Xe are marked in red: SEOP, cryogenic separation (CS) and storage (S). The parts corresponding to the SEOP process are: 1) flow control panel, 2) polarizer box for the laser beam, 3) coils for the holding magnetic field, 4) OP-cell and oven, 5) temperature controller, and 6) laser safety light. The part corresponding to cryogenic separation is 7) freeze/volatilization unit (FVU). The storage area is marked by 8).

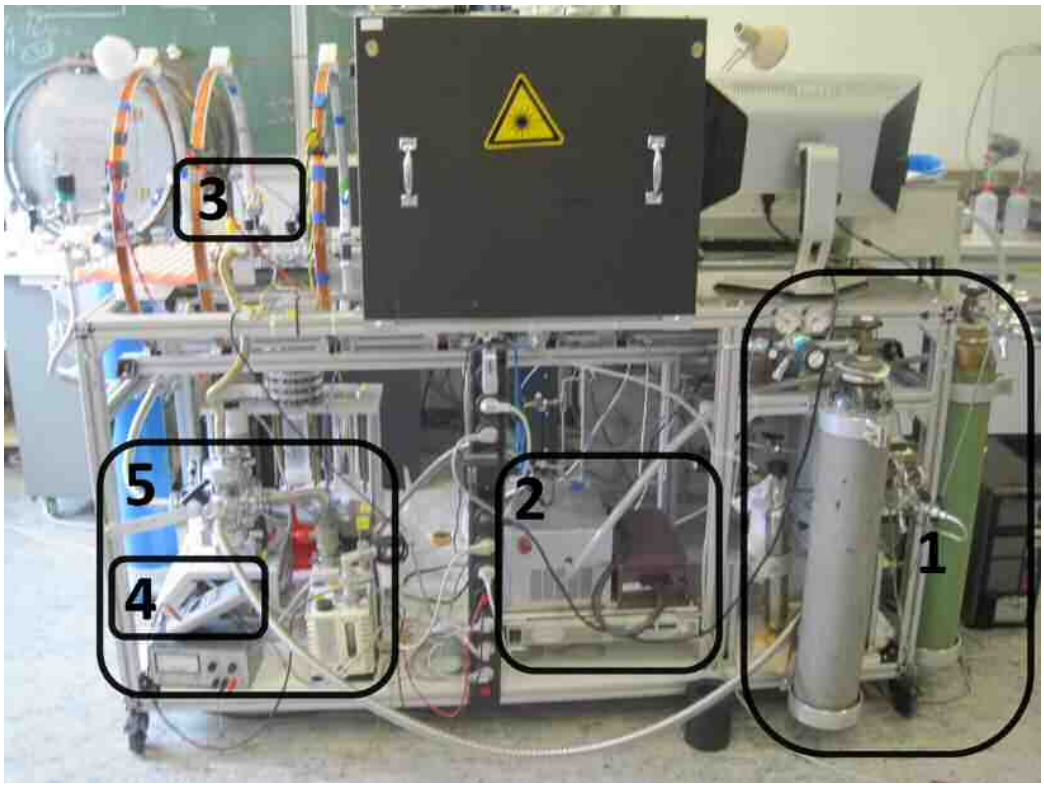

Fig 4.2 : Back part of the Xe-polarizer for fundamental physics applications. The labeled parts are: 1) gas bottles, 2) power supplies of the field coils and the laser, 3) pressure sensor, 4) readout of the pressure sensor and 5) pump system.

4.1 Spin-exchange optical pumping (SEOP) stage

The SEOP stage is sketched in Fig. 4.3. First, the gas mixture composed by He, N_2 and Xe is mixed. This mixture flows inside an oven at temperatures between 100 - 200°C where it is saturated with Rb vapor. The gas mixture containing Rb enters the OP-cell and interacts with the laser. Inside this part, the Rb valence electron is laser polarized and this polarization is transferred to the ^{129}Xe nucleus. The gas mixture, now containing HP-^{129}Xe leaves the OP-cell and the Rb condensates on the cold part at the outlet of the OP-cell. All these processes take place inside a holding magnetic field $\vec{B_0} = B_0 \hat{z}$.

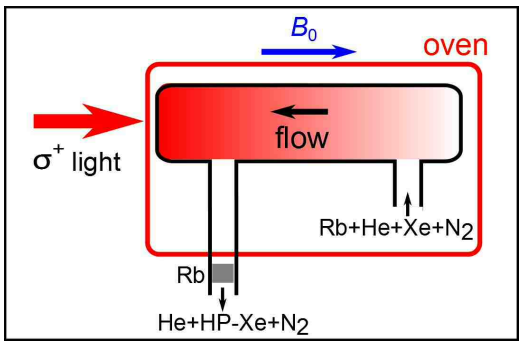

Fig. 4.3: Spin exchange optical pumping stage. For more details see text above.

The parts of the Xe-polarizer involved in this stage are: gas mixture, holding magnetic field, laser, oven, OP-assembly which includes rubidium, OP-cell and Rb-trap. These parts will be described in the following sections.

4.1.1 Gas mixture preparation

The Xe-polarizer operates with a continuous flow of a gas mixture composed from Xe (natural or enriched), N_2 and He. These gases have to be mixed in a certain proportion and flow at a determined pressure to generate an efficient SEOP process. The gas mixture must be free of impurities, especially oxygen, because of possible chemical reactions with Rb which can diminish the efficiency of SEOP (see Sec. 4.1.6). For this purpose, a gas-mixing panel and a flow control panel were built. Both panels are constructed from slightly magnetic materials such as stainless steel. No depolarization effects are expected since these parts are only in contact with unpolarized gas. The elements in contact with HP gas are either made from glass or plastic to preserve the polarization.

A flow chart describing the circuit of the gas mixture is shown in Fig. 4.4 where the gas mixture is prepared in the "gas mixing panel". Then, it flows to the "flow control panel" where the flow is measured and controlled. The gas mixture flows through the optical pumping cell where the HP-Xe is produced. At this point, if the bridge valve is opened, the HP-Xe in the gas mixture can be used directly. However, the operation mode used is this work is the "batch mode" where the bridge valve is closed during polarization. Thus, the gas mixture containing HP-Xe flows to the FVU where the HP-Xe is frozen out and the remaining buffer gases leave through an outlet by the "flow control panel".

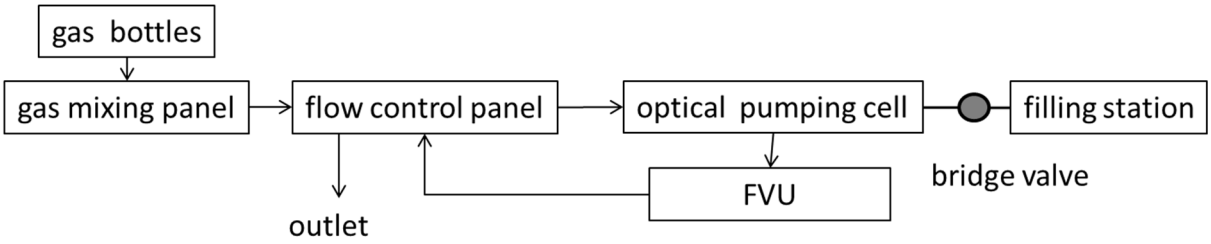

Fig. 4.4: Sketch of the gas mixture flow through the Xe-polarizer for continuos flow mode. The gas bottles (natural Xe, enriched Xe, N_2 and He) are connected to a gas mixing panel which produces the gas mixture with a predetermined relative amount of each gas at a fixed total pressure. The gas mixture flows to the flow control panel where the flow rate can be measured and adjusted, then to the OP-cell and to the freeze/volatilization unit (FVU). It then returns to the flow control panel where is exhausted through the outlet. The OP-cell is connected to the filling station through a valve called "bridge valve" if this valve is opened, the HP-Xe can be used together with the buffer gases.

4.1.1.1 Gas mixing Panel

The gas mixing panel (see Fig. 4.5a) consists of three mass flow controllers (Bronkhorst, Germany) specially calibrated for He, N_2 and Xe [Bro13], a stainless steel

reservoir and a pressure controller (Bronkhorst, Germany) which regulates the pressure and acts as safety valve. These parts are connected by stainless steel tubes and ball valves (Swagelok, USA).

The flow controllers are connected to the bottles through a pressure reducer (GCE, Druva, Germany) which reduces and adjusts the internal pressure of the bottle to an output pressure of about 1 bar above the operation pressure. Particularly, the flow controller for Xe is connected to two bottles, enriched and natural Xe, which can be selected by opening a valve depending on the requirements of the experiment.

The gases are stored in 50 l bottles with an initial pressure of 200 bar in case of N_2 and He (Messer, Germany), 10 l and 50 bar in case of natural Xe (Air Liquide, Germany) and 0.5 l and 20 bar for enriched Xe (85% ^{129}Xe, 0.1% ^{131}Xe, Linde Electronics & Specialty Gases, USA). The chemical purity of the gases is up to 99.99 %.

The flow controllers used in the gas mixing panel measure the flow by the heat capacity of the gas and are specially calibrated to each gas. The flow is regulated by a magnetic valve whose opening can be controlled by a software called "FlowView" by setting the percent of opening (0% and 100% correspond to valve close and valve fully opened respectively). A screenshot of this program is shown in Fig. 4.5b. The maximum flow corresponds to 30 ml/min for Xe, 106.1 ml/min for N_2 and 425.8 ml/min for He.

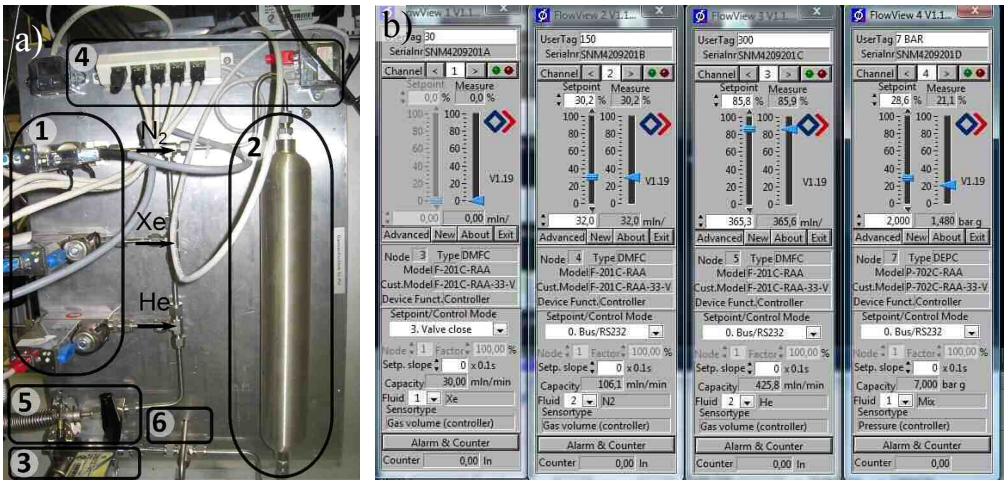

Fig. 4.5: Gas mixing panel. a) 1.Flow controllers, 2. reservoir, 3. pressure controller, 4. interface, 5. exhaust for vacuum, 6. to " flow control panel". b) Graphical interface of the flow meters and the pressure controller in the software "Flow View".

The standard gas mixture used in this work was of 4 ml/min Xe, 32 ml/min N_2 and 364 ml/min He which corresponds to valve openings of 13.3%, 30.2% and 85.5% respectively. The composition of the gas mixture can be varied according to the requirements of each experiment. The flow controllers are connected to a 400 ml stainless steel reservoir which contains the gas mixture. The pressure inside this container can be adjusted by a pressure controller in a range from 0 to 7 bar. This controller opens an

exhaust valve when the set pressure is exceeded until the set pressure is reached again. A description of the operation of the gas mixing panel can be found in Appendix 3.

Alternatively, it is possible to acquire “ready-to-use” gas bottles with a preset gas mixture. In this case, only a flow controller is needed which reduces costs and simplifies significantly the gas preparation. However, this option lacks flexibility in operation of the Xe-polarizer and the possibility to optimize the gas mixture for improving the polarization.

4.1.1.2 Flow control panel

The gas mixture prepared in the gas mixing panel is filled in the reservoir at a fixed pressure and then flows to the flow control panel. On this panel, the flow is measured using a mass flow meter (Aalborg, USA). The flow is manually adjusted by a needle valve (SS-4BMG, Swagelok, USA). A sketch of the panel with the gas path is shown in Fig. 4.6 where the green circles are standard membrane valves (Swagelok, USA), the black trapezoids are glass valves (Hi-Vac, USA), the black circles represent butterfly valves (Pfeiffer, Germany) and the “P” represents a pressure sensor (range from -1 to 10 bar).

During the polarization process, the gas mixture enters the panel by “GAS INLET”, flows through the flow meter and leaves the panel through “TO OP-CELL”. Between this valve and the OP-cell, a gas purifier (FaciliTorr, SAES, Italy) is installed which eliminates traces of H_2O, O_2 and other impurities. The purified gas mixture flows through the optical pumping cell where the Xe is hyperpolarized.

The HP-Xe mixed with the buffer gases flows to the accumulation cell (AC) where it freezes out while the buffer gases keep flowing. The buffer gases re-enter the flow control panel through “FROM SAMPLE” and the total flow is adjusted by “NEEDLE VALVE” while the pressure is monitored by a pressure sensor (WIKA, Germany). This configuration is required for controlling of the difference of pressure between inlet and outlet of the OP-cell. For example, if GAS INLET, TO PUMP CELL and BYPASS 1 are opened, the pressure on the inlet of the OP-cell can be measured. On the other hand, if BYPASS 1 is closed but BYPASS 2, FROM SAMPLE, and the rest of the valves which lead to the OP-cell, the pressure at the outlet of the OP-cell can be measured.

The buffer gases leave the flow control panel via “EXHAUST” through a check valve (Reichelt, Germany) which allows only flow in one direction to prevent air entering the system.

TO VACUUM is used to evacuate the buffer gases from the accumulation cell when sufficient HP-Xe was collected by opening OUT AC, FROM SAMPLE and TO VACUUM. The flow control panel is also evacuated through “TO VACUUM”, e.g. after replacing the OP- cell.

The flow control panel has two by-pass valves which are necessary to regulate and control the pressure on the output of the OP-cell to prevent violent pressure drops which

could displace the Rb inside the cell.

The complete gas manipulation system can be evacuated to 10^{-6} mbar through a mechanical pump (Varian, USA) and a turbo-molecular pump (Pfeiffer, Germany). The connections to the pumps are made by standard ISO-KF-16 stainless steel bellows, FKM O-rings and metallic clamps (Pfeiffer, Germany).

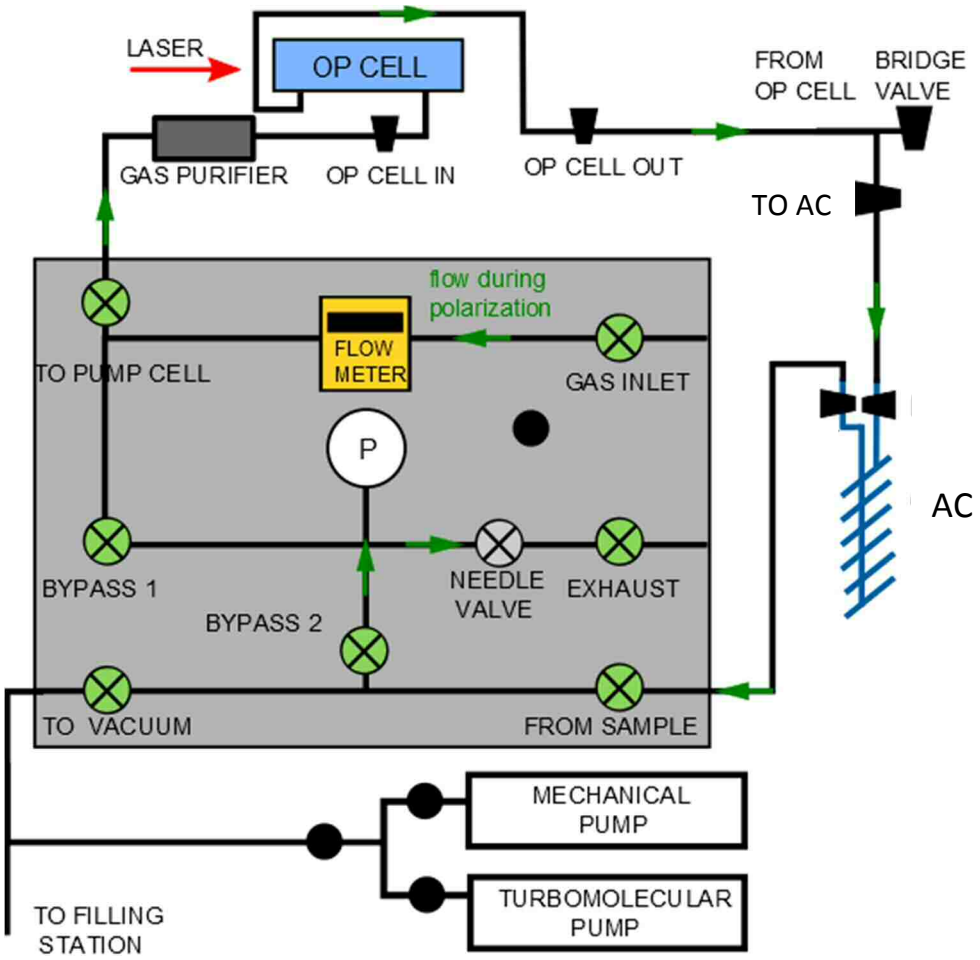

Fig. 4.6: Flow control panel for the gas mixture in the Xe-polarizer. The green arrows show the gas flow during the polarization polarization process. After the gas mixture is produced on the gas mixing panel of Fig. 4.5, it enters the system through "GAS INLET" and flows to "TO PUMP CELL" while the flow is measured by a "FLOW METER". The mixture enters the OP-cell where the Xe is hyperpolarized. After that, the mixture flows to the accumulation cell "AC" where the Xe freezes out and the rest of the buffer gases flow to "FROM SAMPLE" to the "NEEDLE VALVE" and leave the system through "EXHAUST".

4.1.2 Holding magnetic field of the OP-cell

SEOP requires a guiding magnetic field to define a quantization axis for the valence electrons of Rb and a homogeneous magnetic holding field in order to preserve the hyperpolarized state. If the homogeneity of the environmental field is given, the relative field gradient can be improved by applying a homogeneous guiding magnetic field

sufficiently strong to reach the required relative field gradients (see Eq. 2.43). This condition is normally achieved using fields around 2 mT generated by air coils. On the other hand, magnetic fields higher than 0.1 T are required for the cryogenic separation of HP-Xe. As a consequence, there is a transition part with potentially high magnetic field gradients between the holding field for the HP-Xe gas mixture and the holding field for the frozen HP-Xe. This transition should be free of zero field crossings which would immediately destroy the polarization of the HP-Xe gas. Therefore, a holding field of about 2 mT is a good compromise giving a well-defined field direction even in the access part to the permanent magnet where the accumulation cell is positioned. Higher magnetic holding fields are possible, of course, but the effort in electrical power/cooling to provide them is enormous; specially for mobile systems.

The holding field inside the OP-cell and the filling station is provided by a system of six coils. The coils are constructed from 29" (radius: 31 cm) aluminum bicycle rims which magnetic parts of the rim were removed and the sharp edges sealed. The wire used was a high temperature isolated copper wire of about 1 mm diameter which can withstand temperatures over 250°C. The radius of the coils is around 20 times bigger than the radius of the cylindrical OP-cell which is centered along the coil axis. This size allows comfortable manipulation of the components inside the field and, in addition, the transverse gradients over the OP-cell result to be negligible [Ang08].

The number of wire windings and relative distances of the individual air coils were optimized for minimization of the homogeneity along the *z*-axis using a MatLab code [Fuc12]. In this program, the magnetic field of the entire assembly is determined using the Biot-Savart law by overlapping the magnetic field of each individual coil in the same position. Then, the homogeneity in the region of interest is calculated. The number of turns and distance between coils is varied until a predefined value for the homogeneity is reached. This calculation does not consider the finite size of the wire winding which normally leads to a difference of about one order of magnitude between the simulated and the measured homogeneity. However, this difference can be ignored just by setting the requested homogeneity in the program to one order of magnitude higher than actually needed. In this case, the homogeneity input value according to Eq. [2.45] was 10^{-5} cm^{-1} in the region of the optical pumping cell. Finally, the results of the simulation are summarized in Table 4.1.

Each coil was fabricated according to the values of Table 4.1 and mounted in a non-magnetic holder and fixed to standard aluminum profiles (Item, Germany) with brass screws and nuts (non-magnetic) produced by the workshop of the university. The coil system is connected to current regulated power supply (5A, 200V, Heinzinger, Germany). The stationary temperature of the coils under normal operation conditions (I = 2.1 A, $B_0 \approx$ 20 G) is 60°C for the middle coils and 80°C for the two coils at the ends which have the highest number of windings.

Table 4.1: Characteristics of the coil system for the holding magnetic field of the Xe-polarizer for fundamental physics application calculated according to [Fuc12]. The zero distance refers to the symmetry plane of the coil system (total length 1.08 m).

coil	# turns	R [Ω]	distance [cm]
1	190	8.10	54
2	154	6.80	36
3	168	7.10	12
4	168	7.20	-12
5	154	6.70	-36
6	190	8.00	-54

The magnetic field produced by the coil system was measured using a fluxgate (Bartington, England) with a resolution of 10^{-4} G connected to a multimeter (HP 3456A, USA). The dynamic range of the fluxgate is up to 10 G, therefore the characterization was done with a reduced magnetic field of about 8 G (I =1 A) (see Section 3.2.1). For the measurement of the magnetic field, the fluxgate was mounted on a rail placed in the center of the coil system and the field was recorded every 2 cm over a total length of 1.2 m. This field characterization was carried on with most of the magnetic parts of the polarizer such as Halbach magnet, pumps and computers in their positions for obtaining a realistic approach to the homogeneity under operation conditions. The homogeneity was calculated using a simplification of Eq. [2.45][20]

$$H = \frac{\left|B_i - B_{i+1}\right|}{B_i d} \quad , \qquad [4.1]$$

where d is the distance between values (d = 2 cm), B_i is the magnetic field measured in z direction at a position z_i and B_{i+1} is the magnetic field measured at a position $z_i + d$. The measurements using a lower magnetic field should not affect the values of the homogeneity due to the linear dependence of the Biot-Savart law on current.

The magnetic field distribution and homogeneity of the coil system can be seen in Fig. 4.7a. The black points correspond to the measurements while the red line corresponds to the values obtained from the simulation. The simulations and the results agree mostly besides the oscillations in the experimental values. This difference is attributed to the distribution of windings inside each rim. On Fig. 4.7b, the black points represent the homogeneity calculated with the measured magnetic field values and the red line is the homogeneity calculated with the theoretical values of the magnetic field obtained by the program. Both homogeneities were calculated by Eq. [4.1], particularly the values calculated by the program were multiplied by 15 in order to overlap the experimental

[20] Eq. 2.45 is discretized using a step of the size "d" for the numerical calculation of the gradient.

results. This factor is in agreement with the expected difference between the theoretical and experimental results. Finally, the homogeneity in the position of the OP-cell (z = 30 to z = 40 cm) is shown in Fig. 4.7c obtaining an average homogeneity of approximately $3 \cdot 10^{-3}$ cm^{-1}.

The diffusion coefficient of the standard gas mixture at 4 bar is 0.652 cm^2/s (see Eq. [2.44]). According to the homogeneity values shown in Fig. 4.7c, the relaxation time of HP-Xe due to magnetic field gradients is longer than 4 h. Since the volume of the optical pumping cell and the Rb-trap is about 70 ml and the flow is 200 ml/min, the gas mixture remains less than one minute inside the optical pumping cell. Therefore, the losses due diffusion into magnetic field gradients are negligible and the conditions provided by this holding magnetic field fulfill the requirements of SEOP.

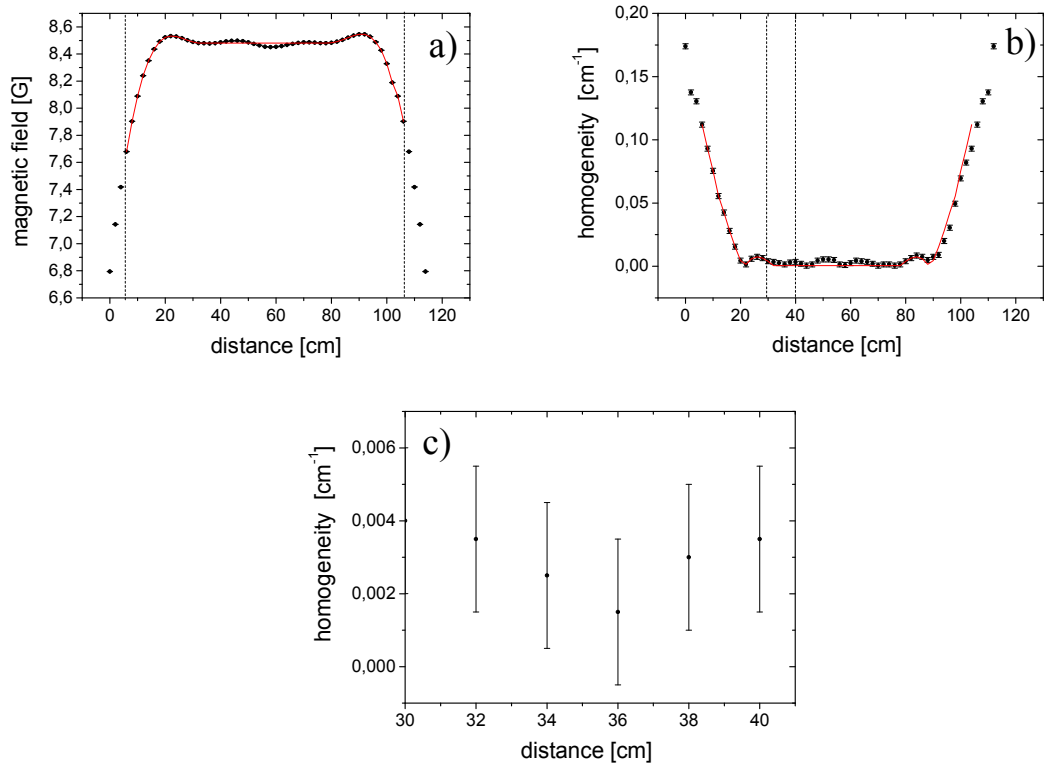

Fig. 4.7: a) Magnetic field produced by the Helmoltz coil configuration. The black dots are the measured points while the red line represents the simulated values. The simulated values were multiplied by 15 in order to match the experimental values. The dotted lines represent the last coils of the coil system (total length of 108 cm). b) Homogeneity calculated using Eq. [4.1]. The black points are the measured points and the red line corresponds to the simulation. The dotted lines represent (30 - 40 cm) the position of the optical pumping cell. c) Homogeneity zoomed for the area of the optical pumping cell.

4.1.3 Laser and optics for spin exchange optical pumping

The very first experiments on SEOP were performed with broadband Rb discharge lamps, which, on average, could provide about 250 mW [Bre61]. Later, the experiments were carried out with Ar ion/Ti: sapphire lasers with the total output power limited to a few Watts [Rut99]. In consequence, the production of HP-Xe was limited to only a few

mbar·l/h.

The development of efficient diode lasers in the wavelength range of $\lambda \sim 795$ nm represented a breakthrough in the production of HP-Xe. These lasers are able to provide tens of Watts allowing an increase both in the Rb vapor pressure and the sizes of the OP-cells. As a result, the production rate of HP-Xe and its polarization could increase considerably. The spectral profile of the emitted light from diode lasers is usually Gaussian distributed with a bandwidth of about 3 nm. The center of the frequency profile shifts as the temperature increases with a rate of typically 0.03 nm/°C. For this reason, diode lasers require thermal stabilization, which can be realized by cooling with air or Peltier elements for output powers up to about 30 W and by water-cooling for higher laser powers. The polarization obtained with these lasers were, in general, not higher than 15%; mainly because most laser power was wasted due to the much broader spectral line of the laser compared to the absorption line of Rb of about 0.04 nm in a buffer gas mixture at 1 bar. This problem was partially solved by broadening the Rb D1 line by increasing the total pressure to about 5 - 10 bar as was explained in Sec. 2.1.5.

However, extremely high powers (c.a. 200W) were needed in SEOP to reach reproducible HP-Xe polarizations in the order of 50% for a bandwidth of 0.16 nm [Zoo02].

Recently, the construction of Littrow cavities [Cha00] [Bab05] reduced the linewidth of laser diodes to about 0.1 nm allowing to lower the total operation pressure of the Xe-polarizers while keeping their high performance [Zhu05].

A Littrow cavity is a resonant cavity composed by lenses and a diffraction grating. The grating is aligned such that the first-order diffraction from the grating is coupled directly back into the laser while the zeroth-order diffraction is reflected as the output beam. The lasing wavelength is dependent on the angle of the incident laser beam with respect to the grating. A sketch of this cavity is shown in Fig. 4.8a.

The central wavelength of the laser is selected by rotation of the grating. This allows a tuning of the laser in a range of frequencies typically between 796 and 804 nm as is shown in Fig 4.8b [Cha00]. In this figure, the different power spectra are plotted vs. the wavelength. In Fig. 4.8c, the peak corresponding to 801 nm was selected to compare the power of the narrowed with the power of the free running laser. This wavelength was chosen because it provides the highest power spectrum of the setup reported in [Cha00]. As a result, the power losses by narrowing the laser are about 30%.

Using this configuration, the temperature stabilization is still crucial using Littrow cavities. First, the central frequency of the diode has to be fixed for a determined angle of the grating, which results on the maximum output power in the bandwidth of interest. Second, the grating has to be cooled as well because is a very sensible element which can be destroyed easily at higher temperatures.

Nowadays, such laser diodes with included Littrow cavities are commercially available with output powers up to 100 W and bandwidths from 0.3 nm [Ams15] down to

0.15 nm [Opt15].

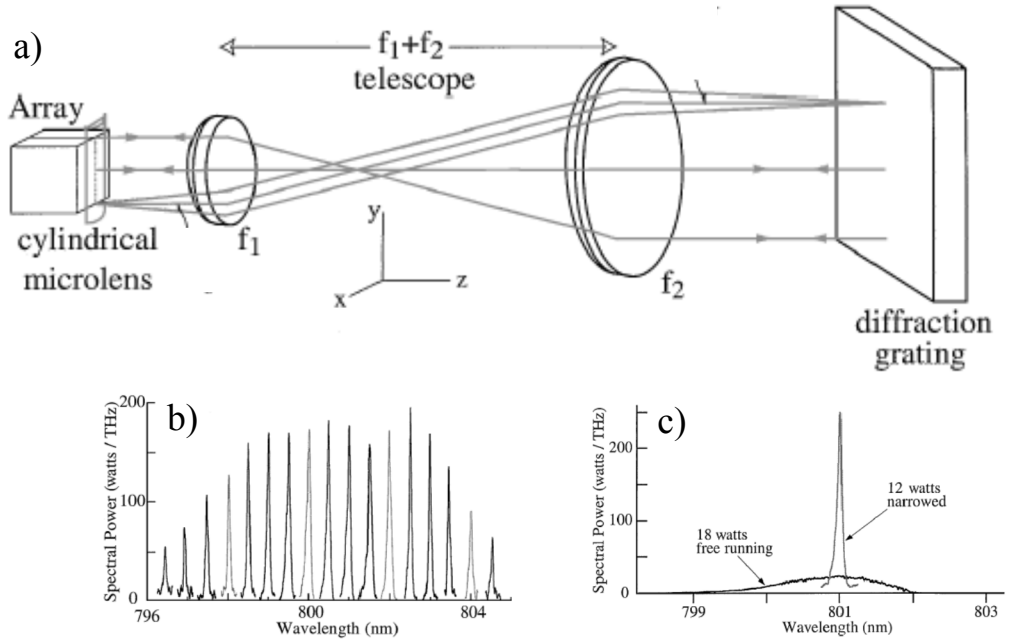

Fig. 4.8: Littrow cavity [Cha00].a) A Litthrow cavity consists of a telescope and a diffraction grating. b) Different central wavelenghts are selected by tilting the grating. c) Spectrum of a free running diode- and narrowed diode laser.

The laser used in this polarizer is a narrowed diode laser of 30 W and λ = 795nm and $\Delta\lambda$ = 0.3 nm with tuning range of ± 0.30 nm (Raytum, USA). The laser beam is generated and narrowed in the polarizing box of Fig. 4.2 and fed through an optical fiber to the "light polarizer unit" where the linear polarized laser light is circularly polarized (σ^+). The polarizing box shown in Fig. 4.9 contains a movable holder for the optical fiber, a lens to broaden the beam to a diameter of 5 cm, a polarizing beam splitter which divides the incoming elliptically polarized beam into two linearly polarized beams (polarization planes rotated by 90°). After the beam splitter, one linear polarized beam goes straight through a $\lambda/4$ plate to obtain σ^+ light polarization. The 90° reflected beam, is reflected again by a dichroitic and polarization preserving mirror and passes the second $\lambda/4$ plate which also produces σ^+ light. The angle between the two beams is about 25°. Both beams converge further downstream at the position of the optical pumping cell where they overlap over the effective volume of the OP-cell which is a cylinder of Pyrex glass with ca. 10 cm in length and 3.8 cm in diameter. The transmitted light is collected with an optical fiber mounted in a beam stopper behind the OP-cell and analyzed by a spectrometer with 0.1 nm resolution (Ocean Optics HR 2000, Holland).

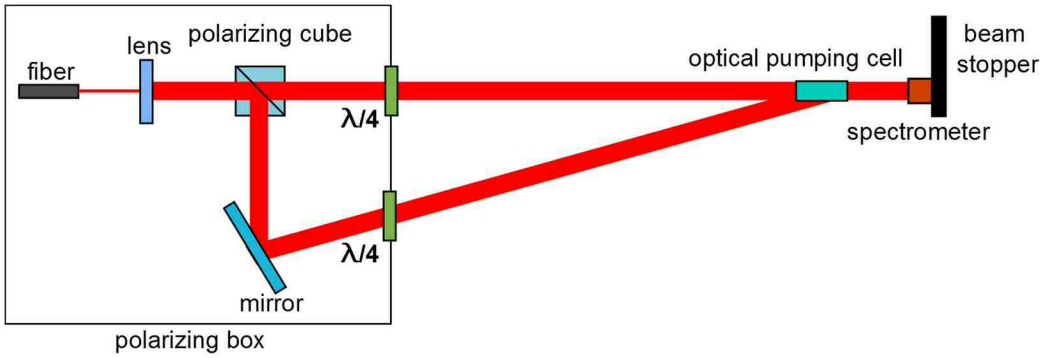

Fig. 4.9: Polarizer unit (not to scale). The incoming elliptically polarized beam passes a lens and to a polarizing cube where the beam splits into two linearly polarized beams with 90° rotation of the respective polarizing planes. The transmitted light is circularly polarized by λ/4 plates. The two beams are then converging again overlapping at the position of the optical pumping cell. See text for details.

The wavelength of the laser can be adjusted by varying the temperature and/or the current. The working temperature range of the diode is from 16°C to 30°C and the maximal current that can be applied is 40 A leading to a maximum beam power of 30 W measured at the beam exit directly behind the polarizing unit. The output power of the laser after the polarizing box vs. the applied current was measured with a powermeter (LASER 2000, Germany) with a range up to 200 W. The result of this measurement was a linear relation between power and current as shown in Fig. 4.10.

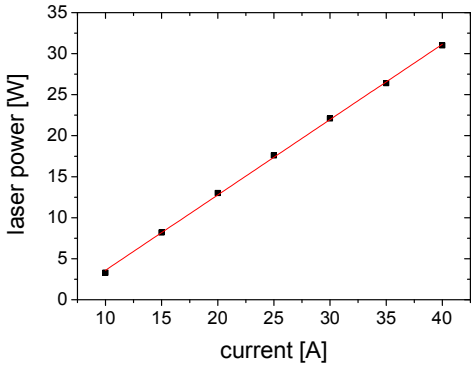

Fig. 4.10: Laser power vs. applied current to the diode. The slope is 0.92 ± 0.01 with a linear correlation coefficient of 0.9998.

To avoid waste of laser power, the bandwidth of the laser must be concentrated to the frequency range of the rubidium D1 absorption line. If the temperature of the laser diode is not appropriate, a significant amount of the laser power concentrates in a frequency or wavelength range that cannot be absorbed by the Rb vapor.

A first adjustment of the wavelength is done with the OP-cell at room temperature, i.e., no light absorption due to the negligible vapor pressure of Rb. The adjustment consists in varying the temperature of the diode until the laser power spectrum concentrates around 795 nm. This is monitored either by the optical spectrometer or a spectrum analyzer

(resolution 0.1 nm). In Fig. 4.11a, an example of this tuning is shown. In this case, the angle of the grating was kept constant but the temperature of the diode was varied from 16°C to 21.6°C, the latter being found as the optimal working temperature for this laser system.

The fine tuning of the spectral profile is performed by measuring the transmitted light when the OP-cell is heated up to the standard operation temperature. At this temperature, the Rb density is sufficient to absorb significant amounts of power. The power spectrum of the laser status is monitored by the optical spectrometer and the grating is rotated to a position where most power is absorbed. At this point, the temperature of the cell also increases. More details about the fine tuning are described in Sec. 4.1.7.3.

In Fig. 4.11b, the spectrum of the tuned laser is shown. This graphic was fit with a Lorentzian function obtaining a width of (0.28 ± 0.3) nm which agrees with the FWHM of 0.3 nm specified by the manufacturer.

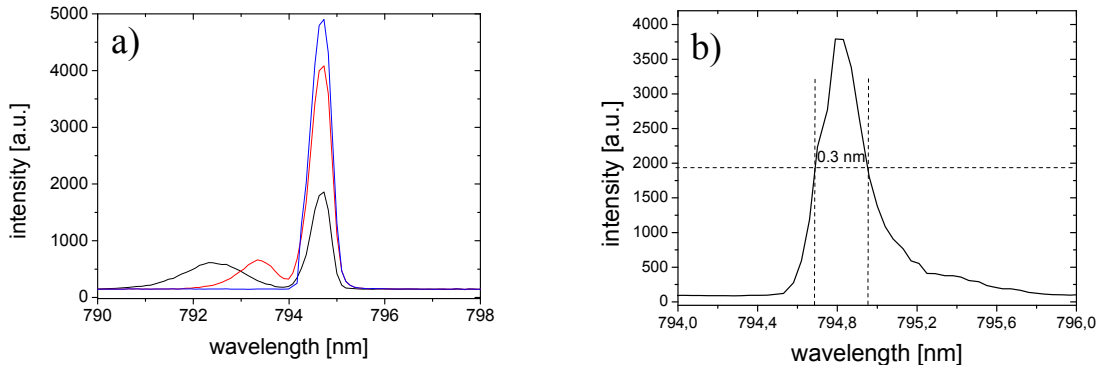

Fig. 4.11: a) Tuning of the spectral profile of the laser via the diode temperature measured through a cold OP-cell at I = 40 A. The black, red and blue lines correspond to diode temperatures of 16°C, 19°C and 21.6°C (laser tuned) respectively. b) Spectrum of the tuned laser with a FWHM = 0.3 nm.

4.1.4 Optical Pumping Assembly (OP- assembly)

The OP-cell is the portion of the Xe-polarizer where SEOP takes place. It is a glass cylinder of 9.3 cm in length, an outer diameter of 3.9 cm and a wall thickness of 6 mm. The volume of the OP-cell is about 40 cm^3 and this particular cell can withstand pressures up to 10 bar.

The OP-cell is placed inside the holding magnetic field described (see Section 4.1.2) from z = 30 cm to $z \approx 40$ cm. In most other Xe-polarizers, the OP-cell contains a drop of Rb but in this work, the Rb is placed outside of the OP-cell inside a Rb-trap. In this way, the OP-cell and the Rb-trap form the OP-assembly.

The division between Rb-trap and OP-cell arises naturally from the construction of the OP-assembly. The OP-cell is first constructed and tested for withstanding a maximal

pressure and then connected to the Rb-trap. The latter can have many shapes and sizes and it can be replaced/modified easily by the glassblower. From the original OP-assembly constructed by S. Appelt [App04], only the OP-cell remained because it can withstand pressures up to 10 bar[21]. The Rb-trap was replaced to increase the saturation volume from 1 to 20 cm^3 and to allow counter-flow operation (see Sec. 4.1.7.1). This Rb-trap (or pre-saturator) is now a 40 cm long glass tube of 8 mm inner diameter which passes completely through the oven length. A big pre-saturation volume has many advantages such as preheating the gas mixture before entering the OP-cell and reducing temperature gradients. Furthermore, it acts like a getter by preventing that impurities, which may be part of the gas mixture, reach the Rb inside the OP-cell. This happens because of chemical reactions of Rb with possible impurities occur already inside the Rb-trap.

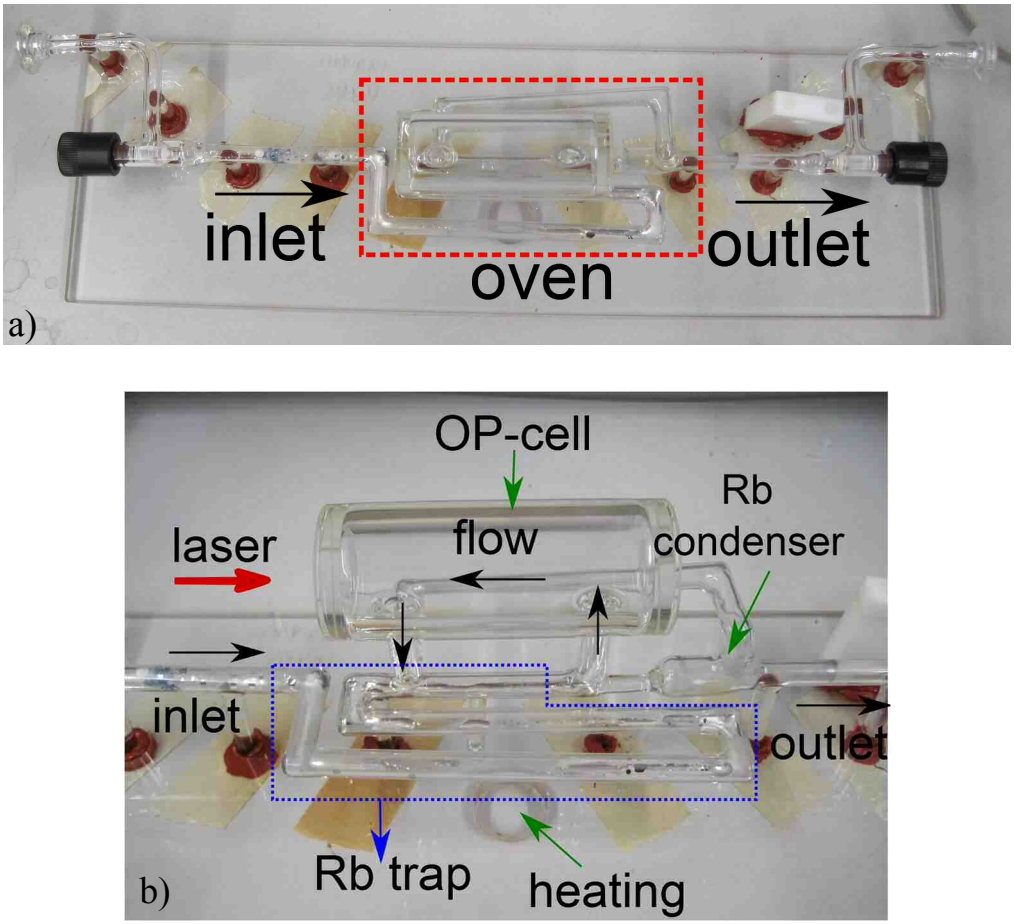

Fig. 4.12: Optical pumping assembly. The gas mixture flows from the inlet to the Rb-trap entering the OP-cell and passing through the outlet. The direction of the flow is marked with black arrows. a) OP-assembly: the position of the oven is marked with a red dotted line. b) Part of the Rb assembly inside of the oven. The Rb-trap is marked by blue dotted line. The direction of propagation of the laser beam is indicated with a red arrow. Hot air enters through a hole marked by a green arrow.

[21] At the end of this work this OP-assembly was replaced by a new one built in the Physics Institute which withstands a total pressure of 3 bar. This assembly is shown in Fig. 7.1.

In addition, it provides a buffer volume to prevent that liquid Rb enters the OP-cell if unwanted pressure gradients are generated between the inlet and outlet (Rb splashes). For this reason, the construction of a Rb-trap separated from the OP-cell simplifies significantly the operation by extending the time between cell recoveries[22] .

The OP-assembly is mounted on a glass plate and glued with standard high temperature silicon glue (Pattex, Germany) to provide stability. The valves for the in- and outlet of the cell (Hi-Vac, USA) use FFKM O-rings which are resistant to strong alkalis (see Appendix 4) and high temperatures (DTH, Germany). The cell is connected to the rest of the system through polished glass KF-16 flanges, standard O-rings and clamps which can withstand temperatures of up to 80°C. A picture of the OP-assembly is shown on Fig. 4.12a where the position of the oven is marked with red dotted lines. The parts inside the oven are shown in Fig. 4.12b the outlet of the cell is connected to a 30 cm long glass tubing with inner diameter of 6 mm. Approximately 13 cm of this glass tube is inside the oven. After, the tube increases its diameter to 2 cm over a length of 4 cm in order to provide a high surface to condense the Rb vapor. This Rb condenser is shown also in Fig. 4.12b.

4.1.5 Glass oven

The Rb-trap requires temperatures over 100°C to evaporate enough Rb into the gas mixture to maintain an efficient SEOP process. The volume of the optical pumping cell and the Rb-trap together is about 150 cm^3. This volume can be efficiently heated by a stream of hot air inside a glass box containing the OP-cell. This oven consists of a glass box (Pyrex) of 15 x 5.2 x 5.6 cm, with 11 mm wall thickness which is glued together by high temperature silicon glue (Pattex). To have a better thermal isolation, the inner walls are covered with ceramic except for the parts where the laser beam enters and leaves the oven. The lid of the oven has 10 holes of about 5 mm in diameter to facilitate sufficient hot air flow through the inner volume of the oven. The heat source is a temperature controlled heating gun which is connected to the bottom of the Rb-trap through a flexible bellow. The temperature sensor is installed on the Rb-trap to regulate the temperature.

As explained in Sec. 2.1.3, the temperature of the OP-cell increases during the polarization process due to the quenching excited states of Rb by N_2. Therefore, the whole absorbed laser power is dissipated into the gas increasing the temperature of the gas mixture and, in consequence, of the OP-cell. This absorbed power can evaporate the Rb which was already condensed inside the OP-cell leading to an increase of the Rb density increasing also the absorbed laser power. Therefore, the number of quenched atoms increases resulting in OP-cell temperatures over 200°C and, according to Fig. 2.8, much higher gas mixture temperatures. This overheating of the OP-cell causes high Rb density and, therefore, Rb runaways. The consequence for both cases is the appearance of dark

[22] The cleaning and re-fill of Rb in the OP-cell is usually done once per year.

areas inside of the OP-cell which affects directly the efficiency of the optical pumping process. However, this problem can be solved by decoupling the temperature of the Rb-trap and the OP-cell using a sort of insulation. For this system, an insulation layer was made from silicone and glass wool and separates the area of the oven where the Rb-trap is placed from the OP-cell as shown in Fig. 4.13. Due to this layer, the temperature of the Rb-trap can be set to 150°C, while the temperature of the OP-cell stays around 80°C for the first 20 min of use, increasing to 90°C after 30 min[23]. Finally, if the Rb density is too high to provide an illumination of the OP-cell free of dark areas, the heating of the trap can be switched off and the polarization process can occur only with the Rb which is already inside of the OP-cell. In both cases, the Rb vapor is condensed in the condenser of Fig. 4.12b which is cooled to about 20°C by a stream of compressed air.

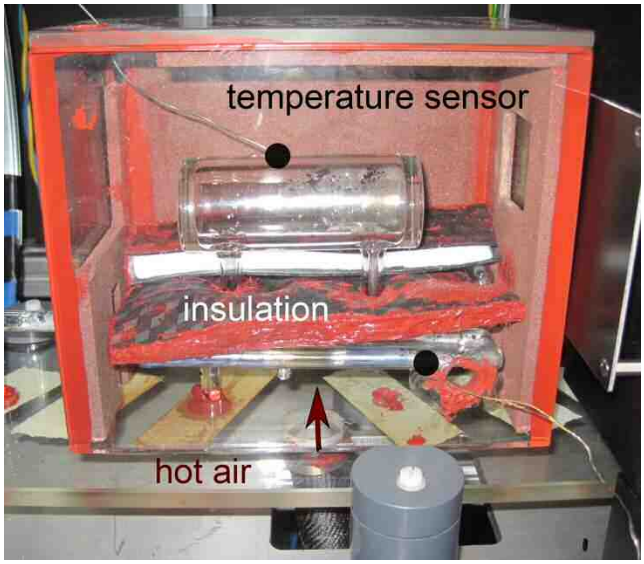

Fig. 4.13: Picture of the glass oven. Hot air enters from the bottom heating the Rb-trap and the gas mixture. The insulation layer allows for regulating the temperature of the OP-cell. The temperature sensors are indicated with black dots. The sensor connected to the heating gun is mounted on the Rb-trap and another sensor measures the temperature on the surface of the OP-cell.

For every new cell, it is crucial to test if the optical windows conserve the polarization of the laser beam under operating conditions. Birefringence is not expected in ordinary Pyrex glass but it could appear due to thermal and pressure gradients produced during SEOP conditions [Wol04]. To test for this, the polarization of the light was measured before and after the OP-cell, included the oven, under usual polarization conditions (150°C, 4 bar and 30 W incident laser power). The circularly polarized beam coming from the polarizing box was characterized by using a polarizing cube and a λ/4 plate downstream in front of the power meter. The transmitted laser power was measured

[23] This difference of temperature can be used also to condense Rb vapor inside the OP-cell

as a function of the λ/4 rotation angle with respect to the fixed polarizing cube. The results of this measurement are represented with the black squares shown in Fig. 4.14. The experiment was repeated analyzing the light which went through the oven and OP-cell during operation conditions. For this, the OP-cell was filled with helium up to 4 bar total pressure and heated up to 150°C. The results of both experiments are compared in Fig. 4.14 in order to determine if some birefringence is induced in the glass under typical working conditions. In both cases, the minimum of the power was found to be at a rotation angle of the λ/4 plate of 38°, therefore the optical windows show no sign of birefringence. The same experiment was repeated increasing the temperature and no evidence of birefringence was found.

In order to test for higher pressures, the angle of the λ/4 plate was fixed to 38°. Since this angle corresponds to the minimum power, an increment on this value will indicate an onset birefringence. It was found that a slight birefringence appears for temperatures exceeding 175°C and pressures over 6 bar. This birefringence can be only attributed to the OP-cell since the oven at the same temperature did not show birefringence at all.

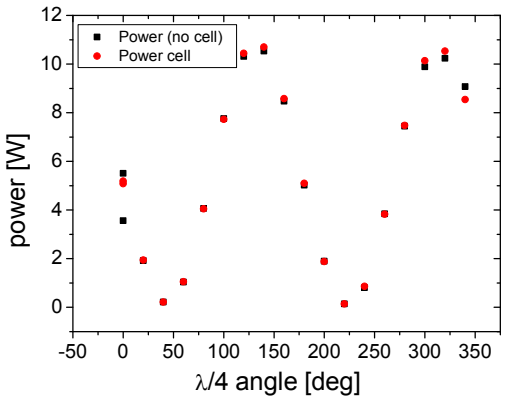

Fig 4.14: Birefringence test of the optical windows (and oven) during operation conditions (4 bar and 150°C) by plotting the power versus the rotation angle of the λ/4 plate. The black dots correspond to the original beam without while the red dots correspond to the beam passing the OP-cell.

The absence of birefringence on the optical windows of the OP-assembly makes the assembly suitable for SEOP. After this test, the assembly was washed, first with HNO_3 to remove possible ferromagnetic impurities and then with distilled water. Then, the assembly was evacuated to 10^{-7} mbar while opening and closing the valves repeatedly to evacuate small volumes between the O-rings of the valves. The next step is to fill the Rb-trap with Rb.

4.1.6 Rubidium

The Rb number density required for optical pumping is in the order of 10^{-14} cm^{-3} according to Fig. 2.3. This value corresponds to 0.73 μg for an OP-cell of about 50 cm^3.

Usually, about 0.5 g of Rb are filled into the Rb-trap and this density is achieved by heating the OP-assembly at temperatures about 150°C.

Rb is extremely reactive, especially with water and oxygen producing exothermic reactions. Particularly, the chemical reaction with H_2O produces H_2 as

$$4Rb+2H_2O \rightarrow 2RbOH+H_2.$$

The heat produced by this reaction can ignite the product H_2 causing fierce explosions, which may damage the OP-cell. Rb is available in quantities of 1 or 5 g filled in ampoules sealed under vacuum or Ar atmosphere with purity of 99 and 99.8% (Alfa Aesar/Strem). The ampoules must be opened and manipulated in a chemically inert atmosphere typically inside a glovebox for avoiding contamination and violent reactions with O_2 and humidity. In addition, the glovebox is required for the safety of the operator since Rb can generate thermal burns in contact with tissue. This is the main risk for the operator because Rb vapor is not toxic, extremely high doses are necessary to produce intoxication [Gar75] [Mel87].

The procedure and the safety protocol for filling Rb inside of the trap are described in detail in Appendix 4. After this process, the pressure in the OP-cell is about 1 bar. Then, the OP-assembly is mounted on the Xe-polarizer and connected to the gas circuit. These connections are evacuated for approximately 48 h until a final pressure of 10^{-6} mbar is reached. Then, the OP-cell is filled with the gas mixture and the polarization process can start.

The Rb quality is critical for the optical pumping process. Impurities decrease the concentration of pure Rb vapor in the OP-cell reducing the efficiency of optical pumping. Most impurities can be spotted due to change in color and metallic shine but some impurities do not affect the look but the melting point and vapor pressure.

The impurity which could normally contaminate Rb is oxygen because of possible leaks in the system, contamination of the gas bottle or impurities in the glovebox. The reaction of Rb with O_2 produces Rb oxide, Rb_2O, superoxide Rb_2O_2 and suboxides. These compounds are formed by an excess of the electropositive element (Rb) relative to the oxides.

The study of the physical properties of Rb suboxides is quite limited because their stability requires very controlled environmental conditions. The chemical composition of some suboxides with their color, melting point or decomposition temperature are summarized in Table 4.2. There are suboxides of Rb not listed in the table which have the same color and metallic shine than Rb and the only way to identify them is via their melting/boiling point [Suz66]. For example, Fig. 4.20 shows the phase diagram of Rb, Rb oxides and suboxides plotted vs. the percent of atomic oxygen.

The suboxides which cannot be identified by a change of color can saturate the gas mixture instead of Rb due to their lower vapor pressure. The Rb in these compounds

cannot be optically polarized by the laser light which leads to a reduced efficiency of SEOP. For this reason, it is crucial for SEOP to work in absence of oxygen.

Table 4.2: Physical properties of suboxides, superoxides and oxide of Rb. The chemical composition is given in the first column. The second column reports the color and the third the melting point of decomposition temperature [Hol07].

Chemical equation	Color	Melting point
Rb_9O_2 (suboxide)	Copper	40.2 °C
Rb_2O (oxide)	Light yellow	567°C
Rb_2O_2 (superoxide)	Yellow	decomposition at 600°C
RbO_2	Orange	432°C
RbO_3	Dark red	decomposition at 20°C

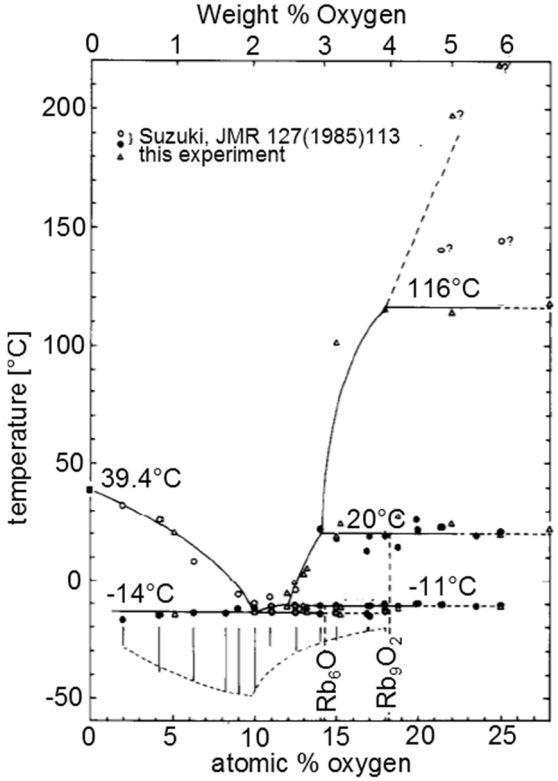

Fig 4.15: Phase diagram of Rb oxides extracted from [Suz66]. On the abscissa, the percentage of atomic oxygen is given while the ordinate gives the melting point. Suboxides with a oxygen percentage under between 4 and 15 % have melting points below the melting point of Rb. Particularly, between 8 and 10%, the melting point is below room temperature.

The purity of Rb in the optical pumping cell can be controlled by analyzing its emission lines. This experiment must be done in absence of N_2 to avoid quenching. For this purpose, the OP- cell is evacuated, heated and illuminated with the laser beam. The laser penetrates the cell just 1 cm and it then shines with a strong violet color (see Fig. 4.15). In this work, this analysis was performed using an optical spectrometer and comparing the results with the Rb emission lines. A quantitative procedure can be performed by analyzing the light with a spectrum analyzer or a digital spectrometer [Sah06].

Fig 4.16: OP-cell filled only with Rb and illuminated with laser light at λ = 795 nm. The emitted light can be analyzed with an optical or digital spectrometer to verify the purity of Rb.

For starting the polarization process, the Rb-trap is heated to 150 - 200°C and the flow is started as explained in the Appendix 3. The gas mixture flows through the OP-cell for about 3 h while the laser is still off. The purpose of this procedure is to transport enough Rb vapor to the OP-cell to absorb most of the laser power in the D1 line of Rb. The insulation panel simplifies significantly this process because it keeps a temperature difference of about 60°C between the Rb-trap and the OP-cell over about one hour, after that more Rb vapor condensates in the OP-cell (see [Eq. 2.1]). Once enough Rb vapor is collected in the OP-cell to identify the absorption of the D1 line, the HP- Xe production can be started for the experiments. This amount of Rb is not macroscopic and it can be seen as a slight mirrored surface in the OP-cell.

As a final remark, the experiments presented in this work were performed with Rb from the company Alfa Aesar with a chemical composition of 99.75 % of Rb and less than 1 ppm of Li, Mg, Si, Cu, Al, Fe, less than 30 ppm of Ca, less than 100 ppm of K and Cs and 10 ppm other impurities. However, better results are reported by [Sal14] with Rb from the company “Strem”. This result was confirmed by recent measurements with this Xe-polarizer using Rb from Strem (Lot number 251037-S: Na < 13ppm, K < 13ppm, Cs 639 ppm). The improvement on the NMR signal was about a factor 3. However, this result must be confirmed by the measurement of the absolute polarization described in Chapter 6.

4.1.6.1 Lifetime of Rb and cleaning of the OP-cell

After several months of use, the Rb accumulates in the OP-cell generating a thin silver layer (see Fig. 4.17a) or some Rb splashes into the OP-cell due to some mistake in the pressure management as is shown in Fig. 4.17b. Both cases lead to an increment of the amount of Rb inside the OP-cell with the already discussed consequences. At this point, the OP-assembly must be cleaned and re-filled with Rb. For this purpose, the OP-assembly is disconnected from the system and carefully opened to air. The oxidation changes Rb from a silver solid to, first a silver liquid suddenly to a slightly golden color, then to violet with metallic shine, copper with metallic shine, black opaque and green and yellow/creme in the final state. This description is in agreement with the colors listed in Table 4.2. The OP-cell with almost completely oxidized Rb is shown in Fig. 4.18a. This oxidation occurs first on the surface and this layer of oxide passivates the metal underneath as shown in Fig. 4.18b. The cleaning of the OP-cell should be performed with dried[24] 2-butanol once most of the Rb has turned into Rb_2O (yellow) as explained in Appendix 4.

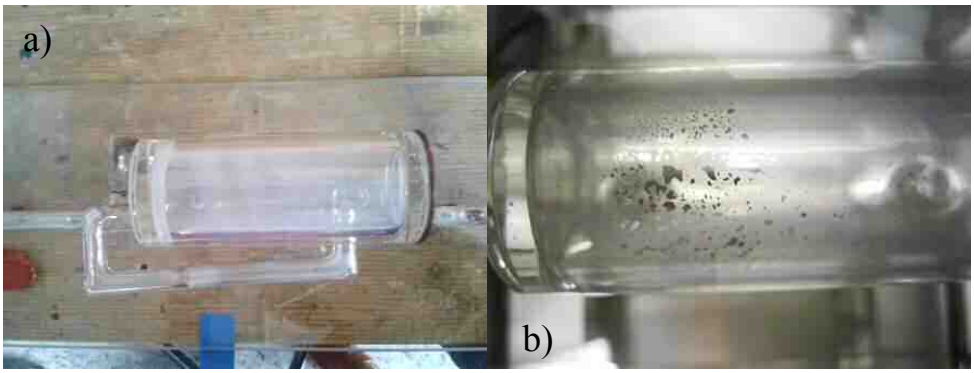

Fig 4.17: Rubidium inside the OP-cell: a) the Rb forms a mirror-like layer in the OP-cell after several months of continuous use. b) A pressure gradient exceeding more than 2 bar between inlet and oulet of the OP-assembly can cause Rb splashes inside of the OP-cell.

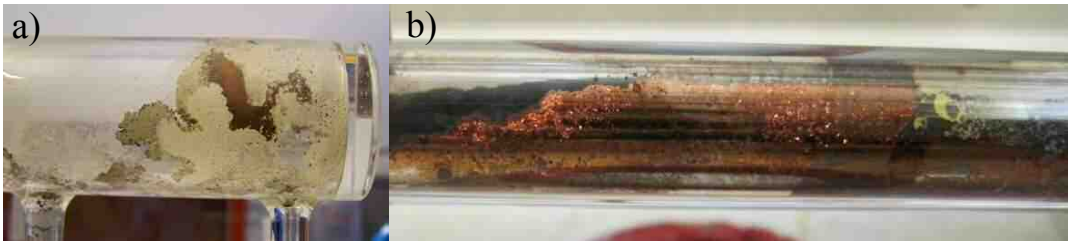

Fig 4.18: a) Oxidized Rb inside the OP-cell. In this case, most of the oxide is composed by Rb_2O (yellow) and Rb_9O_2 (copper). b) Rb oxides and superoxides in the Rb-trap. Here, the black compound is a suboxide which is not listed in Table 4.2 acting as a passivation layer for the copper colored suboxide.

[24] It is crucial that the butanol remains water-free to avoid ignition of H_2. The water absorbed by the butanol can be removed by adding small amounts of Na.

4.1.7 Illumination of the OP-cell

Once the Rb is inside the OP-cell, the conditions for the illumination of its volume have to be set in order to achieve the maximum polarization of Rb and, therefore, of Xe. According to Section 2.1.8, the main source of depolarization for HP-Xe in the OP-cell is unpolarized Rb atoms. Therefore, the contact of HP-Xe with those atoms has to be reduced to the minimum.

In Section 2.1.6, these conditions were explained in a static scenario. In the dynamic case, i.e. in a flowing gas mixture, the strategies to achieve these conditions need to be reviewed.

4.1.7.1 Counter-flow illumination

The intensity I_{OP} of the light as it passes through in the Rb-vapor inside the OP-cell is given by the Lambert-Beer law as

$$I_{OP}(z) = I_{OP}^{0} \exp(-\lambda_{OP} z) \ , \qquad [4.2]$$

where λ_{OP} is the characteristic attenuation factor of the D1 line which essentially depends on the Rb vapor density that is determined by the operation temperature of the OP-cell. The variable z gives actual position along the axis of the OP-cell (from $z = 0$ to $z = L$).

If the direction of the gas flow is parallel to the direction of light propagation, the highest laser power is available at $z \approx 0$. If the light is strongly absorbed, it is quite likely that at the opposite side of the OP-cell ($z \approx L$), the available laser power is not sufficient to polarize the Rb vapor. In that area, the reduced Rb polarization immediately results in a reduced Xe polarization since both species are strongly coupled due to the spin-exchange process discussed in Section 2.1.6. That exchange happens typically at a time scale of seconds, so that even highly polarized HP-Xe will lose a large part of its polarization almost instantaneously by entering such an area.

On the other hand, if the direction of propagation of the light is opposite to that of the gas flow, the HP-Xe leaves the OP-cell at the point where the Rb polarization is probably the highest ($z \approx 0$). Therefore, the spin-exchange interaction of HP-Xe with only poorly polarized Rb vapor is minimized. This operation modus is called “counter-flow” and it was introduced for the first time in [Rus05]. A detailed analysis of the counter-flow dynamics can be found in [Bra13].

In Fig. 4.19, both scenarios of optical pumping are sketched. In Fig. 4.19a, the laser direction of propagation is parallel to the flow. The outlet of the OP-cell is poorly illuminated therefore the polarization of Rb is low. By the counter-flow operation, the HP-Xe which leaves the cell is in contact with highly polarized Rb as shown in Fig. 4.19b.

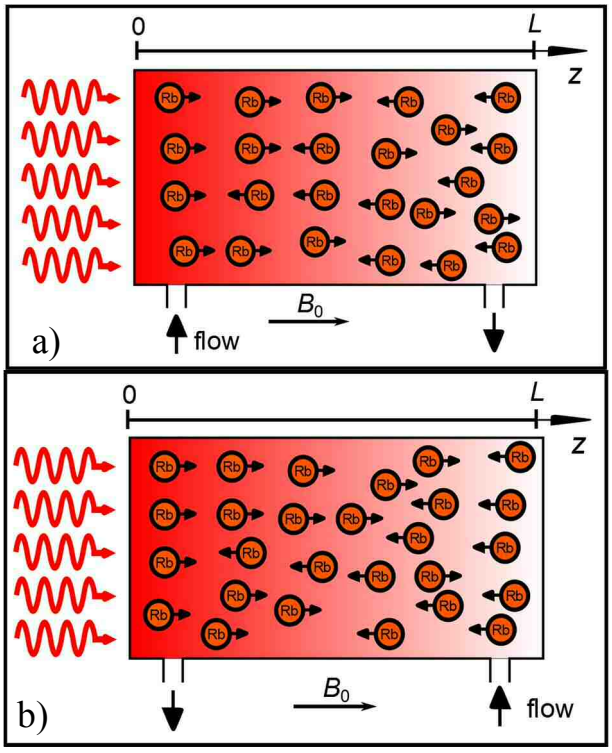

Fig 4.19: Illumination of the OP-cell with different flow directions : a) If the direction of the gas flow is parallel to the direction of the incident laser light, the Rb polarization is maximum at the inlet of the OP-cell where the highest laser power is available. Due to absorption, the laser intensity is strongly reduced (indicated by the red color shades), so the Rb polarization and with it, the Xe polarization is reduced in the area of the outlet. b) The contact unpolarized Rb is reduced in counter-flow operation where the direction of the flow is antiparallel to the direction of propagation of the laser beam.

The counter-flow has another advantage such as reduction of resonant light reflections in the inlet of the OP-cell. These reflections are unavoidable because of the convergence area of the two beams (see optics of Fig. 4.9). However, under counter-flow operation this effect is suppressed since the power of the reflected resonant light is rather low.

4.1.7.2 Adjustment of the spatial profile of the laser beam

Another crucial parameter for the homogeneous illumination of the OP-cell is the spatial distribution of light, i.e. the width of the Gaussian beam. The radius of the beam which will illuminate the OP-cell can be adjusted by moving the position of the optical fiber with respect to the lens in Fig. 4.9. For the adjustment, three different beam sizes were chosen and the power distribution was measured for each of them. The power distribution was determined by measuring the laser power passing a diaphragm which open to different diameters. The openings had a diameter from 5 to 40 mm is steps of 5 mm. With these values the power distribution P_d and the power density P_δ are given by:

$$P_d = \frac{R_{i+1} - R_i}{r_{i+1} - r_i} \text{ [4.2]} \quad \text{and} \quad P_\delta = \frac{R_{i+1} - R_i}{\pi(r_{i+1}^2 - r_{i+1})} \text{ [4.3]},$$

where R_i is the power measured with an opening of a radius r_i ($r_{i+1} > r_i$). The results are shown in Fig. 4.20 where three curves for different beam sizes are shown. The black curve corresponds to "profile 1" with a beam size of about 3.9 cm in diameter (optical fiber far away from the lens). The red curve corresponds to "profile 2" with a beam diameter of 3.0 cm. Finally, the blue curve corresponds to "profile 3" where the optical fiber closer to the lens and a beam diameter of about 2.5 cm. The power distribution and the power density vs. the opening radius are shown in Fig. 4.20a and Fig. 4.20b respectively. In both cases, the data is not sufficient for a fit of the Gaussian profile.

To decide which beam radius leads to a higher polarization, the NMR signal of HP-Xe produced with these three different beam sizes was measured. The highest NMR signal was obtained with a beam of 3 cm (red line in Fig. 4.20). Therefore, this beam size will be used for the rest of the experiments. In addition, the chosen beam size corresponds also to the configuration with concentrates most power density inside of the cell according with Fig. 4.20b.

Since the diameter of the beam is bigger than the diameter of the cell, an anodized ring is glued to the front of the OP-cell to prevent reflections on the frontal optical window. The power losses were calculated integrating the curve of the graphic in Fig. 4.20a between -20 and 20 mm (dashed line). The power losses calculated in this way result to be about 10 % of the total laser power.

The shaping of the beam reduced the initial laser power from 33 W to 29.4 W illuminate the OP-cell due to. This value is again reduced to approximately to 24.9 W due to the reflection on the glass surfaces of the oven and the optical window of the OP-cell. The power losses were calculated considering that the transmission coefficient for Pyrex at 795 nm is about 92% [Tho14]. The power of the beam was measured after the OP-cell without oven[25], in this case, the laser beam passes two glass surfaces, so the result can be compared to the situation where the beam passes the oven and one optical window of the OP-cell since both are constructed with the same material. Finally, the available power for optical pumping resulted to be (24.2 ± 0.2) W which is in agreement with the expected power losses.

[25] The output of the light in the oven is partially blocked by the ceramic coverage.

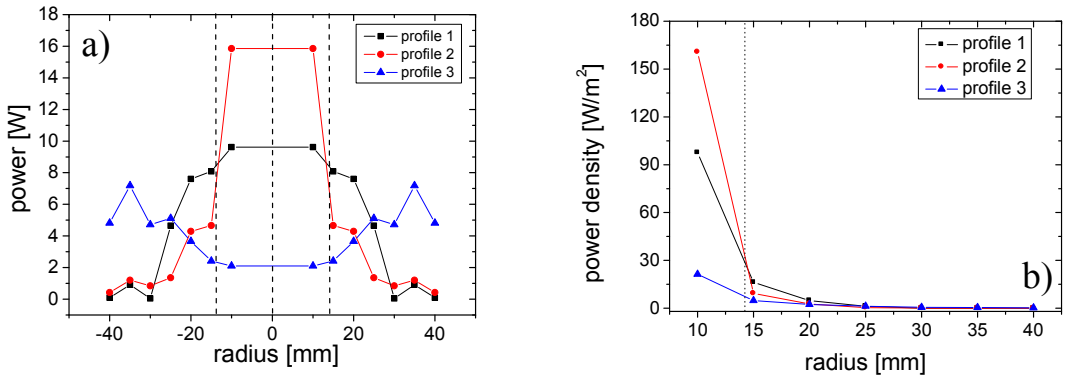

Fig. 4.20: Power distribution of the laser beam for three different beam sizes measured at the optical pumping cell. The dotted lines mark the position of the OP-cell. Profile 1, 2 and 3 correspond to a beam size of about 3.9, 3.0 and 2.5 cm in diameter respectively. a) Total laser power as a function of opening radius of the diaphragm. b) Power between openings vs. the radius of the opening.

4.1.7.3 Absorption of the Rb D1 line

The laser light crossing the OP-cell can be monitored with two devices: an optical spectrometer and an infrared camera (Electroviewer 7215, Electrophysics, USA).

The optical spectrometer analyzes the frequency spectrum of the light after passing through the OP-cell. This light is first attenuated by linear filter to prevent saturation of the detector and then collected by a 0.6 mm diameter optical fiber. The optical fiber is placed at the center of the beam axis of the OP-cell and fed to the spectrometer which processes it and displays the light intensity in arbitrary units vs. wavelength (see Fig.4.21e). The incoming light carries information of the average of all processes occurring over the total length of the OP-cell. On the other hand, the infrared camera is used to study the fluorescence light from re-emitted photons which reveal the spatial distribution of the beam. Using these two devices, the absorption and illumination profile of the beam can be analyzed simultaneously. The illumination profile across the OP-cell is classified here in three well distinguishable regimes:

- No absorption and thus no visible spatial profile (Fig. 4.21a): It occurs when the OP-cell is at room temperature or has not enough Rb vapor. The laser beam crosses the OP-cell without a significant interaction with Rb. No light is absorbed and in consequence, no light (or at least not enough light) is re-emitted to analyse the spatial profile of the laser beam.
- Medium absorption or cylindrical profile (Fig. 4.21b and Fig. 4.21c): . This regime is typically observed in the OP-cell in a temperature range from 90 to 150°C. The laser light is absorbed homogenously over the cell
- Complete absorption or conical profile (Fig. 4.21d): This regime of strong absorption happens in the temperature range of 150 - 200°C measured at the top of the OP-cell.

the laser light is effectively absorbed over the total length L of the OP-cell. So almost no light is transmitted through the OP-cell. The spatial profile from the fluorescence light has a conical shape and is concentrated at $z \approx 0$ where almost all incident laser light is absorbed.

Each of the spatial profiles described above corresponds to a well-defined spectral distribution profile collected by the spectrometer. These frequency distributions are shown in Fig. 4.21e.

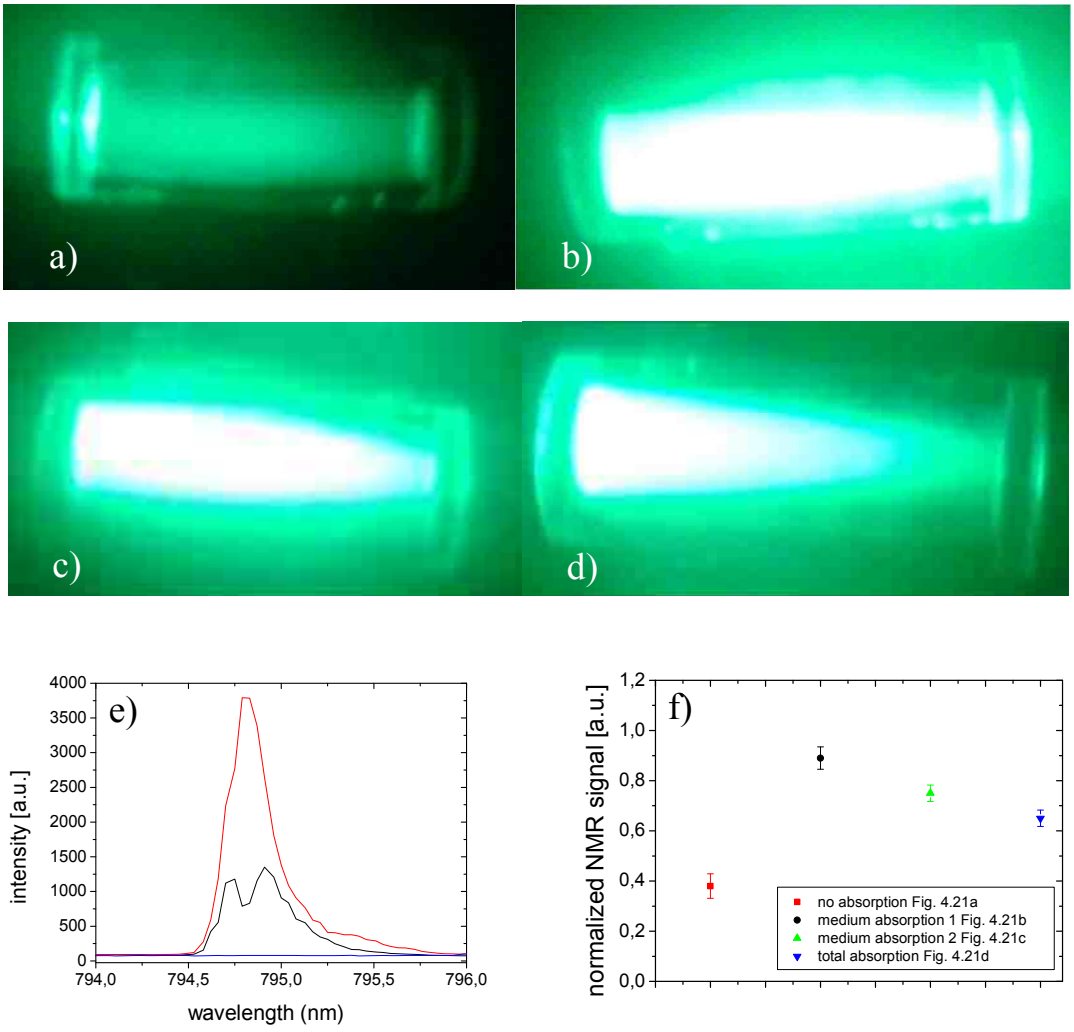

Fig 4.21: Spatial and spectral profiles of the laser beam through the OP- cell obtained with $\vec{B}_0 \neq 0$. a) No absorption regime. b) Cylindrical regime: the absorption of laser light is almost homogeneous throughout the OP-cell volume. c) Transition between cylindrical and conical regime. d) Conical regime: the absorption is essentially concentrated at the entrance of the OP-cell at $z \approx 0$. e) Frequency spectrum of the transmitted laser light: The red curve corresponds to the "no absorption regime", the black curve to the cylindrical regime and the blue curve to the conical regime. f) Normalized NMR signal of HP-Xe for the four different illumination profiles. Each point is calculated as the average of three measurements. The error bars represent the standard deviation of the average.

HP-Xe was produced using each illumination profile in order to check which of the profiles shown above result on the higher polarization. Three samples were produced for each case using a pressure of 6 bar ($\Delta\lambda_{abs}$ = 0.2 nm), flow of 200 ml/min and the standard gas mixture of this work. These polarization conditions were not changed during the experiments. Therefore, it can be assumed that changes in the NMR signal are only attributed to the variation of the illumination conditions. The NMR signal obtained with each sample of HP-Xe was measured by the low field NMR system described in Sec. 3.2 and corrected by the difference of pressure. The result of this measurement is shown in Fig. 4.21f where each point is the average of the measurements normalized to the maximum NMR amplitude obtained after the pressure correction. The maximum NMR signal was obtained with a cylindrical profile or homogeneous illumination of the cell (Fig. 4.21b). The conical profile, however, did not showed such dramatically reduction of the HP-Xe polarization.

The absorption profiles shown of Fig. 4.21 were acquired with the holding magnetic field on, i.e. the quantization axis is well defined. On the contrary, if the holding magnetic field is off, the earth magnetic field acts as a holding field with three spatial components of similar strength. Therefore, the quantization axis is no longer aligned along the OP-cell axis and the spin of the Rb valence electron precesses around this new quantization axis. The transverse component of the magnetic field immediately relaxes the optically polarized Rb according to T_1^{dB} in Eq. [2.43] and only the component along the *z*-axis remains. So, the Rb polarization in equilibrium is significantly reduced and more laser light is absorbed since the level $5S_{-1/2}$ is not completely depopulated. As a consequence, the absorbed light increases by about 50 % as shown in Fig. 4.22a. In this figure, the ratio between the areas under the blue curve (holding field on) and the black curve (holding field off) is about 0.45 stating that the number of absorbed photons with B field off is about the double when compared with B field on. This effect also causes a faster increase of the temperature in the OP-cell as shown in Fig. 4.22b. This temperature increase is due to absorption and subsequent quenching of the excited states of Rb. This effect verifies that the Rb valence electron is being polarized but the T_1 is extremely short due to the poor homogeneity of the earth magnetic field [Kad98]. This effect can be used for heating the OP-cell without using the heating of the oven, e.g. in case of excess of Rb (see Fig. 4.17).

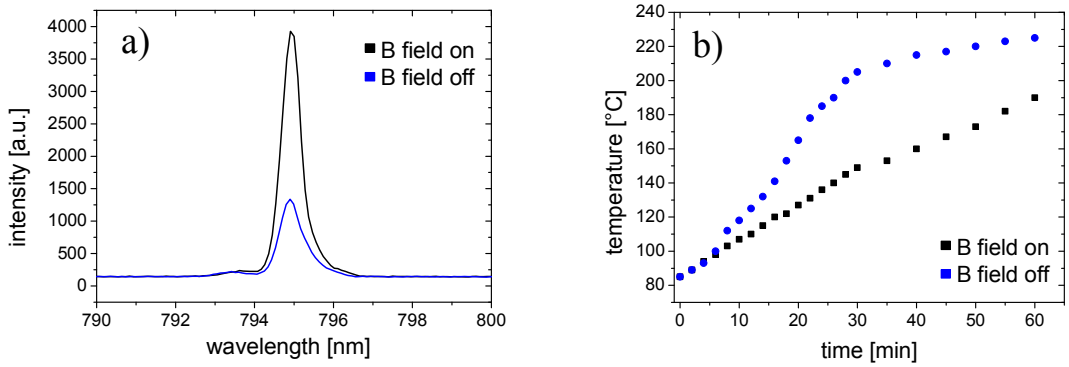

Fig 4.22: a) Absorption profiles at 150°C for $\vec{B}_0$ being switched on (black) and off (blue). The difference in absorption, i.e. the area under both curves, is about 46%. b) Temperature of the OP-cell vs. time.

The graphics in Fig. 4.22 were measured with a total pressure of 6 bar. As explained in Section 2.1.5, the absorbed power depends also on the total pressure due to the broadening of the Rb D1 line as shown in Fig. 4.23a. In this figure, the absorbed power increases with pressure as expected, since the bandwidth of the laser is broader than the Rb D1 line even for the highest pressure. This measurement was performed with a cylindrical illumination profile obtaining a maximum absorbed power of about 20 W for a total gas mixture pressure of 7 bar. During the polarization process, the temperature of the OP-cell remained constant at 150°C, the flow was fixed to 200 ml/min and the FVU settings were identical (see Section 4.2). The gas mixture was prepared with 1% of Xe and the partial pressure of 200 mbar of N_2 remained constant to provide identical quenching conditions.

The NMR signal of the HP-Xe sample prepared with different gas mixture pressures was measured in order to find the pressure which leads to the maximum polarization. The result is shown in Fig. 4.23b where, again, the value results from the average of three measurements and the error bars correspond to the reproducibility of the experiment. This value was about 20 % which include the reproducibility of the NMR signal due to the performance of the Xe-polarizer and the NMR conditions such as position of the cell and environment[26].

The maximum of the NMR signal in Fig. 4.23b is not reached at the pressure which corresponds to the maximum of the absorbed power (7 bar). One possible reason is that the transmitted power does not correspond to the absorption line of Rb since the power meter used cannot differentiate wavelengths and, therefore is not possible to determine the spectrum. The spectrometer could, in principle, provide more information such as intensity and wavelength. However, their readings saturated at powers over 10 W. Another reason could be the increase of the Rb-Xe destruction rate since the partial pressure of Xe increases also with the pressure of the gas mixture.

[26] For example, magnetic parts close to the low field NMR system affect the homogeneity of the system and therefore the T_2^* of the signal. This change in T_2^* affects directly the NMR amplitude through the acquisition delay.

For this comparison, it was assumed that the variations of the NMR signal are entirely attributed to the change in the total pressure of the gas mixture. However, this is not entirely true since the self-diffusion coefficient of Xe in the gas mixture increases slightly with the total pressure of the gas mixture (see Eq. [2.44]). This rise of the diffusion coefficient of Xe could lead to relaxation due to magnetic field gradients, especially in the area were the HP-Xe is frozen. These losses will be studied in Section 4.2.4. Nevertheless, for the purpose of optimization of the production of a sample of pure HP-Xe, the optimal working pressure is found to be 4 bars and this value will be used for the rest of the experiments. At this pressure, the Rb absorption line is centered in 794.8 nm and the broadening of the line is about 0.16 nm.

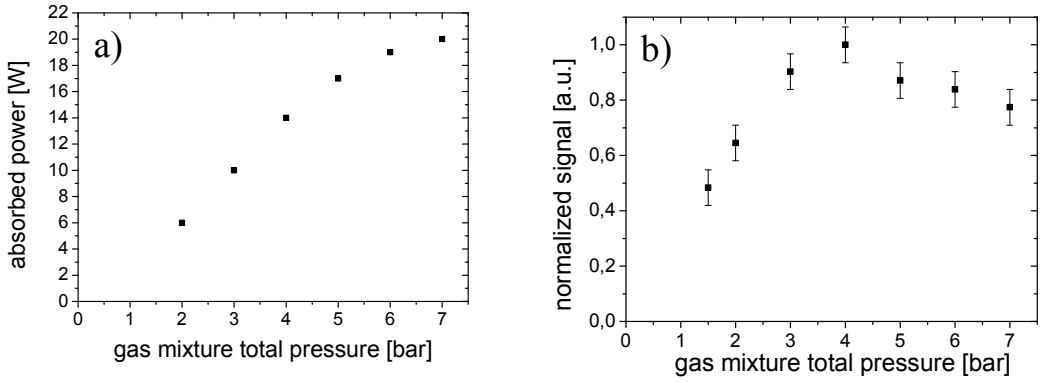

Fig. 4.23: a) Absorbed power vs. the total pressure of the gas mixture. The used gas mixture was composed of 200 mbar of N_2, 1% Xe of the total pressure and the rest He. The error bars are covered by the squares. b) NMR signal of HP-Xe produced with the gas mixtures previously mentioned. For more details, see text.

4.1.8 Polarization losses due to skew light effects and internal reflections

The direction of the polarized light has to be parallel (or antiparallel) to the applied magnetic field to populate the $m_s = 1/2$ (or $m_s = -1/2$) state. If there is an angle θ between the field direction and the *k*-vector of the incident light, the Rb polarization will be reduced by [Cha02B] by a factor *cos*(θ) resulting in:

$$P_{Rb} = \frac{\gamma_{opt}}{\gamma_{opt} + \Gamma_{SD}} \cos(\theta). \qquad [4.3]$$

This effect, however, is small and almost negligible for small divergences of the beam ($\theta < 5^{\circ}$). However, if the circularly polarized laser light is reflected on the walls of the OP-cell, the reflected light does not preserve the correct polarization according to the Fresnel formula [Jen57]. Again, depolarization due to these effects is negligible for small glancing angles as is the case here. More care has to be taken if the OP-cell is considerably longer. For example, in the Xe-polarizer for medical applications described in Appendix 2, this was analyzed in detail since the length of this cell is about 1.2 m. The results of this study can be found on the thesis of [Fuc12] and [Bra13].

4.1.9 Xe polarization

Due to the experimental conditions described above, many corrections to the model discussed on Section 2.1 have to be made for calculating the polarization of Rb and Xe. Many of these factors cannot be easily studied in a systematic way because they interact and depend of each other (see for instance the discussion of Fig. 4.23). The main problem for a realistic modeling is the uncertainty in the temperature of the gas mixture inside of the OP-cell (see Fig. 2.8), which affects dramatically the rest of the parameters. In addition, some other parameters included in the model cannot be directly measured, at least not in this Xe-polarizer, such as the relaxation of HP-Xe due to the interaction with unpolarized Rb or the wall relaxation of the OP-cell[27]. These values are crucial for the calculation of P_{Rb} and P_{Xe} but they can only be estimated.

Under these limitations, the theoretical framework can be used as guide to understand the principles of SEOP but, due to experimental restrictions, cannot be applied as a direct tool for finding the optimal working conditions for obtaining the highest P_{Xe}. Therefore, the optimal working parameters for maximizing the polarization were found by direct experimental evidence varying only one parameter at the time during the polarization procedure.

The polarizing conditions, unless indicated else, were always 4 bar total pressure of the gas mixture made from 1% Xe in natural isotopic abundance, 6% N_2 and 93% He. The flow rate was 200 ml/min and the accumulation times of HP-Xe ice about 7 min. The cryogenic separation was performed under the same conditions which will be described in the next section. The gaseous HP-Xe was filled into a 6 cm diameter storage cell (cell 146) made from GE-180 typically giving pressures of about 250 mbar. At least three samples were measured for each polarization condition. For each sample, the pressure was documented and the NMR signal measured using in all cases a flip angle of $\alpha = (9.84 \pm 0.16)°$. The values obtained were corrected by the pressure and normalized.

Since the optimal pressure was already found in Fig. 4.23, the next parameter to optimize was the amount of Xe in the gas mixture. For this purpose, the gas mixture was prepared with different partial pressures of natural Xe varying from 60 to 450 mbar (1 to 7.5% of the gas mixture) while keeping the N_2 concentration constant (240 mbar). The result of this experiment is shown in Fig. 4.24a where the highest signal is obtained, as expected, for the lowest concentration of Xe.

The same experiment was repeated for studying the dependence of the Xe-polarization on the concentration of N_2 while the percentage of Xe was kept constant. The measurements are shown in Fig. 2.24b. In absence of N_2, the polarization of Xe is zero. For partial pressures from 300 mbar to 0.9 bar, the NMR signals does not seem to be significantly affected. However, for $p_{N2} \geq 1.5$ bar, the NMR signal decreases significantly.

[27] This value can be easily measured with an online NMR system installed in the OP-cell. This system is currently being constructed.

This effect can be explained by Fig. 2.2, where is shown that the relaxation rate of Rb at this p_{N2} is governed by the Rb-Rb relaxation. The relaxation rate of Rb is, in this case, about 10 times higher than for the values previously measured.

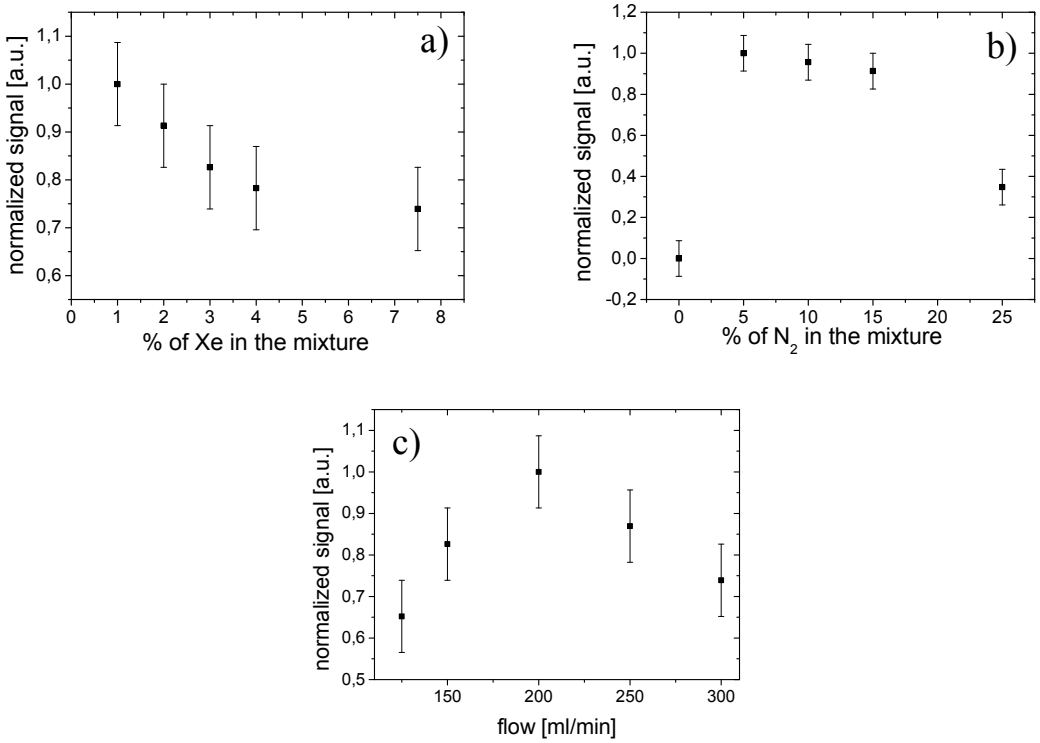

Fig. 4.24: Optimization of the polarization parameters: a) percent of Xe in the gas mixture from 40 to 300 mbar with constant amount of N_2. b) Partial pressure of N_2 (from 0 to 1 bar) mantaining constant the partial pressure of Xe. c) Variation of the flow.

Finally, the flow-rate was varied from 125 to 300 ml/min obtaining the data shown in Fig. 4.24c. In this figure, the maximum value of the NMR signal was obtained using a flow of 200 ml/min. This result is not expected since Eq. 2.33 predicts that longer residence time in the OP-cell would lead to higher Xe polarization in case the equilibrium was not reached. In consequence, the Xe polarization (and the NMR signal) should increase as the flow decreases. In case the equilibrium is reached, the polarization should remain constant. Therefore, the optimum flow at 200 ml/min indicates that some additional relaxation mechanism is present in the system. This relaxation mechanism could be related to the properties of the wall of the OP-cell, depolarization of HP-Xe due to interaction of Rb or with magnetic field gradients. Further alternative equipment has to be developed to identify the origin of this process.

However, the optimal operation conditions of the Xe-polarizer for fundamental physics experiments can be deduced from Fig. 4.24. These conditions are: gas mixture with a total pressure of 4 bar composed by 1% Xe, 200 mbar of N_2 and the rest He. The flow of the mixture should be 200 ml/min and the illumination of the OP-cell has to correspond to the cylindrical profile presented in Fig. 4.21b. These parameters lead to P_{Xe}

= (0.056 ± 0.002) being the maximum value achieved in this work. This value was determined via the absolute measurement of the static magnetic field produced by a HP-Xe sample stored in a spherical cell. This method was developed due to the difficulties inherent to the measurement of P_{Xe} via NMR at low magnetic fields and it will be described in Chapter 6.

4.2 Cryogenic separation of HP-Xe from the gas mixture

Once the gas mixture leaves the OP-cell, the HP-Xe is separated from the buffer gases in the freeze/volatilization unit (FVU). This unit allows the cryogenic separation of the HP-Xe from the other buffer gases (He, N_2) via its accumulation inside a glass cell at 77 K and at high magnetic field (>0.1 T). The FVU consists of three main parts: Halbach magnet, freeze/volatilization structure (FVS) and accumulation cell (AC) as shown in Fig. 4.25a. The process of cryogenic separation is shown in Fig. 4.25b where the accumulation cell is submerged into a Dewar with LN_2 until sufficient HP-Xe is accumulated. Then, the buffer gases are evacuated and the Dewar with LN_2 is pulled down. Consequently, the second Dewar filled with water at approximately 95°C is pulled in as shown in Fig. 4.25c and the HP-Xe ice turns into gas. The parts mentioned above will be described in the next sections.

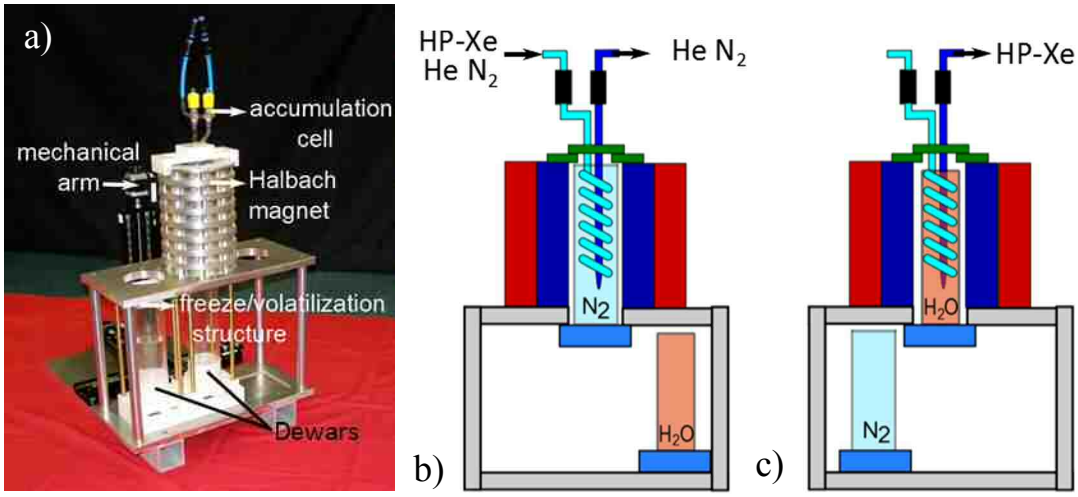

Fig 4.25: Freeze/volatilization unit (FVU). a) This unit is composed by three main parts: Halbach magnet, freeze/volatilization structure and accumulation cell. A computer controlled mechanical arm can be added to lift the dewar with LN_2. b) When the Dewar with LN_2 is pulled upwards, the HP-Xe freezes inside the accumulation cell. c) When sufficient HP-Xe ice was accumulated, the residual buffer gases are evacuated and a Dewar with hot water is lifted up. The fast change of temperature produces a fast volatilization of the HP-Xe ice.

4.2.1 Halbach magnet

A Halbach array is an arrangement of permanent magnets where the magnetic flux density is enhanced on one side of the array and reduced to nearly zero on the other side. This kind of arrays were originally suggested by Klaus Halbach in 1980 who designed several configurations of di- and multipolar arrays like linear, circular, spherical and cylindrical geometry [Hal80]. From all possible geometries of Halbach arrays, the most suited for storage of HP-Xe in solid state is the cylindrical geometry of a dipolar magnet arrangement. This geometry can easily achieve fields inside the Halbach on the order of 0.1 to 0.5 T with a stray field on the order of a few Gauss. In addition, Halbach magnets are stable, robust, economic to construct and easy to transport.

The design and construction of the cylindrical Halbach magnet used in this polarizer was performed by Dr. P. Blümler [Sol04]. This magnet is composed of square FeNbB magnets mounted in aluminum rings with milled sockets for placing the magnets in a fixed position (See Fig 4.26a). The magnets, sixteen in each ring, are glued in the sockets and the rings are stacked with help of brass threads to form the Halbach array.

This Halbach magnet has an outer diameter of 15.5 cm, an inner diameter of 7.3 cm and a height of 34 cm. The weight is around 15 kg and provides a holding magnetic field in the central area of about 0.3 T. The magnetic field inside of this magnet has its main component over the *z*-axis. When the HP-Xe gas enters this magnet, its magnetization will be aligned to this direction as is shown in Fig. 4.26b. The homogeneity of this magnet was measured in a volume of 5 x 5 x 5 mm^3 in the center obtaining $H \approx 4 \cdot 10^{-4}$ cm^{-1} and over the central plane, in a radius of 20 mm giving about 10^{-2} cm^{-1} [Rai04]. The area with the most homogeneous magnetic field is at the middle of the magnet (17 cm of the bottom part) and around the symmetry axis. This value increases rapidly, specially out of the symmetry axis at the top (and bottom) of the magnet (see Fig. 4.28).

In [Rai04], only the central part of this Halbach magnet was characterized. However, the gas mixture has to flow on top and inside of the magnet to reach the part with lower gradients as shown in Fig. 4.29b. The magnetic field of the Halbach has to be known in order to find a path for the HP-Xe in gas phase which minimizes possible polarization losses due to diffusion in magnetic field gradients. In this way, the geometry and position of the accumulation cell can be chosen to match the area where these polarization losses are minimal.

The magnetic field of the Halbach magnet was measured using a Hall probe (Lakeshore, USA) mounted in a 3D table controlled by Lab-View. The scanning range of the 3D-table is 20 cm in the three directions with an error of 0.1 mm. Only the *z*-component of the magnetic field was measured (see Fig. 4.26) because it is three orders of magnitude stronger than the other components. Therefore, a slight misalignment can generate large systematic errors if the perpendicular components are measured.

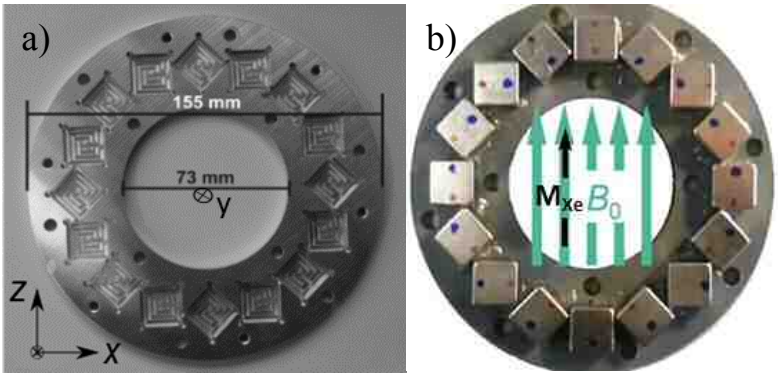

Fig. 4.26: Halbach magnet [Rai04]. a) Aluminuim ring with the shape of the magnets miled. The origin is placed in the center of the magnet being the *y*-axis the coordinate is along the simmetry axis. b) The magnetic field inside of the Halbach array is mainly in the *z* direction. The black arrow indicates the direction of the magnetization of HP-Xe (M_{Xe}).

The magnetic field of the Halbach magnet on the *z*-direction was measured along the symmetry axis (*y*) for positions on top (*y* = -100 mm) and inside (*y* =100 mm) being *y* = 0 the position of the top cover plate of the magnet. The scanning range of the 3D-table was limited to 10 cm inside of the magnet because this area contains the higher magnetic field gradients (together to the same area on the bottom of the magnet). The magnetic field in the center of the magnet (*y* = 170) was measured already in [Rai04] obtaining $H \approx 10^{-4}$ cm^{-1} and, due to its design, the magnetic field of the magnet is symmetric respect to the center.

The coordinates (*x*, *z*) are defined on the transverse plane of the magnet. For a fixed *y*-value, the magnetic field was measured along 34 mm in *x*-direction (-17 < *x* < 17 mm) and 40 mm in *z*-direction (-22 < *z* < 18 mm). This range was chosen because it matches the size of the helical accumulation cell described in the next section of this chapter.

The distance between points (steps) were chosen in order to find a variation of the magnetic field which can be distinguished by the Hall probe. Finally, the magnetic field values were acquired at the next (*x*, *z*) coordinates: (17, 0), (10, 0), (-10, 0) and (-17, 0) and (0, -22), (0, -10), (0, 0), (0, 10) and (0, 18) for a fix value of *y*. The measurements corresponding to the position (*x*, *z*) = (0, 0) over the *y*-axis are shown in Fig. 4.27,. The rest of the measurements of magnetic field vs. distance (in *y*-direction) will not be shown because they are identical to this figure.

According with the figure 4.27, the magnetic field at the entrance of the Halbach 0.1 T at *y* = 0 and increases to 0.3 T as shown in [Rai04]. These magnetic fields fulfill the requirements of the cryogenic separation described in Section 2.2.2.

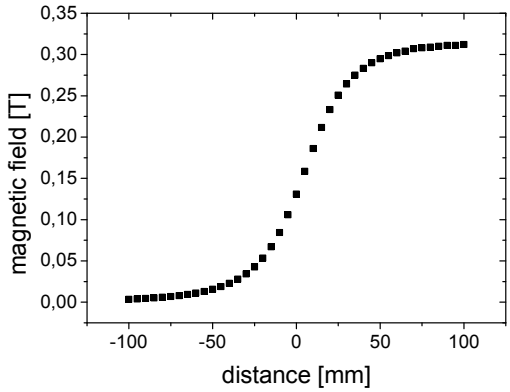

Fig. 4.27: Magnetic field of the Halbach magnet measured from 10 cm over the top plate (y = -100) to 10 cm inside of the magnet (y = 100).

The values of the magnetic field were used to calculate the relative field gradients which are defined as:

$$\nabla B^z_{x_{ij}y_k} / \overline{B}^z_{x_{ij}y_k} = [(B^z_{(x_i,y_k,0)} - B^z_{(x_j,y_k,0)}) / (x_i - x_j)] / [(B^z_{(x_i,y_k,0)} + B^z_{(x_j,y_k,0)}) / 2] \quad [4.4]$$

$$\nabla B^z_{z_{ij}y_k} / \overline{B}^z_{z_{ij}y_k} = [(B^z_{(0,y_k,z_i)} - B^z_{(0,y_k,z_j)}) / (z_i - z_j)] / [(B^z_{(0,y_k,z_i)} + B^z_{(0,y_k,z_j)}) / 2] \quad [4.5]$$

$$\nabla B^z_{x_i y_{kl} z_j} / \overline{B}^z_{x_i y_{kl} z_j} = [(B^z_{(x_i,y_k,z_j)} - B^z_{(x_i,y_l,z_j)}) / (y_i - y_l)] / [(B^z_{(x_i,y_k,z_j)} + B^z_{(x_i,y_l,z_j)}) / 2] \quad [4.6]$$

where $B^z_{(x_i,y_i,z_i)}$ is the z-component of the magnetic field measured at (x_i, y_i, z_i). The results are shown in Fig. 4.28 where the maximum local relative field gradient is around 0.5 cm^{-1}.

From the results of Fig. 4.28, it is concluded that the relative gradients increase with the distance to the symmetry axis (0, 0) (black and blue curves). Therefore, to avoid polarization losses related to these gradients, the HP gas has to be transported and trapped on the symmetry axis of the Halbach within the radial distance of ~ 10 mm. The potential polarization losses due to the gradients will be discussed in detail in Sec. 4.2.4.

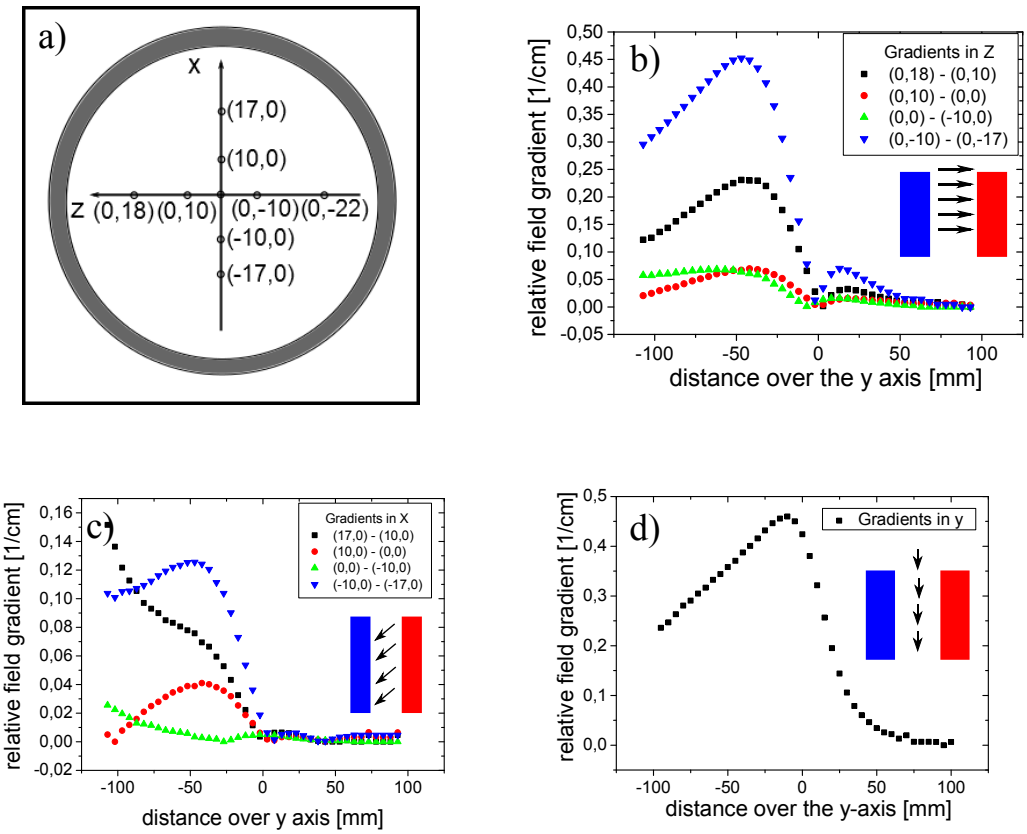

Fig. 4.28: Local field gradient over the *y*-axis according to the definitions of Eq. [4.4], [4.5] and [4.6]. The figure inset represent an axial cut of the Halbach magnet and the black arrows correspond to the direction where the gradient was calculated. a) Sketch of the transverse plane of the Halbach magnet indicating the measuring points (not to scale). b) Gradients in *x*-direction defined by Eq. [4.4]. c) Gradients in *z*-direction according to Eq. [4.5]. d) Gradients in *y*-direction.

4.2.2 Freeze/volatilization structure

The FVS is a non-magnetic mechanical construction which supports the Halbach magnet and contains two Dewars (ThermoFlasks, Germany), one filled with liquid N_2 and other with hot water. These Dewars can be moved horizontally along a rail system and can be moved up and down (see Fig. 4.29a). This movement allows a fast, simple and reproducible change of the Dewars for accumulation and, later, for volatilization of the HP-Xe ice. The Dewar with LN_2 is pulled upwards for freeze out the HP-Xe of the gas mixture. Once enough HP-Xe ice has been accumulated, the flow stops and the rest of the buffer gases are pumped out while the HP-Xe ice remains in the accumulation cell. Then, the Dewar with LN_2 is replaced by the Dewar with water at approximately 95°C and the HP-Xe ice is volatilized. The volatilization process takes around 5 (see Fig 4.39b and 4.39c).

Additionally, the Dewar with LN_2 can be lifted up by means of a computer controlled mechanical level arm in order to submerge the accumulation cell step by step

into the LN_2 bath. These steps can be fixed to a constant increase of some millimeters which contributes to produce a thin layer of Xe ice with almost the same thickness along the whole effective length of the accumulation cell. At the end of the process, this cell is finally completely submerged in the LN_2 bath. However, the mechanical arm was not used in this work. Instead, this procedure was done manually by using a Styrofoam spacer underneath the LN_2 Dewar.

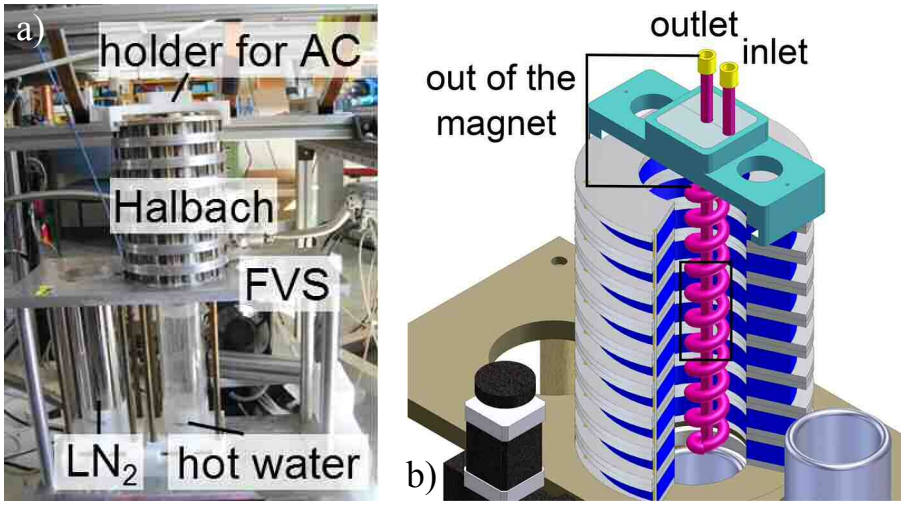

Fig. 4.29: Freeze/volatilization structure (FVS). a) Picture of the FVS with the Halbach magnet mounted. This structure allows to place a Dewar with LN_2 and a Dewar with hot water which could be inserted inside of the core of the Halbach magnet. b) Draw of the accumulation cell mounted in the Halbach magnet. A part of the accumulation cell is outside of the magnet. The area with the smaller magnetic field gradients is shown in a black square in the center of the magnet. Image courtesy of C. Bauer (MPIP).

4.2.3 Accumulation cells

The accumulation cell (AC) is a glass vessel where the HP-Xe gas is frozen out in order to separate it from the buffer gases. During the accumulation of solid HP-Xe, a layer of HP-Xe ice grows over the internal surface of the AC acting as a thermal isolation between the glass and the incoming gas mixture. This layer is simultaneously in contact with the glass at 77 K and with the entering gas mixture at about 293 K.

The maximum accumulation times of HP-Xe are typically about 30 min. During this period, it has to be ensured that no polarization is lost due to the cryogenic separation. As was shown on Fig. 2.16, the relaxation time of HP-Xe in solid phase is about 2.5 h at 77 K while is less than 10 s for temperatures over 160 K. Namely for fields of 0.3 T, the polarization losses of HP-Xe in the solid phase are related mostly with the temperature. Therefore, an efficient accumulation requires that the Xe-ice remains at temperatures close to 77 K which can be achieved only with a good thermal contact between the gas mixture and LN_2. Therefore, the accumulation cell requires a large surface-to-volume ratio in order to maximize the contact area to the surrounding cold/hot temperature bath. In addition, the

geometry of the cell must be compatible with the areas of good homogeneity of the Halbach magnet. This is required to avoid relaxation due to magnetic field gradients (see Eq. 2.43) since the HP-Xe enters the accumulation cell in the gas phase.

Three designs of accumulation cells with different geometries were tested in this work in order to find the geometry which leads to the best performance. All these accumulation cells were built with the same glass type (Duran) and using the same glass stopcocks with rubber O-rings (Hi-Vac, USA) so the difference in the performance can be only attributed to their geometry. The dimensions of these cells are listed in Table 4.3.

The first one used, AC 1, was a cylindrical accumulation cell ("cold finger") designed by Appelt [App04]. This cell is shown in Fig. 4.30a where is indicated how the gas mixture flows into a tube inside a glass jacket without being in direct contact with LN_2. The HP-Xe ice accumulates on the appendix after leaving the internal tube as shown in Fig. 4.30b while the buffer gases flow to the outlet of the accumulation cell. The accumulation volume is determined by the size of the glass appendix attached to the jacket. The distance between the inner tube and the jacket at the bottom part is about 1 cm so some of the HP-Xe ice can possibly accumulate on the walls, but this is not the case of the experiments shown in this work.

The advantage of this geometry is the minimization of gradients over the gas path because the gas flows straight on the *y*-axis of the Halbach magnet. The disadvantage is that the HP-Xe freezes out like a big drop impeding the direct contact of the gas mixture with the glass at 77 K and, for long polarization times, the Xe ice may even block the gas input eventually stoping the flow.

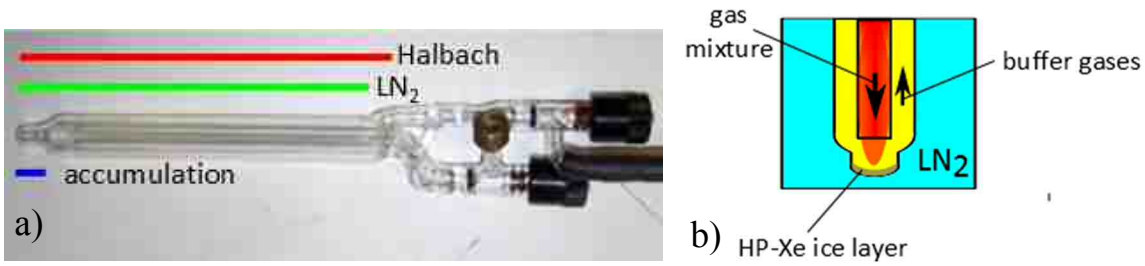

Fig. 4.30: Cylindrical accumulation cell. a) Picture of AC1. The red line indicates the part the cell inside the Halbach. The green line indicates the part of the cell submerged in LN_2 and the blue line indicates the part of the cell available for accumulation. b) Sketch of the accumulation area. The gas mixture flows through the inner tube and the HP-Xe freezes on the bottom part of the appendix. The buffer gases (He and N_2) flow to the outlet of the cell.

The second design is a slight modification of AC 1 replacing the appendix by a glass sphere (see Fig. 4.31a). In this cell, the gas mixture (HP-Xe, He and N_2) enter the accumulation cell and flow through a tube which is, again, inside of a glass jacket and not in direct contact with LN_2. The HP-Xe ice solidifies at the bottom part of the spherical

glass cell (see Fig. 4.31b). The level of LN_2 should cover 1/3 of the radius of the sphere determining the accumulation area. This design was introduced by Killian [Kil01] and it has several advantages like a large accumulation surface and the spherical part of the cell can be produced with low permeability glass like GE-180 which shows a low wall relaxation rate (see Chapter 6). The main disadvantage of this geometry is related to the gradients of the Halbach magnet which may affect the reproducibility of the Xe polarization after the freeze and volatilization process. In addition, the level of LN_2 must be maintained constant which represents a large difficulty since the spherical part is placed at the center of the Halbach magnet.

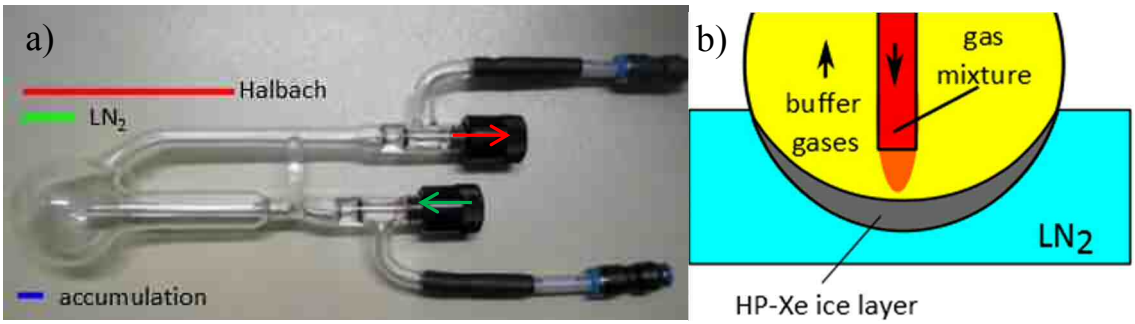

Fig. 4.31: Spherical accumulation cell. a) Picture. The red line indicates the part the cell inside the Halbach. The green line indicates the part of the cell submerged in LN_2 and the blue line indicates the part of the cell available for accumulation. b) Sketch of the accumulation area. The gas mixture flows through the inner tube and the HP-Xe freezes on the bottom part of the sphere. The buffer gases (He and N_2) flow to the outlet of the cell.

The third design is a helical shaped glass cell which was introduced by Hersman [Rus05] (see Fig. 4.32). The inlet is connected to a glass spiral of 16 turns, glass tube of an internal diameter of 5 mm. The loop has a diameter of 2.8 cm. At the end of the spiral, the glass tube is bent upwards again along the axis of the spiral towards the cell output. This cell is progressively submerged into LN_2 in order to control the thickness of the layer of HP-Xe ice. In this accumulation cell, the frozen HP-Xe does not form a homogeneous layer over the cross section of the glass tube but accumulates only the bottom part covering 1/3 of the cross section.

Using the values of Table 4.3, the thickness of the HP-Xe ice layer vs. the accumulation time was calculated for the accumulation cells of Fig. 4.30, 4.31 and 4.32. This value was calculated assuming a homogeneous distribution of the ice over the accumulation area, a flow of 4 ml/min at 4 bar and using the density of Xe in solid state 3.7 g/cm^3 (at 80 K) [Sea62]. The results of this calculation are shown in Fig. 4.33a. In this figure, the cylindrical accumulation cell (Fig. 2.32) resulted on the highest thickness of the HP-Xe ice-layer by far being more than six times higher than in the other accumulation cells. The smallest thickness resulted from the helical accumulation cell which seems to be

the best choice for the accumulation of HP-Xe.

Table 4.3: Characteristics of the cylindrical, spherical and helical accumulation cells tested in this work. The glass thickness of all the cells was 1 mm.

		AC1	AC2	AC3
length [cm]	total	26	23	32
	inside Halbach (red)	16	11	22
	in LN_2 (green)	16	3	22
	available for accumulation (blue)	2	3	22
radius [cm]	total	2	5	outer 3.2
	available for accumulation (blue)	1	5	0.8 (18 turns)
s/v[cm^{-1}]		5	3	21

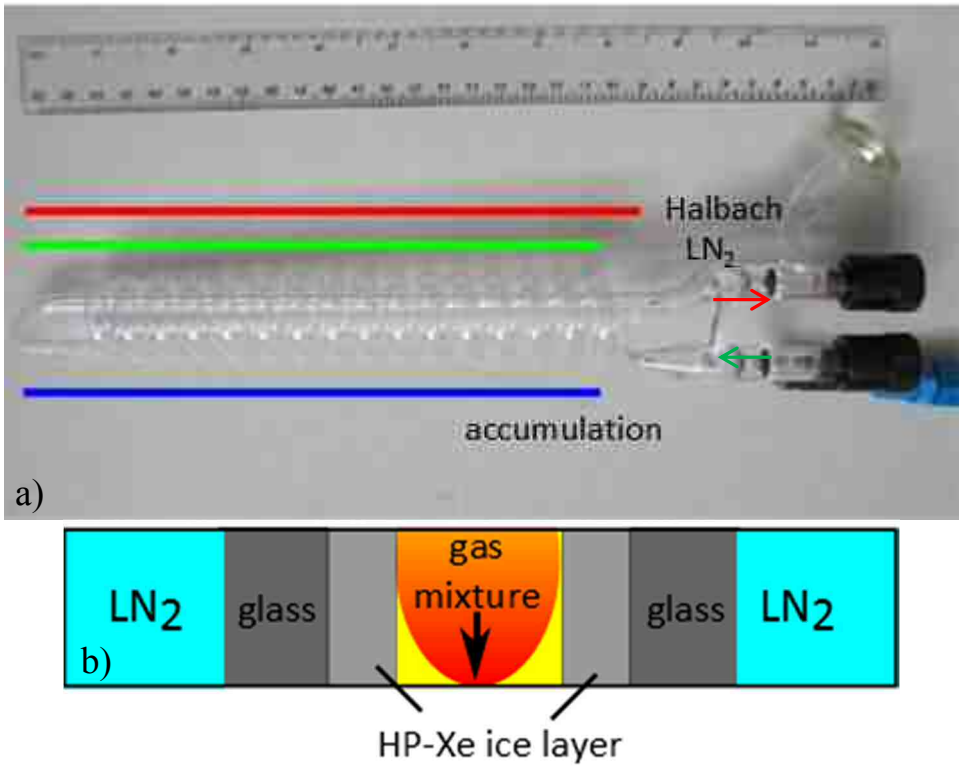

Fig. 4.32: Cylindrical accumulation cell. a) Picture. The red line indicates the part the cell inside the Halbach. The green line indicates the part of the cell submerged in LN_2 and the blue line indicates the part of the cell available for accumulation. b) Sketch of the accumulation area. The gas mixture flows through the inner tube and the HP-Xe freezes on the walls of the spiral. The buffer gases (He and N_2) flow to the outlet of the cell.

This result was confirmed by using the three accumulation cells for cryogenic separation of HP-Xe. This experiment was performed using the same polarization conditions (4 bar, 150°C, 200 ml/min, 1% Xe, accumulation time of 10 min). At least five samples for each accumulation cell were produced. The measured NMR signals of HP-Xe

in gas phase were normalized the gas pressure and to the maximum NMR signal. The results of this experiment are shown in Fig 4.33b where the error bars correspond to the standard deviation of the five measurements done for each cell. The cylindrical accumulation cell showed, as expected, the highest polarization losses. The results obtained with the spherical accumulation cell showed a poor reproducibility mainly because it was difficult to maintain a constant level of LN_2 over the accumulation time. Finally, the helical accumulation cell showed the best performance and reproducibility and therefore, it will be used for rest of the experiments.

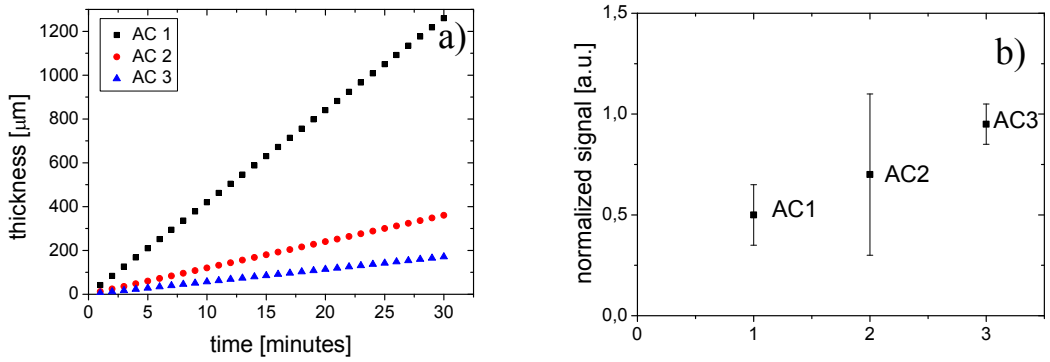

Fig 4.33: Accumulation cells performance. Each point is calculated with the average of five measurements normalized by the pressure and the error bars correspond to the standard deviation.

In the AC3, the level of LN_2 determines the area for accumulation of the HP-Xe ice. If the cell is completely submerged at once and this level of LN_2 remains constant during the accumulation time, the HP-Xe will solidify around the LN_2 level resulting on a thick layer of ice. However, a thin HP-Xe ice is produced if the level of LN_2 increases gradually over the accumulation time. In consequence, the polarization losses due to temperature gradients are reduced. The influence of the thickness of the HP-Xe ice inside the AC3 was studied by varying the number of steps until the cell was completely submerged in LN_2 using a constant accumulation time of 12 min. For example, in 1 step the Dewar was pulled up to full height covering the accumulation cell. Two steps correspond to the situation where the Dewar was first pulled up to half height and then to full height covering then completely the accumulation cell and so forth. The result of this experiment is shown in Fig. 4.34a where the NMR signals are normalized to the pressure and the maximum of the NMR signal. The error bars indicate the reproducibility of the measurements taking also into account the signal fluctuations at the actual position of the AC3 inside the low field NMR spectrometer.

Finally, the accumulation time was varied from 5 to 25 min using 4 accumulation steps. The results are shown in Fig 4.34b.

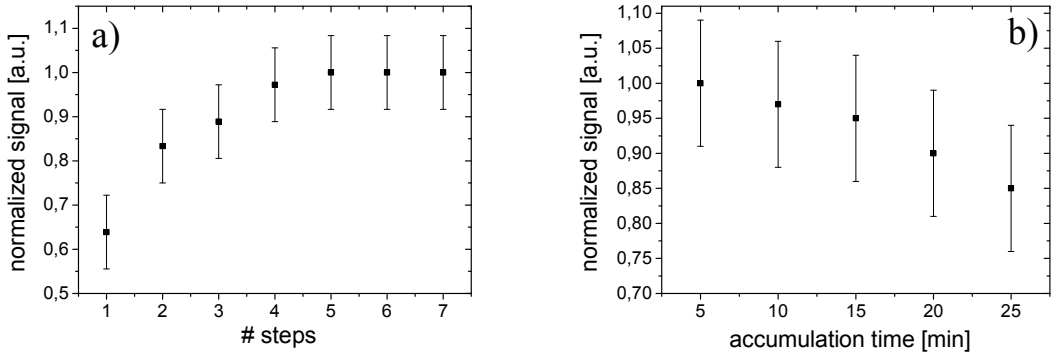

Fig. 4.34: a) Normalized NMR signal vs. the number of steps during accumulation of HP-Xe ice. b) Normalized NMR signal vs. accumulation time using 4 accumulation steps.

From the Fig. 4.34a is deduced that for accumulation times of 12 min, 4 accumulation steps are sufficient to avoid the polarization losses due to the thermal gradients over the HP-Xe ice. However, losses of about 15% are expected is the accumulation time is over 25 min.

4.2.4 Losses during cryogenic separation

As was described before, the SEOP process occurs at magnetic fields of about 2 mT (20 G) while the cryogenic separation of HP-Xe requires fields over 0.1 T (see Fig. 2.16a). In this Xe-polarizer, the Halbach magnet is included on the structure of the coil system. This field configuration is a new design which reduces the size of the polarizer. As was shown in section 4.2.1, the Halbach magnet has strong field gradients out of the symmetry axis in the upper region. Therefore, the position of the Halbach magnet in the assembly of the polarizer was chosen to overlap its magnetic field with that of the coil system.

The Halbach magnet was placed in a position which did not perturb the homogeneity of the air coil system but still close enough to reach a sufficient field to avoid zero field crossings. Furthermore, the transition area from low to high field is indicated in Fig. 4.35a and it was chosen by minimizing the magnetic field gradients in this region. Particularly, this area has a size of 5 x 5 x 24 cm placed on top of the Halbach magnet over the area shown in Fig. 4.35b. This area is trespassed by the HP-Xe in the gas mixture before it is cryogenically separated and after, by pure HP-Xe when volatilized.

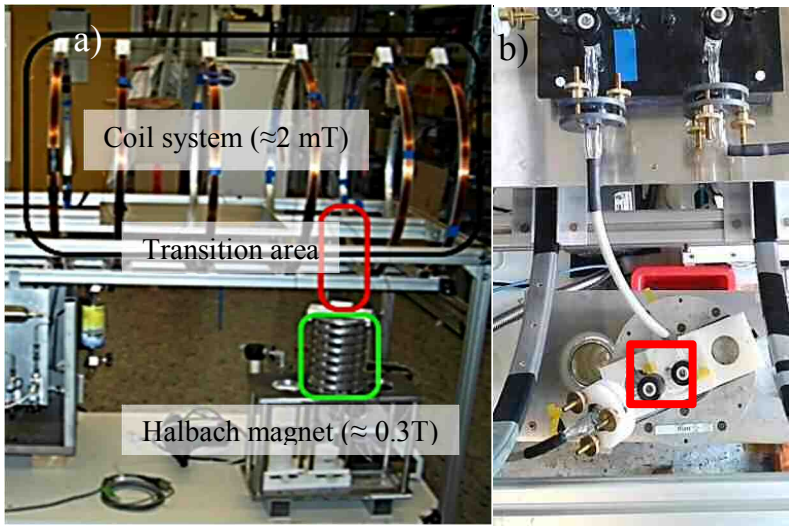

Fig. 4.35: a) Magnetic field in the three areas of the Xe-polarizer. Coil system ($B_0 \approx 2$ mT), transition area and Halbach magnet (0.3 mT). b) Top view of the Halbach magnet installed in the Xe-polarizer structure. The transition area marked in red.

The magnetic field of the transition area was measured in order to avoid polarization losses due to diffusion in gradients of HP-Xe. This measurement was performed in the same way that the characterization of the Halbach magnet using Hall probe mounted on a 3D-table. The magnetic field was measured along the path used by the HP-Xe in gas phase while flowing into the accumulation cell. The result of this measurement confirmed that the dominant magnetic field gradients are produced by the Halbach magnet. These values were already measured in Fig. 4.28 where the highest gradient outside of the Halbach magnet was about 0.5 cm^{-1}. Using this value, the relaxation time due to this magnetic field gradient was calculated through Eq. [2.45] resulted in approximately 7 s. This calculation was done using with D_{Xe}= 0.61 cm^2/s which corresponds to the gas mixture obtained from the optimization. The volume of gas in the transition part is about 8.5 cm^3, therefore the gas mixture requires 2.5 s to flow through, so no dramatic polarization losses are expected because of HP-Xe flowing through the transition area.

Actually, this estimation is made taking the worst-case scenario because only half of the volume is placed on the area with the high magnetic field gradients and the diffusive component of the gas mixture dynamics is negligible in comparison with the flow for tube diameters of 6 mm (surface 0.28 cm^2)[28]. In addition, the characteristic Larmor time ($1/\omega_L$) for fields from 1 mT to 0.1 T is, at least, four orders of magnitude shorter than the diffusion time. So, the gas mixture can be considered as "static" in terms of the characteristics times of the spin precession frequency. Considering this, the behavior shown in the graphic "NMR signal vs. flow" of Fig. 4.24c cannot be clarified. In this graphic, a difference of about 20% was observed between the NMR signals for HP-Xe

[28] By the time the gas mixture diffused to the walls of the tubing, it also moved 5 cm from the original position.

produced with 150 and 200 ml/min. For both flows, the movement of the molecules due to diffusion is negligible compared with the displacement related to the flow.

The assumptions described above can be applied for the estimation of the polarization losses during the volatilization of HP-Xe ice since the measurement cell reaches the equilibrium pressure is 5 s according to Fig. 4.39b (flow higher than 2500 ml/min). However, long residence times of HP-Xe gas in the transition area must be avoided during the operation of the Xe-polarizer. For example, by filling the volatilized HP-Xe into the measurement cell without intermediate steps ("bridge valve" open in Fig. 4.38).

The gradients here discussed were calculated only along the direction of the holding field and the transverse components (x,y) could not be determined without huge systematic errors. Therefore, the possible polarization losses of HP-Xe were investigated using a sample of HP-Xe in the gas phase and observing the decay of its magnetization due to crossing repeatedly the transition area. For this purpose, the AC3 with HP-Xe was transported from the low field NMR system to the Halbach magnet (without LN_2) stayed inside for about 15 s and then back to the low field NMR system. This transport was performed following the field lines adiabatically from the magnetic field of the polarizer to the magnetic field inside the NMR system. Once inside this system, an FID signal was recorded and the NMR amplitude calculated. Then, the AC with the HP-Xe gas was placed again inside of the Halbach magnet following the same path used before. This procedure was repeated until no signal could be observed anymore. Prior to that, it was checked that no measurable polarization losses occurred during the transport of the AC filled with HP-Xe from the homogeneous Xe-polarizer field to the to the low field NMR system without going through the transition area.

This experiment was performed with pure HP-Xe at different pressures of 120, 196, and 600 mbar which diffusion coefficients are 0.48, 0.30 and 0.097 cm^2/s respectively. These pressures were chosen because are the typical values used the experiments of this work. The results are shown in Fig. 4.36a where the NMR signals were normalized to first FID signal of each sample. The polarization losses during transport through the transition region increase when decreasing Xe pressure which can be explained by the increase of the diffusion coefficient.

This experiment was repeated with a sample filled with 300 mbar of HP-Xe (D_{Xe} = 0.19 cm^2/s) but with different residence times inside the Halbach magnet (Fig. 4.36b). In this case, the NMR signal decreases with the duration of the gaseous Xe spin sample inside the Halbach magnet. The error bars correspond to the reproducibility of each individual measurement that includes the possible changes of the actual transfer paths for each cycle and the positioning of the sample in the low field NMR system. In both cases shown in Fig. 4.36, the graphs provide a qualitative picture and show a clear trend of the signal decay. The measurements for 120 mbar HP-Xe are closest case to the gas mixture coming

from the OP-cell (D_{Xe}=0.67 cm^2/s), so the polarization losses are expected to be around 15 % and no losses are expected for pressures around 600 mbar. Since the sample passed the transition area twice, half of the losses represented by the NMR signals in Fig. 4.36a were considered for this estimation.

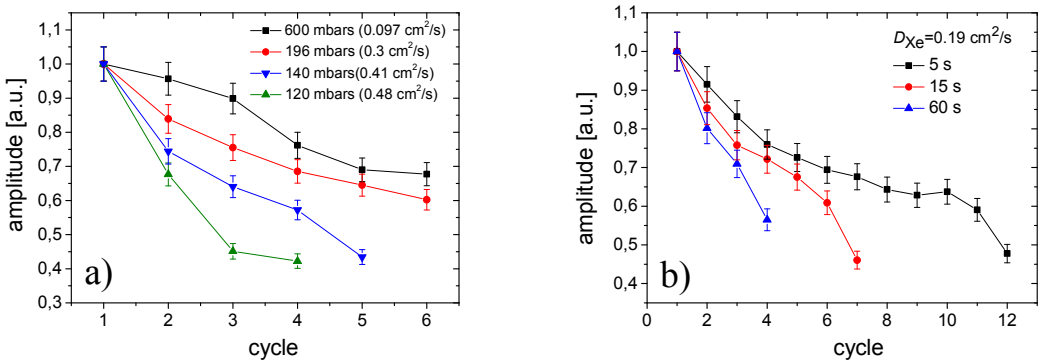

Fig. 4.36: Normalized NMR amplitude vs. number of transport cycles. The diffusion coefficient of Xe is specified for each pressure. a) AC3 filled with different HP-Xe gas pressures. b) AC3 filled with 300 mbar of HP-Xe gas for different residence times in the Halbach magnet.

This experiment was repeated placing the helical accumulation cell inside the Dewar with LN_2 during one minute, heated up again turning the HP-Xe into the gas phase back. The signal coming from HP-Xe gas in the helical accumulation cell was measured in the low field NMR system. The results of this measurement for different total pressures of HP-Xe are shown in Fig. 4.37.

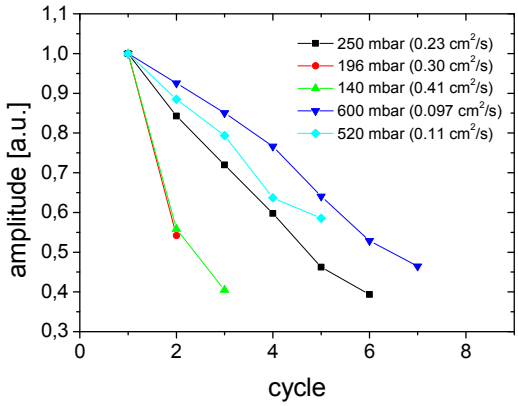

Fig 4.37: Polarization losses due to freezing and sublimating HP-Xe at pressures from 140 to 600 mbar. The diffusion coefficient for each pressure is specified.

As expected, the polarization losses due to volatilization are strongly pressure dependent due to the magnetic field gradients of the Halbach magnet. For total pressures over 500 mbar, the losses are negligible while for pressures below 200 mbar the losses are about 25 %. These losses are attributed not only to the gradients of the Halbach but to the dependence of the wall relaxation time on temperature since the residence time of the HP

gas on the surface increases as the temperature decreases [Ang08]. In addition, the diffusion coefficient is also temperature dependent resulting at 170 K approximately twice of the value at room temperature (see Eq. [2.44]).

So far, no dramatic polarization losses due to diffusion of HP gas on magnetic field gradients were observed if the residence time of the gas in the transition area is minimized. Particularly, the gradients in the transition area cannot explain the behavior of Fig. 4.23b (NMR signal vs. pressure) where a difference of about 20 % was observed when the NMR signal of HP-Xe produced with a gas mixture 4 and 7 bar are compared. This difference cannot be so far explained with the results of Fig. 4.36 since the diffusion coefficients differ only in less than 5%.

The losses due to cryogenic separation will be studied in Chapter 6 via measurement of the absolute polarization of HP-Xe. The losses due to this process were calculated to be around 10% which are in agreement with the estimations done in this part subchapter.

4.3 Storage stage

The accumulation cells have low T_1^{wall} values because of the high surface-to-volume ratio. Particularly, the helical accumulation cell of Fig. 4.34 has a $T_1 \approx 20$ min. For this reason, the volatilized HP-Xe must be filled up into a suitable storage vessel which can provide long T_1 times in terms of Eq. [2.47]. Foremost, some experiments also require admixing buffer gas either for extending the T_1 of HP-Xe or to regulate the total gas pressure in the final sample. For this purpose, the Xe-polarizer here presented includes a a gas manipulation system (GMS) which can bridge the flow circuit of the Xe-polarizer with a filling system. To get a better idea of how this principle works, Fig 4.38a shows the sketch of the GMS and Fig. 4.38b shows a photograph.

Before the HP-Xe in solid phase is volatilized, the outlet valve of the AC3 and the bridge valve are opened and the HP-Xe gas flows directly to the measurement or storage cell. This procedure minimizes the polarization losses by reducing the residence time of the HP gas in the area of high magnetic field gradients.

In addition, controlled amounts of buffer gases can be added through an extra connection using a non-magnetic check valve. The purpose of this valve is to allow the buffer gas to flow into the measurement cell while the partial pressure of HP-Xe remains constant during this filling procedure. The pressure in the measurement/storage cell is measured with a non-magnetic ceramic pressure sensor (ED71FAA, Bourdon Haenni) with a range of 0.01 to 2 bar and an accuracy 1%. The pressure sensor is mounted in a sort of glass “cup” and glued with epoxy (Loctite Hysol 1C) as shown in Fig. 4.39a. The output of the pressure sensor is read with a multimeter (Voltcraft VC 920) with a range 400 mV to 1000 V. The error of the multimeter is given by (0.001+ 0.025%) for voltages below 4 V and (0.01+0.0025%) for voltages over 4 V. The voltage of transition (4 V) corresponds

to a pressure of approximately 1.2 bar.

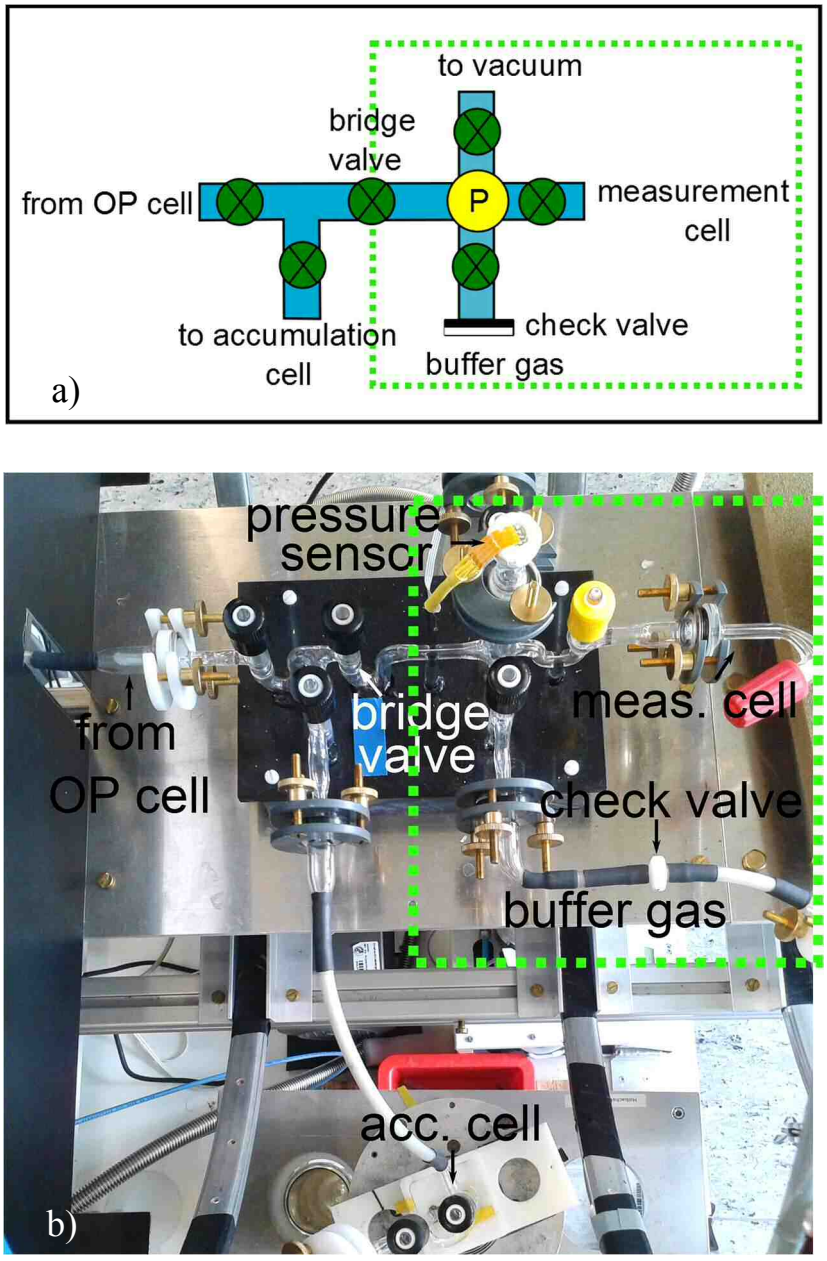

Fig 4.38: Gas manipulation system (GMS) and filling system (green dotted line). a) Sketch of the GMS. b) Photograph of the GMS and filling system with all the connecting lines. During the polarization procedure the "bridge" valve remains closed than the gas mixture flows directly from the OP-cell to the accumulation cell. Once enough HP-Xe is accumulated, the valve to the OP-cell is closed and the residual buffer gases are pumped out. Then, the bridge valve is opened and the HP-Xe ice is volatilized. In this way, the HP-Xe gas fills the measurement cell (not shown in the photograph) minimizing the residence time in the transition area. If additional gases are needed, they can be added through the line with the check valve.

This pressure sensor connected to an oscilloscope allowed the measurement of the time required to freeze and to volatilize the HP-Xe stored in the AC3. These values are

useful to estimate polarization losses due to the magnetic field gradients. For this experiment, about 330 mbar of Xe were filled in the AC3, then the AC3 was closed and the volume between the AC3 and the pressure sensor was evacuated. The Dewar with LN_2 was pulled up, after 30 s, the AC was opened and immersed in hot water. As a consequence, the pressure increased over time as shown in Fig. 4.39b. The asymptotical value is lower than the original pressure because of the dead volume of the filling station. Once the equilibrium pressure was reached, the Dewar with LN_2 was pulled up freezing the Xe inside the AC. The pressure during freezing is shown in Fig. 4.39c.

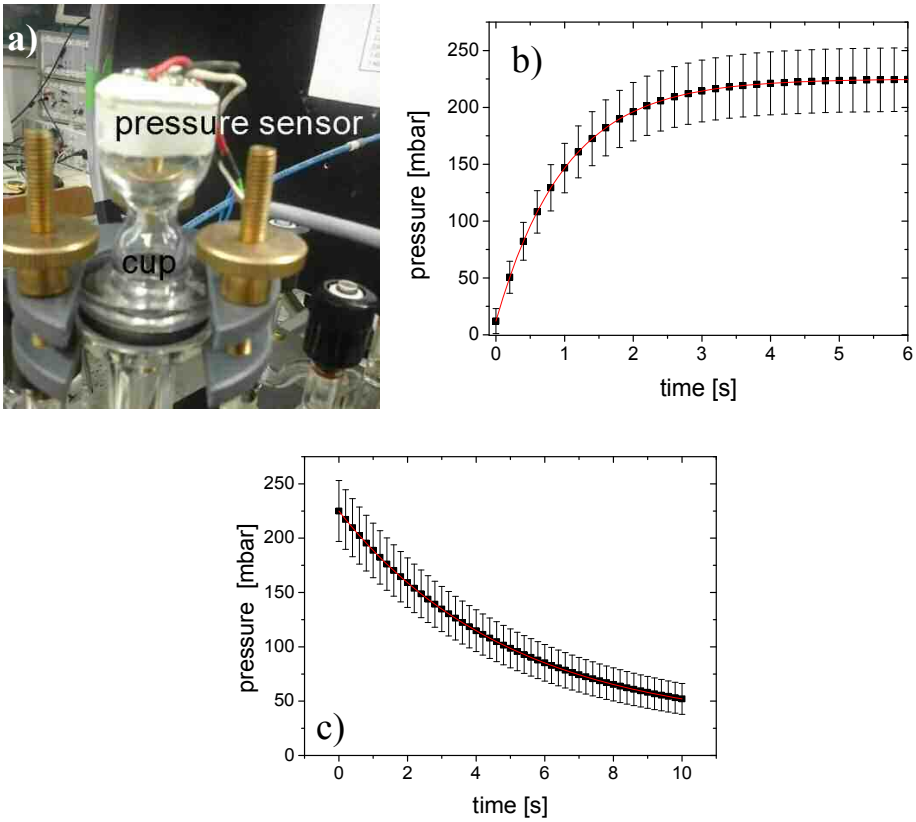

Fig. 4.39: a) Pressure sensor mounted in the filling system. b) Pressure vs. time measured during volatilization of the accumulated HP-Xe ice. c) Pressure vs. time measured during solidification of HP-Xe. The error bars represent the systematic error of the oscilloscope.

The characteristic times extracted from exponential fits to the graphics of Fig. 4.39b and 4.39c result in a characteristic time of 1 s for the volatilization and 5 s with an offset of 25 mbar for the solidification. The experimental conditions for the volatilization represent the real working conditions while for the solidification is just an approximation. However, this measurement establishes a time scale for both processes which contributes to study polarization losses.

A possible source of polarization losses which could be compatible with the results obtained in Fig. 4.24c can be related to the plastic tubing (Festo, Germany) used for some connections between glass parts and the GMS. The potential sources of relaxation could be

O_2 in case they are not tight and/or the interaction of HP-Xe with the wall. After the installation, these tubes need to be evacuated for around two days to ensure a pressure on the order of 10^{-6} mbar and extract all the adsorbed gas and humidity. After this procedure, this pressure can be achieved only by evacuating during some minutes as long the system is not ventilated to air. The tubes and connections were inspected also with a helium leak detector (Oerlikon, Germany) and no leak was found. In this way, the relaxation due to interaction with O_2 is dismissed at this stage.

The polarization losses of HP-Xe due to the interaction with the plastic tubing was investigated by measuring the T_1 of HP-Xe in a GE-180 cell with and without plastic tube pieces inside. For this experiment, about 4 stripes of tube of 7.5 x 0.3 cm were placed inside the measurement cell obtaining the values shown in Fig. 4.40.

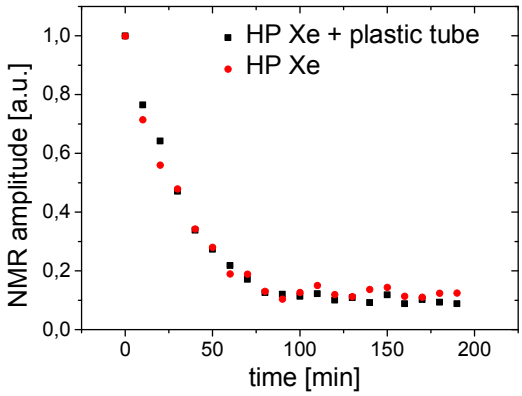

Fig 4.40: T_1 of HP-Xe in a GE-180 cell of 5 cm in diameter. The red points correspond to the T_1 time of HP-Xe and the black points correspond to T_1 of HP-Xe with pieces of plastic tubing inside.

The T_1 is the same in both cases within the accuracy of the measurement. It should be noted that inside the plastic tubing the surface-to-volume ratio is significantly higher and, in consequence, its wall relaxation rate. Therefore, the results of Fig. 4.40 only demonstrate that the tubes are not relaxing the HP-Xe dramatically. In fact, the polarized gas only stays approximately 4 s inside the plastic tubes during the polarization process[29]. So, it is expected that the wall relaxation in this tubes does not contribute significantly to the polarization losses shown in Fig. 4.24c.

The last relaxation mechanism to verify in the filling station is due to the magnetic field gradients over the measurement cell. The holding magnetic field of the filling station is provided by the coil system described is Section 4.1.2 and the homogeneity in this area ($z > 80$ cm) is shown in Fig. 4.41.

[29]However, the T_1 of HP-Xe in the tube was recently measured in our lab by Niederländer finding a T_1= 4 min. This value seems to increase for plastic with less softener additives [Nie15].

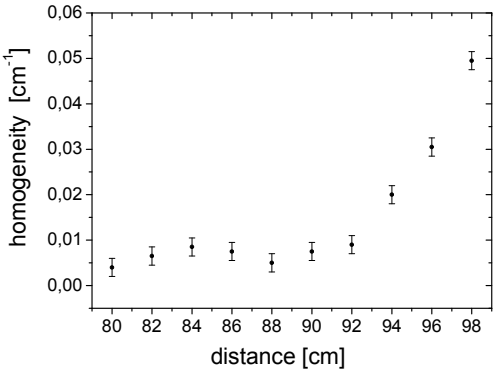

Fig. 4.41: Homogeneity of the area were the measurement cell is placed inside the magnetic field of Fig. 4.7a.

Usually, a 6 cm diameter cell is placed in the area between 90 and 96 cm while a 10 cm diameter cell is placed in the area from 90 to 100 cm. A sample of 100 mbar of pure Xe (D_{Xe} = 0.0645 cm^2/s) inside of any of these cells will have $T_1^{dB} \approx 5$ h for the 6 cm cell and $T_1^{dB} \approx 1$ h for the 10 cm cell. However, the filling system is used for filling and mixing HP-Xe with a manipulation time of less than 5 min for experiments with pure HP-Xe and 10 min for gas mixtures. Therefore the losses due to the manipulation in this are less than 5%.

Once the HP sample is prepared, it is placed inside the field of the low field NMR ($H \approx 10^{-4}$ cm^{-1}) where the main relaxation mechanisms are due to the interaction with the wall of the storage cell and the van der Waals interaction. This mechanism and how to extend the storage time of HP-Xe will be further investigated in the next chapter.

Chapter 5: Optimization of the storage times of HP-Xe

High polarizations for HP-^{129}Xe are an important factor in a successful measurement. This ensures a high S/N for the detection of the signal allowing novel experiments with high resolution, specificity and sensitivity [Che02].

However, the facility where the experiment takes place may not be right next to the facility where the HP-Xe is produced. Therefore, a high polarization level obtained through an efficient SEOP must be combined with efficient storage conditions in order to perform the experiment with the highest polarization possible.

Such polarization losses due to transport can be bypassed partially by using mobile Xe polarizers installed next to the measurement facility [Norq13] [Her07] e.g., in medical applications with a Xe-polarizer installed in the hospital next to the MRI tomograph. The gas is filled into Tedlar bags, which are used both for storage and administration of HP-Xe to patients. Those bags provide a storage volume of about 0.5 liters of HP gas at 1 bar and a storage time of about 1.5 h at best in high fields [Möl11]. This period is usually sufficient for most clinical MRI applications, keeping in mind that more than one Tedlar bag can be filled with HP-Xe to extend the use if needed. Nonetheless, longer storage times simplify significantly the experiment allowing accumulation of high quantities of HP-Xe for several patients or several measurements on the same patient.

While long storage times are convenient in such scenario, they are mandatory for experiments where a long spin coherence or acquisition time is required. Particularly, in ^{3}He - ^{129}Xe co-magnetometers where the frequency resolution σ_ν is related to the spin coherence time T_2^* as $\sigma_\nu \propto T_2^{*\,3/2}$ [Gem10] and T_2^* is given by Eq. [3.15]. In consequence, long longitudinal relaxation times T_1 and low pressures are necessary for achieving long T_2^*.

As it was discussed in Section 2.3.3, the expression for T_1 of HP-Xe on the measurement/storage conditions of this work can be reduced to

$$\frac{1}{T_1} = \frac{1}{T_1^{wall}} + \frac{1}{T_1^{Xe-Xe}\left(1 + r\,\frac{p_B}{p_{Xe}}\right)}. \qquad [5.1]$$

In case of pure Xe ($p_B = 0$) and room temperature, the longitudinal relaxation time T_1 is limited due to the van der Waals interaction to (4.1 ± 0.1) h or (4.5 ± 0.5) h according to Chann [Chan02] and Anger [Ang08] respectively.

The addition of buffer gases ($p_B \neq 0$) suppresses the van der Waals relaxation with an efficiency given by the destruction rate coefficient r. The values for this coefficient were measured at room temperature for He, Ar and N_2 at low fields (B_0 = 20.4 G) by Chann and

only for N_2 at high fields by Anger. The destruction rates found in these publications are summarized in Table 5.1. However, the benefits of adding a buffer gas are limited because of two reasons: first, the dilution of the gas compromises the intensity of the signal for a sample with a limited total pressure, e.g. due to the stability of an apparatus.

Second, the reduction of T_2^* at higher pressures (see Eq. [3.15]). The best strategy to reduce the amount of buffer gas is using gas with a high *r*. So far, no further research on the improvement of *r* was performed besides [Cha02] and [Ang08].

Table 5.1: Destruction rate coefficients (*r*) and relaxation times (T_1^{XeXe}) for van der Waals molecules as determined by two different groups.

Reference	r_{He}	r_{Ar}	r_{N2}	T_1^{XeXe} [h]
[Chan02]	0.25 ± 0.08	0.49 ± 0.06	1.05 ± 0.08	4.13 ± 0.13
[Ang08]	-	-	0.49	4.5 ± 0.5

The two relevant relaxation mechanisms of Eq. [5.1] had to be minimized in order to achieve long storage times. Therefore, it is necessary to produce glass vessels with a long T_1^{wall} and to find a buffer gas with a high destruction rate coefficient. A precise measurement of the wall relaxation time and the destruction rate requires also developing a handling procedure of the glass cell, which ensures reproducible results.

For this purpose, the production and handling of the measurement cells are explained in detail in the first part is of this chapter. The second part is dedicated to the study of the longitudinal relaxation of HP-^{129}Xe (85 % ^{129}Xe, Linde Electronics and Specialty Gases) in three different gas mixtures: Xe-N_2, Xe-SF_6 and Xe-CO_2. The first mixture was chosen for reference to literature values. N_2 had so far, the highest observed destruction rate (see Table 5.1). SF_6 was chosen because it will be used in future measurements of the Xe EDM which involves high voltages (~ 10 kV) between the walls of the cell where a few mbar of HP-Xe are stored. SF_6 prevents electric discharge between the electrodes due to its high electrical insulation coefficient.

Finally, CO_2 was tested to study a possible influence of the molecular radius on the destruction rate coefficient. The values of Table 5.1 suggest a clear relation between the van der Waals radius of the molecules and the destruction rate coefficient as shown in Fig. 5.1. Following this logic, SF_6 should have the highest destruction coefficient rate because its van der Waals radius is about 327 pm. The van der Waals radius of CO_2 is 257 pm, slightly higher than N_2 (249 pm) [CRC09]. Therefore, *r* for CO_2 is expected to be between the value for N_2 and for SF_6.

If the dependence of the destruction rate on the van der Waals radius is confirmed, a buffer gas with the highest vdW radius would lead also to the highest *r*.

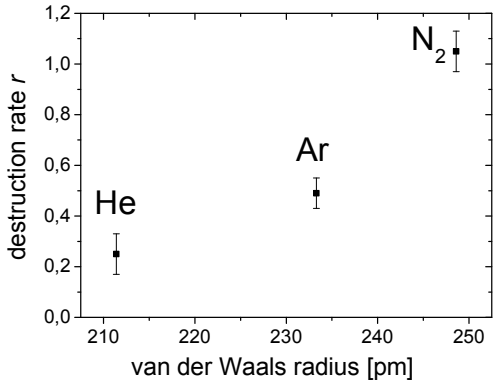

Fig. 5.1: Destruction rate coefficient vs. vdW radius of three different gases Ar, N_2 and He [Cha02].

The measurement of T_1^{wall}, T_1^{XeXe} and r were performed by measuring T_1 of HP-Xe mixed with different partial pressures of the previous mentioned buffer gases maintaining constant the partial pressure of Xe. Consequently, this measurement requires a stable T_1^{wall} over all the measurements in order to extract the parameters of Eq. [5.2]. The procedures and conditions for obtaining a stable T_1^{wall} are presented on the third part of this chapter.

The fourth part of this chapter studies the relation of T_1^{wall} with the geometry of the cell. According to Eq. [2.46], T_1^{wall} of storage vessels made from the same material (same relaxivity η) is inversely proportional to the surface-to-volume ratio. Therefore, a possible way to extend T_1^{wall} in a spherical cell of certain material is to increase the radius of the sphere. This was investigated including the influence of the valve by measuring T_1 of HP-Xe on spherical cells with different diameters.

Finally, the high reproducibility achieved in T_1^{wall} uncovers a so far unknown effect on the longitudinal relaxation of ^{129}Xe depending on the isotopic composition. This difference is not explained or even predicted in the literature. For this reason, it requires exhaustive and detailed experimental evidence to verify this effect. These experiments and their results are summarized in the last part of this chapter.

Most results of this chapter were published in Journal of Magnetic Resonance in 2015. This publication is attached in Appendix 6.

5.1 Preparation of the glass vessels and procedure of the T_1 measurements

5.1.1 Construction of the measurement cells

The cells used in this work are made of aluminum silicate glass called GE-180 (General Electric). This glass is boron-free and it has a low permeability. It is well known that cells produced from this material exhibit extremely long T_1^{wall} for ^{3}He [Rich02] but so far it was not tested with HP-Xe. Historically, the cells used for T_1 measurements of HP-

Xe were made of Corning glass coated with silane/silohexane compounds [Drieh95] [Jam88] or uncoated quartz [Chan02]. The coatings were initially necessary to protect the glass from the chemical attack of the alkali metal in cases where the optical pumping cell was also used for measurements. However, the use of such coatings for prolonging T_1^{wall} in measurement cells has a rather low reproducibility and performance [Sau98]; especially at low magnetic fields [Ang08].

No coatings were employed in this work because the measurement cells are meant to be used to store HP-Xe and HP-^{3}He at high voltages. The coatings may affect T_1 of ^{3}He and the conductivity of the surface reducing the resolution of the experiment.

The measurement cells were blown by the glassblower of the Physics Institute (see Fig 5.2) from a GE-180 tube of about 1.5 m in length and 4 cm in diameter. The tube is mounted in a lathe and rotates while being heated in the center with a flame of acetylene (T ≈ 3000°C). During rotation, the length is reduced to increase the diameter in the center. This procedure is repeated until a sphere with the wanted diameter is reached. Then, a hole is drilled with a high temperature flame and the stem is connected. Subsequently, the cells are baked at 600°C for 3 h to remove residual tensions in the glass. Finally, the cells are cleaned with a solution of Mucasol (Schülke & Mayr GmbH, Noderstedt, Germany) and distilled water 1:5, dried in the oven at 90°C for at least 12 h and evacuated to 10^{-7} mbar through standard glass stopcocks (NS 14.5, HWS, Germany). The stopcocks have an inner diameter of 2 mm, a stem with a length of 2 cm encasing a polished valve which is lubricated with vacuum grease (Apiezon, UK) and a KF-16 glass flange for the connection with the filling system. In Fig. 5.2, these steps of the production of the cells are shown.

Following this procedure, several spherical cells of GE-180 with diameters of 6, 8 and 10 cm were produced.

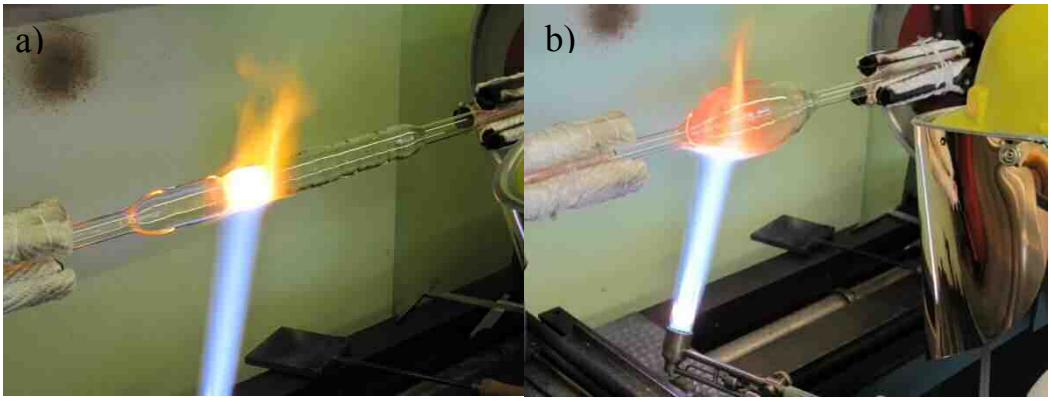

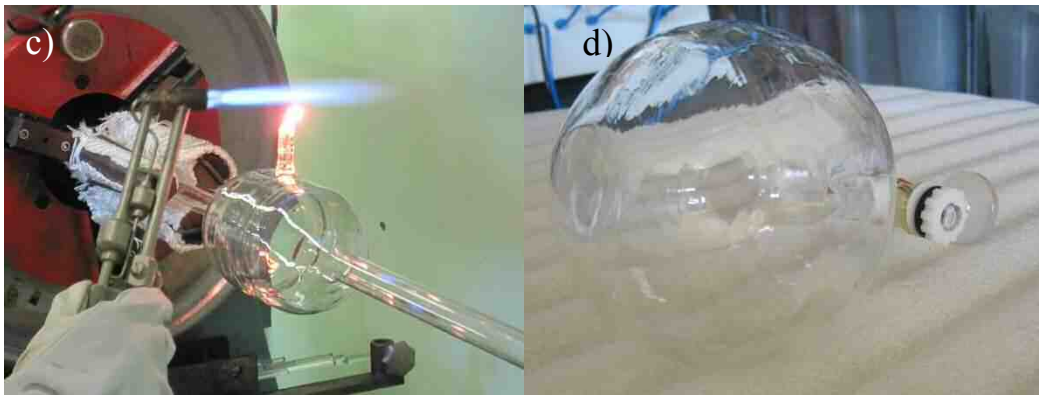

Fig. 5.2: Production of spherical cells of GE-180 glass. a) GE-180 tube mounted on a lathe. b) The tube rotates while being blowed by the glass blower increasing its diameter. c) The stem is connected once the cell is shaped,. d) Cell ready to use.

5.1.2 Selection of the cells for the measurements

Once prepared, the longitudinal relaxation of HP-^{3}He was measured for each cell. The results in this case present a high dispersion for cells with the same diameter. Consequently, the longitudinal relaxation of HP-Xe was measured as well. For this experiment, the measurement cell was connected to the filling system described in Section 4.3. The Xe was hyperpolarized using the polarizer described in Chapter 4 and filled into each cell with a pressure of about 150 mbar. T_1 was measured using the low field NMR as described in Chapter 3. In all cases, an FID (see Section 3.1.1) was recorded every $\Delta t = 20$ minutes using a flip angle $\alpha = (9.6 \pm 0.2)°$. The typical S/N ratio at the beginning of the experiment was about 40.

The measurements with HP-^{3}He and HP-^{129}Xe were performed on cells with the diameters of 6, 8 and 10 cm and with pressures of about 100 mbar on the same day to avoid reproducibility problems due to cell aging (see Sec. 5.3). Table 5.2 summarizes the results of the T_1 measurements for HP-Xe and HP-He.

Table 5.2: T_1 for HP-^{129}Xe and HP-^{3}He. The highest T_1 (highlighted) values for He coincide with the highest T_1 values for Xe.

Diameter [cm]	Cell	T_1 He [h]	T_1 Xe [h]
6	95	23.4 ± 0.5	1.81 ± 0.09
	146	45 ± 2	2.10 ± 0.08
	147	1.6 ± 0.4	1.25 ± 0.07
8	4	100 ± 2	2.13 ± 0.02
	5	23 ± 3	1.45 ± 0.05
	6	150 ± 8	2.43 ± 0.03
10	2	35 ± 1	2.43 ± 0.06
	4	161 ± 1	2.45 ± 0.02
	7	150 ± 3	2.13 ± 0.04

In this table, the highest T_1 for ^{3}He are highlighted and they coincide with the highest T_1 for ^{129}Xe for all three diameters. The selection criteria for the measurement cells in further experiments is based in choosing those cells with the longest T_1.

5.2 T_1 measurements of enriched Xe in gas mixtures

For the determination of the parameters of Eq. [5.1], the HP-Xe must be diluted with buffer gases, in this case, N_2, SF_6 and CO_2. The xenon used in this experiment is 85% enriched in ^{129}Xe with less than 0.1 % ^{131}Xe (Linde electronic gases) while the other gases are standard however with high purity (less than 100 ppm impurities).

The mixture of HP-Xe with buffer gases must be carefully carried out to know precisely the partial pressure of each gas. The procedure for mixing the gases starts when the HP-Xe is filled up into the measurement cell (cell 6-10 in all cases). The pressure of Xe (p_{Xe}) is recorded and the valve of the cell closed. The buffer gas is added until a certain pressure higher than p_{Xe} is reached. Then, the measurement cell is opened and the buffer gases filled. In this way, it is possible to control the final pressure of buffer gas (p_{mix}). The gas mixing ratio f is calculated as $(p_{mix}-p_{Xe})/(p_{Xe}-p_{off})$ where p_{off} is the offset of the pressure sensor.

For each buffer gas - HP-Xe ratio, T_{eff} and T_1 were determined as explained in Section 3.4. Typically, T_{eff} reached values from 180 minutes for pure HP-Xe to 650 minutes for the highest p_{CO2}/p_{Xe}. In all cases, the duration of the experiment was at least four T_{eff} for a precise determination of the background. The uncertainty of the measurement increases for long T_1 because of two reasons: first, the high pressure of buffer gas shortens T_2^*, hence broadening the signal at longer times and second, instabilities in the experimental setup (e.g. changes in the magnetic field and/or temperature) are accumulating for longer operation times.

It is important to verify, as it will be shown in the next section, that the wall relaxation remains constant until the experiment is finished. Therefore, T_1 of pure HP-Xe was repeatedly determined in between the measurements with buffer gas mixtures (consistency measurement) as a control.

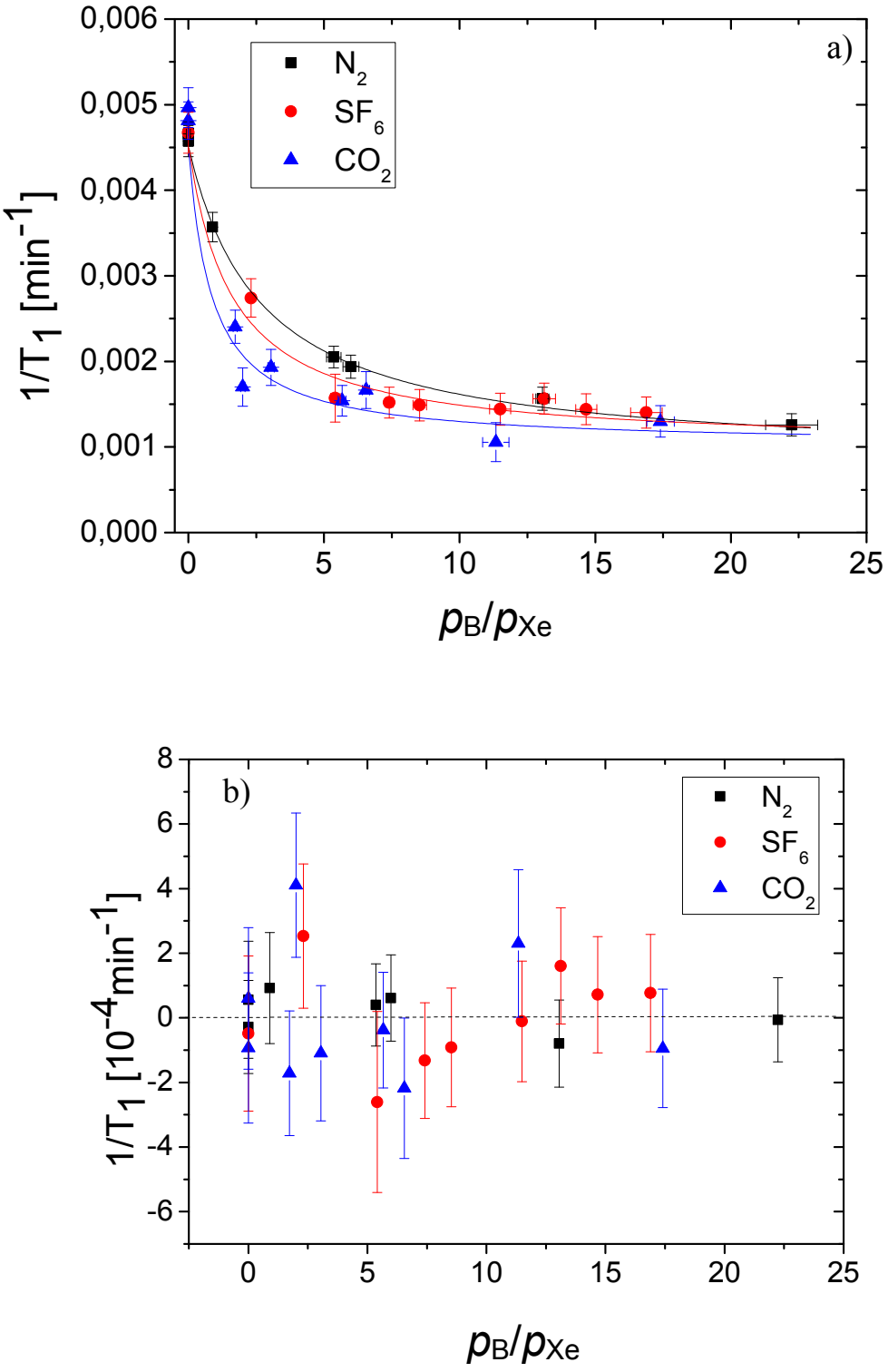

Fig 5.3: Determination of T_1 of HP-Xe in the a spherical GE-180 glass cell of 10 cm diameter mixed with different amounts of three buffer gases. a) Relaxation rate $1/T_1$ vs. p_B/p_{Xe}. The black line is a fit of Eq. [5.1] to the measured values (black squares) for the buffer gas N_2. Red line / circles are the same for SF_6 and blue line / triangles for CO_2. b) Residuals of the fit using the same colors and symbols as in a).

Table 5.3: Results of the fit of Fig. 5.3 according to Eq. [5.1]. For convenience, the results of T_1^{wall} and T_1^{XeXe} are expressed in hours.

Isotopically enriched Xe			
buffer gas	N_2	SF_6	CO_2
χ^2	0.11	1.15	1.57
T_1^{wall} [h]	17.2 ± 1.1	15.7 ± 0.8	17.8 ± 1.2
T_1^{XeXe} [h]	4.53 ± 0.17	4.60 ± 0.22	4.62 ± 0.23
r	0.46 ± 0.05	0.70 ± 0.09	1.40 ± 0.22

The quality of the fitting procedure can be judged in Fig. 5.3b where the scatter of the residuals is shown. This plot is in agreement with the values of the normalized χ^2 of the first row in table 5.3. The measurement with three different buffer gases were performed in the same cell and the values obtained for T_1^{wall} can be combined to a weighted average of $\overline{T}_1^{wall} = (16.6 \pm 0.6)$ h.

This very same cell was used for building a He-Xe co-magnetometer. The free spin precession of the nuclei was measured over some days obtaining $T_2^* \approx 7.5$ h for Xe [All14]. According to Eq. [3.15] and assuming the relative gradients are $|\nabla B|$=0.1 μG /cm in a holding field of B_0 = 4 mG [Tul13], the resulting T_1^{wall} is approximately 16 h. This value agrees with T_1^{XeXe}measured in this work.

The values for $\overline{T}_1^{XeXe}$ in Table 5.3 also overlap within their error bars resulting in a weighted average value of (4.57 ± 0.06) h. This value is in agreement with (4.59 ± 0.43) h reported by Anger [Ang08] but slightly higher than the values obtained by Chann [Cha02].

The destruction rates of the used buffer gases in the last row of Table 5.3 give a value for N_2 which is about half the value reported by Chann but in agreement with the result reported by Anger *et al*, in both works the isotope concentrations of ^{129}Xe were 0.85. The destruction rate for SF_6 is slightly higher than for N_2. However, an unexpected result is the destruction rate for CO_2, which is almost three times more effective that N_2 exhibiting the highest destruction rate reported so far. This result cannot be explained by the simple relation of the destruction rate coefficient with the vdW radius as shown in Fig. 5.1. Therefore, other effects should be considered besides the geometry of the molecule for searching a gas with even higher destruction rate for the Xe-Xe molecules.

The high effectiveness of CO_2 for suppressing van der Waals dimers is particularly useful for fundamental physics experiments because it could provide long measurement times even at low pressures without significantly reducing T_2^*. Long T_1 values could be also useful for medical applications because small quantities of CO_2 result in long storage times for HP- Xe. For example, a one to one mixture gives a T_1^{vdW} of about 11 h which is more than twice the value for pure Xe. This result is very important for medical

applications since CO_2 can be safely inhaled [Gua11].

The experiment described above is the most precise method for the determination of the wall relaxation but it is very time consuming. Usually between one or two weeks are needed to perform one of the curves displayed in Fig 5.3. However, the significantly improved accuracy in T_1^{XeXe} now permits for a much faster estimation of T_1^{wall} using Eq. [5.1] with $r = 0$ (i.e. pure Xe)

$$\frac{1}{T_1} = \frac{1}{T_1^{wall}} + \frac{1}{T_1^{Xe-Xe}} . \qquad [5.2]$$

This procedure leads to a higher uncertainty in T_1^{wall} and this uncertainty increases as T_1 approaches the value of T_1^{XeXe}. However, it is still a good approach for $T_1^{wall} < 40$ h (value where the error is more than 50 %) as shown in Fig. 5.4.

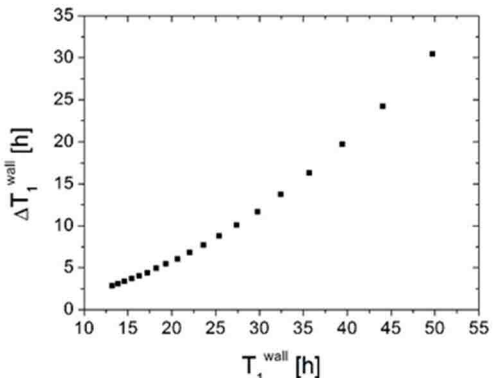

Fig. 5.4: ΔT_1^{wall} vs. T_1^{wall} calculated for T_1^{XeXe}= (4.57 ± 0.06) h using Eq. [5.2].

5.3 Long term studies and recovery of T_1^{wall}

Between experiments, the measurement cells are usually placed in a cabinet. The cells are stored without being opened to atmospheric pressure and far away from high magnetic fields which could be strong enough to magnetize ferromagnetic impurities in the glass [Sch06]. However, if T_1 is measured again some weeks later, most of the cells show a significant reduction of T_1^{wall}. This process was studied on detail in cell 6-10 with the results are shown in Fig 5.5a. In this graph, it can be clearly seen that there is a strong "aging" process which reduces T_1^{wall} from originally 16 h to less than 5 h in 10 weeks. However, the cells are washed with distilled water and Mucasol and dried as explained in Section 5.1, they recover to the original T_1^{wall} in more than 90% of the cases as shown in the Fig 5.5b. Due to this observation, the cleaning process described in Section 5.1 can be interpreted as a "recovery process".

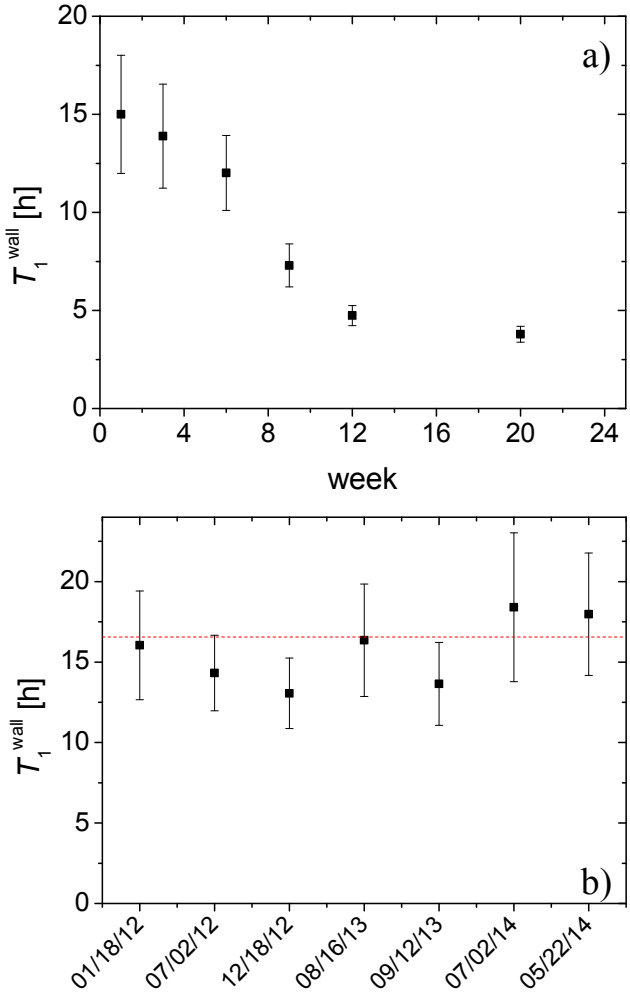

Fig 5.5: Reproducibility study of T_1^{wall} in the cell 6-10: a) T_1^{wall} vs. time in weeks. b) T_1^{wall} recovery of cell 6-10 after rinsing in distilled water and Mucasol and subsequent drying. Pictures extracted from [Rep15].

A possible explanation for this observation is that the internal dynamics of the glass causes migration of paramagnetic centers to the surface over time. Those paramagnetic centers in the glass are temporally neutralized or passivized due to the washing procedure. Such a layer could isolate the gas molecules from possible paramagnetic impurities on the glass surface. Considering that the cell is evacuated at least 10 times per experiment, the evaporation rate of water at 10^{-6} mbar is in agreement with the time scale of Fig. 5.5a [Hob61]. However, it is not clear if this evaporation is homogeneous over the surface or causes the formation of an "island structure". A qualitative characterization of this phenomenon implies many technical difficulties and was not further investigated in this work.

The characterization of the "aging" of T_1^{wall} and its possible recovery was so far not published in the literature. Besides the long T_1^{wall} values obtained in these experiments, the most remarkable point is its reproducibility. For this reason, this systematic study establishes working conditions for measurement/storage cells in experiments where the

relaxation time is a critical parameter.

5.4 Wall Relaxation dependence on the surface to volume ratio

The dependence of T_1^{wall} on the surface-to-volume ratio, S/V, of the container was analyzed in GE-180 glass cells of 6, 8 and 10 cm diameter. Each cell was equipped with stopcocks of similar characteristics (material, length and grease). The cells were washed, dried and evacuated and, directly after, the T_1 of each cell was measured. T_1^{wall} was extracted from this value using Eq. [5.2].

Due to the cell construction in this experiment, the HP gas is in contact with two environments: the spherical cell made from GE-180 and the stopcock. Both environments have different relaxivities, which are differentiated by introducing two indices: "C" for the cell and "S" for the stopcock (see inset in Fig. 5.6). Therefore, η^C is the relaxivity of the GE-180 cell and η^S is the relaxivity for the stopcock (including the grease) and to equate the total wall relaxation rate T_1^{wall} both contributions have to be weighted by their volume resulting in the following equation,

$$\frac{1}{T_1^{wall}} = \frac{1}{V^C + V^S}\left(\frac{V^C}{T_1^{wall,\,C}} + \frac{V^S}{T_1^{wall,\,S}}\right). \qquad [5.3]$$

Considering the expression for $1/T_1^{wall}$ given in Eq. [2.46], T_1^{wall} can be rewritten as

$$\frac{1}{T_1^{wall}} = \frac{1}{V^C + V^S}\left(\eta^C V^C \frac{S^C}{V^C} + \eta^S V^S \frac{S^S}{V^S}\right). \qquad [5.4]$$

For the approximation above it is assumed that $V^C \gg V^S$. If the environment C can be assumed to be a sphere then $V^C = 36\pi\left(S^C/V^C\right)^{-3}$, then Eq. [5.4] results in

$$\frac{1}{T_1^{wall}} \cong \eta^C \frac{S^C}{V^C}\left[1 + \frac{\eta^S}{\eta^C}\frac{L\,d}{36}\left(\frac{S^C}{V^C}\right)^2\right]. \qquad [5.5]$$

This equation for a simple model proposed above describes satisfactorily the trend of $1/T_1^{wall}$ vs. S^C/V^C (Fig. 5.6) as determined for the three different sizes of cells. In Fig. 5.6, the solid line corresponds to a fit without intercept according to Eq. [5.5], resulting in $\eta^C \approx 0.03$ cm/h and $\eta^S \approx 18$ cm/h. The dispersion between identical cells may also allow relaxivities $\eta^C \approx 0.08$ cm/h and $\eta^S \approx 12$ cm/h (dashed line).However, due to the small number of samples, multiple possibilities of fits and the non-statistical variation of T_1^{wall}, no error are given for the fit. For the same reason, estimations of T_1^{wall} for cells of higher diameter than 10 cm must be performed with care.

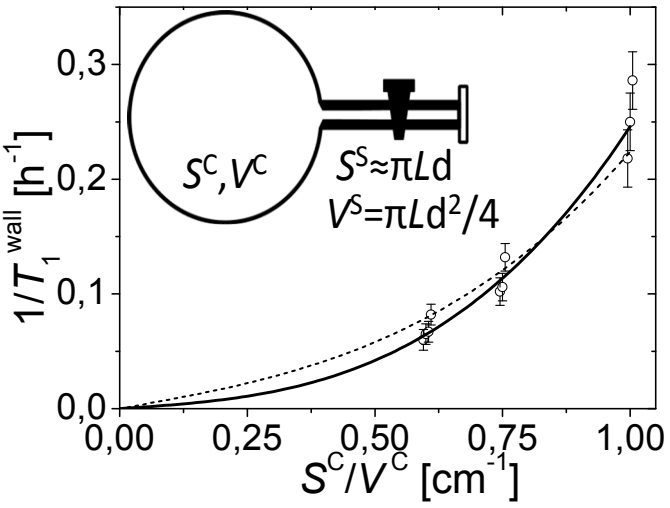

Fig 5.6: Dependence of $1/T_1^{wall}$ on the surface to volume ratio of a spherical cell with volume V^C and surface S^C. The black line represents the fit of Eq. [5.5]. The dotted line represents an alternative fit which uses the parameters the values obtained from the first fit to Eq. [5.5] (black line) but adding their error bars. Picture extracted from [Rep15].

5.5 Relaxation dependence on ^{129}Xe isotope concentration

The T_1 measurements in spherical glass cells of 6, 8 and 10 cm diameter were performed also with Xe of natural isotope abundance (26%). The longest values of T_{eff} for each case are shown in Table 5.4. Consistently, a difference of T_1 for enriched and natural Xe was observed even if these measurements were performed less than one day apart.

Table 5.4: Longest T_1 times for HP-Xe in spherical glass cells of different diameters obtained with enriched Xe (85% ^{129}Xe) and natural Xe (26.4 % ^{129}Xe).

cell diameter	T_1 enriched Xe [min]	T_1 natural Xe [min]
6 cm	144 ± 14	108 ± 13
8 cm	182 ± 13	163 ± 12
10 cm	216 ± 15	195 ± 15

The observed difference could be attributed, for example, to the presence of O_2 in the bottle containing Xe in natural abundance. Even, if the reported chemical purity of the natural Xe is about 99.999%, the gas can be contaminated with traces of O_2. However, the amount of O_2 necessary for producing the observed 20 minutes difference in a T_1 measurement is around 2.3 mbar, nearly 0.5 % of the total Xe pressure in the measurement cell. Polarizing under these conditions is nearly impossible because of Rb oxidation in the OP-cell. Relaxation due to oxygen can therefore be neglected because no early oxidation

of Rb has been observed. Another possibility could be O_2 contamination during the filling process. This option would probably not lead to such reproducible results.

To verify this effect, the T_1 of natural Xe using SF_6 as a buffer gas was measured in two spherical cells of 10 cm diameter (4-10 cm and 7-10 cm) with different T_1^{wall} following the same procedure explained in Section 5.2. The results obtained for both cells are shown in Fig. 5.7 and fitted with Eq. [5.1]. However, these fits were performed with T_1^{XeXe} and r being the same for both curves. This procedure was done by joining both datasets and defining T_1^{XeXe} and r as global parameters, while T_1^{wall} defined as a local fit parameter. The error bars are determined by the correlated error. The results of the fit are presented in Table 5.5.

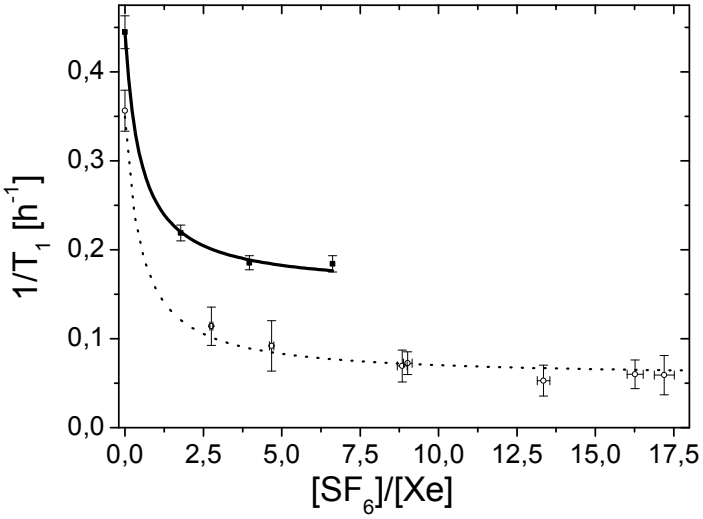

Fig. 5.7: Relaxation rate ($1/T_1$) of HP-Xe (26.4 % ^{129}Xe) as a function of p_{SF6}/p_{Xe}. For this measurement, two spherical cells of 10 cm diameter with different T_1^{wall} were used. The filled squares correspond to cell 4-10, the open circles to cell 7-10 with T_1^{wall} of about 6 h and 18 h, respectively. The complete results of the fit are given in Table 5.5. Picture extracted from [Rep15].

Table 5.5: Results from the combined fit to the data of Fig. 5.7 using Eq. [5.1]. The errors were calculated from the correlated errors of the fit.

Natural Xe	
buffer gas	SF_6
χ^2	0.28
$T_1^{wall, \#4}$ [h]	6.4 ± 0.5
$T_1^{wall, \#7}$ [h]	18.2 ± 2.8
T_1^{XeXe} [h]	3.4 ± 0.2
r	2.0 ± 0.6

If the value of T_1^{XeXe} in Table 5.5 is compared with the value for enriched xenon in

Table 5.2, the first one is about 30% smaller, which points to an additional relaxation term so far not taken into account in the spin-dependent interactions of the Xe dimers.

This value was verified by two consecutive measurements of T_1 in a cell of different geometry and composition. It was a cylindrical cell with walls made of GE-180 of 10 cm in diameter and 5 cm in height. The lids of this cell were two disks of silicon. The first measurement used 85% isotopically enriched HP-^{129}Xe and resulted in T_1^{wall} = (9.84 ± 0.91) h by using Eq. [5.2] and the T_1^{XeXe} from Table 5.5. The second measurement of T_1 was performed with natural Xe immediately after the first one. The wall relaxation of the cell can be assumed to be constant because both measurements were performed within a 24 h period. In this way, T_1^{XeXe} for natural abundance results in (3.72 ± 0.18) h. This value is in good agreement with the observed trend of Table 5.5. A final measurement with enriched Xe was performed confirming the initial wall relaxation time. Therefore, the systematic isotope effect on the Xe relaxation was verified by three independent experiments.

The model described in Sec. 2.3.1.2 employs a Hamiltonian, which contains the spin rotation interaction considering only atoms with non-zero nuclear spin interacting with the angular momentum of the molecule. Before the results obtained in Fig. 5.7, it was assumed that the relaxation of natural Xe should follow the same mechanisms. Especially because the nuclear spin-spin coupling, *J,* between magnetically non-equivalent nuclei J(^{129}Xe-^{131}Xe) is about a factor of 20 smaller than the spin-rotation interaction [Vaa13]. This difference was determined using *ab initio* calculations which, however, are strongly dependent of the boundary conditions.

The value for the destruction rate r of SF_6 seems to be affected if the values from Table 5.2 and 5.5 are compared. This difference is also not predicted by the theory described in Sec. 2.7. A possible explanation could consider all the non ^{129}Xe isotopes present in the mixture act like a “buffer gas” influencing the statistics of the dimer break-up rate r with respect to ^{129}Xe. However, this has to be verified both theoretically and by further experiments using other Xe isotopic mixtures.

5.6 Conclusions

The longitudinal relaxation of HP-^{129}Xe at low magnetic fields was considerably prolonged for storage and detection. It was demonstrated that cells made of GE-180 provided an extraordinary long T_1^{wall} of about 17 h in 10 cm diameter spherical cells. The systematic determination of T_1 over weeks revealed a slow “degradation” of T_1^{wall} which can be recovered through a very simple washing procedure. The reproducibility of this recovery was studied over about 2 years. Due to the very long and reproducible T_1^{wall} obtained in this work, two important factors could be observed:

First, the effectiveness of CO_2 for suppressing van der Waals dimers. This fact is

particularly useful for fundamental physics experiments because it provides a long T_1 even at low pressures. In case of medical applications, the high destruction rate of CO_2 could be useful because small quantities result in long storage times for HP-Xe, e.g. a one to one mixture gives a T_1 of about 7 h. In addition, CO_2 can be safely inhaled. The unexpected high destruction rate of CO_2 cannot simply be related to its geometrical cross-section. Other molecular properties seem to have a similar strong influence on this three-body interaction. This observation opens the door for further experiments using different molecules as buffer gases.

Second, the 30% difference of T_1^{XeXe} when determined for enriched and natural Xe isotope concentration evidences the presence of additional relaxation mechanisms. This effect is yet not understood and needs to be studied in further experiments by mixing different proportions of enriched and natural Xe.

Chapter 6: Absolute Measurement of the Polarization of HP-^{129}Xe

As it was mentioned in Chapter 1, most of the applications of HP-Xe are related to NMR due to its high signal enhancement and chemical shift range. For this reason, the majority of the reported measurements of the HP-Xe polarization are performed via NMR, since the required equipment is already available in most of the NMR labs.

The usual method for the determination of the polarization of HP-Xe (P_{Xe}) is the comparison of the NMR signals coming from a thermally polarized sample (S_T) and a hyperpolarized Xe sample (S_{Xe}). This relation is expressed in the following equation [Her07] [Nor14]

$$\frac{S_{Xe}}{S_T} = a_s \frac{P_{Xe}}{P_T} \frac{N_{Xe}\beta_{129\,Xe}}{N_T} \frac{\gamma_{Xe}}{\gamma_T} \frac{\sin(\alpha_{Xe})}{\sin(\alpha_T)}. \qquad [6.1]$$

Here a_s a is a constant which can include corrections due to T_2^* or receiver response. P is the polarization which in case of a thermally polarized sample is given by $P_T \approx \mu B_0/k_B T$. N is the number of atoms present on the sample, β is the isotopic abundance of ^{129}Xe in Xe, γ is the gyromagnetic ratio and α are the flip angles used to obtain each signal.

The thermally polarized signal is usually obtained from either Xe or protons in ^1H_2O. In both cases, several scans are required to obtain a thermal signal with a sufficient signal-to-noise ratio. For this purpose, T_1 must be manipulated somehow in order to obtain a reasonable duration of the experiment. For example, the T_1 of protons in water is about 2 seconds then 100 scans will require about 15 minutes[30]. This duration is appropriate for performing an experiment. However, the duration of the experiment can be significantly shortened to some seconds by adding $CuSO_4$ as a relaxing agent. A thermal sample of Xe requires high pressures (over 5 bar) for increasing the density of the sample and, consequently, the thermal signal. The longitudinal relaxation of Xe is in the order of hours. Therefore, it requires at least 80 h for 100 scans. In this case, the experiment duration can be significantly shortened by adding some relaxation agent like O_2 or zeolites [Sha00].

The polarization measurement via comparison of NMR signals is a valid method but it has to be performed carefully considering that the characteristics of the thermal and hyperpolarized signal are different. Therefore, several points must be carefully checked for performing an accurate measurement [Wil97]:

The geometry and position of the HP and the thermally polarized sample must be the same. In this way, the geometrical factors in the magnetic flux contribution can cancel

[30] For measuring the magnetization of a thermally polarized sample, the accumulation of scans requires that each new scan start from thermal equilibrium. Therefore, the time between scans should be (at least) $5T_1$'s.

each other. In addition, this requirement is necessary because different contributions of the magnetic field gradients over the sample could lead to differences on the NMR signal.
The holding field (B_0) and/or the frequency of the receiver must be re-adjusted if different nuclei are compared. This adjustment must be done also in case of comparing the same substance but varying the quantity because this changes the dielectric load on the circuit. In this case, the Q factor and the linearity of the receiver circuit must be checked very carefully.
The HP sample signal is often at least three orders of magnitude higher than the thermally polarized. Hence, the dynamical range of the detection unit has to be adjusted and calibrated to ensure the linearity of the detection.

The flip angles of the hyperpolarized and the thermal sample must be well known. The contribution of the flip angles to Eq. [6.1] is given by $A = \sin(\alpha_{Xe})/\sin(\alpha_T)$ and its Gaussian error by $\Delta A^2 = A^2[\ (\Delta\alpha_{Xe}/\tan(\alpha_{Xe}))^2 + (\Delta\alpha_T/\tan(\alpha_T))^2\ ]$. Typically, the thermal polarization is measured with $\alpha_{Xe} = 90°$ to obtain the highest signal possible. Therefore, if the polarization the HP sample is measured also with a $\alpha_{Xe} = 90°$, the maximum signal is acquired and its contribution on the error propagation is canceled. However, a 90° pulse destroys the HP state, which prevents repetitions of the experiment on the same sample. On the other hand, small flip angles allow several scans but the error increases significantly as it can be observed in the graphic of Fig. 6.1 where ΔA vs. α_{Xe} is plotted.

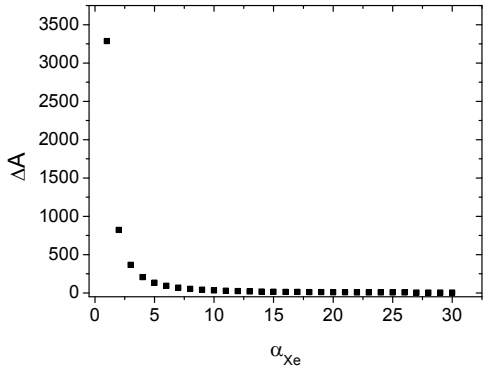

Fig. 6.1: ΔA vs. α_{Xe} with $A = \sin(\alpha_{Xe})/\sin(\alpha_T)$ extracted from Eq. [6.1]. ΔA=0 for those measurements with $\alpha_{Xe} = 90°$ while for $\alpha_{Xe} < 10°$, ΔA increases tremendously.

The T_1 of the thermally polarized sample has to be well known for the determination of the repetition delay between measurements.

The lifetime of the signal, T_2*, depends on the diffusion coefficient (see equations [2.44] and [3.15]), this difference can affect the amplitude and width of the NMR signal due to the acquisition delay time. Therefore, it must be corrected if the hyperpolarized and the thermally polarized sample have for instance different pressures or involve gas mixtures.

The comparison on FID/NMR signals proposed in Eq. [6.1] with the considerations

above mentioned can be also used for the calculation of the polarization of a HP-Xe sample using another HP sample for reference. In this case, the polarization level of the reference HP sample has to be used instead of P_T in Eq. [6.1]. HP-^{3}He is a good candidate for a reference sample since its polarization level, P_{He}, is measured with high accuracy by optical methods [Wol04]. The comparison of the signals of two HP gas samples should be a suitable way to obtain P_{Xe} because many of the requirements mentioned above can be easily fulfilled.

This experiment was performed with a spherical cell of 6 cm in diameter filled with 200 mbar of HP-Xe. The FID was measured in the low field NMR system described in Chapter 3 using $\alpha_{Xe} = (9.84 \pm 0.16)°$. The signal obtained is shown in Fig 6.2a. Then, the same cell was filled with 200 mbar of HP-^{3}He with $P_{He} \approx 50$ %. The acquisition frequency remained constant at 27 kHz but the holding field was reduced to 7.6 G to adjust to the Larmor frequency of ^{3}He. The FID shown in Fig. 6.2b was obtained using a flip angle $\alpha_{He} = (15.6 \pm 0.26)°$. When comparing the FID and the spectra shown in Fig. 6.2, it becomes evident that both FID's have different characteristics. The FID of HP-Xe follows the description given in Sec. 3.1.1 with one resonant frequency while the FID of HP-^{3}He shows a beat resulting of the interference of two frequencies as confirmed by the spectrum.

The spectrum of Fig. 6.2a presents one peak while the spectrum on Fig. 6.2b shows two broad peaks. This phenomenon is related to the self-diffusion coefficient of ^{3}He which is about 32 times higher than that of Xe [Aco06] and the magnetic field gradients of the low field NMR system. In consequence, the HP ^{3}He gas behaves as being immersed in two effective magnetic fields.

In this case, the integrals of the peaks of Fig. 6.2 cannot be directly compared. Further corrections must be performed concerning the detection range, the Q of the pick-up coil and the filter of the spectrometer since both signals have a different width. Therefore, Eq. [6.1] does not allow a precise calculation of P_{Xe} straightaway. This example demonstrates the difficulties of signal comparison using Eq. [6.1] of different HP samples even if those samples are relatively similar.

Finally, the measurement of P_{Xe} using the thermal signal of Xe at fields in the order of 2 mT cannot be realized using the low field NMR system presented here because it would require several weeks of acquisition due to the extremely low S/N ratio ($P_{Xe} < 10^{-9}$) and long T_1.

In order to path these problems; this chapter is dedicated to develop a simple and reliable method for the measurement of the absolute polarization of HP-Xe. This technique has several advantages over the NMR procedure since no spin perturbation is required and it can be applied for different pressures and gas mixtures without further corrections. In addition, it is also suitable for other HP gases such ^{3}He or ^{83}Kr without further modifications.

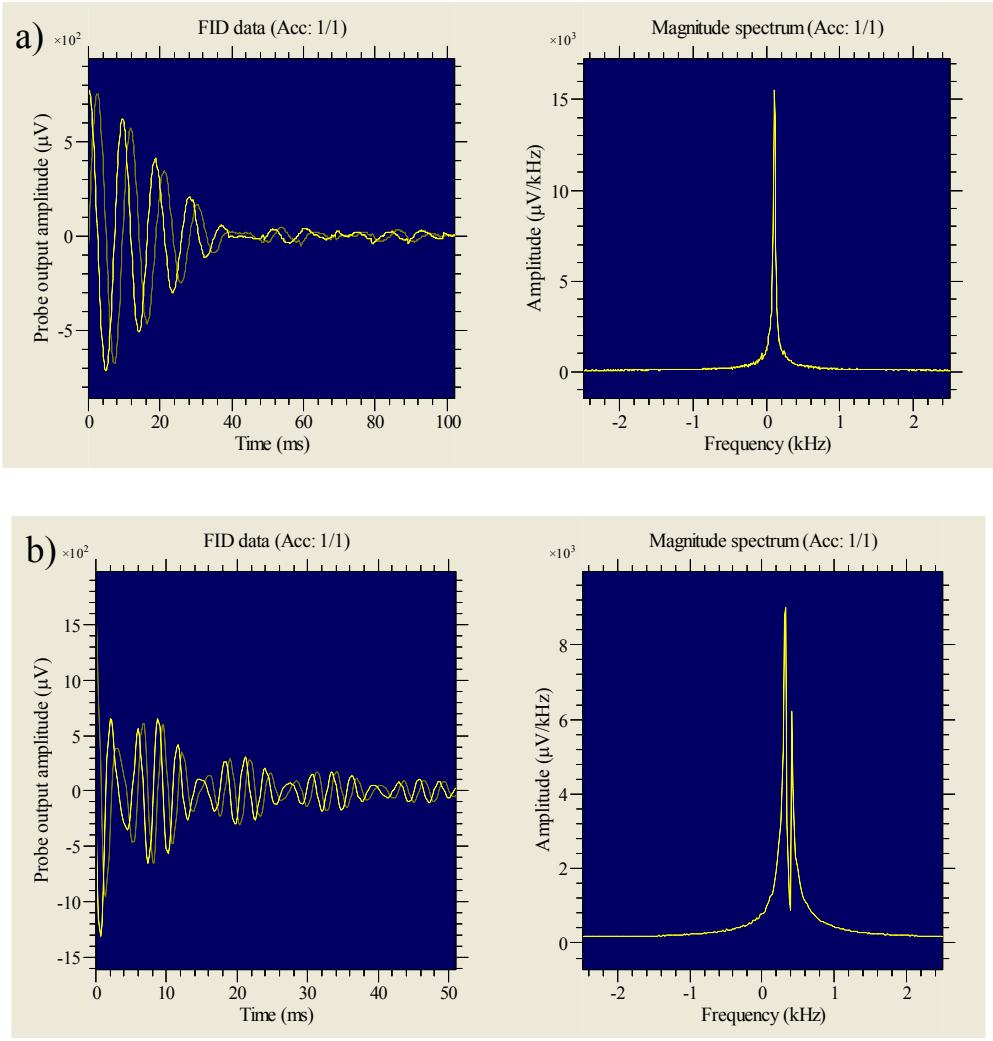

Fig 6.2: FID and Fourier transform from two HP gas samples, Xe and ^{3}He, in a spherical cell of 6 cm in diameter measured with the low field NMR. a) Signal coming from 200 mbar HP-Xe shows one single resonant frequency. b) Signal coming from 200 mbar of HP ^{3}He (B_0 ≈ 7.6 G) shows two resonance frequencies.

6.1 Theory

The basic foundation of this method is the measurement of the static magnetic field produced by HP-Xe sample stored in a spherical cell. This cell is placed in a homogenous holding magnetic field in z direction. Under these conditions, this sample produces a static magnetization $\overrightarrow{M}_{Xe}$ in the z direction given by

$$\overrightarrow{M}_{Xe} = P_{Xe} N \mu_{Xe} \hat{z} \qquad [6.2]$$

where μ_{Xe}=3.929(4)10^{-27} J/T, $N=\beta PV/RT$ with β the isotopic abundance of ^{129}Xe in Xe. The static magnetic dipole field generated by this magnetization is shown on Fig. 6.3a and is expressed in spherical coordinates r, θ and z [Jac98] as

$$B_z(r,\theta) = \frac{\mu_0}{4\pi r^3}\left[3\hat{r}(\hat{r}\cdot\vec{M}_{Xe}) - \vec{M}_{Xe}\right]\hat{z} \quad [6.3]$$

where $\mu_0=4\pi\cdot10^{-7}$ N/A^2 is the magnetic constant and r is the distance from the center of the sphere to the magnetic field sensor. Considering that $\vec{M}_{Xe} = M_{Xe}\hat{z}$, the magnetic field can be written as

$$B_z(r,\theta) = \frac{\mu_0 M_{Xe}(3\cos^2\theta - 1)}{4\pi r^3}\hat{z}. \quad [6.4]$$

Finally, if the magnetic field B_z is observed at $\theta = 0°$ in an additional holding magnetic field $B_0\,\hat{z}$, the total magnetic field experimented by the HP-Xe sample is given by

$$B_z^T(r) = \left(\frac{\mu_0 P_{Xe} N \mu_{Xe}}{2\pi r^3} + B_0\right)\hat{z}. \quad [6.5]$$

Therefore, if the sample of HP-Xe is placed far away ($r\rightarrow\infty$ in Eq. [6.5]) of a magnetic field detector, the measured magnetic field will be $B_0\,\hat{z}$ (see Fig. 6.3b). Then, if the HP-Xe sample is placed close to the detector, the variation of the magnetic field ΔB_z (see Fig. 6.3c) is given by

$$\Delta B_z(r) = B_z^T(r) - B_z^T(r\rightarrow\infty) = \frac{\mu_0 M_{Xe}}{2\pi r^3}\hat{z}. \quad [6.6]$$

Combining the equations [6.2] and [6.5], P_{Xe} and its error are given by [Kri09]

$$P_{Xe} = \frac{2\pi\Delta B_z r^3}{\mu_0\mu_{Xe}N} \quad [6.7]$$

$$\Delta P_{Xe} = |P_{Xe}|\left[\left(\frac{\Delta(\Delta B_z)}{\Delta B_z}\right)^2 + \left(3\frac{\Delta r}{r}\right)^2 + \left(\frac{\Delta N}{N}\right)^2\right]^{\frac{1}{2}}. \quad [6.8]$$

The measurement of the absolute polarization for a HP gas through the static magnetic field produced by a magnetic dipole was proposed for the first time by Cohen Tannoudji in 1969 [Coh69]. In his work, the absolute ^{3}He polarization of a sample of 4 mbar was measured inside a magnetic shielding and Rb-magnetometer. Nowadays, the ^{3}He polarization is measured daily using the same procedure described above but in a holding field of a few mT produced by air coils. In case of ^{3}He, a 15 cm diameter cell filled with 2 bar of this gas and $P_{He} = 0.8$ produces a ΔB_z typically around 0.15 μT. This value can be resolved with an ordinary Bartington fluxgate [Kri11].

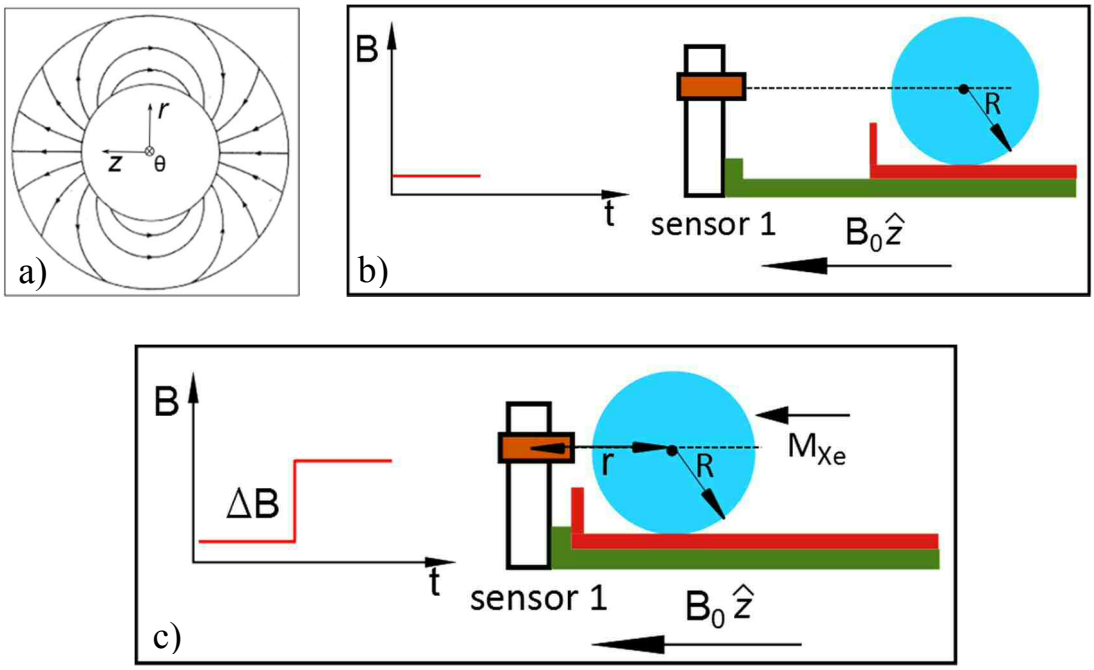

Fig. 6.3: Principle of the absolute measurement of the polarization of a hyperpolarized sample. a) Magnetic field lines of a magnetic dipole. b) If the HP sample is far away of a magnetic field sensor, it registers the holding magnetic field $B_0\hat{z}$. b) If the HP sample is close to the sensor, the measured magnetic field increases by ΔB_z.

Such simple measuring conditions are no applicable for HP-^{129}Xe because of the difficulty of generating pressures beyond 2 bar at high polarization levels. In addition, the isotopic abundance $\beta < 1$ and the magnetic moment of ^{129}Xe is 2.7 times smaller than μ_{He}. Nevertheless, the polarization of HP-^{129}Xe in equation [6.7] can be measured with a few extra effort and the required accuracy as well:

1. The value of ΔB_z produced by 0.5 bar of HP-Xe with P_{Xe} = 10%, in a spherical cell of R= 3 cm, ($M_{Xe} = 6 \cdot 10^{-7}$ Am^2) and measured at r = 4 cm is on the order of 1 nT. This value needs to be measured with accuracy better than, at least, 10 %. The magnetic field sensors, which provide the necessary resolution, operate only in regimes below some few μT with an internal noise of 0.1 nT. Therefore, a magnetic shield is needed to reduce the earth magnetic field below the saturation level of the sensor. In addition, the measurements of magnetic fields on the order of nT are extremely sensitive to environmental noise. This issue can be easily solved by using two magnetic field detectors in gradiometer configuration. Finally, the error of ΔB_z can be significantly reduced by averaging several measurements. This last step is possible due to the long T_1 of HP-Xe in the cells of GE-180 and the very homogeneous holding field inside the magnetic shield.

2. Since the magnetic sensors used in this work are encased coils, it is not possible to determine exactly where the sensitive point of the sensor is located. Consequently, the distance between the center of the cell and the sensor (r) cannot be measured geometrically. For this reason, r was determined by emulating the magnetization of a

dipolar magnetic field using a spherical coil and measuring the relation magnetic field vs. applied current (see equations [6.5] and [6.9]).

3. The number of atoms N is a parameter is proportional to the partial pressure of Xe (p_{Xe}) and it has to be measured for all the different methods that determine the polarization. The uncertainty of this value depends on the resolution of the pressure sensor.

Applying these considerations, this chapter will describe the first successful measurement of HP-Xe absolute polarization using its static magnetic field. With this method, the parameters and error sources of Eq. [6.7] can be measured without further assumptions, corrections or approximations.

6.2 Experimental setup

The experimental setup is composed by a magnetic shield with an internal (holding field) coil, two magnetic sensors (fluxgates), a pneumatic rail, a plastic arm and a solenoid for the transport of the HP sample.

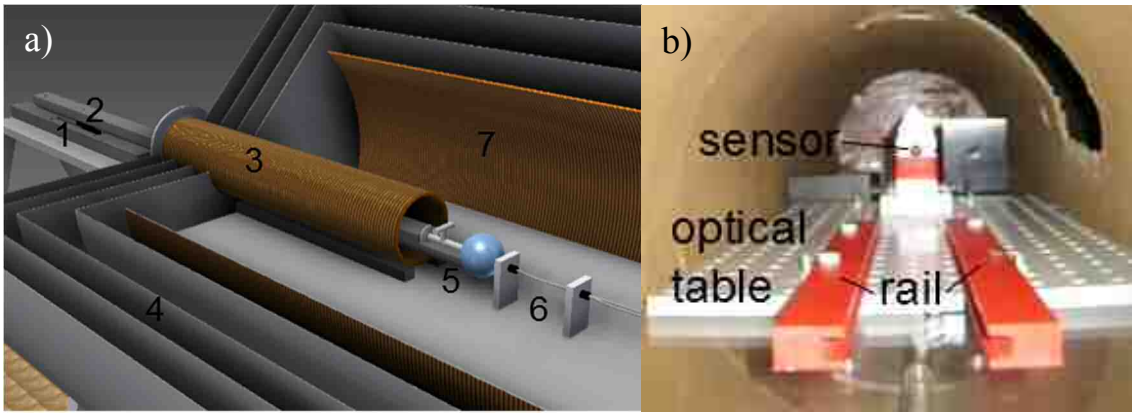

Fig. 6.4: Experimental setup for the measurement of the absolute polarization of HP-Xe. a) The setup is composed by 1: non-magnetic pneumatic rail, 2: plastic arm for holding the measurement cell, 3: solenoid, 4: μ-metal shield, 5: measurement cell and 6: fluxgates in gradiometer configuration. b) Picture of the inside part of the μ-metal shield. For the measurment, the solenoid is placed on the rail. In this way, it is always centered and in the same position.

The magnetic shield is constructed from five concentric cylinders of μ-metal. This material is an alloy of Ni, Mo and Fe with high magnetic permeability, which provides a low reluctance path for the external magnetic flux. The outer cylinder of the shield has a radius of 0.6 m and a length of about 1.6 m (Fig. 6.4a). Each cylinder is closed by a lid and the frontal lids have an opening of 16 cm in diameter. The shielding factor of the magnetic shield along the symmetry (z) axis is 167 (0.24 μT inside 40 μT outside) and the stability is 80 pT/h [Kra12]. Inside the shield, a coil of 80 cm in diameter and 1.5 m in length provides a magnetic field of about 1 μT using a stabilized current source. It is important to

remark that the size of the shield is not relevant as long as the holding magnetic field inside is homogeneous enough to provide a long T_1 time for the HP sample.

The gradiometer is built with two fluxgates with an internal noise of the 0.1 nT for a maximum range of 2 μT (Fluxmaster, Stefan Mayer, Germany). Both fluxgates are installed inside the μ-metal shield by fixing them to a non-magnetic optical table. The sensors are oriented along the symmetry axis of the holding magnetic field and aligned with the center of the cell ($\theta = 0°$ in Eq. [6.4]). The fluxgate, which will register the HP-Xe signal, is placed on the center of the coil. The second fluxgate is installed 15 cm behind the first one and will monitor environmental fluctuations. These fluctuations can then be subtracted online from the signal generated by the HP-Xe sample.

The HP sample is provided in a spherical cell of 6 cm diameter of GE-180 glass filled with about 600 mbar of enriched HP-Xe (85% ^{129}Xe). The T_1 of HP-Xe measured in this cell is about 80 minutes. This time permits the transport of the sample from the Xe-polarizer to the μ-metal shield with nearly no polarization losses. The sample is transported in a holding magnetic field provided by a solenoid. This solenoid was wound from 1 mm thick copper wire, has a length of 49 cm and a diameter of 10 cm. It can provide a holding field of 2 G when connected to the DC power supply. The solenoid is connected to a circuit composed by a Darlington transistor, two 100 Ω resistors and a 4.7 μF capacitor as presented in Fig. 6.6a. The function of this circuit is to produce an exponential decay of about 3 s when the circuit is switched off. This allows an adiabatic field transition once the sample is placed inside the μ-metal shield (Fig. 6.6b).

Besides providing a good homogeneity, the transport solenoid prevents that the sample passes through zero crossings of the magnetic field during its transport. This point is crucial especially during the transition from outside to inside of the μ-metal shield.

For performing the measurement, the sample is fixed to a plastic arm and placed in the middle of the transport solenoid as is shown in Fig. 6.5a. A holder keeps the plastic arm centered, then the sample can move only along the axis of the solenoid (see Fig. 6.5b). The transport solenoid, and with it the sample, are placed inside the outer cylinders of the μ-metal shield (see Fig. 6.4). Then the sample is pushed via the plastic arm inside the internal cylinder of the μ-metal shield and into the holding field of 1 μT.

Once the sample is inside the μT holding field, the solenoid is switched off and the plastic arm is fixed to a non-magnetic pneumatic rail. This rail is controlled by a Lab-View program which moves the plastic arm together with the cell, towards and away from the fluxgates in regular time intervals. This movement is performed with minimal vibrations, which could eventually increase the fluctuations in the measurement.

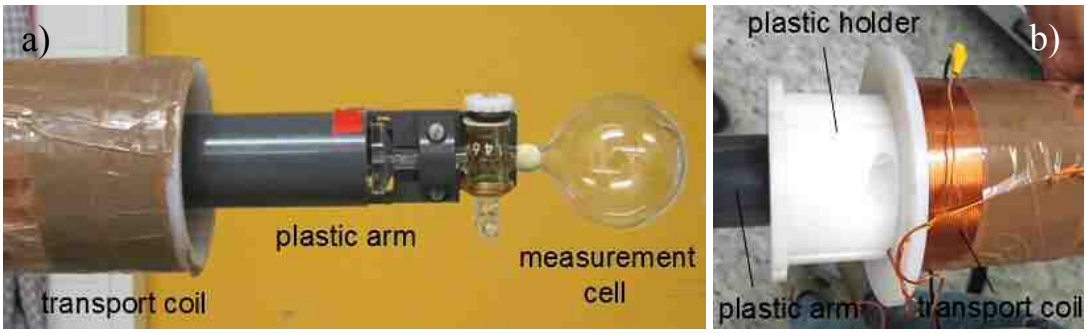

Fig. 6.5: a) The HP-Xe sample is mounted on a plastic arm. b) The plastic arm is fixed and centered inside the solenoid by a plastic holder.

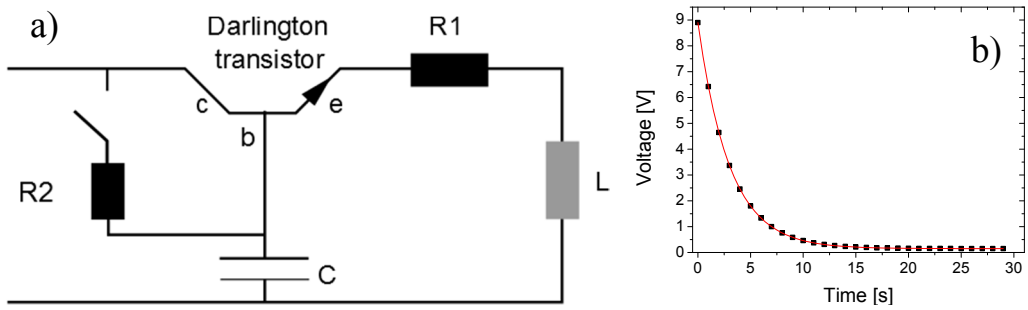

Fig. 6.6: a) Circuit connected to the solenoid for allowing an adiabatic field transition when switched off. b) Measured exponential decay when the solenoid is switched off. The time constant is about 2.5 s.

6.2.1 Noise and stability analysis

The fluxgates were connected to two multimeters (Hewlett Packard, 3456 A, USA) with a resolution of 1μV. First, the stability of the multimeters output was studied by measuring the voltage with the fluxgates being switched off. The values obtained are shown on Fig. 6.7a where the maximum of the peaks is about 30 pT. This value is one order of magnitude smaller than the internal noise of the fluxgates. Therefore, it should not affect the accuracy of the measurement.

The performance of the gradiometer was tested first with the fluxgates being switched on but the holding magnetic field off for an estimation of the background noise. The magnetic field was recorded by both fluxgates over six hours. These values were calculated by averaging the signal over intervals of 10 minutes. The result of this measurement is shown on Fig. 6.7b where the red and black lines correspond to the readings from the two fluxgates. Both readings in Fig. 6.7b overlap very well with small deviations. The readings show peaks with a maximum value of about 3 nT. A green line represents the difference of both signals (gradiometer configuration) which presents fluctuations of approximately 0.4 nT. These magnetic field fluctuations were reduced by more than 50% when this measurement was repeated using a holding field of about 1.7 μT.

Finally, variations of the noise due to the measurement method were explored. This test is needed because, even if the construction of this experiment was performed entirely

with non-magnetic materials, traces of magnetic materials (e.g. from machining) could influence the measurement. In addition, further perturbations could be introduced by the movement of the cell or by placing the transport solenoid inside the μ-metal shield. In order to check for this, an empty glass cell was mounted and the measurement procedure described above was performed. No changes on the noise or other perturbations were detected on the readings of the fluxgates.

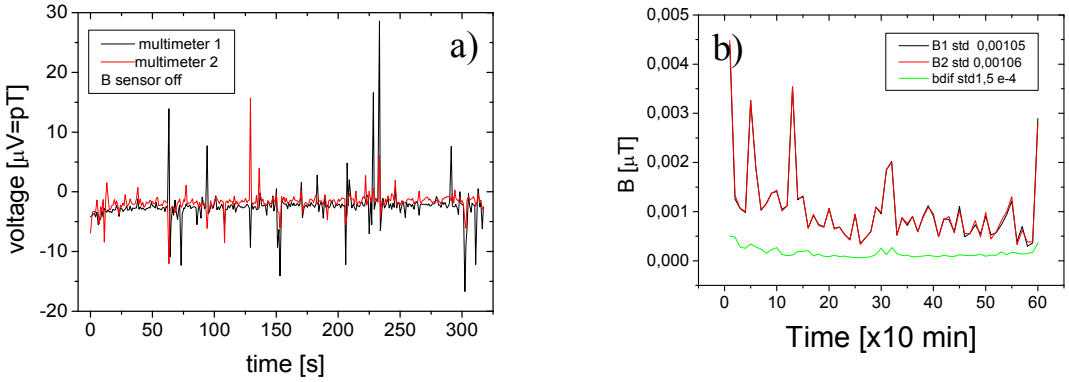

Fig. 6.7: Noise study and stability of the devices used for the absolute measurement of the HP-Xe polarization. a) Stability of the multimeter with the fluxgates off. The red and black lines correspond to the readings of both fluxgates. b) Measurement of the background noise over 6 h with the magnetic field off. Each point represents the average of the magnetic field during 10 minutes. The red line corresponds to the sensor close to the sample, the black line to the sensor for the enviromental noise and the green line is the gradiometer signal.

6.3 Calibration of *r*

A precise determination of the distance between the sensitive spot of the fluxgate and the sample, r, is crucial to obtain the high accuracy necessary for the measurement because of the $3\Delta r/r$ dependence in Eq. [6.8]. For the determination of r, a spherical PVC test coil of R = 3 cm radius was built with 14 windings of 0.1 mm cooper wire having spacing ΔZ = 6 mm between them (see Fig. 6.8a). This configuration will emulate the dipolar magnetic field of a HP-Xe sample of R = 6 cm. The magnetization produced from such a coil is given by [Dan71]

$$M_{coil} = \frac{IR^3}{3\Delta Z}. \qquad [6.9]$$

When this test coil is connected to a current input I in the μA range, its magnetization corresponds to about $1\cdot10^{-7}\mathrm{Am}^2$ which is comparable to the expected value of the HP-Xe sample. This magnetization will generate the magnetic field given by Eq. [6.6] where the magnetization is calculated with M_{coil} instead M_{Xe}.

This test coil was attached to the plastic arm at the same position than the measurement cell and then placed inside the μ-metal shield. The magnetic field induced by this coil was measured for 10, 50, 200 and 500 μA. The exact values for each current and

its corresponding magnetization are shown in Table 6.1. Fig. 6.8b shows a typical measurement where only three cycles were acquired for each current

According to Eq. [6.6] and [6.9], ΔB_z should show a linear dependence on I. This plot is shown on Fig. 6.8c. The values of the ΔB_z shown in this figure are the average of 10 cycles. Each cycle is defined by 30 s where the HP sample is close to the sensor and 30 s where it is faraway. This cycle last of 1 minute and several of them are acquired and then averaged. The slope on Fig. 6.8c is (0.0067 ± 0.0007) and r is determined to be (3.47 ± 0.01) cm via Eq. [6.6].

This calibration must be repeated regularly to prevent misalignments due to the fixation of the plastic arm and the cell when placed inside the μ-metal shield.

Table 6.1: Values of magnetization and intensity of the current applied to the test coil for the calibration of the parameter r.

Label	I	ΔI	M
[μA]	[μA]	[μA]	[nA/m^2]
10	9.97	0.41	22.7
50	50.64	2.04	116
200	208.17	8.34	485
500	491.00	21.00	1150

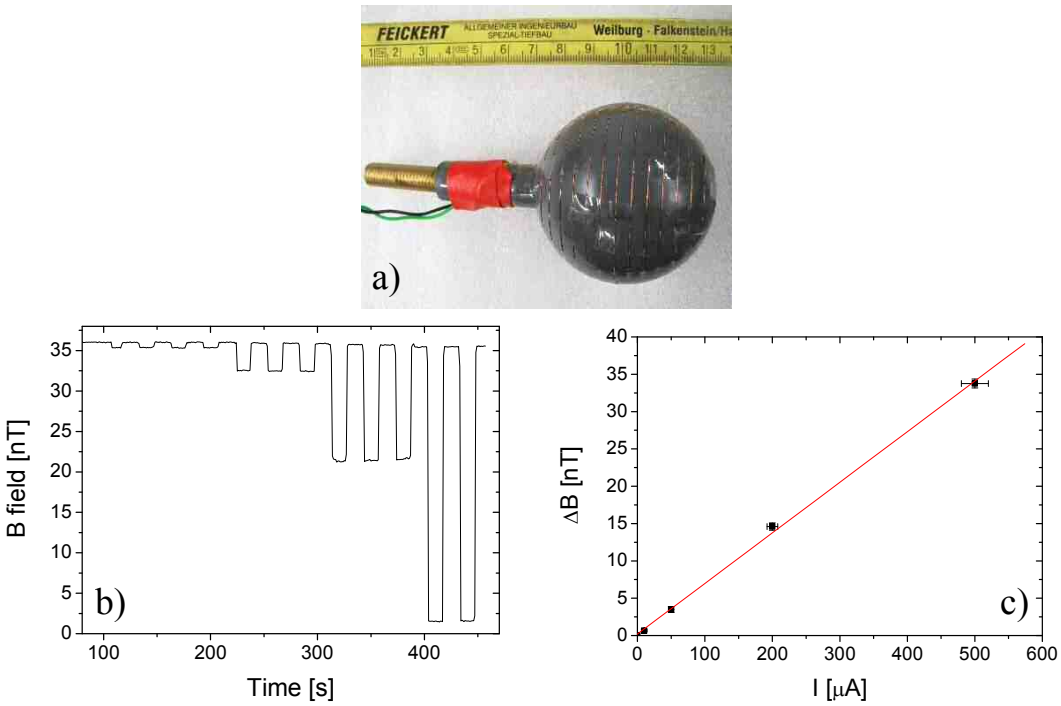

Fig. 6.8: Determination of r. a) Picture of the test coil. b) ΔB_z vs. time for 100 s < t < 240 s I = 10 μA, for 240 s < t < 300 s I= 50 μA, for 300 s < t < 390 s I=100 μA and the rest corresponds to I = 500 μA. c) ΔB_z vs. I. The value of the slope is (0.0067±0.0007) with a coefficient of linear correlation of 0.9998.

6.4 Measurement with HP-^{3}He

The experimental setup was tested with a sample of about 500 mbar of ^{3}He with an initial $P_{He} \approx 30\%$. This value was measured *in situ* in the He polarizer described in [Mro11] and subsequently transported into the µ-metal shield via the solenoid. The signal obtained by the two sensors is shown in Fig. 6.9a where the influence of the environmental noise (red line) is clearly visible. The signal of the gradiometer is shown Fig. 6.9b where $\Delta B_z = (5.7 \pm 0.1)$ nT and the fluctuations are significantly reduced. Using Eq. [6.6], P_{He} results 14 % for $r = 4.2$ cm. After the measurement, the cell was transported back to the He polarizer where $P_{He} = 10$ % was measured. The difference between the values of P_{He} measured in the He polarizer are most likely due to the magnetic field gradients crossed during the sample transport. Considering these circumstances, the value measured with the gradiometer is in good agreement with the values measured in the polarizer.

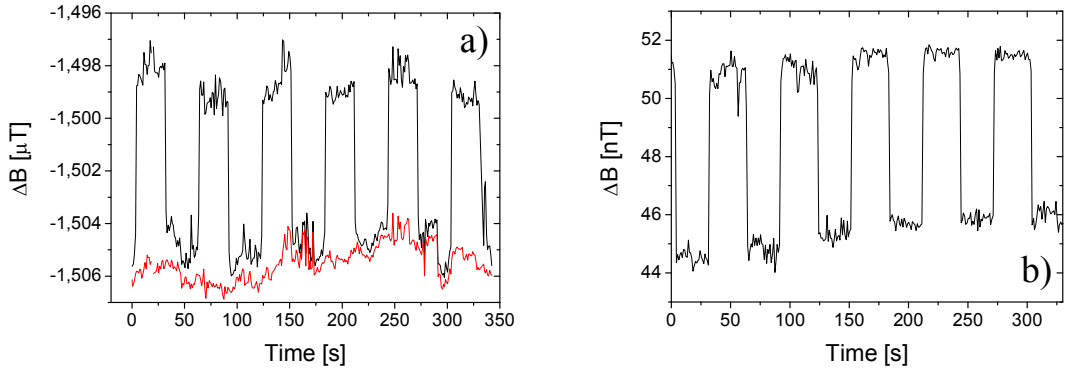

Fig. 6.9: Measurement of the absolute polarization of ^{3}He. a) The black line is the signal of the sensor close to the sample and the red line is the signal obtained from the backround. b) Gradiometer signal.

6.5 Measurement with HP-Xe

For the absolute measurement of HP-Xe polarization, about 600 mbar of HP-Xe (85% ^{129}Xe) were filled into a measurement cell with 6 cm in diameter. The cell was transferred to the low field NMR spectrometer and the NMR signal was recorded (S_1). After this, the HP-Xe sample was transported inside the solenoid and brought inside the µ-metal shield. All the transitions between different magnetic fields were performed under the adiabatic approximation avoiding changes in the direction of the magnetic field.

The measurement was performed as described in Section 6.2. Approximately 30 cycles of 60 seconds were recorded. After this procedure, the measurement cell was transported (again inside the solenoid) back to the low field NMR where a second NMR signal was recorded (S_2). The polarization losses are given by $S_2/S_1=\alpha_L*exp(-t/T_1)$ where α_L is the factor of losses. The time interval between measurements was typically about 35

minutes and the values of α_L oscillated between 0.05 and 0.08.

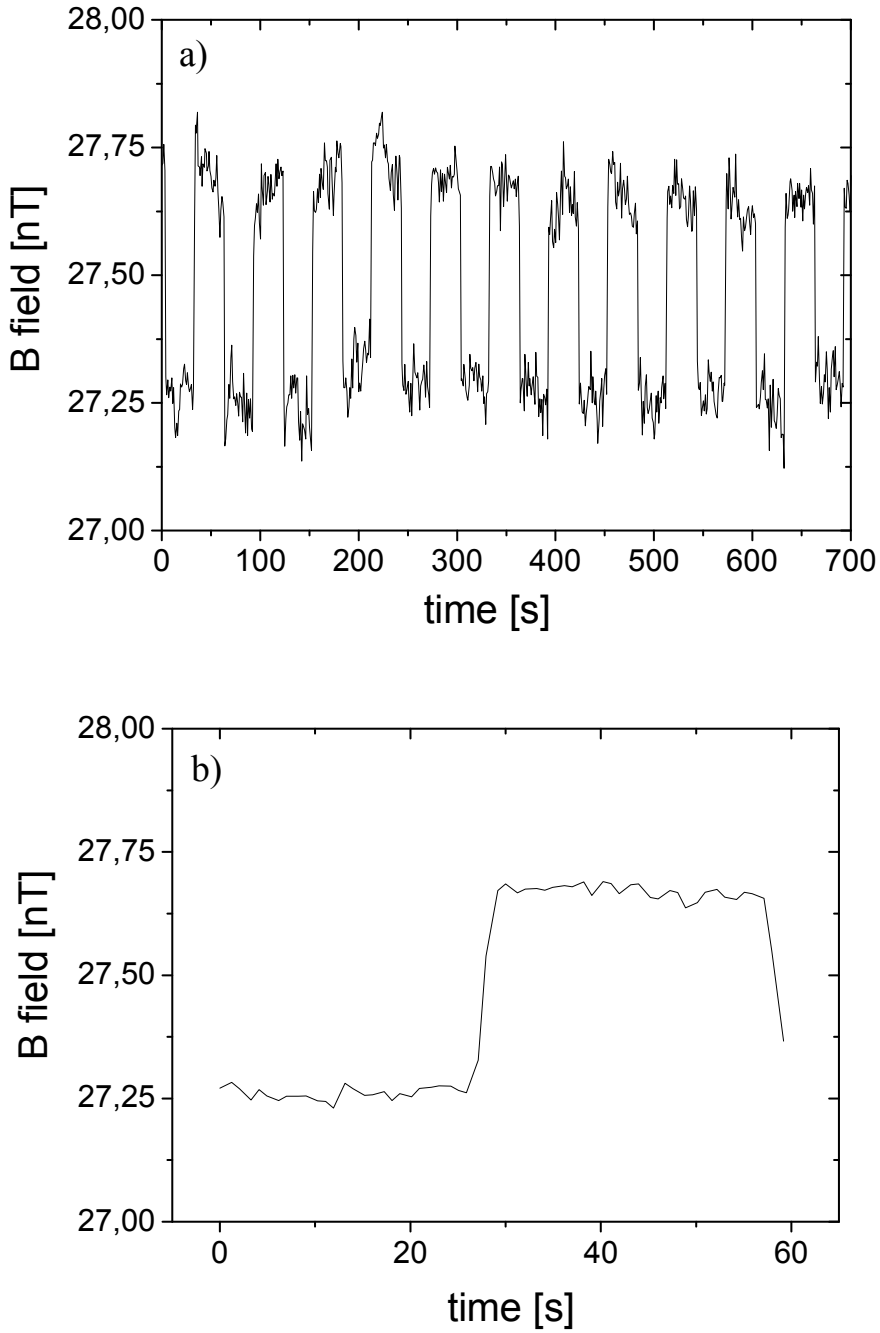

Fig. 6.10: a) Gradiometer signal obtained with a sample of HP-Xe using the setup described in Sec. 6.2. b) Average of the gradiometer signal of a).

Several HP-Xe samples obtained with different production parameters were measured using this method. The lowest value of ΔB_z was obtained with a HP-Xe sample prepared with 2 bar of total gas mixture, 1% of Xe, 6% N_2 flowing at 200 ml/min and four steps of accumulation. The pressure of this sample was p_{Xe} = (612 ± 18) mbar and r = (3.93 ± 0.01) cm. The magnetic field produced by this sample was measured by the gradiometer and it is shown in Fig. 6.10a. If ΔB_z would be calculated with the values of

this figure, its error would be over 0.2 nT. However, this value is reduced by a factor 5 when the average of the 8 cycles from Fig. 6.10a is calculated. The result of the average is shown on Fig. 6.10b where he value of ΔB_z extracted is (0.42 ± 0.04) nT leading to P_{Xe} = (0.022 ± 0.002). This value presents an absolute error for the polarization of about 10 % for a 2% polarization. The minimum value of ΔB_z observed by this method is around 0.1 nT. Therefore, the minimal polarization this method can measure (under the same measurement conditions) is $P_{Xe} \approx 0.008$.

The highest value of ΔB_z was (0.75 ± 0.03) nT obtained with a sample of p_{Xe} = (608 ± 19) mbar prepared with 4 bar of total gas mixture, 1% of Xe, 6% N_2 flowing at 200 ml/min and four steps of accumulation during freezing. Its polarization was measured to be P_{Xe} = (0.056 ± 0.002) using a distance r = (4.41 ± 0.01) cm.

For higher values of P_{Xe}, the relative error is significantly reduced because the error sources remain constant while P_{Xe} increases. The high sensitivity range of the fluxgates can also be used even for measurements of $P_{Xe} \approx 1$ because the generated magnetic flux still stays below the threshold of 2 μT. It is important to note than the high resolution of this experiment is a consequence of the long T_1 of the measurement cell, which allows several scans.

6.6 Application: Losses due to freeze and thaw in a batch-mode Xe- polarizer

The big advantage of this method besides its simplicity is the possibility of measuring HP-^{129}Xe in mixtures with other gases without further corrections. For this reason, this technique was used for the determination of the polarization losses due to freezing/volatilizing HP-Xe. The procedure described above was repeated filling the measurement cell with (1.72 ± 0.03) bar of a gas mixture composed from 7.5% HP-Xe (85% ^{129}Xe), 86.5 % He and 6% N_2 coming from the optical pumping cell. The gas mixture was prepared by the gas mixing system described in Section 4.1.1. The error related in the composition can be neglected since the resolution of the flow controller for Xe is 0.2%. Therefore, p_{Xe} = (129 ± 32) mbar where the error is the corresponding to the resolution of the pressure sensor at 1.7 bar. The sample was transported to the μ-metal shield and measured as explained in the Section 6.2. The average of 12 cycles gave a ΔB_z = (0.14 ± 0.03) nT resulting in P_{Xe} = (0.005 ± 0.010).

P_{Xe} was again measured in a sample of (643 ± 20) mbar of pure HP-Xe produced under the same polarization conditions (laser power, pressure, flow, gas mixture) but cryogenically separated. In this case, ΔB_z = (0.63 ± 0.03) nT and P_{Xe} = (0.044 ± 0.002). With these values, the recovery factor α_R can be defined as the ratio of the polarization measured in the original gas mixture (P_{Xe}^{GM}) and the cryogenically separated sample (P_{Xe}^{CS})

$$\alpha_R = \frac{P_{Xe}^{CS}}{P_{Xe}^{GM}}. \qquad [6.10]$$

The obtained value was $\alpha_R = (0.88 \pm 0.18)$ which is in agreement with estimations reported in Sec. 4.2.4 and in [Rus05].

So far, the polarization losses due to cryogenic separation were so far not precisely measured mainly because the standard experimental setups measure the Xe polarization online when HP-Xe is still mixed with buffer gases and the HP-Xe cannot be easily filled again into the "NMR region" after the cryogenic separation. In this way, the absolute measurement of the ^{129}Xe polarization provides a powerful tool for a precise characterization of the polarization losses along the different stages of HP-Xe production.

6.7 Conclusions

In this chapter, a method for the absolute measurement of the polarization for HP gases is presented. This method overcomes all critical points of the NMR method used by most other groups so far. The resolution of this method is higher than 1 % per bar of HP-Xe. The losses of polarization due to this procedure are less than 10%. The polarization of HP-Xe in gas mixtures can be then measured without further corrections, which was demonstrated by determining the losses due to the cryogenic separation.

The absolute measurement of polarization can also be applied to measurements online using a setup as shown in Fig. 6.11. The idea is to fill the cell with HP-Xe (pure or together with the buffer gases) and measure the difference in magnetic field between the readings with the evacuated cell and the cell full of HP-Xe. The signal-to-noise ratio of this measurement could be further improved either with the same sample and moving the sensor or by evacuating/filling the cell with new HP-gas.

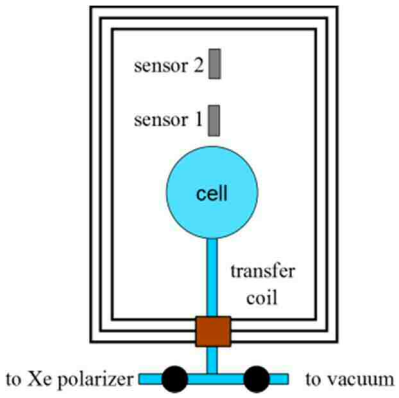

Fig. 6.11: Setup for an online measurement of the absolute polarization. The system is composed by a magnetic shield and a gradiometer. The black circles represent valves. The gas mixture containing HP-Xe is filled into the cell placed in a holding field inside a small magnetic shield. The sensor 1 can move close and faraway from the cell registering ΔB_z. Finally, the gas mixture can be evacuated or reinserted to the system.

Chapter 7: Conclusions and overview

This work achieved successfully the construction, installation and testing of a facility for production, storage and characterization of HP-Xe. This facility consists of:

- A mobile Xe-polarizer which is easy to operate with a wide and flexible range of working conditions. This setup is running since 2013 and it is able to produce 400 mbar·l/h of HP-Xe with $P_{Xe} \approx 5\%$. Many tests concerning design and technical capability were performed using this machine. Those tests lead to the design of an OP-cell which requires maintenance about once per year (under daily operation), a freeze/volatilization unit with polarization losses below 10% and a mixing gas station which minimizes evacuation times and is able to mix HP-Xe with controlled amounts of buffer gases. The robust design of this Xe-polarizer also allows for transport and it will be later relocated in the Jülich Research Center for the search of the electric dipole moment of ^{129}Xe using He-Xe co-magnetometers.
- A second mobile Xe-polarizer constructed up to its final stage. This polarizer was designed to produce high amounts of HP-Xe (about 1 bar·l/h) for medical applications. This polarizer was constructed until its final stage. However, the activities with this polarizer stopped in 2013 due to the lack of interest of the German medical community in lung MRI with HP-Xe. This machine is transferred to the group of Prof. D. Budker for performing NMR experiments with liquid HP-Xe.
- A low field NMR system was built for measuring the NMR signal of HP-Xe and its T_1 under storage conditions (about 2 mT, room temperature, spherical containers with a maximum diameter of 12 cm). Extremely long T_1^{wall} times for HP-Xe in glass cells made from GE-180 with no coating and Rb-free were measured in this device. These results will increase significantly the resolution of experiments related He-Xe co-magnetometers [All14].
- The T_1 measurements resulted on a limit of Xe relaxation $T_1^{XeXe} = (4.57 \pm 0.06)$ h. By measuring the T_1 of HP-Xe with different buffer gases, it was found that CO_2 has the highest efficiency to destroy the Xe-Xe dimers so far reported which will be very valuable especially in spin clock experiments and medical applications.
- In addition, the conditions and methods to obtain a high reproducibility of the wall relaxation time in GE-180 cells were developed. The high reproducibility achieved for the measurement of T_1 of HP-Xe allowed identifying an extra relaxation mechanism related to the isotopic proportion of ^{129}Xe in Xe. This dependence was not considered in the literature and it will be further investigated by measuring T_1 of HP-Xe mixed with buffer gases using different isotopic mixtures. Future experiments are planned for measuring T_1 at different temperatures, magnetic fields and using H_2O as buffer gas.
- Finally, a method for measuring the absolute polarization of HP-Xe (and other HP

gases) was developed obtaining sensitivity better than 1 %. The high resolution of this experiment is strictly related to the long T_1^{wall} of the GE-180 measurement cells which permit several scans for averaging. The next development step for this experiment is to reduce its size so that can be easily transported.

The measurements of the absolute polarization resulted in P_{Xe} values of 2 - 5 % which are rather low when compared to the values reported in the literature. At this point, it must be remarked that all those values were measured via NMR and rarely error bars or confidence intervals are given.

However, the Xe-polarizers that report high polarization values used laser powers over 100 W and/or $\Delta\lambda \approx 0.1$ nm while the laser used in this work has a power of 30 W and $\Delta\lambda \approx 0.3$ nm. Another reason for the low polarization could be related to the OP-cell. Many reports describe an aging of the OP-cell over time due to chemical attack of Rb to the walls. This process increases the wall relaxation rate resulting in longer spin-exchange times and, therefore, poor polarization levels [Bab05] [Wil14]. The original OP-cell of the Xe-polarizer for fundamental physics was built more than ten years ago. This cell was used because it could withstand pressures until 10 bar, which is an extremely high value for this geometry. Since the bandwidth of the new laser does not require such high pressures, a new cell suitable for lower pressures can be installed.

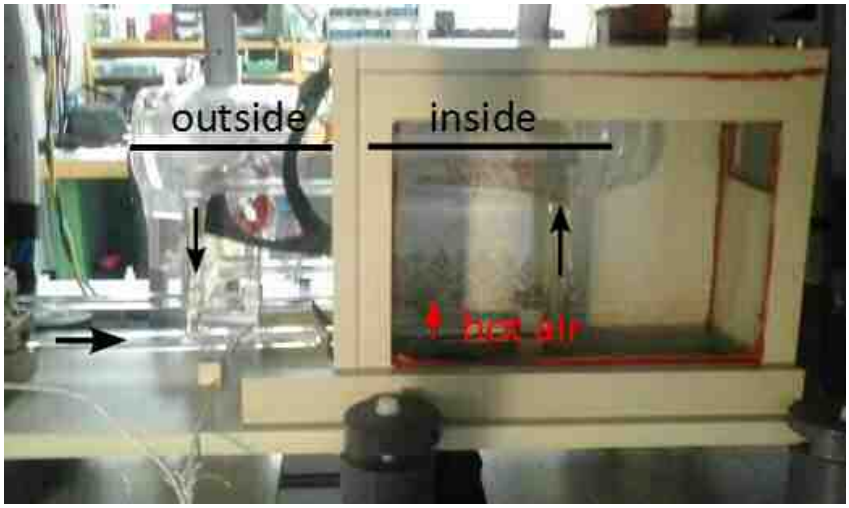

Fig. 7.1: New OP-cell with oven. The position of the oven is variable allowing to select the area of the OP-cell at high temperature. The black lines show the part of the OP-cell inside and outside the oven. The black arrows show the gas mixture flow and the red arrow shows the incoming hot air.

For increasing the polarization, a new laser system was purchased with 65 W and $\Delta\lambda \approx 0.1$ nm (Opti-Grate) and a new OP-cell was constructed and installed. The new OP-cell has 20 cm in length and 3.8 cm in diameter which results in a volume of 227 cm^3. This volume is around five times higher than the OP-cell presented in Chapter 4. This new cell

is mounted in an oven made from PEEK oven which is movable [Wit14] [Kor13] allowing a better temperature control as shown in Fig. 7.1.

At the end of this work, I installed the new laser, the new OP-cell and the mobile oven resulting (without further optimization) in an improvement in the NMR signal of a factor 3. The next step is to optimize the working parameters to the new laser and construct an online monitoring of the NMR signal of HP-Xe in the OP-cell in order to simplify the optimization process.

After all the improvements proposed above, it is expected to obtain polarization levels over 20 %.

Appendix 1: NMR signal as the maximum of the Fourier transform

In this appendix, it will be explained why the maximum of the Fourier transform was chosen as the NMR amplitude.

The first scan of a T_1 measurement has usually S/N ≈ 40. The environmental noise does not influence the FID signal or its Fourier transform as shown in Fig. A1.1a. However, after several scans the signal progressively decreases until reaching a S/N ≈ 2. In this regime, the noise level is substantial as shown in Fig. A1.1b. These data must be treated carefully in order to extract the correct T_1 from any fit routine. For this reason, a good resolution of the curvature of the exponential decay is crucial for a precise determination of T_1.

To check the behavior of the fit of T_1, different methods of determining the NMR amplitude were tested. The exponential decay of T_1 was calculated processing the data extracted from the FID in four different ways: the maximum of the Fourier transform of the FID, integral over 10 and 20 points around the maximum value of the Fourier transform and the maximum (first point) of the FID which is equivalent to the integral of all the spectrum. The four graphics of NMR signal vs. time are plotted together in Fig. A1.2 where the dotted circle shows the critical area where S/N<2.

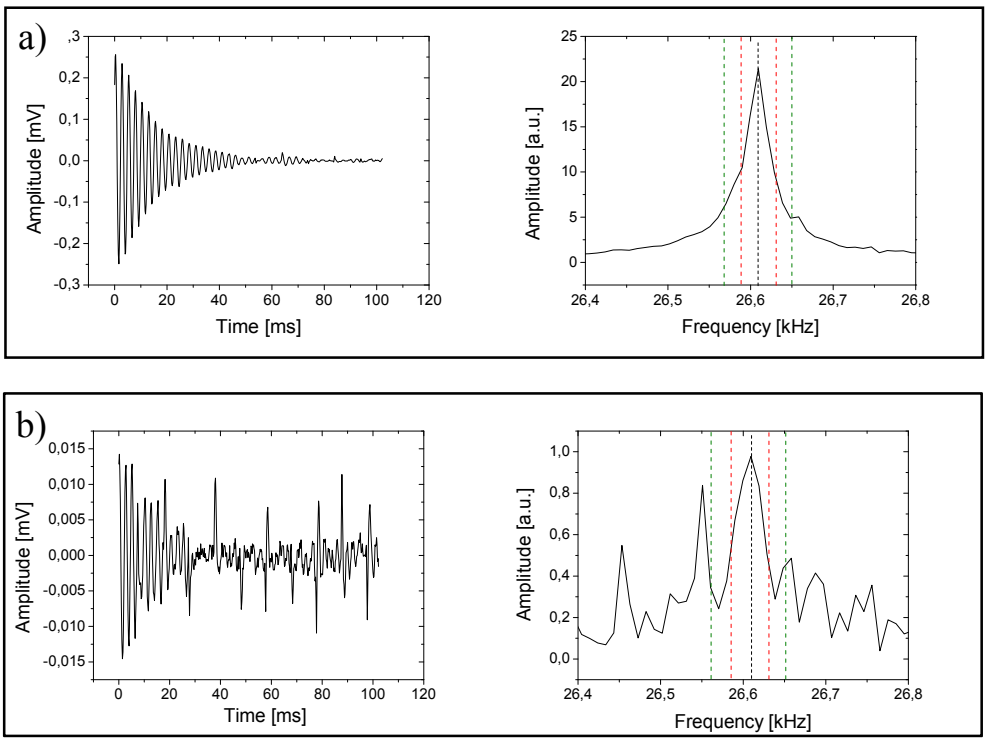

Fig. A1.1: FID and spectrum of a sample of HP-Xe during a T_1 measurment. The black dotted line tags the maximum of the Fourier transform while the red and green dotted lines show the interval of the integral for 10 and 20 points respectively. a) First scan of a T_1

measurement. No evidence of noise is observed. b) NMR signal of 30th scan of the same T_1 measurement. In this case, the environmental noise is evident.

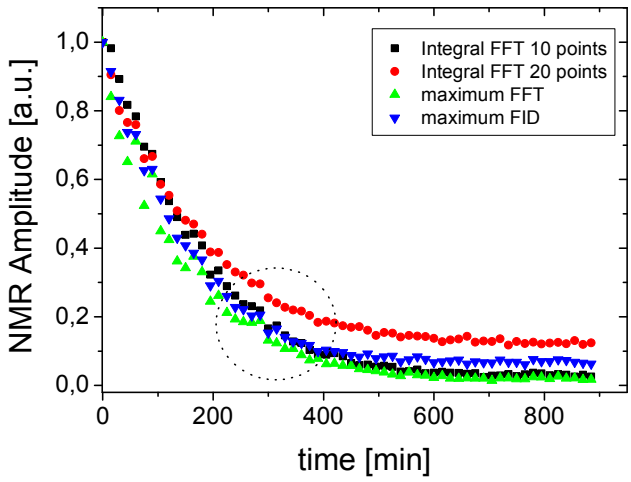

Fig. A1.2: T_1 calculated with different definitions of NMR amplitude. The black squares represent the values obtained by integration the Fourier transform over 10 points around the maximum.

From the figure above, it is evident that both integrals of the Fourier transform and the maximum of the FID saturate much faster than the maximum of the Fourier transform. This effect leads to a shorter T_1 time as when calculated from the maximum of the Fourier transform.

This analysis was performed with about 30 datasets. Different forms of data filters were also tested. In all cases, the maximum of the Fourier transform was the most sensitive method for the determination of the NMR amplitude for T_1 measurements. For this reason, in this work, the NMR amplitude is defined as the maximum of the Fourier transform of the FID.

The width of the Fourier transform and the position of the maximum must be constant for using this method. It is crucial to ensure that T_2^* of the sample remains constant over all the experiment. Otherwise, changes in the maximum of the Fourier transform could be produced by changes in the homogeneity (or T_2*). Particularly in the experiments presented in this work, the position of the maximum of the Fourier transform was checked consistently.

Appendix 2: Concept and construction of the Xe-polarizer for medical applications

The Xe-polarizer for medical applications is designed to produce 1 bar·l/h of HP-Xe with $P_{Xe} > 20\%$ only in batch mode. This high production rate was achieved with a revolutionary design conceived by Hersman and Ruset in [Rus05]. This design introduces four groundbreaking modifications in the development of Xe-polarizers, some of them were applied already on the Xe-polarizer described in Chapter 4:

Use of high power narrowed lasers. The use of high power lasers was first presented by [Zoo02] using a laser of 210 W with $\Delta\lambda \approx 1.6$ nm in a OP-cell of 250 cm^3 with a gas pressure of 4.5 atm obtaining $P_{Xe} > 65\%$. This high performance can be further improved by using efficiently the laser power by adjusting its bandwidth to the bandwidth of the Rb absorption line (see Eq. [2.17]). This condition allows low gas mixture pressures resulting in a lower Rb relaxation rate and, in consequence, achieving higher polarization values. In addition, the spin-exchange rate increases by a factor five allowing higher production rates.

Large Rb pre-saturation volume outside of the OP-cell. It prevents Rb runaways and ensures the thermal equilibrium of the gas mixture when entering the OP-cell.

A vertical OP-cell divided in cold and hot region. SEOP takes place on the hot region (about 150°C) of the OP-cell. The cold region has a temperature of about 20°C, so the Rb condenses on the glass walls or fells to the bottom of the cell by gravity.

Large volume of the OP-cell is necessary to maintain the production rate at low pressures ensuring a lower wall relaxation rate due to a high S/V. This fact contributes to a faster buildup of Rb polarization. The maximum size of the cell is limited by the shaping of the laser beam to where the intensity of the light should be equally distributed over the OP region.

Counter-flow modus in an OP-cell which has a hot region (OP region) and a Rb-free cold region (see Fig. A2.1). This production mode and geometry have two main advantages: First, Rb and Xe are polarized as they move upwards towards the OP-cell outlet achieving highest Xe polarization at the exit from the OP region. In the cold region, the Rb density drops and Rb atoms are condensed on the glass surface. Second, the laser intensity and the optical pumping rate are highest at the outlet of the OP region, which should lead to full Rb polarization and minimum Xe polarization losses.

Automated freeze/volatilization unit using spiral shaped accumulation cell. The benefits of this design were already discussed on Section 4.2.

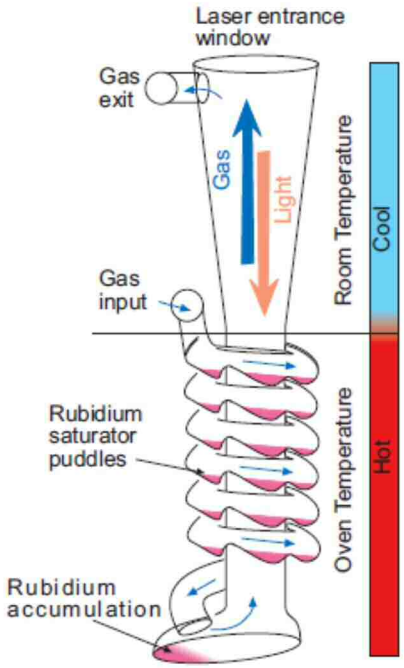

Fig. A2.1: Sketch of the OP-cell of the Xe-polarizer designed by Hersman and Ruset extracted from [Rus05]. The gas mixture (He, N_2 and Xe) enters to the Rb saturator through the gas input. The Rb saturator is a glass spiral with puddles which prevent that liquid Rb flows rapidly to the bottom part when the saturator is heated. The gas mixture saturated with Rb vapor enters the OP-cell and interacts with the laser. This part of the OP-cell and the Rb saturator have the same temperature since they are immersed in an oil bath. The condensed Rb and Rb drops, which could eventually reach the OP-cell, are out of the light path in an appendix at the bottom of the cell (Rb accumulation). The gas mixture with HP-Xe leaves the hot part of the OP-cell flowing through a cooling jacket cooled by a water flow at 20°C. The Rb condensates in this part and plunges to the bottom of the cell while the gas mixture containing HP-Xe flows out of the OP-cell to the separation unit.

In the work of Ruset, the OP-cell is 1.8 m in length; 1 m is used for optical pumping and 80 cm for cooling of the gas mixture. The volume of the OP-cell (1.2 l) is about 20 times higher than the standard Xe-polarizers. Therefore it requires a high power laser (150 W before narrowing and about 90 W on the OP-cell) according to [Rus05]. The Rb saturator is filled with 25 g of Rb. The optimum conditions for polarization were: pressure of 0.67 bar, a total flow 1360 ml/min of gas mixture containing 350 ml/min N_2 and 5 to 20 ml/min Xe and the rest He. The optimum working temperature of the oil bath was 160°C. The separation of HP-Xe from the buffer gases is performed with an automatic FVU unit using a helical accumulation cell and a c-magnet with a magnetic field of about 0.1 T.

A2.1 Xe-polarizer for medical applications at the Uni-Mainz

This Xe-polarizer uses a similar design than the design presented by Ruset *et al* but with some modifications such as:
The height of the OP-cell is reduced about 50%.
The bottom part of the optical pumping cell is shaped in a different way which allows working pressure regimes until 1.5 bar.
The holding magnetic fields are composed by a system of coils, a c-magnet and a Halbach magnet for accumulation of frozen Xe.
Addition of a mixing gas station which allows storage and mixing of HP-Xe with other buffer gases.

Due to the similarities with the polarizer described in Chapter 4, this polarizer was constructed in close collaboration with four students performing their Diploma thesis in physics: The first attempt in montage and narrowing of the laser was performed by E. Venzner in [Ven11] in teamwork with Dr. S. Karpuk. The system of coils, heating and structure and montage of the cell were performed by M. Fuchs in [Fuc12]. The construction and characterization of the c-magnet and Halbach magnet were performed by B. Niederländer in [Nie13] together with Dr. P. Blümler. The regulation of the temperature, construction of the gas module, adjustments in the laser and its casing in the laminar flow were performed by M. Braun in [Bra13]. In addition, much expertise from the mechanical workshop and the glassblower of the Physics Institute was required for the construction of this machine.

This polarizer is composed by three independent modules: gas mixing module, polarizing module and the power module. Each one is a robust structure which can be transported separately and the modules can be reconnected when required.

A sketch of this Xe-polarizer is shown in Fig. A2.2 while a photograph of all modules is shown in Fig. A2.3.

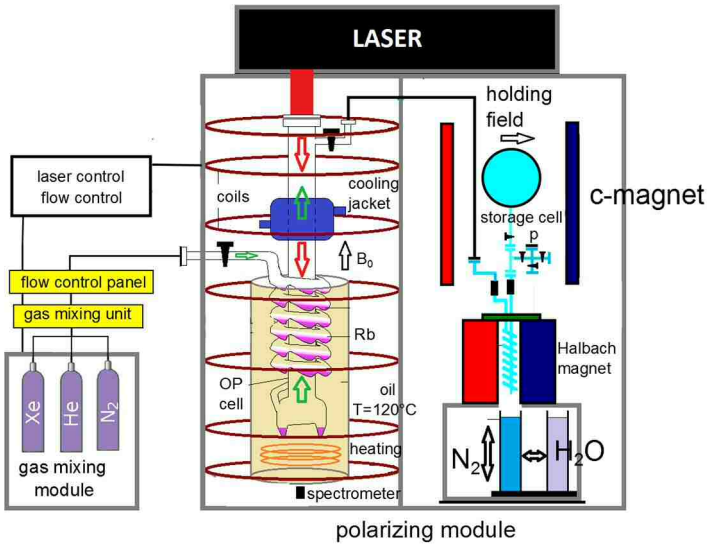

Fig. A2.2: Xe-polarizer for medical applications at the Uni-Mainz (figure modified from [Bra13]). The gas mixture is produced in the gas mixing unit which mixes He, N_2 and Xe in a determined proportion. Then, it is controlled by the flow control panel which measures and regulates the flow. The gas mixture enters the OP-cell, first flowing through the Rb saturator and then entering the hot region where the Xe is hyperpolarized. The hot region of the OP-cell and the Rb saturator are heated by a silicon oil bath. The gas mixture with HP-Xe and Rb flow through the cold region where the Rb condensates on the walls of the cooling jacket.

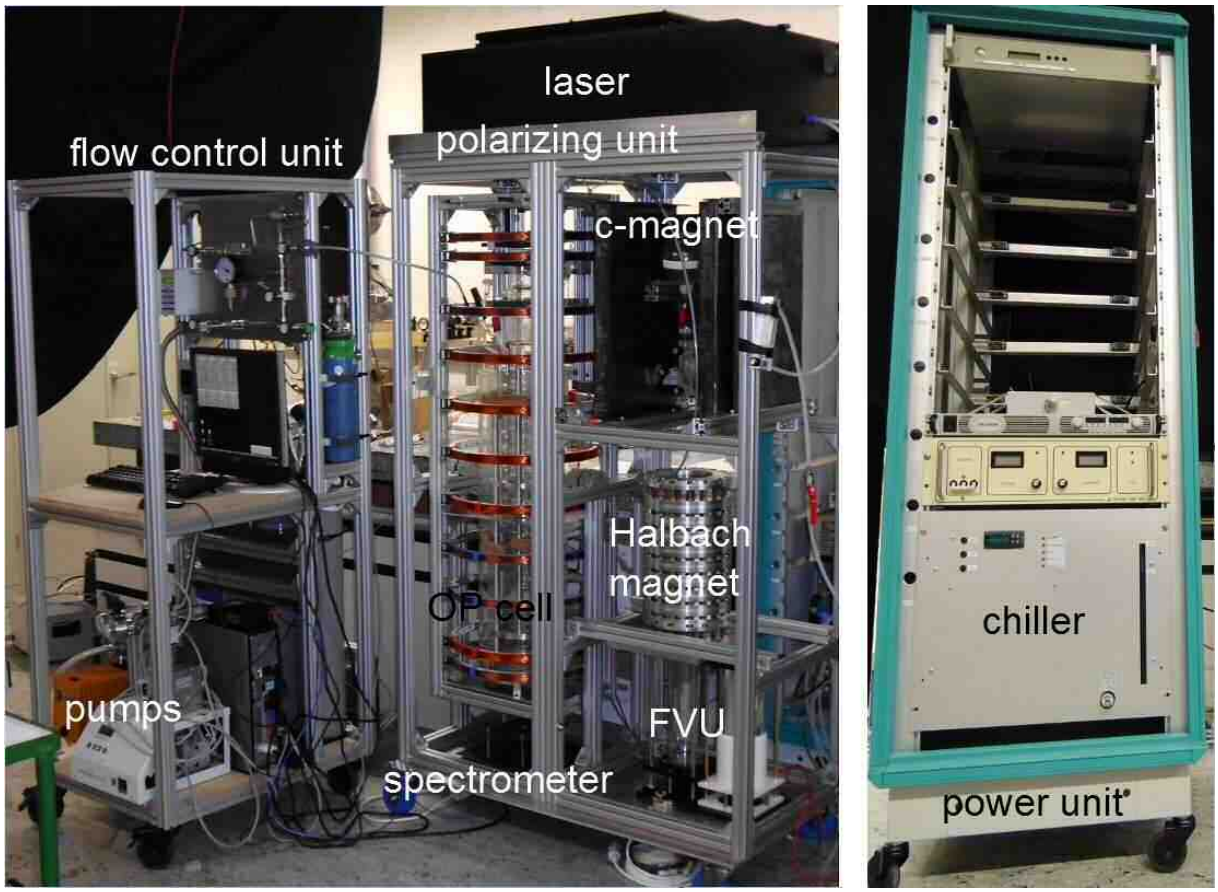

Fig. A2.3: Photograph of all modules of the low-pressure Xe-polarizer. The flow control unit consists of the gas bottles, pumps, PC for operation, gas mixing unit and flow control unit. The second module is the polarizing unit which contains the OP-cell, laser, oil bath, FVU, Halbach magnet and filling station. The third unit contains all power supplies and the chiller for the temperature control of the laser.

A2.2 Flow control unit

The flow control unit consists of a gas mixing unit, the flow control panel, a mechanical and turbo pump and the PC for control of the flow, temperature and laser. The gas mixing unit is constructed in the same way as shown in Fig. 4.5 with three flow controllers (Bronkhorst, Germany), a pressure controller and a buffer volume of 3.5 l. The maximum flow provided by the flow controllers is 50 ml/min for Xe, 700 ml/min for He and 500 ml/min for N_2. These values were chosen based in the work of Ruset [Rus05]. Each flow controller is connected to the pressure reducer of each bottle (Xe, He and N_2 respectively). The proportion of each gas in the gas mixture is set by the opening of each flow controller as explained in Sec. 4.1.1.1. The pressure controller sets the total pressure in the buffer volume and the gas control panel. A picture of the gas-mixing unit is shown in Fig. A2.4a.

The flow control panel of the Xe-polarizer for medical applications is a simplified version of the Xe-polarizer described in Sec. 4.1.1.2 but using only a bypass valve instead of two. A picture of this panel is shown in Fig. A2.4b. The components of this panel are: input and output membrane valves (Swagelok, USA), a flow controller (maximum 2000 ml/h of He, Analyt, Germany), a gas filter, a pressure sensor from -1 to 3 bar , by-pass valve and a needle valve to regulate the flow (Swagelok, USA). This panel was built using magnetic parts (stainless steel) because no hyperpolarized gas will be in contact with any of these parts.

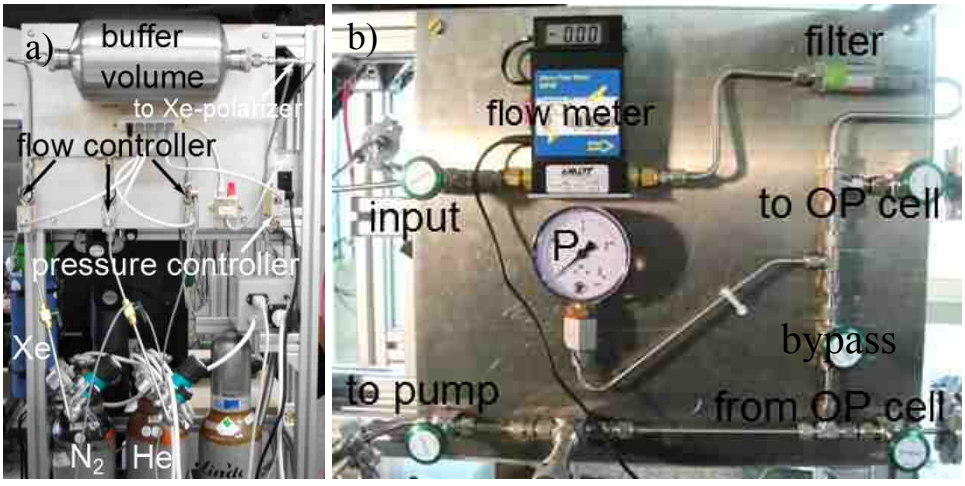

Fig. A2.4: a) Gas mixing unit of the low-pressure Xe-polarizer. Each gas bottle is connected to a pressure reducer and to a flow controller especially calibrated for each gas. The gases mix in the buffer volume which pressure is regulated by a pressure controller. b) Flow control panel. The gas mixture (He, Xe and N2) enters the panel and its flow is measured

by a flow meter. Then, the gas mixture flows through the filter to the OP-cell. The flow coming from the separation unit is regulated by a needle valve and is evacuated.

A2.3 Magnetic fields

The holding magnetic fields consist on three independent systems: system of coils, a homemade c-magnet and a homemade Halbach magnet as is shown in Fig. A2.5. The magnetic field of the three parts overlap in such a way that not changes of sign are observed in the magnetic field flux lines. This was checked with a compass (Magnaprobe).

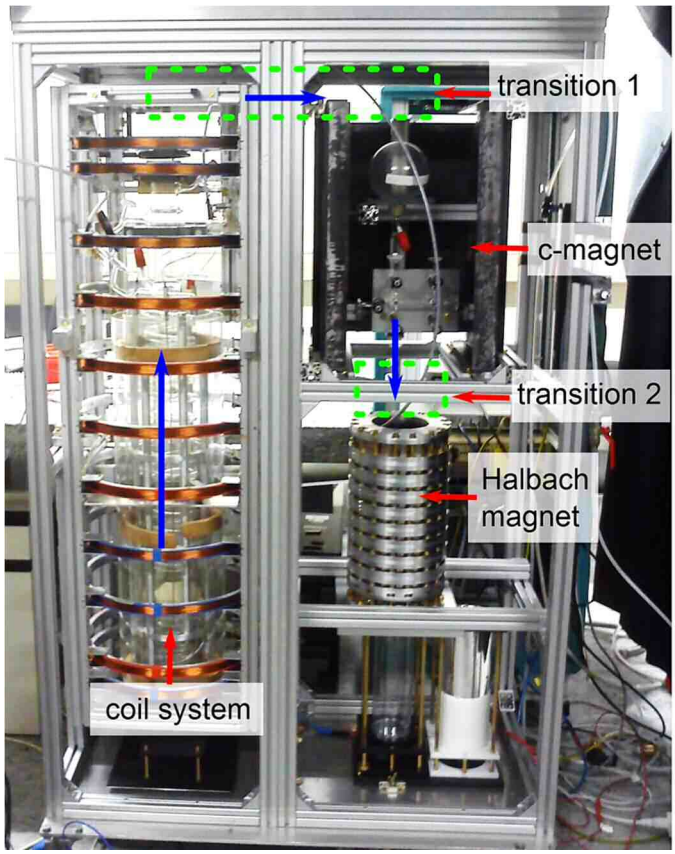

Fig. A2.5: Holding magnetic fields of the low-pressure Xe-polarizer: a system of coils, a c-magnet and a Halbach magnet. The blue arrow shows the gas mixture path. The green dotted line shows the transition areas where the gas mixture (with HP-Xe) flows through.

The system of coils is composed by 11 coils. The distance and the number of turns were calculated and optimized by [Fuc13] and the results are given in Table A2.1.

Table A2.1: Characteristics of the coil system of the low-pressure Xe-polarizer calculated by [Fuc12].

Coil	1	2	3	4	5	6	7	8	9	10	11
Turns	129	123	126	125	126	124	126	125	126	123	129
Position [cm]	-59	-53.8	-39.5	-26.6	-13.3	0	13.3	26.6	39.5	53.8	59

The magnetic field of the coils system was measured on the axis of the coil system by a Bartington fluxgate using the same procedure described in Sec. 4.1.2. These values were used to calculate the average homogeneity over the optical pumping cell which results to be $(4.7 \pm 2.6)\ 10^{-4}$ cm^{-1}. The details of this measurement can be found in [Fuc12] and [Bra13].

A2.3.1 C-magnet

The c-magnet was designed to host a spherical storage cell of 20 cm in diameter with a holding field lower than 5mT and $H \approx 10^{-3}$ cm^{-1}. The magnetic field was decided in order to prevent the magnetization of the cell and the homogeneity was established to ensure a long storage time (at least 1 h).

The c-magnet is built with magnetic rubber plates mounted in an iron structure for homogenization of the magnetic field. The position and size of the rubber plates were calculated and optimized to provide an optimum homogeneity on the region where the storage cell will be placed. The holding magnetic field and its homogeneity on the area of the storage cell are (4.307 ±0.027) mT and $(1.6 \pm 2.2)\ 10^{-3}$ cm^{-1} respectively (see Fig. A2.6). The size of the structure is 55 cm in height, 40.3 cm in width and 40.7 cm in depth and its weight is about 40 kg. The details of the construction and characterization of this magnet can be found in [Nie13].

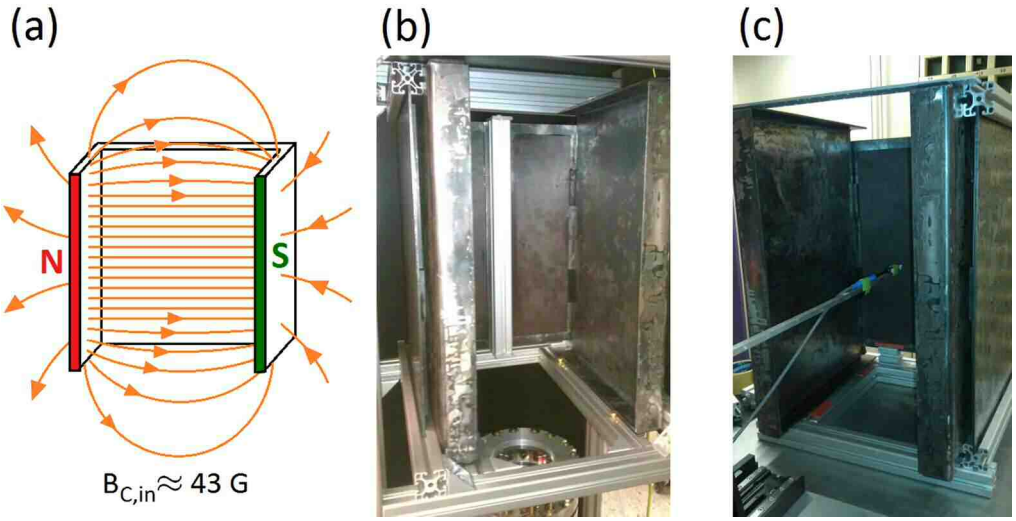

Fig. A2.6: C- magnet (Figure courtesy of M. Braun). a) Sketch of the magnetic flux lines of the c-magnet. b) Mountage of the c-magnet in the polarizing module. c) Measurement of the magnetic field produced by this c-magnet using a 3D table with a gaussmeter (Lakeshore 4220, USA).

A2.3.2 Halbach Magnet

This Halbach magnet was built with 12 aluminum rings harboring 16 octagonal

NdFeB-46MGO permanent magnets (see Fig. A2.7). It has 43.6 cm in height, its inner and outer diameter are 22.7 and 13 cm respectively. The holding magnetic field is about 0.2028 T and the homogeneity is (2.5 ± 2.4) 10^{-3} cm^{-1} in a cylindrical volume determined by a radius of 3.75 cm and a height of 24 cm (9.4 cm of the top surface of the magnet).

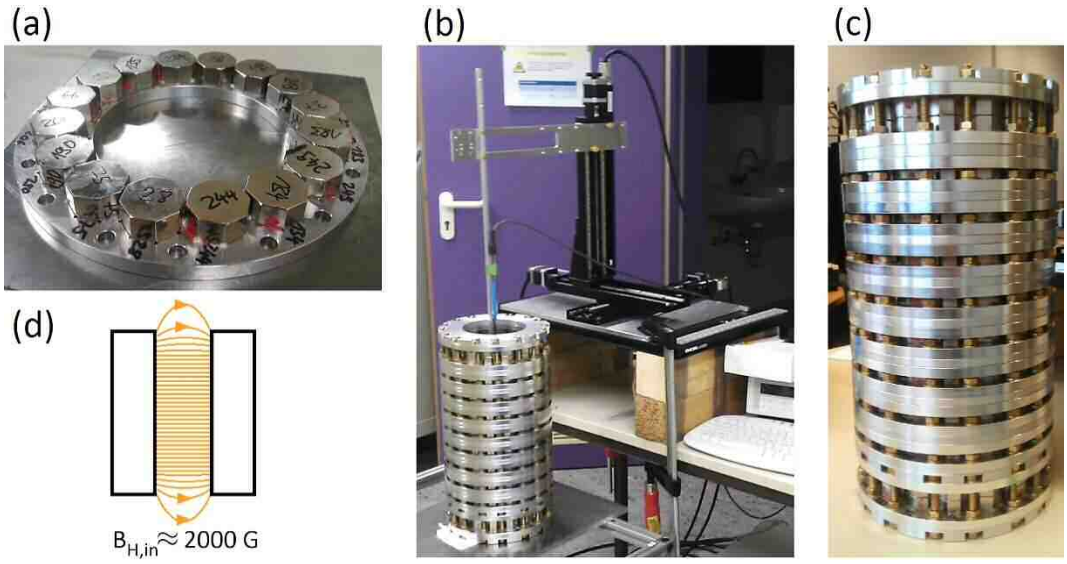

Fig. A2.7: Halbach magnet constructed in [Nie13], figure courtesy of M. Braun [Bra13]. a) Aluminum disk with the octogonal magnets mounted. b) Measurement of the magnetic field performed with a 3D table and a gaussmeter. d) Halbach magnet. d) Sketch of the magnetic flux lines in a Halbach magnet.

The magnetic field and homogeneity of the transition areas where the gas mixture flows through was measured in [Nie13] obtaining homogeneities in the order of 10^{-2} cm^{-1}. According to Sec. 4.1.2 this should not lead to polarization losses.

A2.4 Laser

The narrowed laser system is based in the design presented in [Nel02]. This design was modified in order to correct the divergence of the laser beam produced by the diode and provide a proper beam for the geometry of the OP-cell. The sketch of the arrangement of the laser is shown in Fig. A2.8a. The laser is composed by a diode laser of 100 W and $\Delta\lambda \approx 0.3$ nm (n-Light, USA) (see Fig. A2.8b), a $\lambda/2$ plate, a beam splitter, spherical and cylindrical lenses for beam shaping, a $\lambda/4$ plate, Richardson grating (stepped grating made out of gold mirrors and a diaphragm. Due to the high laser power, the components must be protected against dust, which could eventually damage the optics. For this reason, the laser and its optics are mounted in a homemade closed case with a laminar flow [Bra13]. A photograph of the status of the laser together with a sketch are shown in Fig. A2.8c.

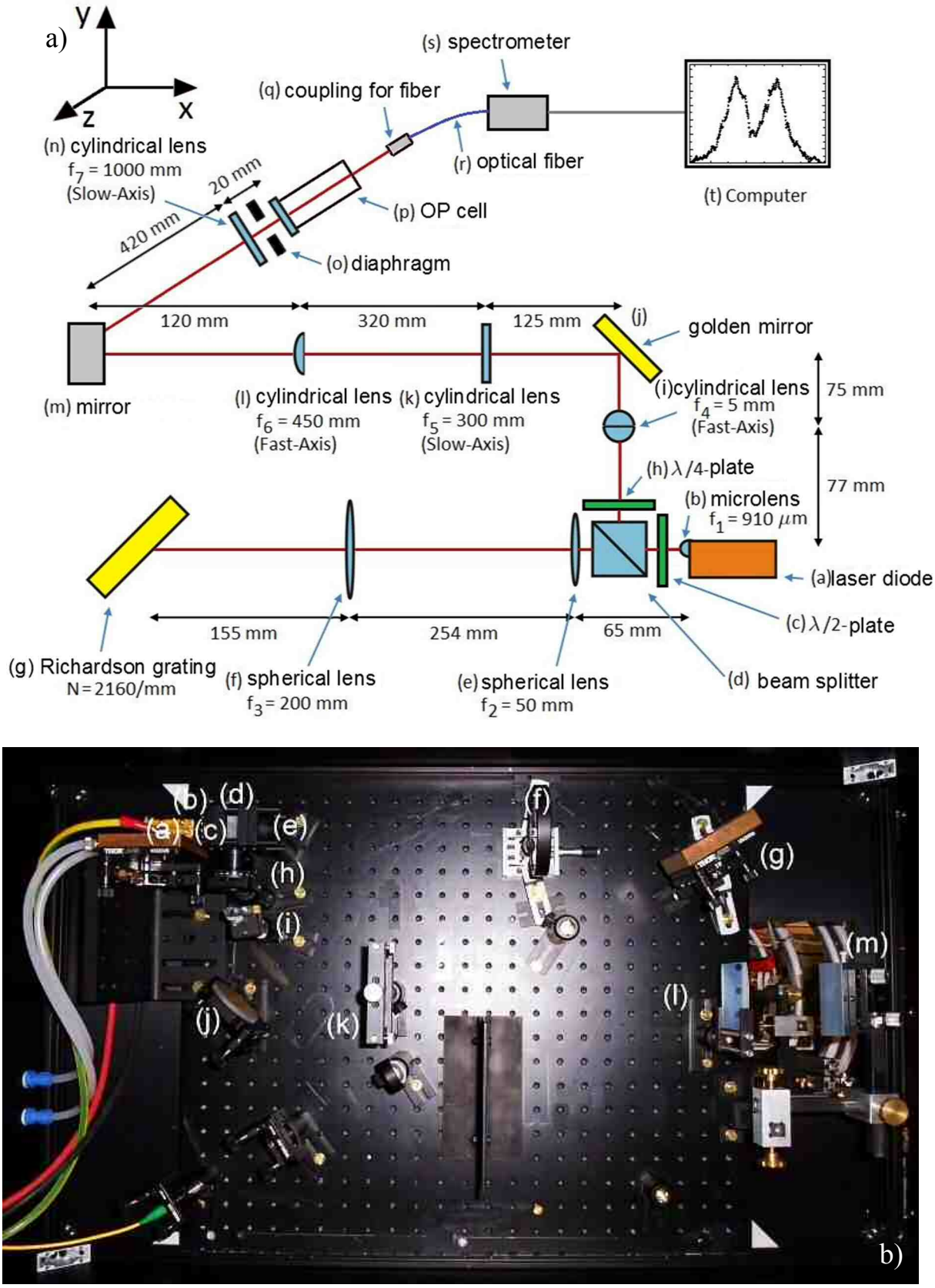

Fig. A2.8: a) Sketch of the laser. b) Photograph of the current status of the laser.The symbols correspond to a). Figure courtesy of M. Braun.

The spectrum of the laser is shown in Fig. A2.9:

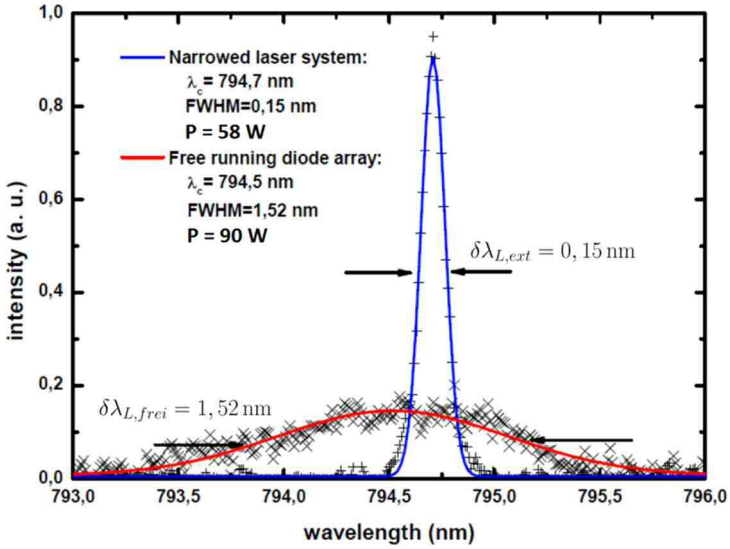

Fig. A2.9: Free running (red line) and narrowed (blue line) spectrum of the laser system of the low-pressure Xe-polarizer [Bra13]. The spectral width is reduced in one order of magnitude while the power is reduced in about 40 %.

This laser was planned and constructed in 2010. Recently, laser of the same characteristics are commercially available even with higher power and smaller bandwidth.

A2.5 Optical pumping cell

The OP-cell consists in a cylinder of borosilicate glass with an inner diameter of 49 mm and a wall thickness of 3 mm and a length of 100 cm. This cell is divided in a hot region which is immersed in oil and where the SEOP takes place and the cold part where Rb condensates. The hot region is about 80 cm long and has a pumping volume of about 1.5 l to ensure a long contact time between Xe and Rb (see Fig. A2.10a). The upper part of the cell is closed with an optical window. The window is made out of quartz (Dorotek, Germany) has an anti-reflection coating (max 220°C). The reactivity of the coating is smaller than 0.25%. The window is glued with a non-degasing epoxy glue (LOCTITE Hysol 1C, USA) as shown in Fig. A2.10c. The maximum temperature this glue withstands is 120°C. This glue can be removed by heating (200°C) with the heating gun. The cold region (around 25 cm) has a cooling jacket where water or compressed air can flow cooling the inner walls and condensing the Rb on the glass walls. The difference with the design proposed by Hersman is the bottom part of the cell which is “champagne bottle” shaped (see Fig. A2.10d). This shape allows working pressures about 1.7 bar with a maximum of 2.2 bar. The liquid Rb which eventually could reach the OP-cell is confined to the pool of the bottom part (see Fig. A2.10e). In this way, the light path is not blocked and can be still analyzed by the optical spectrometer. Since the bottom part is parallel to the optical window, the conditions for reflected light are improved when compared with

the design of [Rus05]. For more detail, see [Bra13].

The OP-cell is surrounded by a glass spiral of about 2.5 cm in diameter. It has pools each 20 cm where the liquid Rb is confined. This spiral has two functions: pre-heat the gas mixture and saturation of the gas mixture with Rb vapor. In this way, the gas mixture and the Rb vapor in equilibrium enter the OP-cell.

The light absorption is monitored constantly during the OP process by a system analogous to the Xe-polarizer described in Chapter 4. The light which crosses the OP-cell is collected by an optical fiber and analyzed by a spectrometer (HR2000, Ocean Optics, Holland).

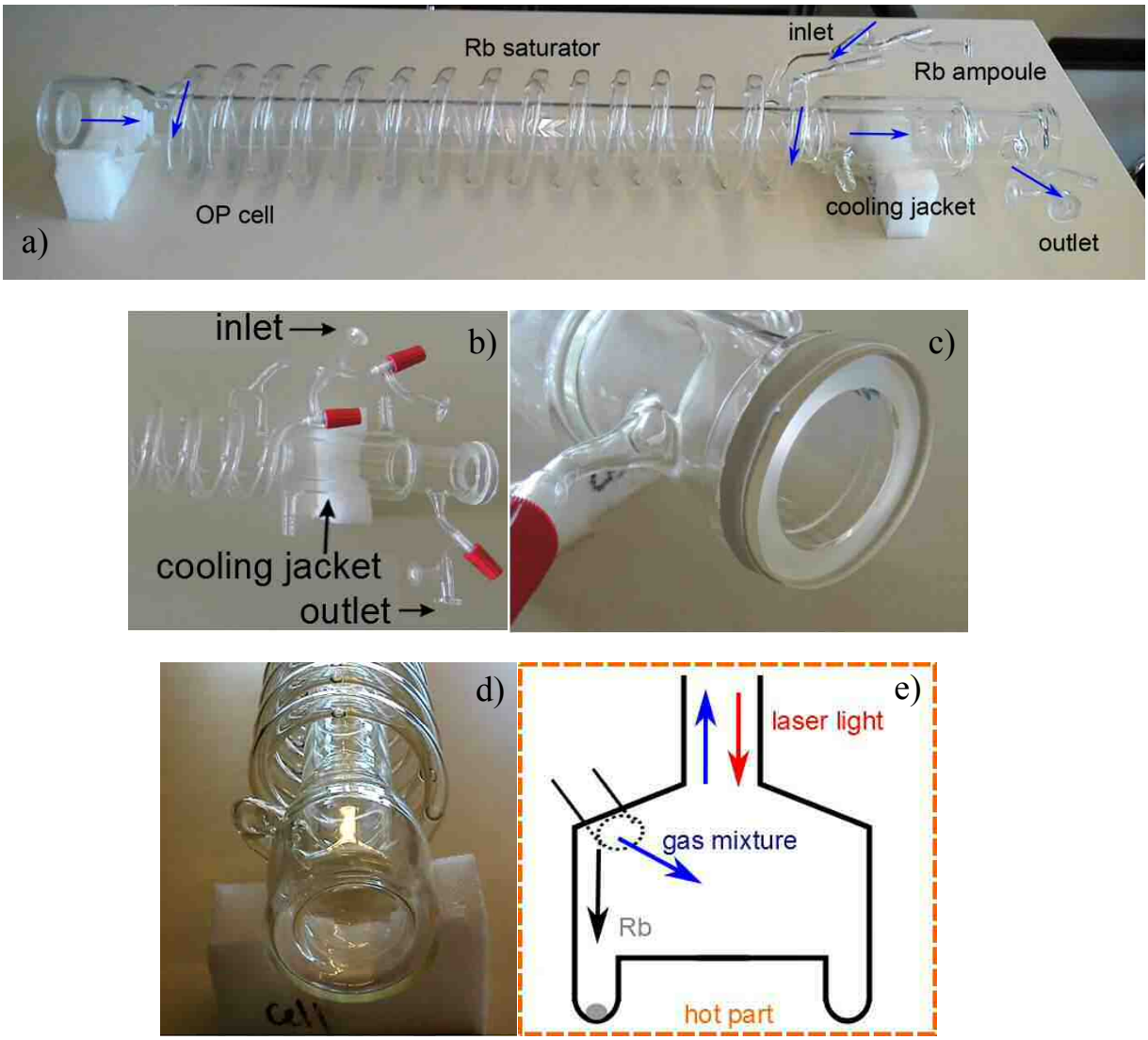

Fig. A2.10: Optical pumping cell. a) Picture of the cell. The direction of the gas mixture flow is marked with blue arrows. b) Picture of the top part of the OP-cell. c) Optical window glued to the top of the OP-cell. d) Bottom part of the OP-cell. e) Sketch of the Rb-trap at the bottom part of the OP-cell.

The Rb is filled into the Rb saturator through the second input as is shown in Fig. A2.11.

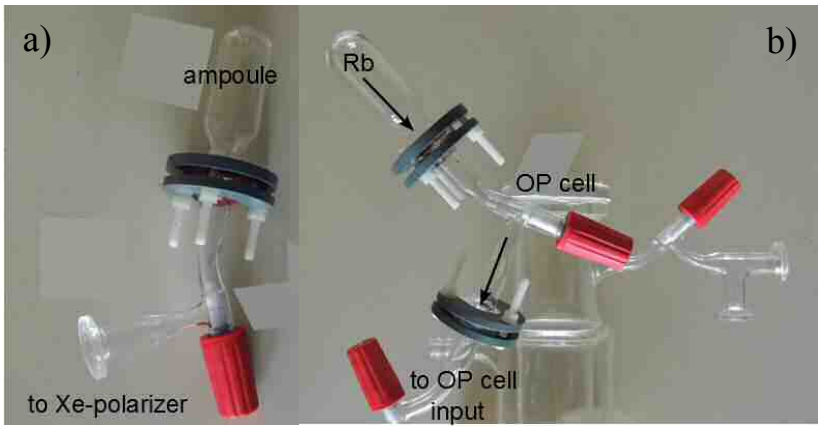

Fig. A2.11: Rb filling procedure into the OP-cell a) The Rb is filled in an ampoule in a glovebox. The ampoule is closed with a valve using a plastic clam and a FKM o-ring. b) The valve of the ampule is connected to the input of the Rb saturator. The volume between the Rb saturator and the ampoule can be evacuated trhough the output of the OP-cell. Then, the valve of the ampoule is opened and the Rb is carefully heated until it liquifies and can be moved to the Rb saturator. If some residual Rb remains in the ampoule or in the valves, it can be slowly oxidized over some days/weeks by opening the clam carefully. Once all Rb is oxidized, the ampoule can be safely removed.

A2.6 Oil bath

Due to the large volume of the OP-cell (over 1 l), the heating cannot be performed with an air oven because of high thermal losses. For this reason, the Rb saturator and the hot part of the OP-cell are immersed in a silicon oil bath which generates a homogeneous heating using relatively low power. The silicon oil has many advantages, for example, its chemical reaction with Rb is extremely slow. It is transparent allowing the monitoring of the absorption, it is inodorous and it has a high boiling point (over 300°C).

The silicon oil is heated using coaxial wire (Thermocoax, France) which produces no residual magnetic field because the distance between the wires less than 1.5 mm (see Fig. A2.12a). Three coaxial cables are connected in parallel resulting in a length of the wire is 3 m and the resistance 9 Ω. This cable is connected to a temperature controller which is also connected to a temperature sensor and a power supply set to 200 V and 2 A. The temperature sensor is just a resistance, which varies with temperature, and it is in contact with the silicon oil. The controller grounds the connection between the power supply and the coaxial cable when the measured temperature is the same or higher than the set temperature. The coaxial cable is mounted in an aluminum structure as is shown in Fig. A2.12b.

The silicon oil is filled in a homemade Dewar composed by two glass vessels, one inside the other separated by some slices of cork. In this way, a good thermal isolation is achieved and, in case of breakage; the silicon oil has a container preventing leakages. The internal Dewar is filled with silicon oil until about 30 cm of the border because of the thermal expansion silicon oil. See [Bra13] for more details.

The thermal bath was first tested using a sealed tube of the same dimensions than the OP-cell but without the Rb saturator. The temperature inside of this cell was measured with a thermocouple while heating the silicon oil to obtain the required time of preparation of the Xe-polarizer. The results of this experiment are shown in Fig. A2.13a obtaining a preparation time of about 120 minutes. Once the desired temperature was achieved, the temperature distribution over the dummy cell was measured displacing the thermocouple each 2 cm. The graphic temperature vs. distance inside of the OP-cell is shown in Fig. A2.13b (extracted from [Fuc13]). Of course, during working conditions, the values of Fig. 13 will change because of the heat produced by quenching.

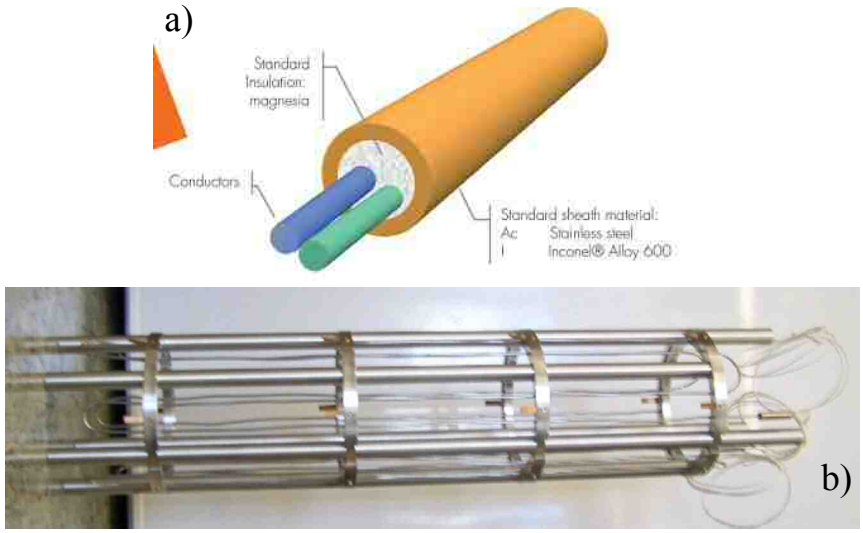

Fig. A2.12: a) Sketch of the coaxial wire Thermocoax extracted from the webpage. The green cable transports incoming current while the green wire the outcoming current. The magnetic fields produced by the two opposite current results to be zero because of the short distance between both wires. To check this, the magnetic field with and without current was measured with a gaussmeter. No variations on the reading of the gaussmeter were determined comparing the values with the power supply on and off. b) Aluminum structure to mount the coaxial wire. This structure helps also with the positioning of the OP-cell.

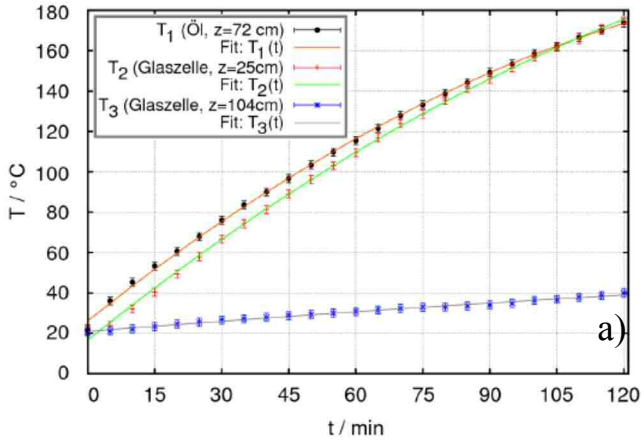

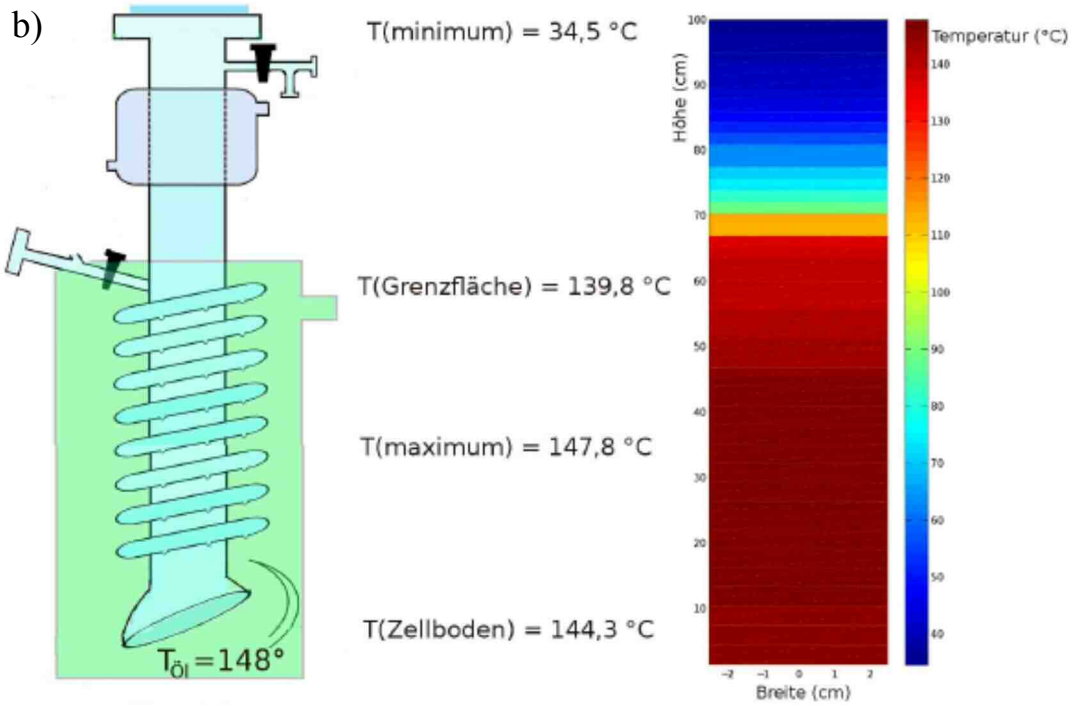

Fig. A2.13: a) Temperature vs. time in three critical positions of the cell. The green line corresponds to z = 25 cm (0 is the bottom of the cell), the red line corresponds to z = 72 cm and the blue line corresponds to z = 104 cm, 3 cm over the oil level at the end of the measurement. b) Temperature distribution inside the OP-cell (extracted from [Fuc12]).

A2.7 FUV unit and filling station

This part of this Xe-polarizer follows the same principles explained in Sec. 4.2 but the sizes are modified to fulfill the high production rate requirements. The Halbach magnet was already described in Sec. 4.2.1, a precise knowledge of the homogenous region is crucial to construct the helical accumulation cell which is about 24 cm in length and 6 cm in outer diameter. Special care was taken so the inlet and the outlet parallel to the symmetry axis of the Halbach magnet.

The path of the gas mixture and the working procedures are analogous to the described in Fig. 4.35 and they are schematized in Fig. A2.14. The gas mixture containing HP-Xe flows out of the OP-cell directly through the FVU where the HP-Xe freezes and the buffer gases flow to the filling station and to the flow control panel. A mechanical pump forces the flow because in case the polarization process occurs at pressures below atmospheric pressures. The helical accumulation cell is immersed in liquid N_2 progressively while the Dewar is pulled up. Once enough HP-Xe ice is accumulated, the buffer gases are evacuated. The Dewar with liquid N_2 is pulled down and the Dewar with hot water is pulled up. The HP- Xe ice turns into gas and is filled in the measurement cell.

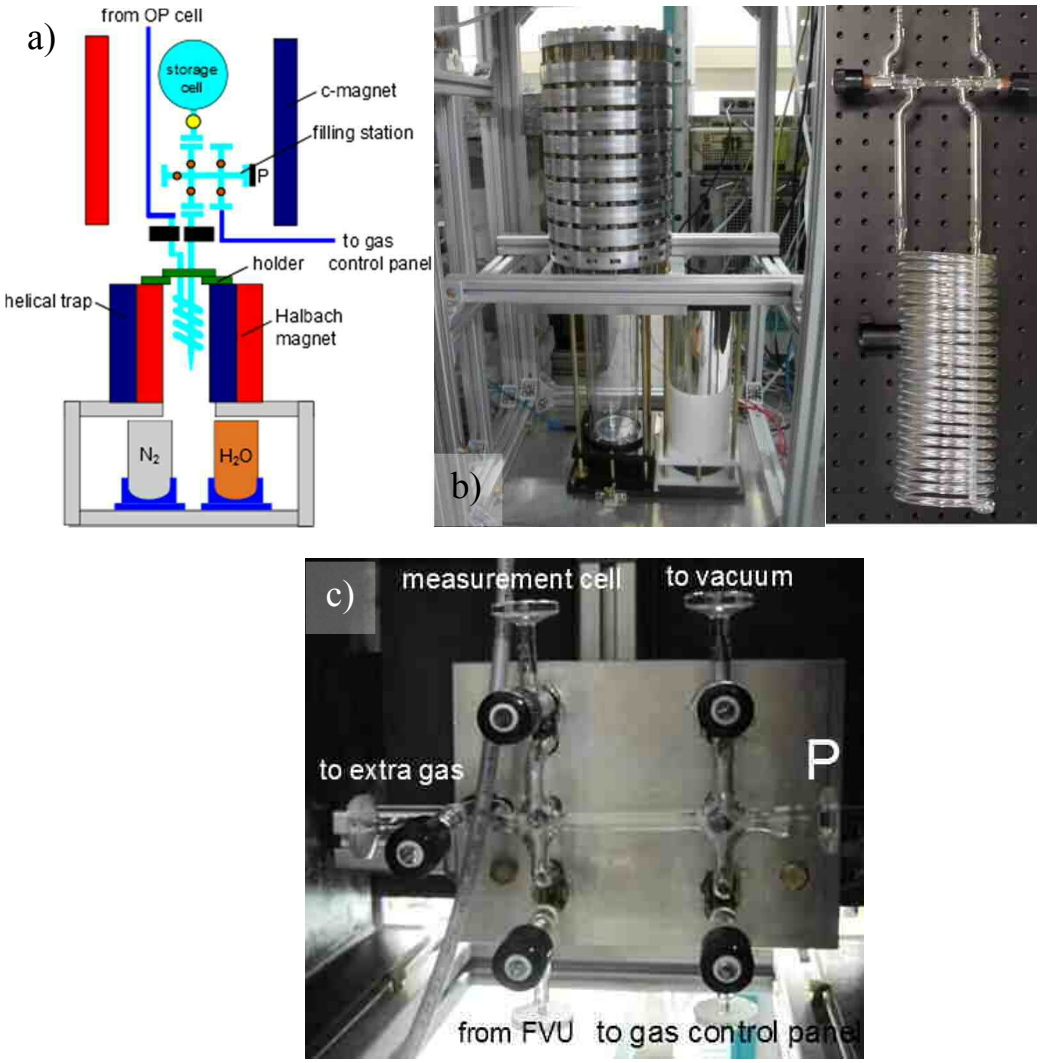

Fig. A2.14: a) Sketch of the gas mixture path after the OP-cell. During the polarization process, the gas mixture flows to the FVU unit and the buffer gases flow through the filling station to the gas control panel. b) Photograph of the FVU composed by a Halbach magnet and a rotating plate containing the Dewar for liquid N_2 and a cylinder made of acryl for hot water. c) Helical accumulation cell. d) Filling station (P is the pressure sensor).

Appendix 3: Use of the Xe-polarizer for fundamental physics applications

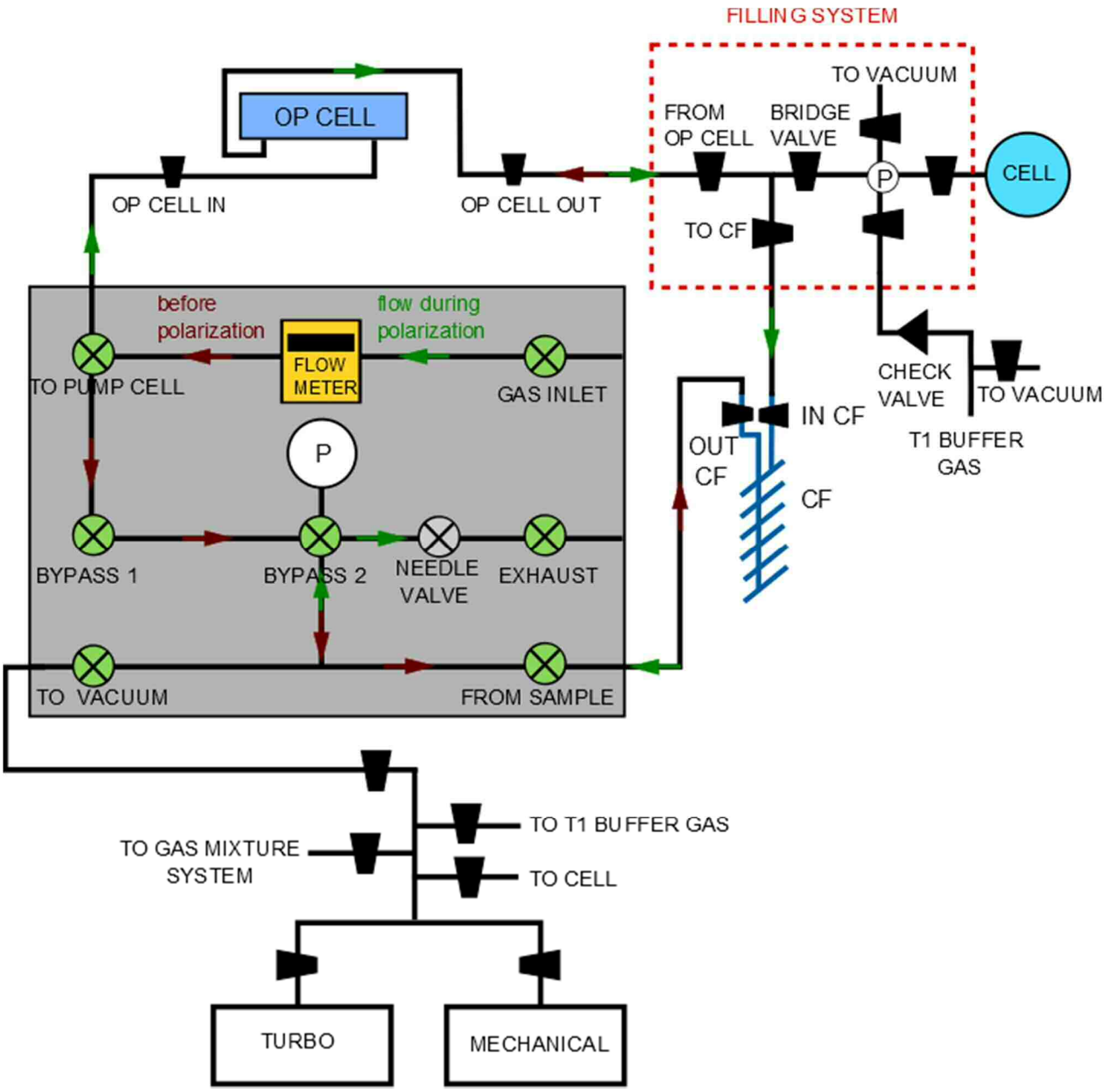

Fig. A3.1: Polarizer scheme. The description of this part can be found in the figure caption of Fig. 4.6. Here, accumulation cell is called cold finger (CF). The brown arrows indicate the flow direction for adjusting the pressure in the OP-cell before polarization. The green arrows indicate the flow while polarizing.

First, the polarizer is divided in two independent circuits:

-The **polarization circuit** where the gas is hyperpolarized and accumulated as Xe-snow. During this process the **BRIDGE VALVE remains closed**. This is mandatory

because the measurement cells will not withstand pressures higher than 2 bar.

-The **filling system circuit** where the HP-Xe (as gas or snow) is manipulated and can be mixed with different buffer gases. In this case **FROM OP-CELL and CF-OUT remain closed**.

GOLDEN RULES

Never pump out the OP-CELL with Rb inside specially if the Rb is hot.

For starting the flow is only necessary 1 bar difference between OP-CELL IN and OP-CELL OUT.

Only open GAS INLET when the flow will start.

BRIDGE VALVE, BYPASS1 and TO VACUUM remain closed during the polarization process.

While opening OP-CELL IN, be sure there is a small overpressure in the cell to prevent suck in of the O-ring.

If something goes wrong (no flow, too much flow, funny noise), the first thing you do is to switch off the laser and close the OP- CELL.

A3.1 Before polarization **(normal use).**

Preparation takes around 45 min. The polarizer should be pre-pumped with the mechanical pump and the turbo with all valves open besides **GAS INLET, OP-CELL (both) and EXHAUST**. The filling system circuit is also pumped out simultaneously (pressure 10^{-6} mbar)

Switch on the coils. I = 2.3 A and V= 101.3 V. Normally the power supply is always on and set. Only the output (green light) is on and off.

Fig. A3.2: Power supply for the coil system.

Switch on the laser in the following order: -Laser ON –Unlock – Open software Raytum

set *I*=40 A *T*=19.6°C. Press “Enable Servo” and wait the temperature to stabilize (about 5 min).

If in the top part of the window you may find that the laser is still locked, refresh it with the button next. If still remains locked, try turning (not pressing) the emergency button on the laser box and refresh.

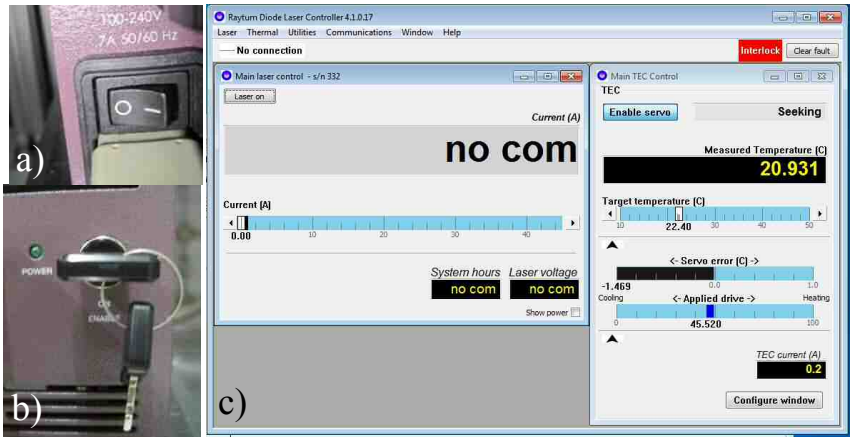

Fig. A3.3: Switching on the laser. a) Main switch. b) Safety key. c) Graphical interface of the laser.

Switch on the heating. For setting the temperature you should press MENU, when the number blinks it is possible with MAX to change the value and with MIN the position of the cursor. When the value is correct press ENTER. Set the temperature first at 100°C and after 15 min to 150°C. These values can change depending of the amount of Rb in the cell (less Rb then more temperature). Green value: set temperature. Red value: measured temperature (temperature of the Rb-trap). The temperature is also measured on the cell with an independent temperature sensor (Tcell).

Fig. A3.4: Temperature control panel.

Open the software FlowDDE (Bronkhorst). In the ribbon-> open communication. After open FlowView. To expand the menu you press Advanced, for a new Flow View press

NEW (you have to press NEW 3 times). Each channel represents Xe-N_2-He and pressure controller respectively. Use in all channels the setpoint BUSRS232.

NOTE: if the number of nodes is higher than 7, the program will complain. For solving this run the program Clear in the Bronkhorst Menu.

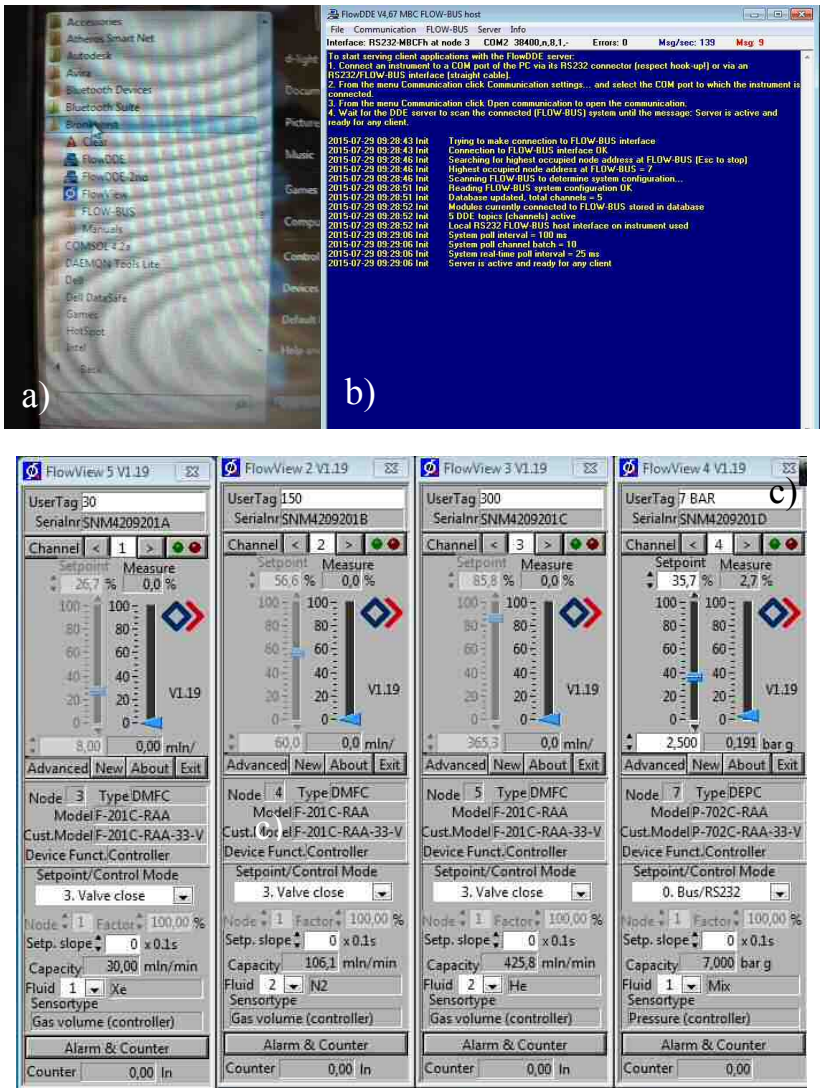

Fig. A3.5: Starting the flow controllers. a) Selecting Bronkhorst FlowDE in the program menu (note also that the program "clear" is there. b) In FlowDE, seach for open communication. C)Open FlowView and press new 3 times to get the other windows. The program recognize the controller for it self.

You will use only 3 set points of the Setpoint/control mode. VALVE CLOSE (I think it is quite clear), BUSRS232 for using and changing how open the valve is (in percent) and VALVE FULLY OPEN which is used for pumping out the connections after a bottle was changed. For controlling the flow must be in mode "BUS232" and you can change the % for generating new gas mixtures. For closing FlowView press QUIT and in DDEFlow, close communication and after closed the program. If the software is closed directly (or the computer crashes), the valves remain open in the fixed %.

Open the software SpectraSuite and press the button, which looks like a magnifying glass with, numbers and there you can select the properties of the graph. λmin= 794 nm λ max=795.6 nm.

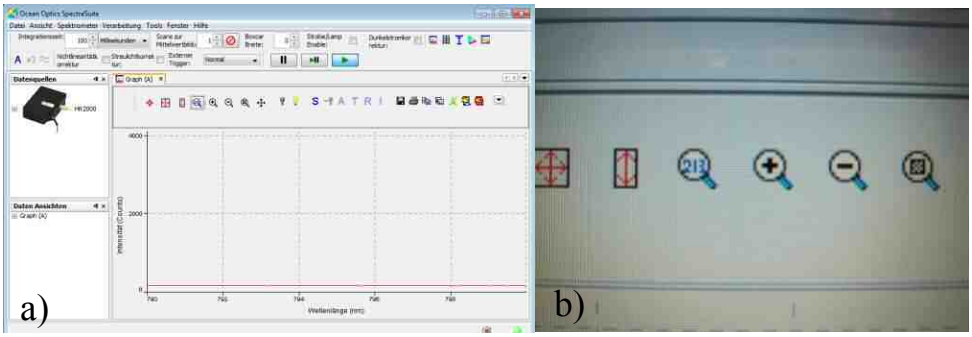

Fig. A3.6: Graphical interphase of the spectrometer "SpectraSuite". a) Complete view of the graphical interface. b) Area of the screen for seting the scale.

Open the bottles until the final pressure is reached (pressure controller does "psss") and after close them.

Close BRIDGE VALVE and TO VACUUM in the polarizer box. In this way, only the filling system and cell are pumped out. When the pressure is around 10^{-6} mbar, close this circuit and be **REALLY SURE that BRIDGE VALVE is closed**.

Check the vacuum of the polarizer, should be at least 10^{-5} mbar **with the mechanical pump closed**. Sometimes when BYPASS1 is closed with pressure (several polarizations in a row) there are leaks of the valve in the circuit and the pressure is around 10^{-4} mbar.

A3.2 Starting the polarization

Tcell must be around 90°C, polarizer pressure at the turbo-pump must be around 10^{-5} mbar, and the measurement cell vacuum at 10^{-6} mbar.

CLOSE all the valves in the polarizer besides CF IN, CF OUT, TO CF and from OP-CELL. Leave the mechanical pump and the butterfly valve which connect to the polarizer open and turbo closed. **TO VACUUM will remain closed during all the polarization process**.

Open the bottles. Open the compressed air cooling. When the max pressure is reached. (You will hear a "pssss" from the pressure controller) open GAS INLET and BYPASS 1. You can now read the pressure in the manometer. Open BYPASS 2 and slowly FROM SAMPLE. The idea is to put 1 bar less at the cell's output so the flow is slowly induced. (See brown arrow on Fig. A3.1)

Close BYPASS 1, BYPASS 2 and FROM SAMPLE. Open "TO PUMPING CELL" and wait until the pressure is reached. Open in this order: CELL INPUT, CELL OUTPUT, FROM SAMPLE, BYPASS 2 (now you must read the total pressure in the manometer of the frontal panel) and EXHAUST. In this way, the flow has started. You can regulate the flow with the NEEDLE VALVE. It must be adjust around 200 ml/min. If there is no flow,

this means a valve is not properly open. Normally the problem is in the valves with O-rings. In this case, you have to first close the OP-CELL, reestablish the pressure difference and open the cell again. This prevents Rb splashes into the cell. On the contrary, if the flow is always 590-600 ml/min (maximum reading of the flowmeter), this means there is a leak. In this case, close all the valves starting with the OP-CELL. Check all the O-ring valves are properly open and not "too" open. With the OP-cell closed, search for the leak with overpressure step by step. Once found, everything but the OP-cell must be evacuated and start all over again from 1.

Close the shield.

Go to the laser software, start the laser.

Wait for the absorption.

Fill the reservoir with LN_2.

There are some tricks, for example, to illuminate the OP-cell with full power laser with the magnetic field on to speed the heating of the gas mixture and increase the Rb density in the OP-cell.

A3.3 During Polarization

When the absorption looks like Fig. 4.22a, pull the reservoir with LN_2 up till the first level and start the stopwatch. During this process, the flow will increase until 600ml/min and the absorption may be gone, after 20 seconds everything should stabilize again.

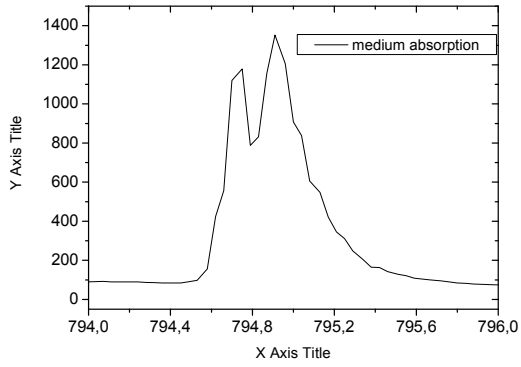

Fig. A3.7: Absorption spectrum measured at 6 bar.

Check constantly the temperature and absorption with the spectrometer and the infrared camera. It may happen you have to adjust them if the accumulation time is more than 5 minutes. The same with the LN_2 level.

Adjust the accumulation steps of LN_2 to the accumulation time you require.

A3.4 Finishing Polarization

Close EXHAUST, GAS INLET and TO PUMPING CELL.
Switch off laser and heating.
Close OP-cell and check it several times. Use a spotlight if necessary.
Open TO VACUUM (you should see the pressure going to zero). Close TO VACUUM. Open shortly FROM SAMPLE, close it again and pump out the gases. Repeat this until the pressure is around 1 bar. Then you can open FROM SAMPLE and TO VACUUM to evacuate the rest of the buffer gases. Close the cold finger. Close the rest of the polarizer. Close the connection that goes to the polarizer vacuum.

A3.5 Filling system

Check the vacuum in the cell again. Close the valve which connects to the OP-Cell and pump out the system.
Heat water.
Switch on the pressure power supply for the pressure sensor. The value in vacuum should be 1.19V and the calibration is: P (mbar)= 491.2 *V-590 (June 2015).
When the pressure is around 10^{-6} mbar, fill up the Dewar with hot water, close the vacuum valve, open the cold finger and bridge valve and thaw the Xe ice with hot water. You can read the pressure in the multimeter.
When the experiment is finished evacuate the polarizer and filling system with the mechanical pump until a new experiment.

A3.6 Demounting the cell for cleaning

When the optical path on the cell is full with Rb or Rb oxide it must be cleaned. Before removal, the pressure of the cell should be 1 bar. After the cell can be disconnected.

A3.7 Starting the polarizer again after cleaning

Connect the cell and pump out during about 24 h.
Cell pressurization: Stop pumping. Inside of the cell should be around 1 bar, so it is necessary to start with P=1 bar or less. The idea is to prevent a big pressure difference in "OP-CELL IN". With the cell COLD, open "OP-CELL IN" carefully and increase the pressure until the value you need by controlling it with Flowview. For this procedure GAS INLET, TO PUMP CELL and OP CELL IN are open. The rest is closed.
Close the cell and you can start.

A3.8 Changing gas bottles

Set all setpoints in FLOWView to VALVE CLOSE.

Close the “hidden valve” (between the output of the gas mixture chamber and GAS INLET).

Take the bottle out. It is not necessary to pump the system out. Install the new one.

For pumping out, the valve in the mixing panel must be open because has a direct connection to the pumps, the hidden valve remain closed.

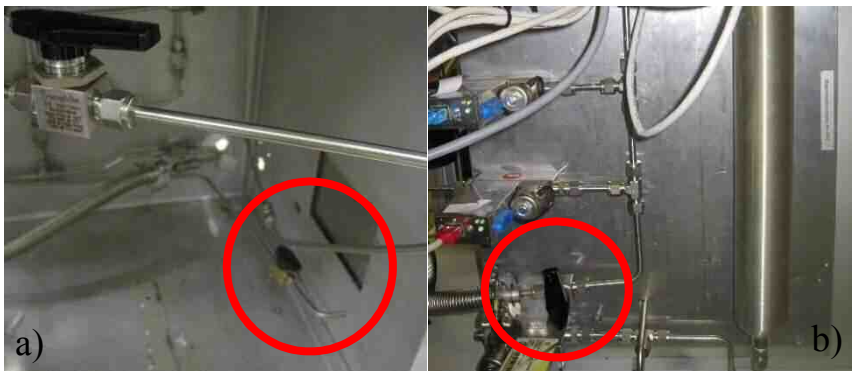

Fig. A3.8: Hidden valve and mixing chamber valve.

Device	Characteristics	Company	Purchase in
Power supply	TDK Lambda 150V-10A	Heinzinger	2012
Laser	795 nm, 0.3 nm	Raytum	2013
Spectrometer	HR 2000 0.3nm resolution	Ocean Optics	around 2004
Flow controller	Is written on the sensors!	Wagner/Bronkhorst	around 2004
Pressure controller	P-702C-21KR-RAD-33V	Wagner/Bronkhorst	around 2004
Flowmeter	Here provided by Analyt	Aalborg	around 2004
Temperature controller		Selfmade	Very old
O rings OP-Cell	FFKM	DTH	2013
Ceramic pressure sensor	0-2 bars, Haenni	Metallux	2009
Needle valve	Standart needle	Swagelok	2004
Comand valves (pol box)	Standard membrane	Swagelok	2004
Glas Valves	826450-0004/826460-0004	Kleinfeld	2011
Hidden valve	SS-43GS6MM	Swagelok	2010
Festo tube	PUN-H-8X1,25-SI	Festo	new
Glue	High temperature for ovens	Baumarkt	
Swagelok tubes	6mm out diam - 1mm wall **316TI-T6M-S-1.0M-2ME**	Swagelok	
Chiller	Self-made/ 1 kW	Delta Therm	2011
Dewar		Isotherm	
Gas filter	FaciliTorr (Saes)	Lammertz	

Appendix 4: Manipulation of Rubidium

A4.1 Cleaning the cell

It is very convenient to leave the cell open to air at least 12 h so the Rb oxidizes slowly until reaching a yellow butter color. If you see black spots, wait a little bit longer because this "black oxide" is extremely reactive.

You will need: Glass pipettes, rubber pump, beaker, gloves, goggles, isopropanol as dry as possible (keep it close).

If the isopropanol is dry and safe, fill up the Rb-trap in the cell using the pipette and the rubber pump. Wait until all Rb reacts (no metallic shine). After the trap is clean, you can repeat this procedure with the OP-Cell.

When all Rb is gone, you should wash the pumping cell with distilled water and dry it with free oil air and/or dry it inside an oven.

Put the valves again and start with vacuum (mechanical and after turbo) around 4 h. The vacuum of the dried cell is about 10^{-6} mbar.

A4.2 For filling with Rb (Under Ar/N_2 atmosphere in a glove box)

You need: 2 pairs of nitryl gloves (usually large size), 1 pair of cloth gloves, 3 glasses with plastic top (for waste), glass cutter in case you need to open a new Rb ampoule, glass pipettes, rubber pump (better if it is made of silicone), heating gun, paper for cleaning, cotton swabs and, of course, Rb.

Procedure: Put everything (besides the cloth gloves) in the communication chamber of the glovebox. First, you must evacuate during 15 min and then fill with Ar. Repeat this procedure 3 times and be sure than the small chamber is full of Ar before you begin. (The absence of oxygen and water is fundamental). You should use cloth gloves below the rubber gloves of the glovebox and the nitryl gloves on top. Open the inner door. Take the things out and plug the heating gun.

Take one of the Rb ampoules and open it with the glass cutter (placing the thumbs on the cut and bending in the direction as we would like to have the thumbs parallel and in contact).Weight the opened ampoule. Heat it (with the heating gun in 2 or 3) until the Rb is liquid and try to heat at the same time the pipette. When YOU ARE SURE, both are hot, extract some Rb with the pipette and place it inside the Rb-trap. Put as much Rb as you need. Weight the container again when you are finished. The typical amount of Rb in the cell is 0.3 to 0.5 gr.

After filling the cell, you should clean the entrance with a swab and close the cell with the valves. (Notice than now the OP-cell is full with Ar at 1 bar). Be sure that the

contact between O-ring and glass is clean.

Clean everything and put the waste in the glasses including the swabs cotton heads. The remaining Rb should stay inside the glovebox, you should take it out only if there is a small amount inside. Close all with tops.

Put everything in the communication chamber and take it out from the Ar- box. Open the door slowly and wait some minutes for possible oxidation.

Drop the gloves in water. If only some traces of Rb are present, open carefully the glasses with waste and put water on it (all the Rb will react). If there is too much Rb waste (drops), open the reservoir a little and let it oxidize over time inside a bucket with sand.

A4.3 Reactivity of Rb with materials of the Xe-polarizer.

The reactivity of Rb was checked on some crucial materials for the construction of a Xe-polarizer. Fundamentally, the parts which are in contact with Rb: O-rings and alternative materials to glass such as Teflon, PVC or PEEK. The epoxy glue used to fix the optical window in the Xe-polarizer for medical applications and silicon oil described for the oil bath in Appendix 2 were also tested.

The test was performed in an automatized glovebox (Lab Star, MBRAUN, Germany). This glovebox has an inert atmosphere of Ar and the concentrations of water and O_2 are less than some ppm. Before the test, the samples were located in glass containers. The containers were placed in the antechamber and evacuated. Then, the antechamber was flushed out with argon and evacuated again. This procedure was repeated three times and, then, the samples were placed inside the glovebox. Each sample was in contact with a drop of Rb (≈0.05 g). In case of the solid samples, it was placed on the surface and in the liquid sample was directly in contact with the liquid. In the Fig. A4.1, a picture with the samples before contact with Rb. From left to right, Teflon, epoxy glue, high temperature silicon glue and FKM O-ring. The results after the contact with Rb are shown in Fig. A4.2.

Fig. A4.1: Samples before the contact with Rb. From left to right: Teflon, epoxy glue, silicon glue and FKM.

Fig. A4.2: Samples after the contact with Rb. From left to right: Teflon, silicon glue, FKM o-ring, piece of PEEK and silicon oil. The Teflon absorbed the Rb, in the grey regions, the material has a rubber consistency. In the silicon glue, the drops of Rb are printed on the surface when the Rb is removed. The o-ring did not show mayor changes after 6 months and PEEK as well. The reaction with silicon oil was really slow even at temperatures of about 80°C. The diameter of each Rb drop is about 5 mm and the bubbles are hydrogen gas.

Table A4.1: Reaction of Rb with different components.

	Reaction?	immediate?	violent?	Characteristics	Recommended for use?
Teflon	Y	Y	N	Fast absorption of liquid Rb, the material softens	N
Silicon oil	Y	Y	N	slow reaction, also when heated	Y (but carefully)
FKM	N	N	N	long term exposure frazzles the material	Y
Silicon glue	N	N	N		Y
Epoxy glue	Y	N	N		Y (cold parts)
PEEK	Y	N	N	slow reaction, material frazzle appears after 6 months	Y (but carefully)

The main conclusions of this test are:

- The durability of FKM O-rings exposed to Rb.
- The slow chemical reaction between Rb and silicon oil, which is crucial for a safe manipulation of the Xe-polarizer for medical applications.
- The resistance to Rb of PEEK.

Appendix 5: MPIP-Xe Polarizer

The MPIP Xe-polarizer was originally designed by S. Appelt but it was upgraded over the years. A complete description can be found in [Düw12].

This polarizer consisted of a diode laser with about 40 W total power and $\Delta\lambda$=0.3 nm, a gas mixing unit (see Fig. A5.1b), an OP-cell (see Fig. A5.1d), an optical spectrometer and a pair of Helmholtz coils (see Fig. A5.1c). The OP-cell and the coils were placed inside of a box in order to shield the laser light. The front of this box is now used as flow control panel.

Fig A5.1: a) Fotograph of the MPIP Xe-polarizer. b) Gas mixing panel and gas bottles fix to the wall of the lab. c) SEOP area. d) Optical pumping cell and oven.

A comparison between the operation parameters of the MPIP Xe-polarizer and the Xe-polarizer for fundamental physics applications is shown in Table A5.1.

Table A5.1: Features of the MPIP and the Uni-Mainz Xe-polarizer.

	MPIP Xe-polarizer	Uni-Mainz Xe-polarizer
Production rate	=	
Rb change	Each 4-6 months	Each 1 year
Vacuum	10-4 mbar	10-6 mbar
filling system	no	yes
gas purifier	no	yes
homogeneity	10-2	10-3
evacuation time		
preparation time	45	45-60
pre-saturation volume	<2	
connections	Self made Brass	Standard o‘rings

Appendix 6: Publications

This publication is available in
http://dx.doi.org/doi:10.1016/j.jmr.2015.01.015

References

A

[Abr83] A. Abragham "Principles of Nuclear Magnetism". International Series of Monographs on Physics. Oxford Science Publications (1983).

[Aco06] R. H. Acosta, L. Agulles-Pedrós, S. Komin, D. Sebastiani, H.W. Spiess, and P. Blümler, "Diffusion in binary gas mixtures studied by NMR of hyperpolarized gases and molecular dynamic simulations". Phys. Chem. Chem. Phys. **8** 4182-4188 (2006).

[Adr64] F.J. Adrian, "Theory of the Nuclear Magnetic Resonance Chemical Shift of Xe in Xenon Gas". Phys. Rev. **136** A980 (1964).

[Alb94] GD. Albert, M.S. Cates, B. Driehuys, W. Happer, B. Saam. "Biological magnetic resonance imaging using hyperpolarized ^{129}Xe". Nature **370** 199 (1994).

[All14] F. Allmendinger, W. Heil, S. Karpuk, W. Kilian, A. Scharth, U. Schmidt, A. Schnabel, Y. Sobolev, and K. Tullney,"New Limit on Lorentz-Invariance- and CPT-Violating Neutron Spin Interactions Using a Free-Spin-Precession ^{3}He-^{129}Xe Co-magnetometer". Phys. Rev. Lett. **112** 110801 (2014).

[Amo09] N. Amor, P.P. Zänker, P. Blümler, F.M. Meise, L.M. Schreiber, A. Scholz, J. Schmiedeskamp, H.W. Spiess, K. Münnemann, "Magnetic resonance imaging of dissolved hyperpolarized ^{129}Xe using a membrane-based continuous flow system", Jour. of Magn. Res. **201** (1) 93–99 (2009).

[Ams15] www.amstechnologies.com

[Ang08] B.C. Anger, G. Schrank, A. Schoeck, K.A. Butler, M.S. Solum, R.J. Pugmire, and B. Saam, "Gas-phase spin relaxation of ^{129}Xe". Phys. Rev. A **78** 043406-1-10 (2008).

[App04] S. Appelt "From photon spin to magnetic resonance imaging". Habilitation (2004).

B

[Bab05] E. Babcock, B. Chann, I. A. Nelson, and T.G. Walker. "Frequency-narrowed diode array bar", App. Opt. **44**, (15) 20 3098 (2005).

[BabD05] E. Babcock, "Spin-exchange optical pumping with alkali metal atoms". PhD Thesis. University of Wisconsin- Madison (2005).

[Bai12] Y. Bai, P. Aru Hill, and I. J. Dmochowski. "Utilizing a Water-Soluble Cryptophane with Fast Xenon Exchange Rates for Picomolar Sensitivity NMR Measurements". Anal. Chem. **84** (22) 9935–9941 (2012).

[Bar98] A. B.-A. Baranga, S. Applet, C.J. Erickson, A.R. Young, and W. Happer. "Alkali metal- atom polarization imaging in high-pressure optical-pumping cells". Phys. Rev. A, **58** (3) 2282-2294, (1998).

[Bee03] E.J.R. van Beek, J.Schmiedeskamp, J.M.Wild, M.N.J.Paley, F.Filbir,

S.Fichele, F.Knitz, G.H.Mills, N.Woodhouse, A.Swift, W.Heil, M.Wolf, E.Otten, "Hyperpolarized 3-helium MR imaging of the lungs: testing the concept of a central production facility". Eur. Radiol.**13** 2583–2586 (2003).

[Ben65] R. Benumof. "Optical pumping theory and experiments". Am. J. Phys. **33** 151-160 (1965).

[Ber59] N. Bernardes and H. Primakoff, "Molecule Formation in the Inert Gases". J. Chem. Phys. **30** 691 (1959).

[Bow87] C. Russell Bowers, D. P. Weitekamp. "Parahydrogen and synthesis allow dramatically enhanced nuclear alignment". Jour. Am. Chem. Soc. **109** (18) 5541–5542 (1987).

[Bow99] C.R. Bowers, V. Storhaug, C.E. Webster, J. Bharatam, A. Cottone III, R. Gianna, K. Betsey, and B.J. Gaffney, "Exploring Surfaces and Cavities in Lipoxygenase and Other Proteins by Hyperpolarized Xenon-129 NMR." Jour. Am. Chem. Soc. **121** 9370-9377 (1999).

[Bra11] N. Brahms, T. V. Tscherbul, P. Zhang, J. Klos, R. C. Forrey,Y. Shan Au, H. R. Sadeghpour, A. Dalgarno, J. M. Doyle, and T. G.Walker. "Formation and dynamics of van der Waals molecules in buffer-gas traps". Phys. Chem. Chem. Phys. **13**, 19125-19141 (2011).

[Bra13] M. Braun „Entwicklung eines kompakten ^{129}Xe-Polarisators" (schwerpunkt laser). Johannes Gutenberg Universität Diplomarbeit AG Heil. July September 2013

[Bre61] R. G. Brewer "High Intensity Low Noise Rubidium Light Source". Review of Scientific Instruments **32**, 1356 (1961);

[Bre00] S.R. Breeze, S. Lang, I.L. Moudrakovski, C.I. Ratcliffe, J.A. Ripmeester, G. Santyr, B. Simard, and I. Zuger, "Coatings for optical pumping cells and short-term storage of hyperpolarized xenon". Jour. Appl. Phys. **87** 8013-8017 (2000).

[Bri62] D. Brinkmann, E. Brun, H.H. Staub, "Kernresonanz im gasförmigen Xenon" Helv. Phys. Acta **35** 431 (1962).

[Bro13] Bronkhorst Operation Manual available in http://www.bronkhorst-nord.de/de/produkte/gas_durchflussmesser_und_-regler/elflow_select/.

[Bur11] M Burghoff, C Gemmel, W Heil, S Karpuk, W Kilian, S Knappe-Grüneberg, K Lenz, W Müller, K Tullney, U Schmidt, A Schnabel, F Seifert, Yu Sobolev and L Trahms "Probing Lorentz invariance and other fundamental symmetries in ^{3}He/^{129}Xe clock-comparison experiments". Jour of Phys. **295** 0120176 (2011).

C

[Cat88] G.D. Cates, S.R. Schaefer, and W. Happer. "Relaxation of spins due to field inhomogeneities in gaseous samples at low magnetic fields and low pressure". Phys. Rev. A,**37** 2877 (1988).

[Cat92] G. D. Cates, R. J. Fitzgerald, A. S. Barton, P. Bogorad, M. Gatzke, N. R.

Newbury, and B. Saam. “Rb-129xe spin-exchange rates due to binary and three-body collisions at high xe pressures”. Phys. Rev. A **45** (7) 4631-4639 (1992).

[Chan00] B. Chann, I. Nelson, and T. G. Walker “Frequency-narrowed external-cavity diode-laser-array bar”. Opt. Lett. **25** 18 (2000).

[Cha02] B. Chann, I.A. Nelson, L.W. Anderson, B. Driehuys, and T.G. Walker, “^{129}Xe-Xe Molecular Spin Relaxation”. Phys. Rev. Lett. **88** 113201 (2002).

[Cha02B] B. Chann, E. Babcock, L.W: Anderson and TG Walker “Skew Light propagation in optically thick optical pumping cells”. Phys. Rev. A **66** 033406 (2002).

[Cha03] B. Chann “Studies on spin exchange optical pumping”. Dissertation University of Wisconsin-Madison (2003).

[Cha14] Chang YV, Quirk JD, Ruset IC, Atkinson JJ, Hersman FW, Woods JC. “Quantification of human lung structure and physiology using hyperpolarized 129Xe”. Magn. Res. Med. **71** (1) 339-44, (2014).

[Che02] A. Cherubini, A. Bifone. “Hyperpolarised xenon in biology”. Prog. in Nucl. Mag. Res. Spec. **42** 1–30 (2003).

[Coh69] C. Cohen-Tannoudji, J. DuPont-Roc, S. Haroche and F. Laloe. “Detection of the static magnetic field produced by the oriented nuclei of optically pumped ^{3}He gas”. Phys. Rev. Let. **22** (15) 758-760 (1969).

[Coh92] C. Cohen-Tannoudji, B. Diu, Frank Laloe “Quantum Mechanics”, 2 Volume Set Wiley. ISBN: 978-0-471-56952-7 (1992).

[Com94] A. Compaan, A. Wagoner, and A. Aydinli. “Rotational Raman scattering in the in-structional laboratory”. Am. J. Phys. **62** 639 (1994).

[Com10] A. Comment, S. Jannin, J.-N. Hyacinthe, P. Miéville, R. Sarkar, P. Ahuja, P. R. Vasos, X. Montet, F. Lazeyras, J.-P. Vallée, P. Hautle, J. A. Konter, B. van den Brandt, J.-Ph. Ansermet, R. Gruetter, and G. Bodenhausen. “Hyperpolarizing Gases via Dynamic Nuclear Polarization and Sublimation”. Phys. Rev. Lett. **105** 018104 (2010).

[Coo61] G.E: Cook (Eds.), “Argon, Helium and the Rare Gases” Interscience Publishers, New York, (1961).

[CRC09] Handbook of Chemistry and Physics 2009.

D

[Dan71] J. Daniels, A. Kiang, P. Kirkby, “A Large Volume Homogeneous Low Field Electromagnet”. Can. J. Phys. **49** 576. (1971).

[Dit41] R. W. Ditchburn and J. C. Gilmour “The vapor pressures of monoatomic atoms”. Rev. of Mod. Phys. **13** 310 (1941).

[Dri95] B. Driehuys, C.G. D., W. Happer, “Surface Relaxation Mechanisms of Laser-Polarized Xe-129”, Phys. Rev. Lett. **74** 4943-4946 (1995).

[Dri96] B. Driehuys, G. D. Cates, E. Miron, K. Sauer, D. K. Walter and W. Happer, “High-volume production of laser-polarized ^{129}Xe”. Appl. Phys. Lett. **69** 1668 (1996)

[Dri12] B. Driehuys, S. Martinez-Jimenez, Z. I. Cleveland, G. M. Metz, D. M. Beaver, J. C. Nouls S. Sivaram Kaushik , R. Firszt , C. Willis , K. T. Kelly , J. Wolber, M. Kraft , H. Page McAdams, "Chronic Obstructive Pulmonary Disease: Safety and Tolerability of Hyperpolarized ^{129} Xe MR Imaging in Healthy Volunteers and Patients". Radiology **262** 1 (2012).

[Düw12] Mathis Düwel "^{129}Xe NMR for Investigations of Complex and Dynamic Systems". Doktorarbeit MPIP 2012.

E

[Eri00] C. J. Erickson, D. Levron, D. Happer, S. Kadlecek, B. Chann, L. W. Anderson, and T. G. Walker. "Spin relaxation resonances due to the spin-axis interaction in dense rubidium and cesium vapor". Phys. Rev. Lett., **85** (20) 4237-4240, (2000).

F

[Fin05] A. Fink, D. Baumer, and E. Brunner "Production of hyperpolarized xenon in a static pump cell: Numerical simulations and experiments". Phys. Rev. A **72**, 053411 (2005).

[Fra13] M. B. Franzoni, D. Graafen, L. Buljubasich, L. M. Schreiber, H. W. Spiess, and K. Münnemann "Hyperpolarized 1H long lived states originating from parahydrogen accessed by rf irradiation". Phys. Chem. Chem. Phys. **15**, 17233-17239 (2013).

[Fro98] G. Frossati "Polarization of ^{3}He, D_2 and (eventually) ^{129}Xe Using Low Temperatures and High Magnetic Fields". Jour. of Low Temp. Phys. **111**, 521-532 (1998).

[Fuc12] Martin Fuchs "Konstruktion eines ^{129}Xe-Polarisators" Johannes Gutenberg Universität Diplomarbeit AG Heil September 2012.

G

[Gar75] G. T. Johnson, T. R. Lewis and W. D. Wagner. "Acute Toxicity of Cesium and Rubidium Compounds". Tox. and App. Pharm. **32**, 239-245 (1975).

[Gat93] M. Gatzke, G.D. Cates, D.F. Driehuys, W. Happer, B. Saam, "Extraordinarily slow nuclear spin relaxation in frozen laser-polarized ^{129}Xe". Phys. Rev. Lett. **70** 690 (1993).

[Gem10] C. Gemmel, W. Heil, S. Karpuk, K. Lenz, Yu. Sobolev, K. Tullney, M. Burghoff, W. Kilian, S. Knappe-Grüneberg, W. Müller, A. Schnabel, F. Seifert, L. Trahms, and U. Schmidt "Limit on Lorentz and CPT violation of the bound neutron using a free precession He3/Xe129 comagnetometer". Phys. Rev. D **82** 111901 (2010).

[Gen05] T.R. Gentile, E. Babcock, J.A. Borchers, W.C. Chen, D. Hussey, G.L. Jones, W.T. Lee, C.F. Majkzrak, K.V. O'Donovan, W.M. Snow, X. Tong, S.G.E. te Velthuis, T.G. Walker, H. Yan, "Polarized ^{3}He spin filters in neutron scattering", Physica B: Condensed Matter, **356**, 96-102 (2005).

[God02] Boyd M. Goodson “Nuclear Magnetic Resonance of Laser-Polarized Noble Gases in Molecules, Materials, and Organisms”. Jour. of Magn. Res. **155**, 157–216 (2002).

[Gol76] R. Goldhor and David P., “Bound and quasibound states of alkali–rare gas molecules”. Jour. of Chem. Phys. **64**, 1189 (1976).

[Gua11] A. Guais, G. Brand, L. Jacquot, M. Karrer, S. Dukan, G. Grévillot, T.J. Molina, J. Bonte, M. Regnier, and L. Schwartz, “Toxicity of Carbon Dioxide: A Review”. Chem. Res. in Tox. **24** 2061-2070 (2011).

[Gül11] M. Güldner, „Bau und Entwicklung eines Applikators zur Verabreichung hyperpolarisierter Gase in der MRT der Lunge“. Dissertation University of Mainz (2011).

[GUV87] GUV-V B2 Unfallverhütungsvorschrift “Laserstrahlung” von November 1987, in der Fassung vom Januar available in www. Arbeitsschutz.uni-mainz.de/begriffsbestimmung

H

[Hal80] K. Halbach: “Design of permanent multipole magnets with oriented rare earth cobalt material” Nuc. Inst. and Meth. **169** (1) 1-10 (1980).

[Hap72] W. Happer “Optical Pumping”. Rew. Of Mod. Phys. **44** (2) (1972).

[Hap84] W. Happer, E. Miron, S. Schaefer, D. Schreiber, W. A. van Wijngaarden, and X. Zeng. „Polarization of the nuclear spins of noble-gas atoms by spin exchange with optically pumped alkali-metal atoms”. Phys. Rev. A **29** (6) 3092-3110, 1984.

[Hei13] W. Heil, C. Gemmel, S. Karpuk, Y. Sobolev, K. Tullney, F. Allmendinger, Ulrich Schmidt, M. Burghoff, W. Kilian, S. Knappe-Grüneberg, A. Schnabel, F. Seifert and L. Trahms. “Spin clocks: Probing fundamental symmetries in nature”. Annalen der Physik Special Issue: Precision Experiments and Fundamental Physics at Low Energies - Part II **525** (8-9) 539–549 (2013).

[Her07] F.W. Hersman , I.C. Ruset , S. Ketel , I. Muradian , S.D. Covrig, J. Distelbrink ,W. Porter , D. Watt, J. Ketel, J. Brackett, A. Hope, S. Patz”. “Large production system for hyperpolarized 129Xe for human lung imaging studies”. Acad Radiol. **15** (6) 683 (2008).

[Hie06] S. Hiebel. “Mehtodische und technische Weiterentwicklung der ^{3}He-MRT in Hinblick aud erweiterte lungendiagnostische Anwendungsmöglichkeiten”. Doctoral Thesis, University of Mainz (2006).

[Hie10] S. Hiebel, T. Großmann, D. Kiselev, J. Schmiedeskamp, Y. Gusev, W. Heil, S. Karpuk, J. Krimmer, E. W. Otten, Z. Salhi. "Magnetized boxes for housing polarized spins in homogeneous fields". Jour. of Mag. Res. **204** 37-49 (2010).

[Hob61] J.P. Hobson, “Desorption of Adsorbed Gas and Re-emission of Gas Previously Pumped by Ionic Pumping”. Trans. 8th AVS Vac. Symp. (1961) 26-30.

[Hol07] A.F. Holleman, N. Wiberg, „Lehrbuch der Anorganischen Chemie“, 102. Auflage, de Gruyter-Verlag S. 1284 ff (2007).

[Hue11] M Hügle „Aufbau und Test einer Niederfeld-NMR-Apparatur zur Messung der Kernspin-Polarisation von ^{129}Xe“ Staatsexam Johannes Gutenberg University (2011).

[Hun63]E. Hunt and H. Carr, “Nuclear Magnetic Resonance of 129Xe in Natural Xenon”. Phys. Rev. **130**, 2302 (1963).

[Hus79] X Husson and J P Grandin. “Measurements of g factors of Xe and Kr”. J. Phys. B: At. Mol. Phys. 12 3649 (1979).

J

[Jac98] J.D. Jackson “Classical Electrodynamics”. John Wiley and Sons, (1998).

[Jam88] C.J. Jameson, A.K. Jameson, J.K. Hwang, “Nuclear spin relaxation by intermolecular magnetic dipole coupling in the gas phase. 129Xe in oxygen”. J. Chem. Phys. **89** 4074-4081(1988).

[Jän98] H.J. Jänsch, T. Hof, U. Ruth, J. Schmidt, D. Stahl, and D. Fick, “NMR of surfaces: sub-monolayer sensitivity with hyperpolarized 129Xe”. Chem. Phys. Lett. **296** 146-150 (1998).

[Jän03] H.J. Jänsch, P. Gerhard, M. Koch and D. Stahl “^{129}Xe chemical shift measurements on a single crystal surface”. Chem. Phys. Let. **372** 325-330 (2003)

[Jau03] Y. Y. Jau, N. N. Kuzma, and W. Happer. “Magnetic decoupling of 129xe-rb and 129xe-cs binary spin exchange”. Phys. Rev. A, **67** (2) 022720, 2003.

[Jen57] F. Jenkins and H. White, “Fundamentals of Optics” 3rd Ed. Mc Graw Hill (1957).

K

[Kad98] S. Kadlecek, L. W. Anderson, and T. G. Walker. “Field Dependence of Spin Relaxation in a Dense Rb Vapor”. Phys. Rev. Lett. **80**, 5512 (1998).

[Kad01] S. Kadlecek, T. Walker, D.K. Walter, C. Erickson, and W. Happer. “Spin-axis relaxation in spin-exchange collisions of alkali-metal atoms”. Phys. Rev. A, **63** 052717, (2001).

[Kar13] S. Karpuk, F. Allmendinger, M. Burghoff, C. Gemmel, M. Güldner, W. Heil, W. Kilian, S. Knappe-Grüneberg, Ch. Mrozik, W. Müller, E. W. Otten, M. Repetto, Z. Salhi, U. Schmidt, A. Schnabel, F. Seifert, Y. Sobolev, L. Trahms, K. Tullney, “Spin polarized ^{3}He: From basic research to medical applications”. Phys. of Part. and Nucl. **44** 904-908 (2013).

[Kha15] Najat S. Khan, Brittany A. Riggle, Garry K. Seward, Yubin Bai, and Ivan J. Dmochowski “Cryptophane-Folate Biosensor for ^{129}Xe NMR”. Bioconjugate Chemistry **26** (1), 101-109 (2015).

[Kil27] T. Killian “Thermionic phenomena cause by vapors of rubidium and potassium” Phys. Rew. **27** 578 (1926).

[Kil01] W. Killian “Erzeugung von hyperpolarisiertem 129-Xe-Gas und Nachweis

mittles in vivo NMR-Bildgebung, NMR-Spektroskopie sowie SQUID-Messtechnik“ Doktorarbeit FreienFreie Universität Berlin (2001)

[Kna06] K. Knagge, J. R. Smith, L. J. Smith, J. Buriak, D. Raftery. “Analysis of porosity in porous silicon using hyperpolarized 129Xe two-dimensional exchange experiments”. Solid State Nuclear Magnetic Resonance **29**, (1–3), 85–89 (2006).

[Kon01] V.A. Konstantinov, VP Revyakin, M.A. Pokhodenko “Lower limit on the thermal conductivity of krypton-xenon solid solutions”. Low Temp. Phys. **27**, 7 (2001).

[Kor13] Korchak SE, Kilian W, Mitschang L. “Configuration and Performance of a Mobile (129) Xe Polarizer”. Appl. Magn. Reson. **44** (1-2), 65-80 (2013).

[Kra12] A. Kraft „Aufbau und Inbetriebnahme eines hochsensitiven 3He – Magnetometers für ein zukünftiges Experiment zur Bestimmung eines elektrischen Dipolmoments des freien Neutrons“. Doktorarbeit. University of Mainz (2012).

[Kri09] J. Krimmer, M. Distler, W. Heil, S. Karpuk, D. Kiselev, Z. Salhi, E. W. Otten, “A highly polarized 3He target for the electron beam at MAMI” Nuclear Instruments and Methods in Physics Research A **611** 18–24 (2009).

[Kri11] J. Krimmer, P. Aguar Bartolome, J. Ahrens, S. Altieri, W.Heil, S.Karpuk, E.W.Otten, P. Pedroni, Z.Salhi and A. Thomas, “A polarized ^{3}He target for proton beam at MAMI”. Nuc. Instr. and Meth. in Phys. Res. A **648** 35-40 (2011).

[Kuz02] N.N. Kuzma, B. Patton, K. Raman, W. Happer, “Fast Nuclear Spin Relaxation in Hyperpolarized Solid ^{129}Xe“Phys. Rev. Lett. **88** 147602 (2002).

L

[Lan02] S. Lang, I. L. Moudrakovski, C. I. Ratcliffe, J. A. Ripmeester and G. Santyr “Increasing the spin-lattice relaxation time of hyperpolarized xenon ice at 4.2 K“. Appl Phys Lett **80**, 886 (2002).

[Lar91] B. Larson, O. Hausser, P. P. J. Delheij, D. M. Whittal, and D. Thiessen. “Optical pumping of Rb in the presence of high-pressure ^{3}He buffer gas”. Phys. Rev. A **44**(5) 3108-3118, (1991).

[Lev07] Malcolm H. Levitt “Spin Dynamics: Basics of Nuclear Magnetic Resonance”, 2nd Edition ISBN: 978-0-470-51117-6 Wiley (2007).

M

[Maj32] E. Majorana, “Oriented atoms in a variable magnetic field” Nuovo Cimento **9** 43 (1932).

[Mee15] Edited by Thomas Meersmann and Eike Brunner. “Hyperpolarized Xenon-129 Magnetic Resonance Concepts, Production, Techniques and Applications”. 1st edition. Royal Society of Chemistry (2015).

[Mei10] F. M. Meise, J. Rivoire, M. Terekhov, G. C. Wiggins, B. Keil, S. Karpuk, Z. Salhi, L. L. Wald, and L. M. Schreiber. “Design and Evaluation of a 32-Channel Phased-

Array Coil for Lung Imaging with Hyperpolarized 3-Helium". Magn. Res. in Med. **63** 456–464 (2010).

[Mel87] M Tuoni, M Marchitiello, G Paternoster, S Gerace, R Palla, GF Placidi, A Lenzi, D Toschi and HL Meltzer "Renal tolerance of rubidium chloride: short-term clinical evaluation". Jour. Clin. Pharm. **27** 503 (1987).

[Möl99] H. E. Möller, M. S. Chawla, X. Josette Chen, B. Driehuys, L. W. Hedlund, C. T. Wheeler and G. Allan Johnson. "Magnetic resonance angiography with hyperpolarized 129Xe dissolved in a lipid emulsion". Mag. Res. in Med. **41** (5) 1058–1064 (1999).

[Möl11] H. E. Möller, Z. I. Cleveland, B. Driehuys. "Relaxation of hyperpolarized ^{129}Xe in a deflating polymer bag". Jour. Magn Res. **212** (1) 109–115 (2011).

[Mou01] I. L. Moudrakovski, S. R. Breeze, B. Simard, C. I. Ratcliffe, J. A. Ripmeester, T. Seideman, J. S. Tse and G. Santyr. "Gas-phase nuclear magnetic relaxation in ^{129}Xe revisited ", J. Chem. Phys. **114**, 2173 (2001).

[Mro11] C. Mrozik, O. Endner, C Hauke, W Heil, S Karpuk, J Klemmer and E W Otten, "Construction of a compact ^{3}He polarizing facility" Journal of Physics: Conference Series **294** 012007 (2011).

N

[Nel02]I.A. Nelson and T.G. Walker. Rb-Xe spin relaxation in dilute Xe mixtures. Phys. Rev. A, **65** 012712 (2002).

[Nic84] A.T. Nicol, "Effect of several surface treatments on xenon nuclear-polarization and relaxation in optically pumped Rb-Xe systems". Phys. Rev. B **29** 2397-2403 (1984).

[Nie13] Benjamin Niederlander. „Entwicklung eines kompakten ^{129}Xe-Polarisators" Johannes Gutenberg Universität, Diplomarbeit AG Heil, September 2013.

[Nie15] Private comunication with Benjamin Niederländer.

[Nor13] G. Norquay, S. R. Parnell, X. Xu, J. Parra-Robles, and J. M. Wild. "Optimized production of hyperpolarized 129Xe at 2 bars for in vivo lung magnetic resonance imaging". J. of App. Phys. **113** 044908 (2013).

O

[One08] Jason Darren O'Neill, "Brute Force Polarization of Xe-129". Master Phys. Thesis submitted to the University of Nottingham 2008.

[Opt15] http://www.optigrate.com/

P

[Pas74] J. Pascale and J. Vandeplanque. "Excited molecular terms of the alkali-rare gas atom pairs". J. Chem. Phys. **60** (6) 2278-2289, (1974).

[Pro10] Manual of Prospa

R

[Rõõ97] T. T. Rõõm, S. Appelt, R. Seydoux, E.L. Hahn, A. Pines, "Enhancement of surface NMR by laser-polarized noble gases". Phys.Rev. B **55** 11604 (1997).

[Rai04] H. Raich, P. Blümler "Design and Construction of a Dipolar Halbach Array with a Homogeneous Field from Identical Bar Magnets: NMR Mandhalas" Conc. in Magn. Res. Part B (Magnetic Resonance Engineering), **23**B (1) 16–25 (2004).

[Rao14] M. Rao. "Spectroscopy of dissolved 129Xe in the human brain at 1.5 T". Presentation PING 14 Hiperpolarised noble gases in Les Houches September 2014.

[Ren89] P.M. Rentzepis, D.C. Douglass, "Xenon as a solvent". Nature **293** 165 (1981)

[Rep15] M. Repetto, E. Babcock, P. Blümler, W. Heil, S. Karpuk , K. Tullney "Systematic T_1 improvement for hyperpolarized 129-xenon". Jour. of Magn. Res. 252 163–169 (2015).

[Ric02] C. V. Rice and D. Raftery. "Rubidium-xenon spin exchange and relaxation rates measured at high pressure and high magnetic field". J. Chem. Phys. **117** (12) 5632-5641 (2002).

[Rich02] D.R. Rich, T.R. Gentile, T.B. Smith, A.K. Thompson, G.L. Jones, "Spin exchange optical pumping at pressures near 1 bar for neutron spin filters", Appl. Phys. Lett. **80** 2210-2212 (2002).

[Ril13] Hughes-Riley T, Six J.S., Lilburn D.M., Stupic K.F., Dorkes A.C., Shaw D.E., Pavlovskaya G.E., Meersmann T., "Cryogenics free production of hyperpolarized ^{129}Xe and ^{83}Kr for biomedical MRI applications". Jour. Magn Res. 237:23-33 (2013).

[Rom97] M. V. Romalis, E. Miron, and G. D. Cates. "Pressure broadening of Rb D1 and D2 lines by ^{3}He, ^{4}He, N^2, and Xe: Line cores and near wings". Phys. Rev. A **56** 6 (1997).

[Ros01] M. S. Rosen. "Laser-polarized 129Xe magnetic resonance spectroscopy and imaging; the development of a method for in vivo perfusion measurement". PhD thesis, University of Michigan, (2001).

[Rus05] I. C. Ruset "Hyperpolarized ^{129}Xe Production and Applications", PhD thesis for the University of New Hampshire (2005).

[Rus06] I.C. Ruset, S. Ketel, and F.W. Hersman, "Optical pumping system design for large production of hyperpolarized Xe-129". Phys. Rev. Lett. **96** 053002-4 (2006).

[Rut99] U.Ruth, T.Hof, J. Schmidt, D. Fick, H.J. Jänsch "Production of nitrogen-free, hyperpolarized ^{129}Xe gas". Appl. Phys. B **68**, 93–97 (1999).

S

[Sah06] Indrajit Saha, Panayiotis Nikolaou, Nicholas Whiting, Boyd M. Goodson.

"Characterization of violet emission from Rb optical pumping cells used in laser-polarized xenon NMR experiments". Chem. Phys. Lett. **428** (4–6) 268–276 (2006).

[Sau97] K.L. Sauer, R.J. Fitzgerald, W. Happer, "Laser polarized liquid Xe" Chem. Phys. Lett. **277** 153 (1997).

[Sau98] K. Sauer, "Laser polarized liquid Xe". Dissertation of Princeton University (1998).

[Sea62] D. R. Sears and H. P. Klug. "Density and Expansivity of Solid Xenon". Jour. Chem. Phys. **37**, 3002 (1962).

[Sch06] J. Schmiedeskamp, H.-J. Elmers, W. Heil, E.W. Otten, Y. Sobolev, W. Kilian, H. Rinneberg, T. Sander-Thömmes, F. Seifert, and J. Zimmer, "Relaxation of spin polarized 3He by magnetized ferromagnetic contaminants". Part III. Eur. Phys. J. D **38** (2006) 445-454.

[Sch09] G. Schrank, Z. Ma, A. Schoeck, and B. Saam. "Characterization of a low-pressure high-capacity ^{129}Xe flow-through polarizer". Phys. Rev. A **80**, 063424 (2009).

[Sha00] Nadim J. Shah, Timur Ünlü, Hans-Peter Wegener, Horst Halling, Karl Zilles and Stephan Appelt, "Measurement of rubidium and xenon absolute polarization at high temperatures as a means of improved production of hyperpolarized ^{129}Xe". NMR in Biomedicine **13** (4) 214–219 (2000).

[Sli90] Slichter, Charles P "Principles of Magnetic Resonance" Springer Series in Solid-State Sciences (1990).

[Sol04] H. Soltner, P. Blümler "Dipolar Halbach Magnet Stacks Made from Identically Shaped Permanent Magnets for Magnetic Resonance". Concepts in Magnetic Resonance **36** A (4) 211-222 (2010).

[Str61] R.L. Streever, H.Y. Carr, "Nuclear Magnetic Resonance of Xe-129 in Natural Xenon". Phys. Rev. **121** 20 (1961).

[Sur97] R. Surkau, J. Becker, M. Ebert, T. Grossmann, W. Heil, D. Hofmann, H. Humblot, M. Leduc, E.W. Otten, D. Rohe, K. Siemensmeyer, M. Steiner, F. Tasset, N. Trautmann, "Realization of a broad band neutron spin filter with compressed, polarized 3He gas", Nucl. Ins. and Methods in Phys. Res. A **384** 444-450 (1997).

[Suz66] T. Suzuki "Phase diagram of the Rb-0 System and disproportionation of rubidium suboxides". Jour. of Nuc. Mat. **137** 250-255 (1966).

T

[Thi08] F. Thien, M. Friese, G. Cowin, D. Maillet, D. Wang, G. Galloway, Ian Brereton, P. J. Robinson, W. Heil and B. Thompson, "Feasibility of functional magnetic resonance lung imaging in Australia with long distance transport of hyperpolarized helium from Germany" Respirology **13**, 599–602 (2008).

[Tho14] Datasheet of Corning Pyrex glass available in Thorlabs.com

[Tor63] H. C. Torrey "Chemical Shift and Relaxation of Xe-129 in Xenon Gas".

Phys. Rev. **130** 2306 (1963).

[Tul13] K. Tullney, F. Allmendinger, M. Burghoff, W. Heil, S. Karpuk, W. Kilian, S. Knappe-Grüneberg, W. Müller, U. Schmidt, A. Schnabel, F. Seifert, Y. Sobolev, and L. Trahms, "Constraints on Spin-Dependent Short-Range Interaction between Nucleons". Phys. Rev. Lett. **111** 100801-5 (2013).

V

[Vaa13] J. Vaara, M. Hanni, and J. Jokisaari, "Nuclear spin-spin coupling in a van der Waals-bonded system: Xenon dimer". J. Chem. Phys. **138** 104313 1-9 (2013).

W

[Wag89] M.E. Wagshul and T.E. Chupp "Optical pumping of high-density Rb with a broadband dye laser and GaAlAs diode laser arrays: Application to ^{3}He polarization". Phys. Rev. A **40** 4447-4454 (1989).

[Wag91] M. E. Wagshul. "Polarization of ^{3}He by spin exchange with high density laser optically pumped Rb vapor". PhD thesis, Harvard University, (1991).

[Wag94] M. E.Wagshul and T. E. Chupp. "Laser optical pumping of high-density Rb in polarized ^{3}He targets". Phys. Rev. A **49** (5) 3854-3869 (1994).

[Wal32] I Waller. „Über die Magnetisierung von paramagnetischen Kristallen in Wechselfeldern" . Z. Phys **79** (5-6) 370, (1932).

[Wal97] T. G. Walker, W. Happer. "Spin-exchange optical pumping of noble-gas nuclei". Rev. of Mod. Phys. **69** (2) (1997).

[Wal01] D. K. Walter, W. M. Griffith, and W. Happer. "Energy transport in high-density spin-exchange optical pumping cells". Phys. Rev. Lett. **86** (15), 3264-3267 (2001).

[Wal02] D.K. Walter, W.M. Griffith and W. Happer. "Magnetic slowing down of spin relaxation due to binary collisions of Alkali-metal atoms with buffer gas atoms". Phys. Rev. Lett. **88** (9) (2002).

[Whi11] N. Whiting, N. A. Eschmann, and B. M. Goodson "^{129}Xe-Cs (D1,D2) versus ^{129}Xe-Rb (D1) spin-exchange optical pumping at high xenon densities using high-power laser diode arrays" . Phys. Rew. A **83** 053428 (2011).

[Wil97] E. Wilms, M. Ebert, W. Heil, R. Surkau. "Polarimetry on dense samples of spin-polarized ^{3}He by magnetostatic detection". Nuc. Ins. and Meth. in Phys Res. A **401** 491-498 (1997).

[Wil14] Private communication with Dr. Jim Wild, Sheffield, (2014).

[Wit14] C. Witte, M. Kunth, F. Rossella, and L. Schröder. "Observing and preventing rubidium runaway in a direct-infusion xenon-spin hyperpolarizer optimized for high-resolution hyper-CEST (chemical exchange saturation transfer using hyperpolarized nuclei) NMR". J. Chem. Phys. 140, 084203 (2014).

[Wol04] Michael Wolf. „Erzeugung höchster ^{3}He Kernspinpolarisation durch

metastabiles optisches Pumpen". Doktorarbeit. Johannes Gutenberg University (2004).

[Wol99] J. Wolber, A. Cherubini, A.S.K. Dzik-Jurasz, M.O. Leach, and A. Bifone, "Spin-lattice relaxation of laser-polarized xenon in human blood". Proc. Natl. Acad. Sci. USA **96** 3664-3669 (1999).

Z

[Zen83] X. Zeng, E. Miron, W.A. van Wijngaarden, D. Schreiber, and W. Happer, "Wall Relaxation of Spin Polarized ^{129}Xe Nuclei". Phys. Lett. A **96** 191-194 (1983).

[Zhu05] H. Zhu, I C Ruset and FW Hersman. "Spectrally narrowed external-cavity high power stack of laser diode arrays". Optic letters **30** (11) (2005).

[Zoo02] A. Zook; B. Adhyaru and C. Bowers. "High capacity production of >65% spin polarized xenon-129 for NMR spectroscopy and imaging". Jour. of Mag. Res. **159** 175-182 (2002).

Danksagung

Hiermit möchte ich mich bei allen Menschen ganz herzlich bedanken, die mich in den vergangenen Jahren unterstützt haben und somit zum Gelingen dieser Arbeit beigetragen haben.

Mein besonderer Dank gilt:

Meinem Doktorvater, der es mir ermöglicht hat diese Arbeit in einer außergewöhnlichen Gruppe anzufertigen. Besonders hervorheben möchte ich außerdem die motivierende Arbeitsatmosphäre und den immer spannenden wissenschaftlichen Austausch. Auch für die Unterstützung (and guide) beim Sprung über diverse Hürden der deutschen Bürokratie möchte ich mich herzlich bedanken.

Dr. Pedro B. für den fruchtbaren und intensiven wissenschaftlichen (und unwissenschaftlichen) Erfahrungsaustausch, seinen Humor, die gute Zusammenarbeit und das ausführliche Lesen dieses Manuskripts.

Meinen wunderbaren Kollegen (es ist unmöglich bessere zu finden): S. K., K. T., señor C. M., Anna, A. W., C. S., S. Z. (auch für das Lesen dieses Manuskripts), B. N. und A. M. für die Unterstützung und viele schöne gemeinsame Stunden.

R. J. und der Werkstatt für die ausgezeichnete Arbeit, Ratschläge und angenehme Zusammenarbeit.

C. B. (MPIP) für den Aufbau der „FVU“ und der Urversion des Filling- Systems.

Unseren Super-Sekretärinnen „C. und E.”, die in der Lage sind jedes Problem auf der Welt mit Geduld und Humor zu lösen.

Den Studenten, die zu dieser Arbeit beigetragen haben. Besonders M. F., B. N. und M. B..

A mi familia por la confianza, el Fernet con coca cola, las rabas, los Manitón, el cariño y el apoyo a la distancia.

A mi “hado madrino” Filippi por su amistad y ayuda.

A las físicas más lindas e inteligentes de la tierra: E. C. y N. A..

A mis amigos de la academia de insultos “Guillermo Francella”: A. P. F., R. B. y F. G..

Den Familia(en) M.

Besonderes an T. M..